Application of Microneedles to Enhance Delivery of Micro-particles from Gene Guns

Dongwei Zhang

A Doctoral Thesis Submitted in Partial Fulfilment of the Requirements for the Degree of Doctor of Philosophy (PhD)

Loughborough University

2009 - 2013

Abstract

Gene gun assisted micro-particle delivery system is an excellent method for the delivery of DNA into target tissue so as to carry out gene transfection in the target cells. The gene gun is primarily a particle accelerator which accelerates DNA-coated micro-particles to sufficient velocities to breach the target layer enabling the micro-particles to penetrate to a desired depth and target the cells of interest to achieve gene transfer. However, an inevitable problem in this process is the tissue/cell damage due to the impaction of the pressurized gas and micro-particles on the target.

The purpose of this research is developing a new conceptual system which improves the penetration depth of micro-particles at less imposed pressure and particle injection velocity. This is achieved by applying a microneedle array and ground slide in the gene gun system, thus a study involving microneedle assisted micro-particle delivery is conducted in this work. Microneedle array is used to create holes in the target which allows a number of micro-particles to penetrate through the skin which enhances the penetration depth inside target. The ground slide is used to load a pellet of the micro-particles and prevent the pressurized gas to avoid the impaction on the target. The operation principle is that the pellet is attached to ground slide which is accelerated to a sufficient velocity by the pressurized gas. The pellet is released from the ground slide which separates into individual micro-particles by a mesh and penetrates to a desired depth inside the target.

An experimental rig to study various aspects of microneedle assisted micro-particle delivery is designed in this PhD research. The passage percentage of the micro-particles and size of the separated micro-particles are analysed in relation to the operating pressure, mesh pore size and Polyvinylpyrrolidone (PVP) concentration to verify the applicability of this system for the micro-particle delivery.

The results have shown that the passage percentage increases from an increase in the mesh pore size and operating pressure and a decrease in PVP concentration. A mesh pore size of 178 μm and pellet PVP concentration of 40 mg/ml were used for the bulk of the experiments in this study as these seem to provide higher passage percentage and the narrow size distribution of the separated micro-particles. In addition, the velocity of the ground slide is detected by the photoelectric sensor and shown that it increases from an increase in operating

pressure and reaches 148 m/s at 6 bar pressure, A further analysis in the penetration depths of the micro-particles to determine whether they achieve enhanced penetration depths inside the target after using microneedles is carried out. A skin mimicked agarose gel is obtained from comparing the viscoelastic properties of various concentration of agarose gel in comparison with the porcine skin, which is assumed to mimic the human skin. These experiments are used to relate the micro-particle penetration depth with the operating pressure, microneedle length and particle size.

In addition, a theoretical model is developed based on the experimental data to simulate the microneedle assisted micro-particle delivery which provide further understanding of the microneedle assisted micro-particle delivery. The developed model was used to analyse the penetration depth of micro-particles in relation to the operation pressure, target properties, microneedle length and particle size and density. The modelling results were compared with the experimental results to verify the feasibility of the microneedle assisted micro-particle delivery for micro-particles delivery. As expected, both experimental and theoretical results show that the micro-particles achieve an enhanced penetration depth inside target. The maximum penetration depth of micro-particles is increased from an increase in operating pressure, microneedle length, particle size and density.

Acknowledgement

Firstly, I'm grateful to my co-supervisors Dr Diganta B Das and Professor Chris D Rielly. Under their excellent supervision with valuable advice and guidance, I was able to develop this project. Without their help, this project could not have progressed.

I would like to thank Mr Tony Eyre, Mr Mark Barron and Mr Jim Muddimer for the help of the experimental rig. Moreover, I would like to thank Mr Dave Smith, Mr Graham Moody, Mrs Kim Robertshaw and Mr Sean Creedon for their constant technical help for my lab work.

Furthermore I'd like to thank Mr Amish Patel and Mrs Sandhy Moise for their help in the experiment.

I would like to thank the Loughborough University for the financial support. I would also like to thank my dear friends - they have used their spare time to help me to improve my language.

I'd like to thank my fellow PhD students in room S169 and in the chemical engineering department for their friendship and making my time here a memorable learning experience.

Finally, I'm grateful to my family for their continuous support for these years.

Nomenclature

Symbol	Description	Unit
ν	Heat capacity ratio	-
γ	Strain	-
γ_0	Strain amplitude	%
μ	Gas viscosity	Pa· s
μ_t	Friction coefficient between particle of the target	Pa· s
μ'	Friction coefficient between particle and porcine skin tissue/gel	Pa· s
ρ	Density of air	kg/m^3
ρ_p	Density of micro-particle	kg/m^3
ρ_t	Density of target	kg/m^3
σ_y	Yield stress of the target	MPa
σ	Stress	Pa
σ_0	Stress amplitude	Pa
δ	A phase lag between the strain and stress	degrees
ω	Angular frequency	rad/sec
θ	The angle of boundary of the gap between mesh and skin	degrees
d	The penetration depth of micro-particle in the skin	m
f_d	Drag force on the micro-particle in the target	N
k	Percentage of the axial component	%
l	Travelling distance between mesh and target	m
l_z	Displacement of the separated micro-particle at axial component in the deceleration stage	m
l_r	Displacement of the separated micro-particle at radial component in the deceleration stage	m
m	Mass of an individual micro-particle	g
m_p	Mass of the pellet	g
n	Number of micro-particles in the pellet	-
r_p	Radius of the micro-particle	m
t	Time	s
u	Velocity of the ground slide	m/s
u_d	Velocity of the separated micro-particle in the target	m/s
u_r	Velocity of the separated micro-particle at radial component	m/s

u_z	Velocity of the separated micro-particle at axial component	m/s
u_1	Velocity of the separated micro-particle after passing through the mesh	m/s
u_2	Velocity of the separated micro-particle in the space between mesh and target	m/s
v_i	Velocity of the micro-particle	m/s
x	Percentage of energy loss during separation stage	%
A_p	Projected cross-sectional area of the separated micro-particle	m^2
C_d	Air drag coefficient	-
E	Kinetic energy of the ground slide	J
E_1	Kinetic energy of the separated micro-particle	J
E_{sfe}	Surface free energy of the pellet	J
E_d	Energy lose during micro-particle traveling through the space between mesh and target due to the frictional drag force	J
F_d	Air drag force	N
F_y	Yield force	N
F_f	Frictional force	N
F_i	Resistive inertial force of target material	N
G’	Storage modulus	Pa
G’’	Loss modulus	Pa
I	The impact point	-
L	Length of the barrel(the acceleration stage)	m
L_1	Space between the mesh and target	m
M	Mass of the pellet attached ground slide	g
P_1	Initial pressure to push the ground slide	bar
P_2	The pressure decreased from the initial pressure	bar
R	Radius of the ground slide/the barrel	m
Re	Reynolds number of separated particle	-
V_1	Initial volume of the receiver	L
V_2	The expanded volume	L
V_i	The velocity on impact	m/s
V_{ri}	The radial velocity component on impact	m/s
V_{zi}	The axial velocity component on impact	m/s
V_r	The velocity on rebound	m/s

V_{rr}	The radial velocity component on rebound	m/s
V_{zr}	The axial velocity component on rebound	m/s
V_{xi}	The tangential velocity component on impact	m/s
V_{yi}	The normal velocity component on impact	m/s
V_{xr}	The tangential velocity on rebound	m/s
V_{yr}	The normal velocity on rebound	m/s

Abbreviations

CDN	Converging-diverging Nozzle,
CN	Conical Nozzle
DNA	Deoxyribonucleic acid
HDA	Helium-driven Apparatus
LGG	Light gas gun
Micro-CT	Micro computed tomography
MN	Microneedle
OCT	Optical coherence tomography
PC	Polycarbonate
PG	Pneumatic Gun
PGA	Poly-glycolic acid
PPG	Powder Particle Gun
PS	Photoelectric sensor
PT	Pressure transducer
PTFE	Polytetrafluoroethylene
PVA	Poly (vinyl) alcohol
PVP	Polyvinylpyrrolidone
SC	Stratum Corneum
SEM	Scanning electron microscope
VE	Viable Epidermis

Publications

Journals

- Zhang D.W., Das D.B., Rielly C.D. (2013). Poteential of microneedle assisted micro-particle delivery: A review. Drug Delivery (in press) (Chapeter 2)
- Zhang D.W., Das D.B., Rielly C.D. (2013). An experimental study of microneedle assisted micro-particle delivery, Journal of Pharmaceutical Sciences, 102(10): 3632-3644, DOI: 10.1002/jps.23665. (Chapter 3)
- Zhang D.W., Das D.B., Rielly C.D. (2013). Microneedle assisted micro-particle delivery: Experiments using skin mimicking agarose gel. Journal of Pharmaceutical Sciences (revised version resubmitted) (Chapter 4)
- Zhang D.W., Das D.B., Rielly C.D. (2013). Microneedle assisted micro-particle delivery: Mathematical model formulation and experimental verification (submitted) (Chapter 5)
- Zhang D.W., Das D.B., Rielly C.D. (2013). Microneedle assisted micro-particle delivery: Experiments and modelling on the effects of particle characteristics (submitted) (Chapter 6)

List of Figures

List of Tables

Table of content

1. Introduction

1.1 Problem Statement

Particle gene transfer has been used for transferring genes into plant cells for many years, but this technique has been modified so that it is suitable for use in mammalian cells too. It requires a gene gun system which can accelerate deoxyribonucleic acid (DNA) coated micro-particles to breach the skin and further deliver into biological cells to achieve gene transfer. It indicates that the gene gun system is an advanced technology for the transdermal gene delivery. However, the skin provides a great resistance on the process of the particle delivery especially the top layer of stratum corneum, and the viable epidermis is the applicable layer for gene therapy which means the micro-particles require penetrating into the epidermis layer of the skin or further (Ziegler, 2008). This makes gene gun system an area of very broad research where the research community attempts to seek out a variety of ways to deliver DNA coated micro-particle to a deeper depth through the skin barrier.

In recent years various methods have been attempted to increases the penetration depth of the micro-particle, which can vary the particle size, density and velocity. However, the maximum penetration of the micro-particle only can breach the stratum corneum and end inside the epidermis layer of the tissue for the existed gene gun systems. Therefore, the epidermis layer is normally considered to be the target tissue for gene delivery due to its accessibility (Trainer et. al. 1997). However, a high pressure is required for those gene gun systems, which might damage the tissue after the impaction of the pressurized gas on the skin. In order to satisfy both reduced tissue damage and increased penetration depth of the micro-particle in the target, an innovative concept of combining microneedles with a particle delivery system, namely microneedle assisted micro-particle delivery system, is proposed in this work. The operating principle of micro-particle delivery is that a pellet of micro-particles is loaded on the ground slide which is accelerated by the pressurized gas to a sufficient velocity. The pellet will be released after the ground slide reaches the end of the barrel, separated to a narrow size distribution of small micro-particles by a mesh, and then penetrated into the target.

Microneedle assisted micro-particle delivery is a novel field of gene gun system which requires using solid microneedles to make some holes on the skin, and a number of micro-particles may penetrate further through the holes. In addition, the system is used a ground slide to prevent the pressurized gas to avoid the impaction on the skin to achieve the purpose of less tissue damage. In order to exhibit the advantage of the microneedle assisted

micro-particle delivery, a quantitative analysis between the key variables of this system and the particle penetration depth inside the target is required. Such is the major purpose of microneedle assisted micro-particle delivery research.

1.2 Objectives

The overall aim of this research is to explore a low cost way for effective micro-particle delivery into human body. Gold particle was widely used as micro carriers in biolistic bombardment because of their high density, low toxicity and chemically inert. In our research, the use of stainless steel and tungsten as a replacement for gold will be investigated due to the lower cost, and the penetration depth of stainless steel and tungsten particles will be analysed to verify the improvement of microneedle assisted micro-particle delivery if compared with any other gene gun systems. As introduced, the major method being explored is via a new injection system which is based on microneedles to overcome the tissue to achieve the effectively particle delivery process to target. This involves gaining an understanding of the micro-particle delivery process and microneedle insertion mechanics. The thesis progressively present a theoretical model that has been developed in this research and reports a microneedle assisted micro-particle delivery system which is based on this model.

The specific objectives of the research are as follows:

- Design an experimental rig based on the purposed design of the microneedle assisted micro-particle delivery.
- Mimick the porcine skin by investigating a special concentration of agarose gel which has close dynamic viscoelastic properties to porcine skin
- Investigate the passage percentage of the pellet in relation to the operating pressure, mesh pore size and PVP concentration, and further to find out the suitable mesh pore size and PVP concentration for the microneedle assisted micro-particle delivery system based on the analysis of the separated particle
- Apply the skin mimicked concentration of agarose gel in the experiment to carry out numerical analysis to identify the effects of various parameters on the particle penetration depth. The parameters considered here are the size of the microneedle, operating pressure, PVP concentration, mesh pore size and micro-particle density.
- Compare the stainless steel particle penetration depth by using microneedle assisted micro-particle delivery with particle penetration depths based on normal gene gun to

ensure the improvement of this system.

- Develop a theoretical model to relate the microneedle assisted micro-particle delivery to particle transfer process. Compare the theoretical results with the experimental results to verify the applicability of the model.
- Compare the penetration depth of tungsten micro-particles with stainless steel to determine the density and size effects on the penetration depth based on the experimental and theoretical studies.

1.3 Thesis Outline

There are a total of seven (7) chapters which make up this thesis including a final chapter on the conclusion and recommendations from this thesis. Chapter 1 presents an introduction which focus on the brief background, aims of the research and relevance of this research work.

Chapter 2 gives a background on this research include gene gun systems, recommended particle material and size, gas and particle, a description of the microneedle assisted micro-particle delivery system, microneedle design, microneedle insertion in the skin, the effect of the physical approaches on drug delivery, modelling micro-particle transport in skin to understand the basic knowledge of gene gun system for micro-particle delivery and the operation principle for the experimental rig.

Chapter 3 presents the method and materials of the experimental rig based on the purposed design of the microneedle assisted micro-particle delivery. In this chapter, the applied chemicals, and equipments are introduced. In addition, the detail experimental methods for the detection of ground slide velocity and passage percentage of the pellet after separation are explained. Based on the experimental rig, carry out numerical analysis to identify the effects of various variables on the ground slide acceleration, passage percentage. The variables considered on ground slide acceleration are materials and the size of the barrel. However, the passage percentage analysis is the major purpose. These are analysed in relation to the operating pressure, PVP concentration and mesh pore size. In addition, the pellet separation condition is analysed based on the analysis of the separated particle size. Finally, the micro-particle penetration in a 2 g/ml concentration of agarose gel is briefly discussed to investigate the improvement of the microneedle assisted micro-particle delivery.

Chapter 4 presents the improved design of the experimental rig which is specific for the analysis of the particle penetration. The upgraded experimental method and the methods of the penetration depth measurement and skin mimicking are explained. The results of the dynamic vsicoelastic property of the porcine skin and the agarose gel mimicking porcine skin are discussed. The particle penetration in the skin mimicked concentration is major objective which analysed in relation to the operating pressure, particle size, microneedle length mesh gel concentration to further demonstrate the improvement compare with the existed gene gun systems.

Chapter 5 shows the simulation study of the microneedle assisted micro-particle delivery. The detailed parameters considered in the experimental rig are introduced; thereby a theoretical model is developed based on these parameters. A comparison of the hollow and solid microneedles assisted micro-particle delivery systems is discussed briefly to state the reason to choose solid microneedles for the system using this model. Besides, a comparison of the penetration depth of stainless steel particle between the model and experimental results is detailed discussed to further to show the achievement of the enhanced penetration depth of micro-particles and the reliability of the model for the solid microneedle assisted micro-particle delivery system.

In Chapter 6 the tungsten micro-particle is applied to compare with the stainless steel micro-particles. In the experiment, the effects of the operating pressure and microneedle length on the penetration depth of the tungsten micro-particles are discussed. Besides, a comparison of the penetration depth between stainless steel and tungsten particles has been done. In the model, the penetration depth is analysed in relation to operating pressure, particle size and microneedle length. The model results are compared with experimental result to prove the advantage of microneedle assisted micro-particle delivery system and further to demonstrate the applicability of the model. In addition, the passage percentage of the tungsten pellet is illustrated and compared with the stainless steel pellet.

Conclusions and recommendations are presented in Chapter 7.

2. Literature review

2.1 Chapter Overview

Gene guns have been used to deliver deoxyribonucleic acid (DNA) loaded micro-particle and breach the muscle tissue to target cells of interest to achieve gene transfection. This chapter aims to discuss the potential of microneedle (MN) assisted micro-particle delivery from gene guns, with a view to reducing tissue damage. Using a range of sources, the main gene guns for micro-particle delivery are reviewed along with the primary features of their technology, e.g., their design configurations, the material selection of the micro-particle, the driving gas type and pressure. Depending on the gene gun system, the achieved penetration depths in the skin are discussed as a function of the gas pressure, the type of the gene gun system, and particle size, velocity and density. The concept of MN-assisted micro-particles delivery which consists of three stages (namely, acceleration, separation and deceleration stage) is discussed. In this method, solid MNs are inserted into the skin to penetrate the epidermis/dermis layer and create holes for particle injection. Several designs of MN array are discussed and the insertion mechanism is explored, as it determines the feasibility of the MN based system for particle transfer. The review suggests that one of the problems of gene guns is that they need high operating pressures, which may result in direct or indirect tissue/cells damage. MNs seem to be a promising method which if combined with the gene guns may reduce the operating pressures for these devices and reduce tissue/cell damages. There is sufficient potential for MN-assisted particle develivery systems.

2.2 Introduction

A Gene gun, involving “particle bombardment” or “biolistic delivery” is a particle accelerator, which can deliver deoxyribonucleic acid (DNA) loaded micro-particles at sufficiently high velocitiesto breach the surface of target tissue and to penetrate to a depth to achieve gene transfection in the cells. A Gene gun is considered to be a unique concept which was first used to deliver genetic materials into plant cells (Klein *et al*., 1987; Klein *et al*., 1992; Sanford *et al*., 1993; Svarovsky, 2008; Huang *et al*., 2011; O’Brien and Lummis, 2011; Manjila *et al*., 2013). The technique has been used to transfer DNA-coated micro-particles to achieve gene transfection into many types of cells and organs (e.g., Meacham *et al*., 2013; Bennett *et al*., 1999), for example, mammals (Cao *et al*., 2013; Ettinger *et al*. 2012; Da’dara *et al*., 2002; Kuriyama *et al*., 2000; Sakai *et al*., 2000; Williams *et al*., 1991), plants

(Kuriakose *et al*., 2012; Zuraida *et al*., 2010; Klein *et al*., 1992), artificially cultured cells (O'Brien and Lummis, 2011; O'Brien and Lummis, 2006), fungi (Gu *et al*., 2011; Armaleo *et al*., 1990) and bacteria (Nagata *et al*., 2010; Smith *et al*., 1992). A number of commercial gene guns have been manufactured and used for *in vivo* gene transfection in plants, living animals, cultured cells, e.g., the PowderJect system developed originally by the University of Oxford (UK) (Bellhouse *et al*., 2006), the Helios gene gun by Bio-rad, Hercules, CA (USA) (Belyantseva, 2009), and the SJ-500 portable gene gun by Biotech instrument, New Jersey (USA). The Helios and portable gene guns are shown in Figure 2.1. In a research context, Da'dara *et al*. (2002) have used a Helios gene gun to delivery Sm23-pcDNA (an integral membrane protein) to mice to evaluate the immunogenicity of the protective efficacy of the DNA vaccination. Ahlen *et al*. (2013) have used a Helios gene gun to explore a method for monitoring hepatitis B and C viruses (HBV/HCV) specific to immune responses in mouse.

Loading the micro-particles with DNA (for example onto gold particles) is an important step in using this technology as discussed by Zhao *et al*. (2012), O'Brien and Lummis (2011, 2006), Rao (2010); Satish (2009) Svarovsky *et al*. (2008) and *T*homas *et al*. (2001). However, a detailed discussion on these issues is outside the scope of these research.

Such guns have been proposed for gene delivery in the treatment of some of the major diseases such as cancer (Nguyen-Hoai *et al*., 2012; Aravindaram *et al*., 2009; Han *et al*., 2002; Chen *et al*., 2002). These researchers have fired gene loaded micro-particles into mammalians or cultured cells instead of humans to study gene expression and cell damage. For example, Yoshida *et al*. (1997) used a gene gun to deliver DNA coated Au micro-particle into the liver of living rat at 250 psi (17.2 bar) pressure, which resulted in a good gene expression but caused a number of cell deaths. The work also showed that cell damage was not obtained below 150 psi of pressure. Sato *et al*. (2000) have used various types of gene guns to transfer genes into live rodent brain tissue, which confirmed gene expression but with mechanical damage to cells. Uchida *et al*. (2009) have fired plasmid DNA into cultured mammalian cells (e.g., human embryonic kidney (HEK293) cell, human breast adenocarcinoma (MCF7) cell) using a gene gun, which showed that transfection is achieved in the cells but the cell damage occurs at operating pressures greater than 200 psi (~13.8 bar). O'Brien and Lummis (2011) have cultured HEK293 cells as a target for the biolistic transfection using a gene gun. Their

work showed that nano-particles gave a similar performance to micro-particles for biolistic transfection, but created less cell damage.

The above works show that cell damage may be a problem for biolistic micro-particle delivery due to significant gas and particle impactions on the tissue. This also means that while gene guns have been reported to be successful in many instances, they may have some disadvantages. Generally, for most gene gun systems, the maximum penetration of the micro-particle can breach the *stratum corneum* and end inside the epidermis layer of the tissue (Yager *et al*., 2013; Liu, 2006; Quinlan *et al*., 2001; Bennett *et al*., 1999). The epidermis layer is normally considered to be a target site for gene delivery where langerhans cells are located (Soliman *et al*., 2011; Liu, 2006; Quinlan *et al*., 2001; Trainer *et al*., 1997). However, a high pressure is required for most gene guns, which might damage the tissue after the impaction of the pressurized gas on the skin.

Figure 2.1: Left: The commercial hand-held gene gun of SJ-500 (Biopex, 2013), Right: The commercial Helios gene gun (Bio-rad, 2013)

Cell damage can be reduced by decreasing the particle size and/or operating pressure as both reduce the impact forces. In order to satisfy these conditions and, possibly, increase the penetration depth of the micro-particle in the target, an innovative concept of combining MNs with a particle delivery system, namely MN assisted micro-particle delivery, has been proposed recently by Zhang *et al*. (2013) (Chapter 3). The MNs are discussed in section of this chapter. The operating principle of the micro-particle delivery in this approach is that a pellet of micro-particles is loaded on a ground slide which is accelerated by a pressurized gas

to a sufficient velocity. The pellet is released after the ground slide reaches the end of a barrel in the system, and separates into micro-particles of a narrow size distribution by impaction on an open mesh; these separated micro-particles then penetrate into the desired target. The resistance of the target/skin to the penetration of the micro-particles is reduced using MN to create a number of holes through which the micro-particles can enter without the need for very high gas pressures.

MN assisted micro-particle delivery seems to be a promising approach for dry particulate delivery but the potential of this method needs to be discussed thoroughly as it is still at an early stage of development. To this end, the main types of gene gun systems for micro-particle delivery and their operating principles are reviewed. The micro-particle material and size for the previous gene guns are discussed, and the used gas and achieved particle velocity are studied as well to enrich the background of the previous gene gun systems.

In this chapter, MN arrays are discussed to understand how various geometries affect penetration of the target material and formation of holes which remain after the needles are removed. The discussion provides relevant background knowledge and a sound foundation for further improvement of gene gun systems with the help ofMN assisted micro-particle delivery. to achieve similar levels of the penetration depth, but with less cell damage. To further understand the advantage of MN assisted micro-particle delivery, a comparison with other physical cell targeting approaches is discussed. Finally, some simplified models of the micro-particle delivery in the skin are described, which will be useful in predicting the penetration depths achieved by MN assisted gene gun delivery.

2.3 Main gene guns

2.3.1 Configurations and operating conditions

Based on the principles of the operation process and driving forces, we define that the gene guns can be divided into three types, namely: powder gene gun, high-voltage electric gene gun and gas gene gun.

A powder gene gun is the original device which uses an ignition gunpowder as a driving force to promote the movement of bullets of macro-projectiles, and thus accelerating the

micro-particles which are loaded on to the bullet (Huang *et al*., 2011; O'Brien and Lummis, 2007; Zhou, 1995; Klein *et al*., 1987; Sanford *et al*., 1987). An electric gene gun uses a high voltage (HV) to vaporize water droplets; the expanding gas is used to achieve the acceleration of micro-particle (Christou *et al*., 1990). A gas gene gun releases a high pressure to accelerate the micro-particles (or micro-particles loaded ground slide) to a sufficient velocity to breach the barrier of the target (Zhang *et al*., 2013; Soliman *et al*., 2011; Liu, 2007; Kendall *et al*., 2002; Zhou, 2000).

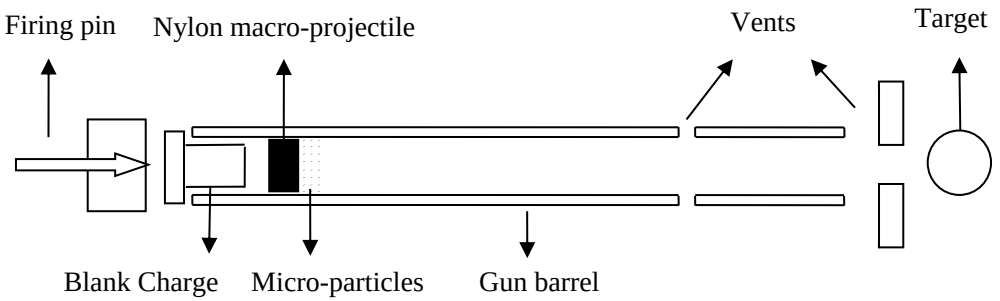

Figure 2.2: A schematic sketch of the powder gun (redrawn from Klein *et al*. (1987))

Powder gene guns were originally developed to deliver genetic material coated micro-particles into plant cells (Klein *et al*., 1987; Klein *et al*., 1992; Svarovsky, 2008; O'Brien and Lummis, 2011; Manjila *et al*., 2013). As shown in Figure 2.2, an explosion of gun powder accelerates DNA-coated micro-particles attached onto the front surface of the macro projectile. Klein *et al*. used tungsten micro-particles of 4 μm average diameter, which could be accelerated to 400 m/s. However, the explosion of the gun powder is noisy and may cause cell/tissue damage.

Zhou (1995) improved the design of Klein et al. (1987) and patented a powder gun (Figure 2.3) which is composed of a gun body, a gun barrel, a ground slide, a baffle plate and a baffle plate fixed pipe.An ignition of gunpowder caused the bullet to accelerate and hit a ground slide, which then impacts on a baffle plate. Thus, the micro-particles gain an initial velocity to leave the ground slide, pass through the central hole of the baffle plate and penetrate into the tissue. The advantage of this powder gene gun is that the use of ground slide can reduce the explosion damage to tissue. The base is designed as a shock absorber to reduce the recoil force, using a spring attached to the firing pin.

Christou *et al*. (1990) have used a type of electronic gene gun to deliver DNA-coated gold micro-particles into soybean seeds;a schematic sketch of the high-voltage electric gene gun is shown in Figure 2.4. Yang *et al*. (1990) have applied an electronic gene gun to transfer genes into tissue and liver of amouse using 1-3 μm diameter golden particles. The disadvantage of their gun is that a high voltage up to 18 kV is required to deliver a micro-particle penetration depth of 125 μm. Recently, Ikemoto *et al*. (2012) used a type of high-voltage electric gene gun, namely, an electrospray device to accelerate liquid droplets in a high voltage (12 kV) to collide with DNA coated micro-particles and deliver them into living cells.

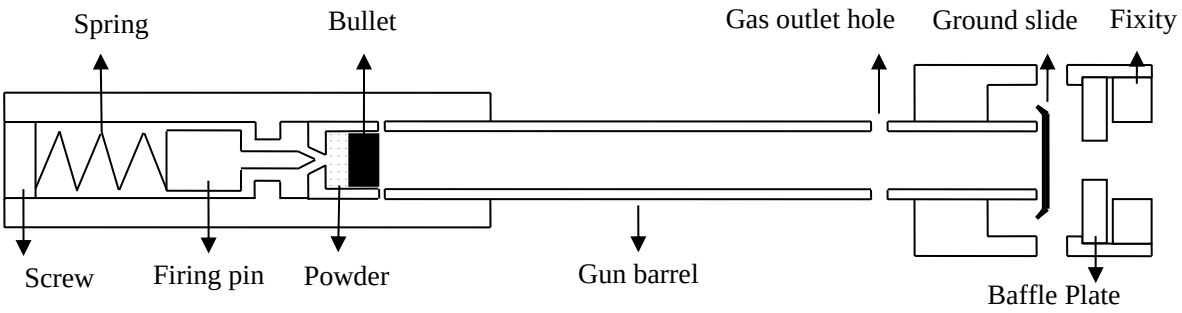

Figure 2.3: The layout of powder gene gun (redrawn from Zhou (1995))

Gas gene guns can be classified into two different delivery methods. The first uses a high pressure gas to push the micro-particle coated ground slide to achieve the goal of particle acceleration. The disadvantage is that a very high operating pressure is required to achieve the desired micro-particle impact velocity. However, the advantage is that the ground slide prevents the released gas from impacting on tissue. The second method mainly uses a high pressure gas (e.g., N_2, He) to directly push the DNA-coated micro-particles to a sufficient velocity to breach the stratum corneum, penetrate into the epidermis layer of the skin or deeper tissues. The disadvantage is that very high gas pressure may damage the tissue. The advantage is that the micro-particle can reach a desired velocity under lower operation pressure as the micro-particles have very small mass.

Using the principles of the first delivery method, Zhou (2000) has invented a kind of high-pressure gene gun which consists of a casing, the compressed gas inlet pipe, emitting cavity and bombarding cavity. The schematic diagram of this gun is shown in Figure 2.5 which shows both the states of the gun before and after operation. The emitting cavity consists of an air storage house, membrane, bullet, baffle plate and sample holder. The

membrane will be ruptured when the air storage house reaches a certain pressure. High pressure gas is able to accelerate the bullet to the baffle plate. Since the bullet is blocked by the baffle plate, the coated particles will leave the surface of the bullet, go through the centre hole of the baffle plate and launch into the sample, thus completing the gene injection. In addition, the gas will be released from the vent hole. It has been claimed that this instrument has good stability, high efficiency, does not produce impurities, and particles can also attain a higher initial speed. However, it is generally applied for plant tissues.

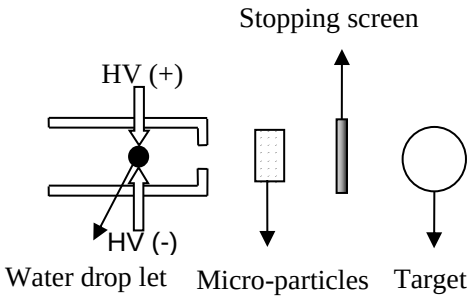

Figure 2.4: The schematic sketch of the high-voltage electric gene gun (redrawn from Christou *et al*. (1990))

Mitchell *et al*. (2003) have conducted many experimental and numerical studies on the light gas gun (LGG) as shown schematically in Figure 2.6. The LGG uses a high pressure helium gas to drive the micro-particle coated ground slide to a certain velocity. In this case, the polystyrene particles of 99 μm diameter have been usedand the impact velocities of the particles have been shown to reach 170, 250 and 330 m/s under 20, 40 and 60 bar operation pressures.

Williams *et al*. (1991) have studies a helium-driven gene gun which is somewhat similar to the design of Zhou's (2000) as shown in Figure 2.7. In this case, a membrane in the system breaks after the gas pressure reaches a certain value. The micro-projectiles are accelerated by the helium gas and separated well by a stopping screen. In addition, the large particle is blocked by a screen to avoid tissue damage. In this case, golden particles of 1 - 3 μm and 2 - 5 μm diameters have been fired and penetration depths of 150 μm and 200 μm have been obtained in a mouse liver under 1300 psi operating pressure.

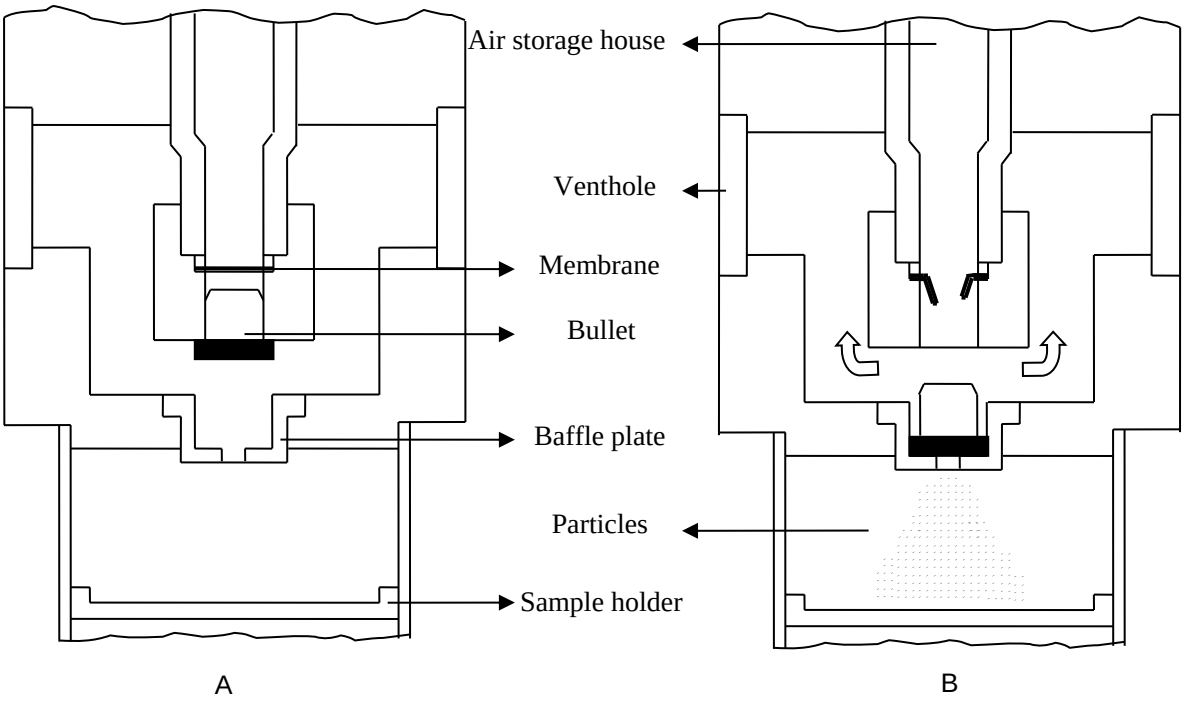

Figure 2.5: The schematic diagram and principle of high-pressure gas gene gun (redrawn from Zhou (2000))

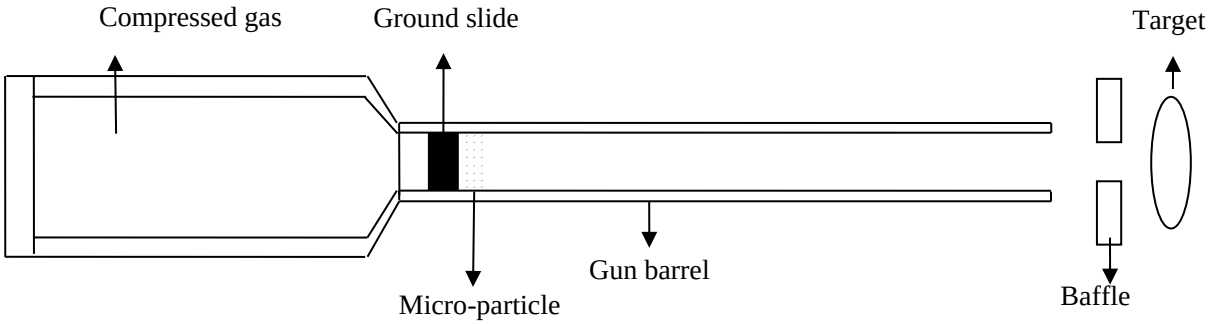

Figure 2.6: The schematic sketch of light gas gun (redrawn from Mitchell *et al*. (2003))

Kendall (2002) has reported a contoured shock tube which is shown in Figure 2.8. In this case, the compressed gas will pressurize the membrane, and the micro-particle will be accelerated by a shock wave as the gas pressure rises to the point where the membrane ruptures. Liu *et al*. (2004a) and Liu (2006) have described an injection device, namely PowderJect (Figure 2.9), which uses helium gas as the source of momentum. A triggeractuates a mechanism to release helium gas which expanded to accelerate the micro-particles to a sufficient momentum to pierce the outer layer of the target and into the cells of interest.

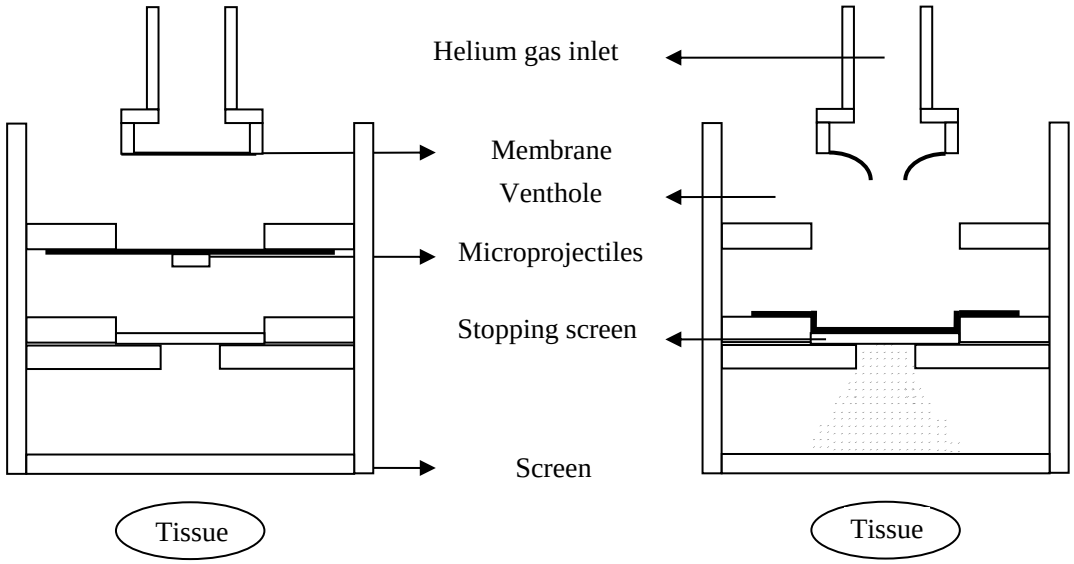

Figure 2.7: The schematic sketch of helium-driven gene gun (redrawn from Williams *et al*. (1991))

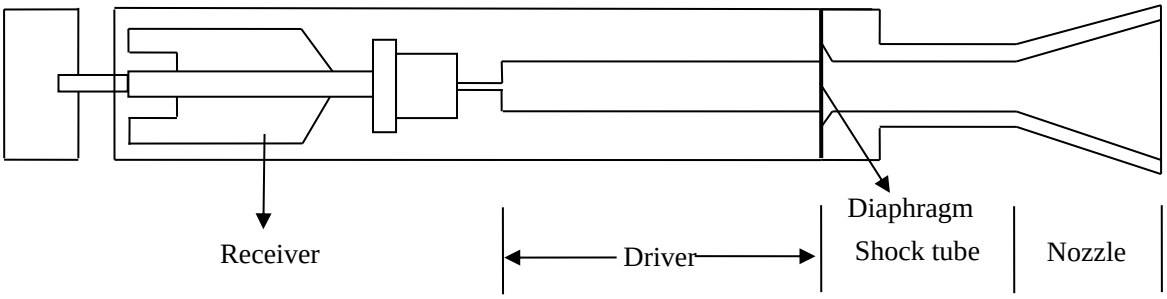

Figure 2.8: The schematic diagram of contoured shock tube (redrawn from Kendall (2002))

Zhang *et al*. (2007) have introduced the principle of the Helios gene gun which contains acceleration, separation and deceleration stages. The process of micro-particle delivery is shown in Figure 2.10. This gene gun uses helium gas to accelerate DNA-coated micro-carriers which are separated by a stopping screen. The separated micro-particles exit from the gene gun at high speed, penetrate the tissue to the targeting area, enter into the cell and hit the nucleus membrane.

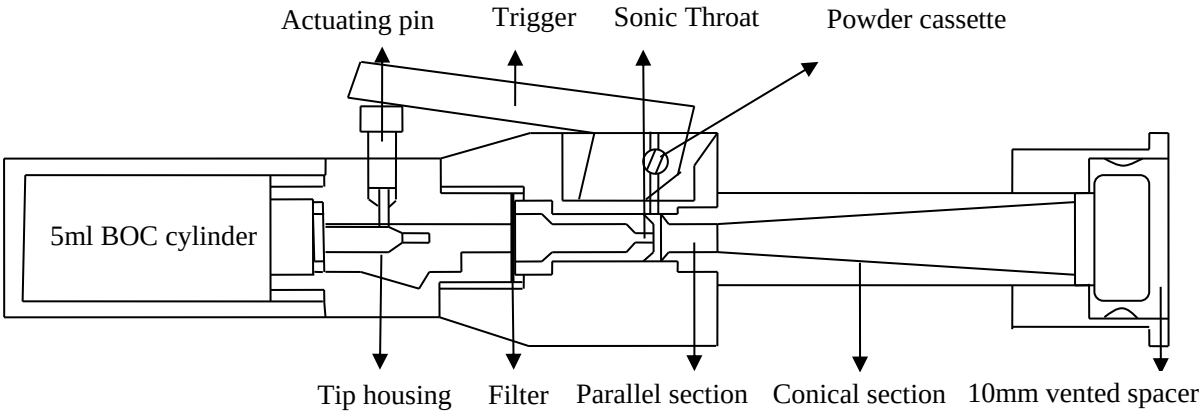

Figure 2.9: A schematic diagram of the PowderJect (redrawn from Liu (2006))

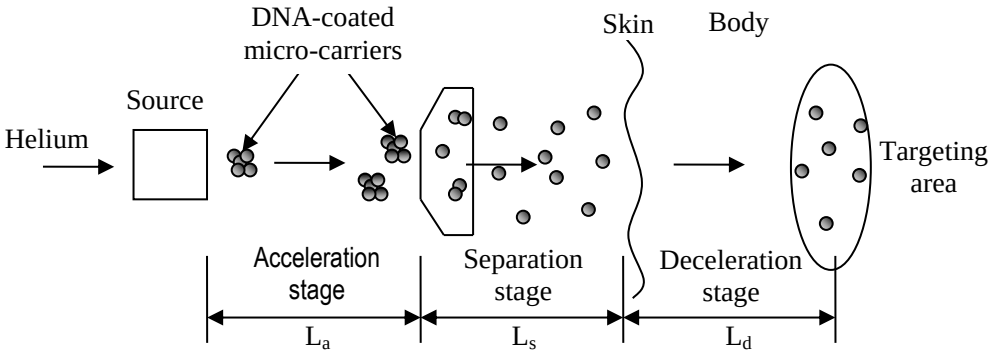

Figure 2.10: Gene transfer stages of the biolistic gene gun (redrawn from Zhang *et al*. (2007)); L_a, L_s and L_d are the distance of acceleration, separation and deceleration stages.

In addition, Zhou (2007) has created a special liquid gene sprayer (Figure 2.11) which is different from the above three gene gun types. It has been used to deliver liquid-form medication into the human bodyand consists of an interconnected casing and magazine. The magazine comprises of a hollow cylinder and sliding piston rod set; emission holes are arranged at the front end of the cylinder and the front end of the casing is fixed to rear end opening. An energy-storage driving mechanism consists of a spring and impeller and set in the internal cavity of the casing. The impeller moves backward to press the spring to store he energy, and pushes forward by a driving force from the released spring. This device uses a small volume energy storage device to inject the required amount of biological gene, and does not need any separate air supply equipment; it is easy to handle and carry. It uses the liquid as the DNA particle's carrier and hence golden particles are not required in this device. The DNA particles will be suspended in the liquid. Before using this device, the head of the

hollow cylinder is inserted into the DNA particle coated liquid, and the sliding piston rod is pulled outto extract the liquid and load the gun. Then the spring is compressed very tightly, storing energy, which is released to (see Figure 2.11a). accelerate the impeller and sliding piston rod; then the DNA particle coated with liquid are pushed out from the emission hole and penetrate into the tissue of plant or human to the target cells of interest. The state of the liquid gene gun after injection is shown in Figure 2.11b.

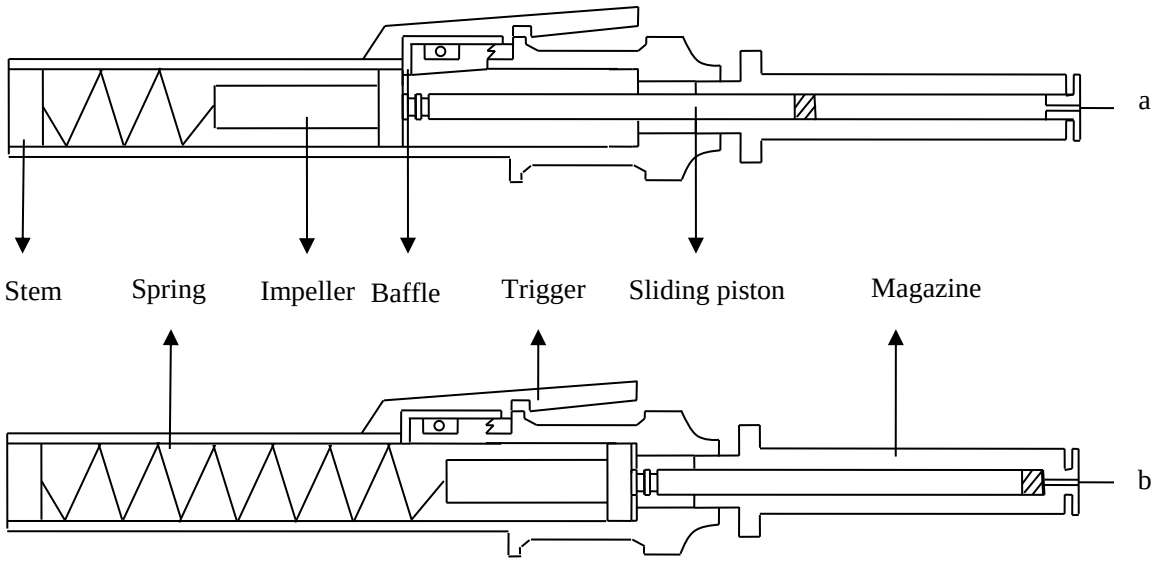

Figure 2.11: The liquid gene sprayer: A: The liquid gene gun at energy storage state, B: The state of liquid gene gun after injection (redrawn from Zhou (2007))

Recently, Menezes *et al*. (2012) have designed an advanced laser plasma jet (see Figure 2.12) to deliver DNA-coated micro-particle. The operating principle is that a laser beam is fired and ablates a thin aluminum foil, using lenses for focusing. The laser ablation is confined by the BK7 glass overlay to improve performance. Thus, it causes the foil to evaporate into an ionized vapor and the sudden blow-off causes a shock wave to breach the foil to accelerate DNA coated micro-particles. The device provides micro-particles impact velocities of up to 1100 m/s, which is faster than other gen guns (e.g. CST, LLG). However, this technique is costly due to the use of laser ablation.

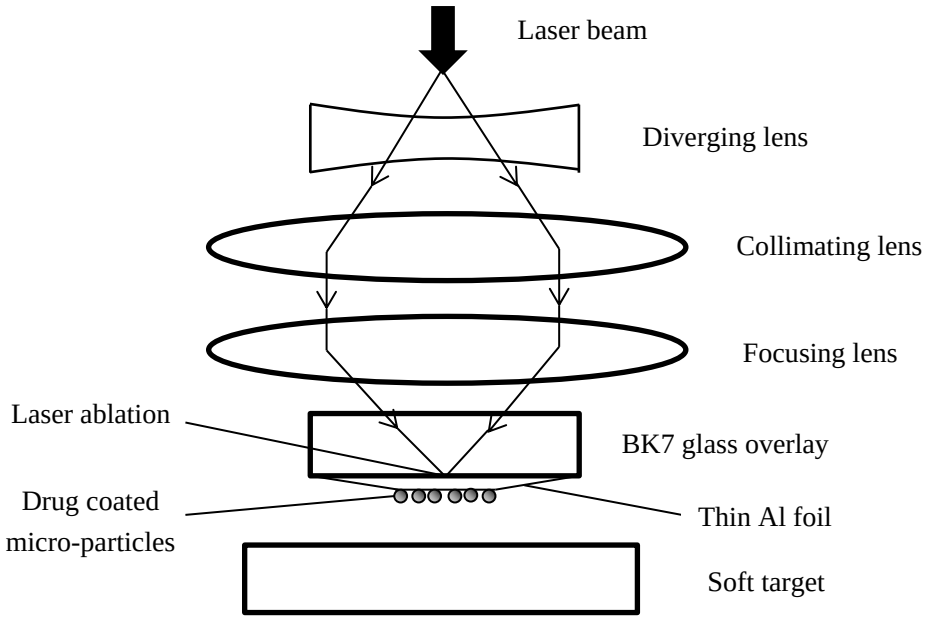

Figure 2.12: The schematic of the laser plasma jet (redrawn from Menezes *et al*. (2012))

2.3.2 Micro-particle material and size

The materials and size of the micro-particles which are used in gene guns have significant importance on the operation of the system, e.g. by determining the routes and extent of particle penetration into tissue. In general, the routes of the micro-particle penetration in the tissue are normally divided into two types, which are the extracellular and intercellular routes (Bryan et al., 2013; Soliman, 2011; Mitchell et al., 2003). As presented in Figure 2.13(a-b), the penetration routes of the micro-particles in tissue depend on the particle size. The extracellular route is followed for large particle delivery, e.g., for epidermal powder immunization (Soliman, 2011; Hardy et al., 2005). An illustration of the range of particle material and sizes for the relevant gene gun systems is listed in Table 2.1. It shows that the extracellular route is normally followed for the less dense materials (e.g., stainless steel, polystyrene and glass) with diameters ranging from 15 to 99 μm. Hardy et al. (2005) have reported that particle diameters ranging from 25 to 100 μm are expected to follow the extracellular route, as their momentum is insufficient to breach the target barrier of target, due to the combination of relatively low density and small size. It has been recommended that stainless steel or polymer micro-particles should be used for extracellular routes, due to their biocompatibility and low cost (Soliman, 2011; Sung et al., 2011; Singh and Dahotre, 2007; Binyamin et al., 2006; Disegi et al., 2000).

In contrast, the intercellular route (e.g. for DNA immunization), uses smaller size, but much more dense gold or tungsten micro-particles (Soliman, 2011; Mitchell et al., 2003). In order to deliver DNA into cells effectively, dense materials are preferred which are prepared into micro-particles of diameters ranging from 0.6 to 6 μm (Soliman, 2011; Rao, 2010; Hardy et al., 2005) which are also smaller than the cell diameters. High-speed micro-particles breach the skin and may penetrate through the individual cell membranes. It is well known that the most recommended material of these micro-particles for gene gun system is gold due to its high density, low toxicity and lack of chemical reactivity (Valenstein, 2012; Rosi et al., 2006; Macklin, 2000). However, tungsten micro-particles have also been used as micro carriers in gene gun systems, due to their lower cost. Tungsten particles have some disadvantages for genetic transformation, such as non-biocompatibility and toxicity (Bastian et al., 2009; Yoshimisu et al., 2009; Russell et al., 1992). Recently, Hou et al. (2013) have used titanium dioxide (TiO_2) for biolistic micro-particle delivery due to their biocompatibility (Singh and Dahotre, 2007) and low density (2 g/cm^3) which may reduce the cell damage after particle impaction. The particle impaction may cause cell damage (O'Brien and Lummis, 2011; Sato et al., 2000), which is a significant area for gene gun research.

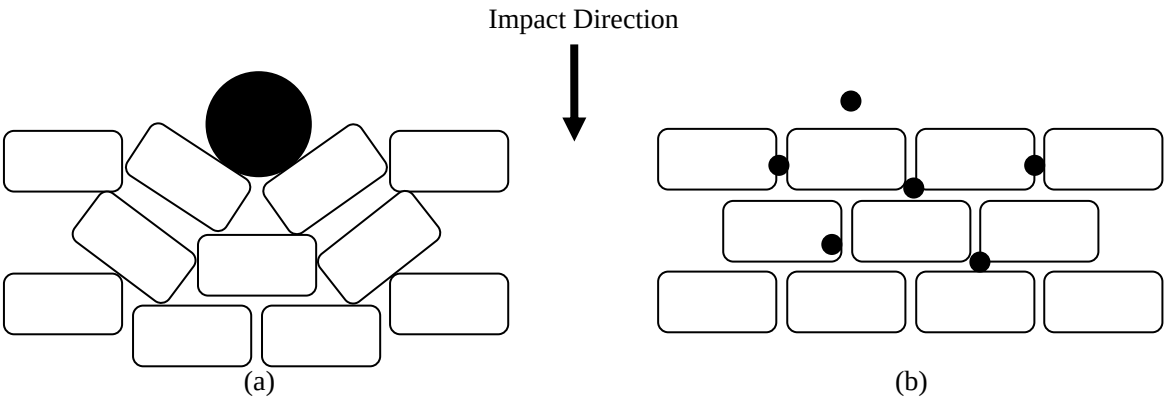

Figure 2.13: Schematic diagram of the extracellular and intercellular failure mechanisms (a): extracellular failure mechanism for large particles (b): intercellular failure mechanism for small particles (redrawn from Mitchell *et al*. (2003)).

Table 2.1: Illustration of the particle material and size for the relevant gene gun systems

Type of gene gun	**Material of particles**	**Particle density(g/cm3)**	**Average diameter of micro-particles(μm)**	**Reference**
Powder particle gun	Tungsten	19.25	4	Klein *et al*. (1987)
Helium-driven apparatus (HDA)	Tungsten	19.25	3.9	Williams *et al*. (1991)
	Gold	19.3	1-3, 3-5	
Conical nozzle (CN)	Polymeric	0.9	4.7, 15.5 and 26.1	Quinlan *et al*. (2001)
Converging-diverging nozzle (CDN)	Polystyrene	1.05	4.7	Kendall *et al*. (2004a)
Pneumatic gun (PG)	Gold	19.3	0.47 ± 0.15, 1.1 ± 0.1	Rinberg *et al*. (2005)
	Silicon	2.33	2 – 18	Zilony *et al*. (2013)
	Gold	19.3	1.6	
Light gas gun (LGG)	Stainless steel	8.0	25	Mitchell *et al*. (2003)
Contoured shock tube (CST)/LGG	Polystyrene	1.05	15.5, 25.2, 48 and 99	
CST	Gold	19.3	3.03	Truong *et al*. (2006)
	Polystyrene	1.05	15 and 48	
	Glass	2.5	46	
	Gold	19.3	2.7 and 3.5	
	Polystyrene		39 ± 1	Liu *et al*. (2006)
Helios gene gun	Gold	19.3	0.6, 1.0 and 1.6	Uchida *et al*. (2009)
			1	O'Brien and Lummis (2011); Kuriakose *et al*. (2012); Cao *et al*. (2013)
Biolistic PDS/1000 Helium system	Gold	19.3	0.6, 1.0 and 1.6	Zuraida *et al*. (2010)
BioWare low pressure gene gun	Gold	19.3	1	Yen and Lai (2013)

2.3.3 Gas pressure and particle velocity

Up to now, gene gun systems have been widely used to deliver DNA loaded micro-particles into cells for research of DNA transfection, e.g., CST (Rasel et al., 2013; Liu, 2008; Truong et al., 2006; Liu et al., 2006; Kendall, 2002) and Helios gene gun (O'Brien and Lummis, 2011; Belyantseva, 2009). Helium and compressed air gases are often used as driving forces to accelerate micro-particles for gene gun system. Especially, helium gas is recommended for most gene gun systems due to its non-toxic, low density, lack of chemical inactivity and high compressibility factor (Marrion et al., 2005), which allow the particles to reach higher velocities (Tekeuchi et al., 1992). Compressed air is often used as a substitute for helium due to its lower cost.

The gas pressure is a major factor which should be considered for gas gene gun systems. It directly affects the velocity of the micro-particles, e.g., Liu et al. (2008) demonstrated that 1.8 μm diameter gold micro-particles can reach a velocity of 580, 650, 685 and 710 at 3, 4, 5 and 6 MPa, respectively. In addition, the velocity is also related to the micro-particle size and density: particle velocity is increased from an increase in operating pressure and a decrease in particle size.

Along with the development of gene gun technology, the achievable particle velocity and penetration depth in the target vary between gene gun systems. For example, Quinlan et al. (2001) have applied a conical nozzle to accelerate polymeric micro-particles of 4.7, 15.5 and 26.1 μm diameters, to reach velocities of 350, 460 and 465 m/s at 60 bar pressure, respectively. A contoured nozzle has been tested by Quinlan et al. (2001) who employed 60 bar to accelerate polymeric micro-particles of 4.7 μm diameter to a velocities of about 1000 m/s, but 26.1 μm diameter of particles only reached 740 to 810 m/s. The velocity of polymeric micro-particles of 15.5 μm diameter only reaches 330 m/s at 60 bar for the LGG system (Mitchell et al., 2003). Kis et al. (2012) have concluded that the particle velocity reached about 700 m/s for CST (Liu et al., 2006) and range from 200 to 800 m/s for converging-diverging nozzles (Liu et al., 2004b; Kendall, 2002; Quinlan et al., 2001). Recently, Menezes et al. (2012) have operated an advanced laser plasma jet to drive gold micro-particles of 1 μm diameter to achieve an average velocity of 1100 m/s within a distance of only 10 mm. The particular achievements (e.g., particle velocity, operating pressure and penetration depth) for various gene gun systems are listed in Table 2.2.

Table 2.2: Illustration of the materials and size of micro-particles used in gene gun systems

Type of gene gun	**Material and average diameter of micro-particles**	**Operating pressure (bar)**	**Velocity at impact (m/s)**	**Target and maximum Penetration depth in target**	**Reference**
PPG	Tungsten, 4 μm	N/A	430	Onion, 40 μm	Klein *et al*. (1987)
HAD	Gold, 1 - 3 μm	90	N/A	Mouse liver tissue, approximately 130 μm	Williams *et al*. (1991)
CN	Polymers, 4.7, 15.5 and 26.1 μm	60	350, 460 and 465	N/A	Quinlan *et al*. (2001)
LGG	Stainless steel, 25 μm	20	170	Canine buccal mucosa, 124 μm	Mitchell *et al*. (2003)
CST	Gold, 3.03 μm	60	550	Canine buccal mucosa, 60 μm	
CST	Gold, 1 ± 0.2 μm	40	580	Human skin, 66 μm	Kendall (2002)
CST	Polystyrene, 39 μm	60	570 ± 14.7	N/A	Liu *et al*. (2006)
Helios Gene Gun	Gold, 40 nm and 1 μm	5	N/A	Mouse ear tissue, 50 ± 11 μm and 31 ± 6 μm	O'Brien and Lummis (2011)
Laser plasma jet	Gold, 1 μm Tungsten, 1 μm	N/A	1100	N/A	Menezes *et al*. (2012)

From the above studies, it can be concluded that the operating pressures for gene gun systems generally vary from 20 to 60 bars. Xia et al. (2011) have suggested that the pressure should be held below about 13 bar to minimise damage from the impaction of pressurized gas on soft tissue. Uchida et al. (2009) achieved gene transfection is cells but noted damage if the

operating pressure is over 13 bar. These reports demonstrate that cell death is unavoidable for many of the current generation of gene gun systems. Mitchell et al. (2003) show that golden micro-particles of 3.03 μm diameter employed at 60 bar pressure in the CST only reach a maximum penetration depth of 60 μm in the canine buccal mucosa. Normally, the viable epidermis layer of skin is the target area for gene gun systems. Mitchell et al.'s (2003) results show that micro-particles require a still higher velocity to penetrate through the *stratum corneum*, which means higher operating pressures are necessary. However, Mitchell et al. (2003) also show stainless steel micro-particles of 25 μm diameter can achieve 124 μm penetration depths in the canine buccal mucosa at 20 bar pressure (see Table 2.2). But O'Brien and Lummis (2011) show that cultured cells are damaged by gold micro-particle of 1 μm diameter, when operating at 3.4 bar pressure using a Helios gene gun. They indicate that stainless steel micro-particles of 25 μm diameter impact on the tissue at a velocity of 170 m/s will damage the target tissue and cells. Thus, a new concept of applying MN to micro-particle delivery, which may reduce the cell damage, is discussed in section 2.5.1.

2.4 Microneedles

2.4.1 Types and configurations of microneedles

Henry and Prausnitz's group (1998) are widely regarded as the first to have developed a method of transdermal drug delivery using MNs, which has gradually developed for various applications of drug delivery. MN arrays are minimally invasive device that bypass the outer layer of skin, namely the *stratum corneum*, to achieve enhanced transdermal drug delivery (Olatunji et al., 2013; Donnelly et al., 2012; Prausnitz and Langer, 2008). MN are normally separated into two categories, namely, solid and hollow (Koelmans et al., 2013; Han et al., 2008; Qi et al., 2007). Each of these can be made of different materials and used for various functionalities, depending on their designs. The most common materials used for fabricating MN are metal, silicon, and polymer (Kim et al., 2012; Memon et al., 2011; Zhao et al., 2006). The primary metals used for MNs are stainless steel (Kim et al., 2012; Quan et al., 2010; Bal et al., 2008; Martanto et al., 2004) and titanium (Kim et al., 2010; Fermandez et al., 2009; Parker et al., 2007). Metal MNs have the advantages of low cost, tougher hardness, ease of penetration into the tissue and they are not easily broken in the tissue. Silicon and silica materials have better biocompatibility than metallic materials, but they are expensive (Chen et al., 2013, 2008). Furthermore, they break up more easily and fragments may be left inside the tissue after MN removal (Memon et al., 2011; Zhao et al., 2006). However, silicon is the first

material used to fabricate MNs for pre-treatment of skin prior to patch application, e.g., Henry's group (1998) have used solid conical silicon MNs (Figure 2.14a) with a height of 0.15 mm, inner diameter of 80 μm and tip diameter of 1 μm to increase skin permeability and to provide an effective delivery of drugs to diffuse through the skin. Mikszta et al. (2002) used a silicon MN array (see Figure 2.14b) for gene delivery in skin.

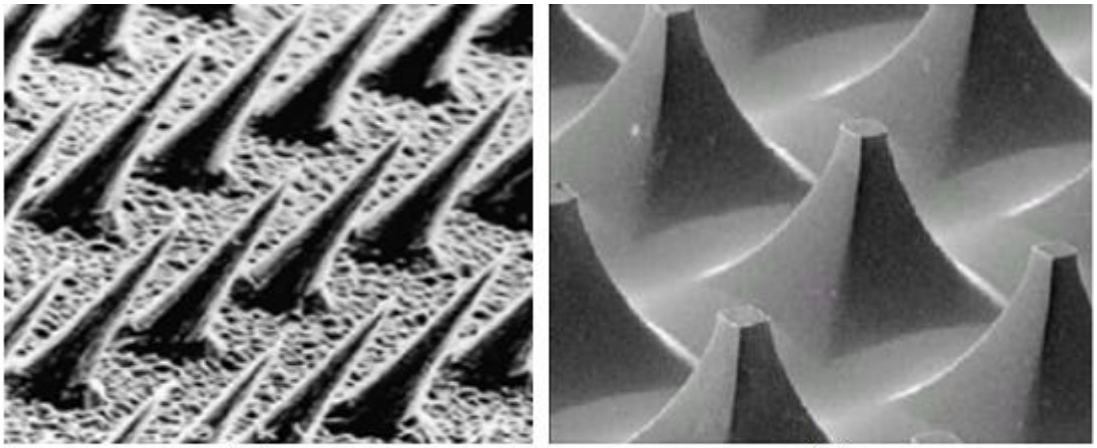

Figure 2.14: (a). Solid conical microneedle arrays (Henry *et al*., 1998) (b) Silicon microneedle array used for gene delivery in skin (Mikszta *et al*., 2002).

Polymeric materials are a cheap option which can exhibit biocompatibility and biodegradability, but the hardness is generally lower (Nayak and Das, 2013; Oh *et al*., 2008; Han *et al*., 2007; Park *et al*., 2005). Various types of polymer have been used for fabricating MNs, such as poly-glycolic acid (PGA) (Park *et al*., 2006, 2005) and polycarbonate (PC) (Han *et al*., 2007). Park *et al*. (2005) have fabricated a PGA solid MN array with needle length of 1500 μm, base diameter of 200 μm tapering to tip diameter of 20 μm. An example of solid polymer MN array is shown in Figure 2.15a. Recently, Donnelly *et al.* (2011) have used poly (vinyl) alcohol (PVA) to fabricate solid MN arrays with a needle height of 600 μm, base width of 300 μm, and MN interspacing of 300 μm. As can be seen from Figure 2.15b, MNs have been fabricated into uniform conical-shaped needles.

(a)

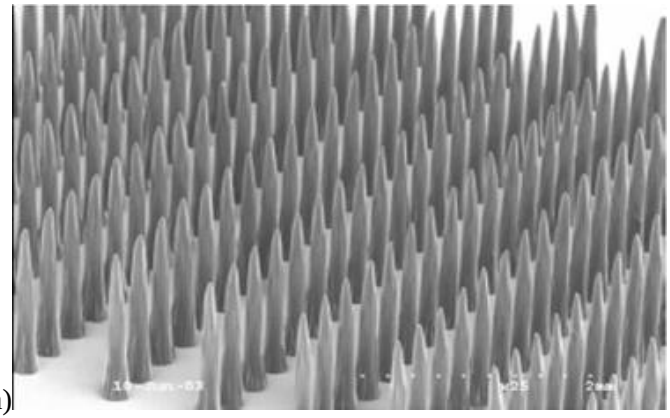

(b)

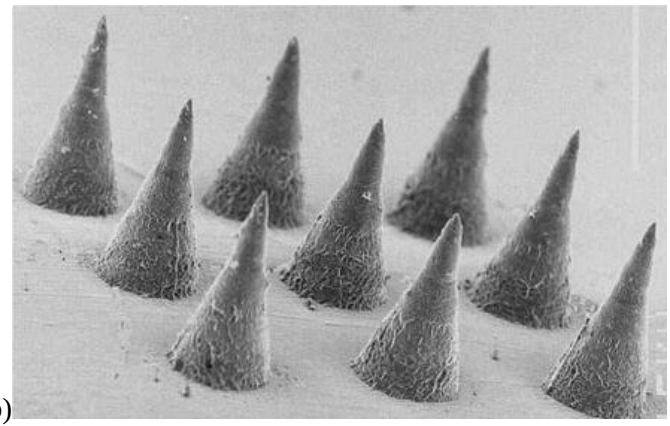

Figure 2.15: (a): Solid MN array made with the help of PGA (Park *et al*., 2005) (b): Solid MN array made with the help of PVA (Donnelly *et al*., 2011)

Hollow MN arrays are normally used for fluid infusion of liquid drug and nanoparticles into the skin (Han *et al.*, 2008). However, they are not widely used due to their costly and complex fabrication methods (Zhu *et al*., 2012). An example of the hollow MN array designed by Stoeber *et al*. (2000) is shown in Figure 2.16a. It is a hollow conical MN array with a height of 200 μm and a channel diameter of 40 μm. McAllister *et al*. (2000) have improved Henry *et al*.'s (1998) design, by inserting a hole in the centre of each MN to fabricate a hollow silicon MN array.

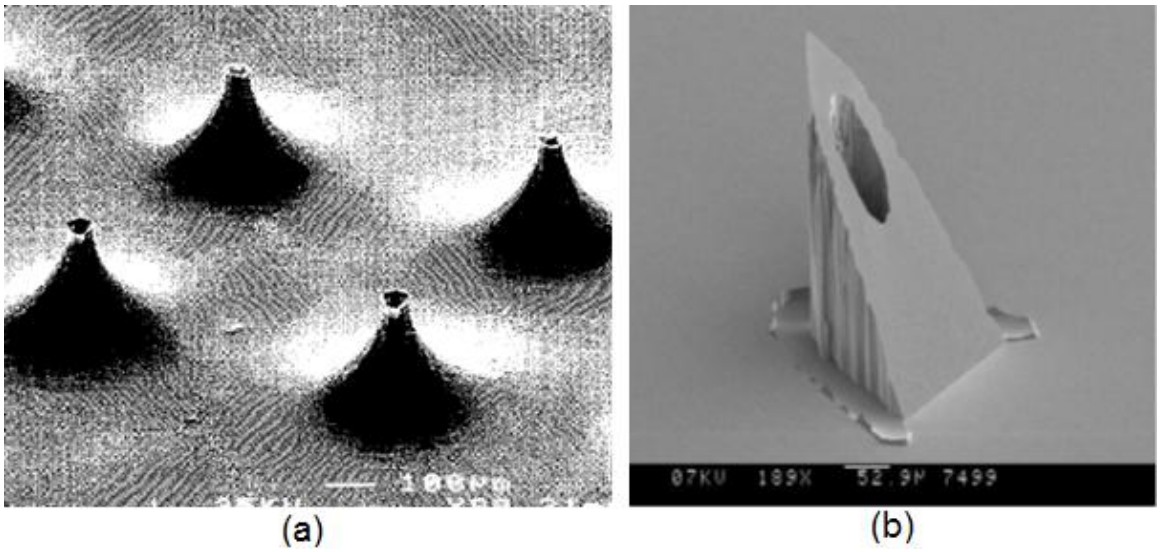

Figure 2.16: (a) Hollow conical MN arrays on the right (Stoeber *et al*., 2000) (b) hollow silicon MN array with sloping side walls (Gardenier *et al*., 2003)

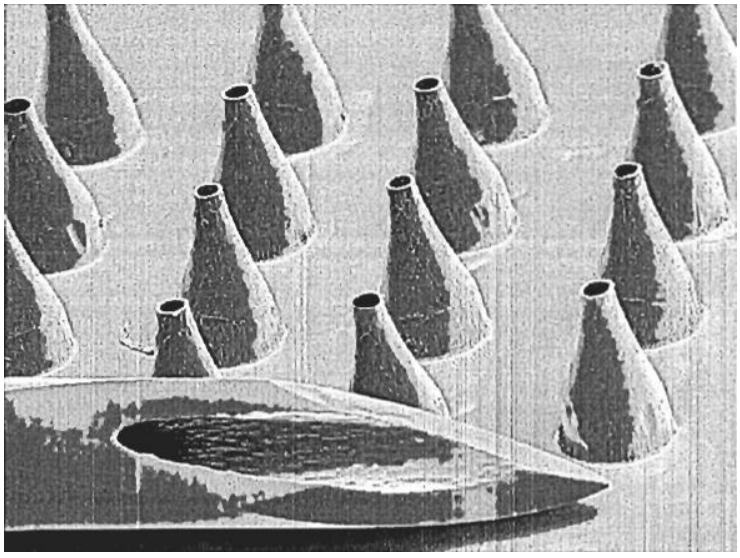

Figure 2.17: Hollow metal MNs (Davis *et al*., 2004)

Subsequently, Gardenier *et al*. (2003) have designed a hollow silicon MN array with sloping side wall, which is shown in Figure 2.16b. The length of the needles varies between 150 and 350 μm, with a base diameter of 250 μm (measured at the widest section) and a maximum hole width of 70 μm. The centre of the hole is positioned 40 μm from the tip of the needle. Davis *et al*. (2004) have used a hollow metal MN array (Figure 2.17) with a tip diameter of 75 μm, base diameter of 300 μm, wall thicknesses of 5 μm and heightof 500 μm to measure the

required force for the insertion of MNs into the tissue. They reported that a force ranging between approximately 0.1 – 3 N is sufficient to penetrate a single MN into the tissue.

Until now, MN have been developed as a minimally invasive means to deliver genes via the transdermal route (Tuan-Mahmood *et al*., 2013; Coulman *et al*., 2009; Henry *et al*., 1998), e.g., Chabrai *et al*. (2004) have successfully used micro-fabricated silicon MNs for non-viral gene delivery without causing pain. Recently, we have proposed the use MNs with a gene gun system to assist the micro-particle delivery in the skin. In particular, solid MNs can create holes in the tissue to provide an environment for the penetration of high-speed micro-particles. Furthermore, hollow MNs may allow a number of micro-particles to go through the hollow needles and penetrate to a greater depth into deeper tissue layers (epidermis) to be gene transfected. However, the waste of micro-particles is likely to be higher as the hollow MNs have blockage problems.

There have been a number of studies which report on the effects of MNs types and configuration on drug delivery (Han and Das, 2013; Olatunji et al., 2012; Al-Qallaf and Das, 2009a,b, 2008; Al-Qallaf et al., 2009a,b, 2007; Davidson et al., 2008). The current contribution will focus on the most relevant MNs types and configurations; reviews of other aspects related to the application of MN may be found elsewhere (Olatunji and Das, 2011, 2010).

2.4.2 Microneedle insertion in skin

MNs can overcome a target surface to provide an advantageous condition for micro-particle delivery (Zhang et al., 2013). Human skin consists of two distinct macroscopic layers called the dermis and the epidermis (Marks et al., 2006; Parker, 1991; Phipps, 1988) which are shown in Figure 2.18. The epidermis layer consists of the *stratum corneum* (SC), the *stratum basale* (or *stratum germinativum*), *stratum sinosum*, and the s*tratum granulosum* (Tortora et al., 2011; Marks et al., 2006; Holbrook, 1994). The top layer of the skin is the SC which is the major barrier for entry of foreign substances. The thickness of the epidermis varies with gender, age, ethnicity and the regions of the body, but has an average thickness of between 20 and 100 μm (Matteucci et al., 2009; Schaefer and Redelmeier, 1997). The thickness of the *stratum corneum* also varies with the above conditions, but the average thickness is between 10 and 20 μm (Mohammed et al., 2012; Holbrook et al., 1974).

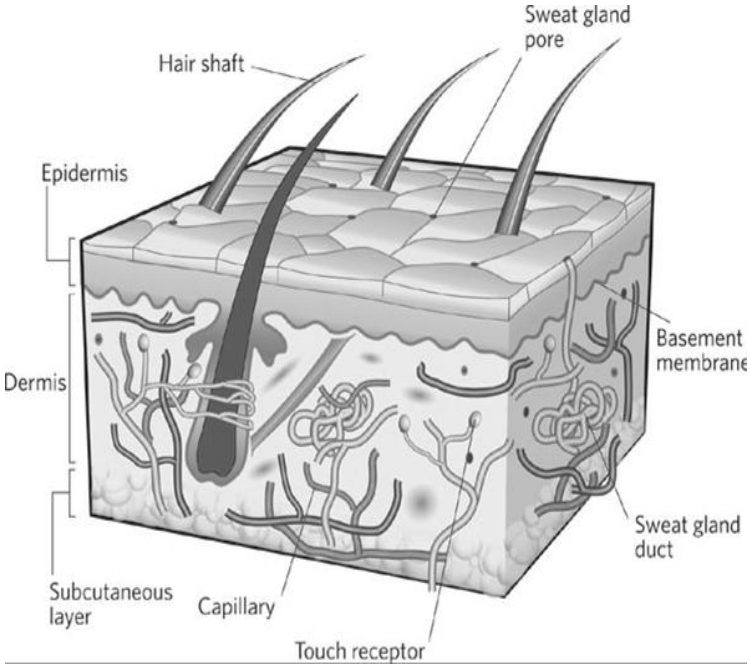

Figure 2.18: The structure of the skin (MacNeil, 2007)

Normally, MN insertion is painless as it simply penetrates the skin surface without reaching the dermis layer, which contains the nerves ending. (Gupta *et al*., 2011a; Silpi *et al*., 2011; Donnelly *et al*., 2010a; Henry *et al*., 1998). Pain sensation also depends on the MN designs which is generally small enough to avoid significant damage to the nerves in the tissue (Shah *et al*., 2011; Palastanga *et al*., 2006; Kaushik *et al*., 2001). Also, as pain sensation is related to the MN design, an increased size increases the likelihood of stimulating the nerves (Sachdeva and Banga, 2011; Shah *et al*., 2011; Gupta *et al*., 2011a,b; Gill et al., 2008). There are a number of clinical studies which show that MNs insertions into skin are painless or the pain is undetectable. For example, Mikolajewska *et al*. (2010) have used polymeric MN cones with needle height of 644 μm, base diameter of 217 μm tapering to tip diameter of 41 μm to progress the skin pre-treatment and report that the MNs insertion is a painless process. Previously, Haq *et al*. (2009) have used several MN arrays with lengths of 180 and 280 μm and compared the pain responses of a number of subjects for these MNs with the the pain responses from hypodermic needles. They indicated that hypodermic needle is painful after insertion into skin, and the pain response of MN insertion is less and decreases with a decrease in needle height.

The irregular surfaces and viscoelasticity of skin causes difficulty with MN insertion. In addition, the skin is generally folded after the insertion of MNs, which may cause MNs to pierce partially, depending on the MN length (Verbaan *et al*., 2008). Thus, there is a need to understand the required force to insert a given MNs in the skin; the depth of MN penetration into the skin is directly related to the used force for penetration (Olatunji *et al*., 2012; Donnelly *et al*., 2010b). In addition, the depth of MN penetration in the skin is dependent on the length of MNs (Badran *et al*., 2009).

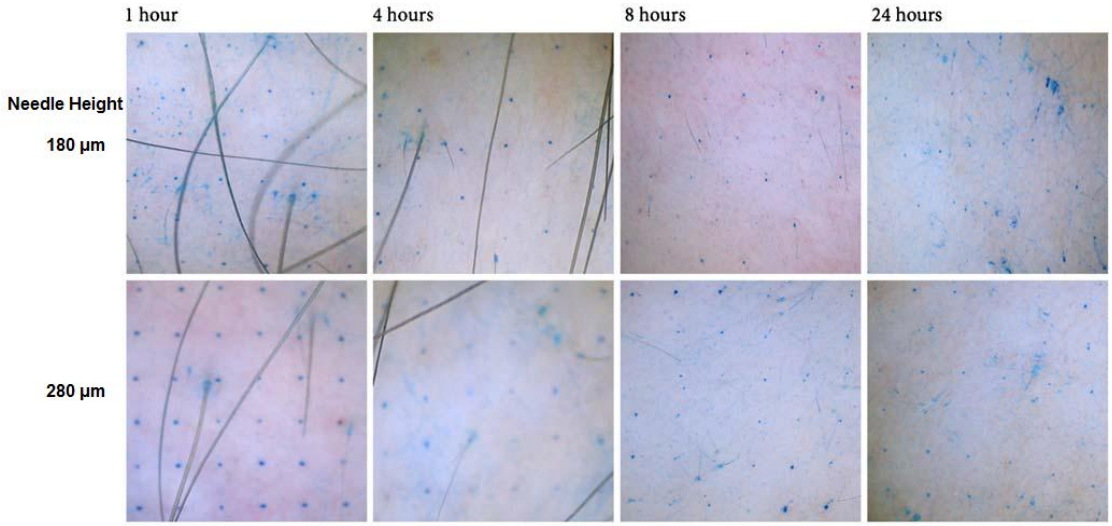

Figure 2.19: Methylene blue staining of MN holes on the human skin (needle height: 180 and 280 µm) (Haq *et al*., 2009)

Several studies of MN insertion in skin show that the holes remain in the skin after the removal of the MNs (e.g., Haq et al., 2009), as shown in Figure 2.19. Previously, McAllister et al. (2003) have applied a cylindrical MN of 20 µm diameter to perform staining experiments, which indicates that a hole will remain after the removal of MNs. Martanto et al. (2004) have shown that a number of visible holes remained when MNs were applied with needle lengths of 1000 µm and width of 200 µm by 50 µm on a rat skin. In addition, McAllister et al. (2003) have reported a residual MN hole of radius 6 µm following insertion of MNs with radius of 10 µm, which means that the holes shrink to ~60 percent of the diameter of the MNs. While inserting the MNs, it can also be seen that the entire MN length cannot be inserted into the skin completely, and the depth of penentration of MN in skin is related to its length and the application force. These factors directly affect the size of pierced holes before and after the removal of MNs, Donnelly et al. (2010b) have used optical

coherence tomography (OCT) to detect the effect of MN height and application force on the depth of penentration inside the porcine skin. As shown in Figure 2.20a, the penetration depth is increased significantly by an increase in MN height and application force. In addition, the application force presents a positive effect on the penetration depth of the MN inside skin, as shown in Figure 2.20b: the pore width is increased by an increase in needle height and application force, when the base width is kept constant. However, there is a clear gap left between the MN base plate and the skin surface. Donnelly et al. (2011) have further used OCT to obtain 3D views of MN embedded in the human skin. They reported that a MN with needle height of 600 μm and base diameter of 300 μm penetrated approximately 460 μm into the human skin with a clear gap of 136 μm between the MN base plate and skin. They also indicated that the width of the pierced holes in the skin was about 265 μm in diameter. These reports demonstrate that MN assisted micro-particle delivery is expected to realize a greater penetration depth of micro-particles in the skin.

2.5 Potential of microneedle assisted micro-particle delivery

2.5.1 Microneedle assisted micro-particle delivery

As mentioned earlier, cell and tissue damages are particular problems for the biolistic gene transfection (O'Brien and Lummis, 2011; Uchida *et al*., 2009; Thomas *et al*., 2001; Sato *et al*., 2000; Yoshida *et al*., 1997). Reduction in the operation pressure and in the particle size can minimize the cell damage, but these also decrease the momentum of the micro-particles. This minimizes the penetration depth of the micro-particles in the tissue and may cause a failure of the DNA transfection.

Based on a consideration of reducing the operating pressure, a new concept of combining MNs with gene gun for micro-particle delivery has been presented by Zhang *et al*. (2013) (See chapter 3). As presented in Figure 2.21, the concept may be developed from the light and Helios gas gun systems. The operating process consists of particle acceleration, separation and deceleration stages. For the acceleration stage, a pellet of micro-particles is loaded onto the ground slide which is accelerated by pressurized gas. The pellet is then separated into individual micro-particles by impaction onto a mesh stopping screen in the separation stage. The separated micro-particles spray forward through a conical nozzle with a uniform velocity and distribution to breach the skin tissue to target the cells of interest.

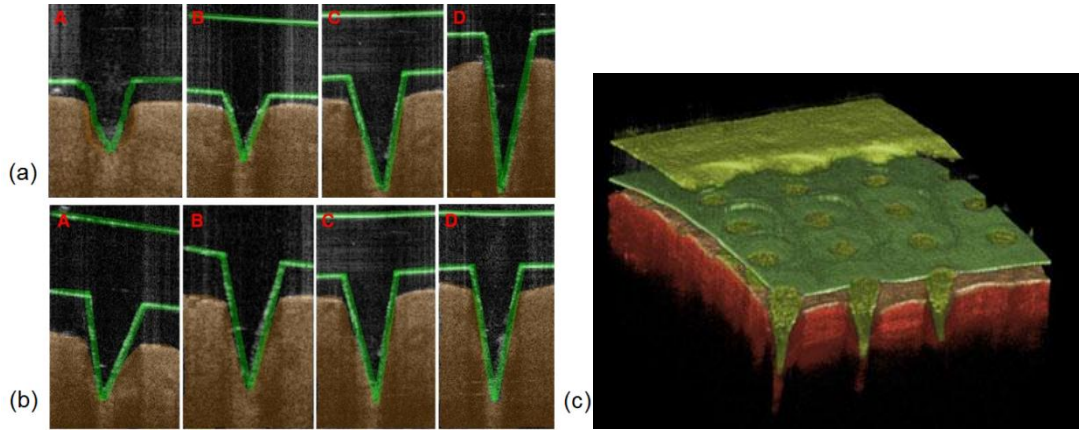

Figure 2.20: (a): A 2D OCT image for the investigation of the effect of the MN height on the penetration depth inside the porcine skin (A: 280 µm; B: 350µm; C: 600µm; D: 900µm) (Donnelly *et al*., 2010b) (b): A 2D OCT image to analyse the effect of the application force on the penetration depth of MN inside the porcine skin (A: 4.4 N (newton); B: 7.0 N; C: 11 N; D: 16.4 N) (Donnelly *et al*., 2010b) (c): A 3D OCT image showing MN insertion in the skin (needle height: 600 µm; base width: 300 µm; spacing: 300 µm) (Donnelly *et al*., 2011)

As shown by Zhang et al (2013), by using an array of MNs it is possible to overcome the effect of the skin on the particle penetration. One of the many advantages of this new concept is that the pressurized gas will be released from the vent holes (see Figure 2.21), which is likely to avoid the damage of the target from the impaction of pressurized gas on tissue. In addition, the use of the ground slide slows down the velocities of micro-particles to reduce the impact force on tissue to minimize the cell damage. As required, the velocity is controllable by changing the driving pressure of compressed gas, if higher micro-particle velocities are necessary. Even if the micro-particles cannot reach the desired penetration depth due to insufficient momentum, the use of MNs allows a number of micro-particles to penetrate further to achieve the purpose of gene transfection in the desired depth of the tissue. However, the disadvantage of this concept is that a very high impact velocity of micro-particles is not easy to achieve, because the ground slide has significant mass.

The solid MN used by Zhang *et al*. (2013) aimed to create holes on the skin to allow a number of micro-particles penetrate through the pierced holes and increase the penetration depth. Zhang *et al*. (2013) also indicate that some agglomerated micro-particle may be present in the target; the size of the agglomerates is controllable and decreases with a decrease in mesh pore size and binder concentration. Results have shown that a number of micro-particles

are able to penetrate through the pierced holes (created by the MNs) and reached a greater penetration depth inside the target, demonstrating the feasibility of MN assisted micro-particle delivery. In principle, the maximum penetration depth of micro-particles is affected by the particle size, density and operating pressure which determine the momentum of the micro-particles and hence the impact of the particles on the target. An increased length of the pierced holes enhances the particle penetration depth due to a decreased resistance when micro-particle travel in the hole. The length of the pierced holes depends on the height of MN. However, the effect of the above parameters on the penetration depth of micro-particles will be analysed in our following works.

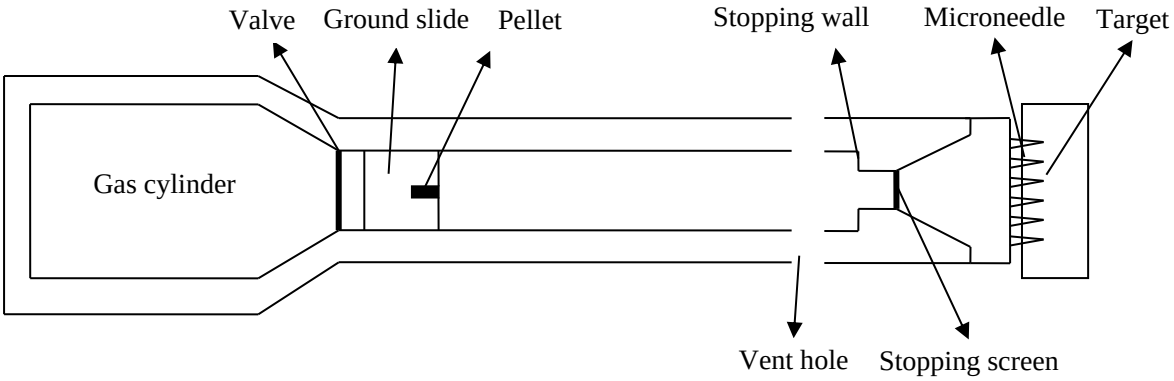

Figure 2.21: A possible structure of a MNs assisted micro-particle delivery system

2.5.2 Effects of physical approaches to drug delivery

With the development of the transdermal drug delivery, several physical technologies have been developed, particularly in needle free gene gun system. In order to understand the advantages of MN assisted micro-particle delivery for the drug/gene delivery, a comparison with other physical cell targeting approaches is presented in this section. Figure 2.22 illustrates a schematic of four physical cell targeting approaches which include diffusional delivery (Figure 2.22a), solid MN assisted micro-particle delivery (Figure 2.22b), hollow MN assisted micro-particle delivery (Figure 2.22c) and needle free biolistic micro-particle injection (Figure 2.22d). The route of the diffusion delivery (Figure 2.22a) is that the molecules permeates through the aperture of the SC and diffuses into the target (Glenn *et al*., 2003). It is a method which operates without damage to the skin.

In recent years, needle-free biolistic micro-particle delivery (Figure 2.22d) provides a great improvement for transdermal gene delivery. The principle of this technique is that DNA is

loaded on micro-particles which are accelerated to a sufficient velocity to pierce the skin and travel to a certain depth to achieve the DNA transfection in the viable epidermis layer. It can be seen from Figure 2.22d that micro-particles penetrate to greater than diffusion delivery. In addition, biolistic micro-particle delivery is painless as the micro-particles settle within epidermis without reaching the nerves (Quinlan *et al*., 2001). There are some disadvantages for biolistic micro-particle delivery such as micro-particle penetration causes a significant cell death in the skin due to the impaction (O'Brien and Lummis, 2011; Raju *et al.*, 2006; Sato *et al*., 2000). In addition, pressurized gas may damage the skin surface if the pressure is over than 200 psi (Belyantseva, 2009; Uchida *et al*., 2009; Yoshida *et al*., 1997).

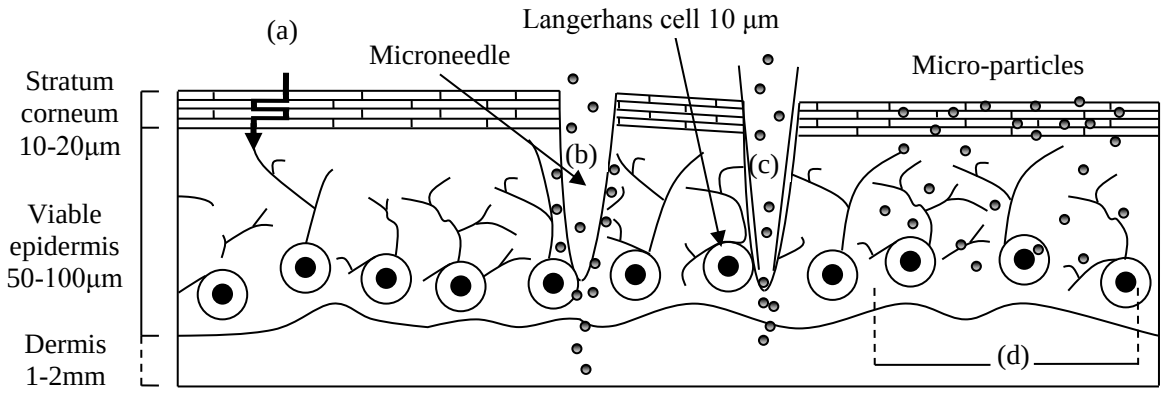

Figure 2.22: A schematic cross-section of the skin: (a) the normally diffusion route (b)route of solid MN assisted micro-particle delivery (c) route of hollow MN assisted micro-particle delivery (d) route of normal micro-particle penetration using a gene gun system (Kendall, 2006)

As mentioned earlier, the method of MN assisted micro-particle delivery requires use of a MN to overcome the skin surface to deliver micro-particles to a greater depth. The projected routes are presented in Figure 2.22b-c. In Figure 2.22b the penetration depths of micro-particles are greater than for needle-free biolistic micro-particle delivery due to the pierced holes providing a low resistance path skin for micro-particle penetration. Figure 2.22c shows hollow MN assisted micro-particle delivery which should allow particles to penetrate further in the skin via the hollow needles. However, the disadvantage of MN assisted micro-particle delivery is that the process may be painful if the micro-particles are deliver into dermis which have nerves ending in that layer.

Overall, it is obvious that needle-free biolistic micro-particle injection present more efficiency than diffusion delivery. Ziegler (2008) has shown that acceptable DNA vaccination requires the coated micro-particle to penetrate the skin surface with around 20-100 μm penetration depth. It indicated that needle-free biolistic micro-particle injection achieves a more efficient pharmaceutical effect than diffusion delivery. Further, MN assisted micro-particle delivery may deliver micro-particles deeper than the needle-free gene gun system in the skin to allow deeper tissue to be transfected. It has been demonstrated that MN assisted micro-particle delivery may achieve a further enhanced DNA transfection in the target.

2.5.3 Modelling micro-particle delivery in skin

The process of micro-particle delivery is normally divided into two stages which are particle acceleration stage and penetration stage. In the modeling, the acceleration stage is required to consider the driving source (gas pressure) which accelerates the micro-particle to a sufficient velocity to pierce the skin surface. The velocity is varies with the gene gun system design, particle density and size. For the penetration stage, the effect of the skin is the major resistence to prevent the micro-particle delivery. Micro-particle delivery requires breaching the SC and piercing into the epidermis layer (Yager *et al*., 2013; Soliman *et al*., 2011; Liu, 2006; Quinlan *et al*., 2001; Bennett *et al*., 1999; Trainer *et al*., 1997). The impact velocity, particle size and density, target density and yield stress are the major variables affecting the penetration depth.

Normally, the micro-particle acceleration stage is gas and particle flow for gas gene gun systems, e.g., CST, PowderJect and Helios Gene gun. The flow is defined as symmetric and fully turbulent in the device for various studies (Liu, 2006; Soliman and Abdallah, 2011). A model which has been widely adopted is force balance law which is based on the Newton's second law and Stokes's law. For example, Liu (2006) has focused on simulating the velocity distribution in the converging (conical) section of a venturi system which is developed from a gene gun, namely, the PowderJect system (Powderject Research Ltd., Oxford, UK) (Bellhouse *et al*., 1999, 2003, 2006). The particle velocity has been simulated based on a balance between the inertia of micro-particles and other resistance forces acting on the particles. Zhang *et al*. (2007) have used the MATrix LABoratory (MATLAB, The MathWorks Inc., Natick , USA) (Shampine *et al*., 1997) to simulate three different stages of the particle delivery in the gene gun, namely, acceleration, separation and deceleration stages.

In their work, the particle velocity is analysed on the basis of Newton's second law in the acceleration stage; an energy conservation law is applied to describe the separation of micro-carriers into micro-particles in the separation stage, and Stocks' law is applied to model the penetration of micro-particles in the deceleration stage into a various target. Soliman *et al*. (2011) have used a commercial turbo-machinery flow simulator, namely, FINE^{TM}/Turbo (NUMECA International, Brussel, Belgium) to simulate the behavior of gas and particle flow in a supersonic core jet in a gene gun. This work used Newton's second law to mimic the particle trajectories and determine the penetration depths of micro-particles in the skin. As discussed below, a number of studies have shown that the penetration depth depends on the momentum of micro-particles which again depend on the particle size, density and velocity.

For the penetration stage, various studies have separated the resistance force on the micro-particle into a yield force (F_y), frictional resistive force (F_f) and resistive inertial force of the target material (F_i) (Soliman et al., 2011b; Liu, 2007; Mitchell et al., 2003; Kendall et al., 2001; Dehn, 1987). The force balance equation is shown below:

$$m\frac{dv}{dt} = -(F_i + F_f + F_y) \tag{2.1}$$

From this the stopping distance can be calculated as

$$d = \frac{4\rho_p r_p}{3\rho_t}\left\{\ln\left(\frac{1}{2}\rho_t v_i^2 + 3\sigma_y\right) - \ln(3\sigma_y)\right\} \tag{2.2}$$

Based on this force balance equation, the theoretical penetration depth (equation 2.2) is obtained and adopted for the modelling. This model has been widely adopted in several studies. For example, Soliman et al. (2011b) have modelled the delivery of golden particle of diameters 1.8 and 5 μm using 3 MPa pressure and have shown that penetration depths of 95μm and 135μm can be achieved for particle of diameters 1.8 and 5 μm, respectively. Kendall et al. (2001) have analysed the golden particle penetration by using equation (2.2) for particle penetration in human and porcine skins. In addition, predictions from the theoretical model have been shown to agree well with the experimental results by Kendall et al. (2001). More recently, Soliman et al. (2011b) have also implemented equation (2.2) in a theoretical model which is implemented using FINE/Turbo code to calculate the penetration depth of gold micro-particle inside the skin.

2.6 Chapter Summary

The background of the gene gun system for micro-particle delivery is reviewed in this paper. A number of gene gun systems have been listed and the operating principles along with their advantages and disadvantages have been studied briefly. In addition, the recommended gas type, particle material and size for these type engineering systems are discussed. The range of particle velocities and applied operating pressures for several gene gun systems are described, which indicated that cell/tissue damage is a major problem for biolistic micro-particle delivery, due to the impaction of pressurized gas and high-speed micro-particles on the target tissue. In addressing this point, a new concept is proposed of MN assisted micro-particle delivery, which combines a gene gun system with MN to enhance the penetration depth of micro-particles. This technique may reduce the cell damage from pressurized gas and reduce the impact velocity of micro-particle. In order to further understand the MN assisted micro-particle delivery, a number of MN designs have been discussed, paying attention to key characteristics that affect biolistic delivery.

A number of researchers have studied the MN insertion in the skin which suggests that holes remained on the skin after the removal of MNs. These indirectly show the feasibility of the MN assisted micro-particle delivery to enhance the penetration depths of micro-particles inside the target. Based on the above research works, the detailed penetration route of MN assisted micro-particle delivery is also discussed and compared with other physical approaches on drug delivery. Finally, various models of micro-particle delivery for different gene gun systems are described to understand the theoretical principles of micro-particle penetration and which may be used for modelling of MN assisted micro-particle delivery.

3. Microneedle assisted micro-particles delivery: Proof of concept

3.1 Chapter Overview

A set of well defined experiments has been carried out to explore if microneedles (MNs) can enhance the penetration depths of micro-particles moving at high velocity such as those expected in gene guns for delivery of gene loaded micro-particles into target tissues. These experiments are based on applying solid MNs which are used to reduce the effect of mechanical barrier function of the target so as to allow delivery of micro-particles at less imposed pressure as compared to most typical gene guns. Further, a low cost material, namely, biomedical grade stainless steel micro-particle with size ranging between 1 - 20 μm, has been used in this study. The micro-particles are compressed and bound in the form of a cylindrical pellet and mounted on a ground slide, which are then accelerated together by compressed air through a barrel. When the ground slide reaches the end of the barrel, the pellet is separated from the ground slide and is broken down into particle form by a mesh that is placed at the end of the barrel. Subsequently, these particles penetrate into the target. This chapter investigates the implications of velocity of the pellet along with various other important factors that affect the particle delivery into the target. Our results suggest that the particle passage increases with an increase in pressure, mesh pore size and decreases with increase in PVP concentration. Most importantly, it is shown that MNs increase the penetration depths of the particles.

3.2 Introduction

Micro-particle delivery systems (e.g., gene guns) have been used for transferring genes into cells and tissues (e.g. plant tissues) for some time (Klein *et al*., 1987; Heiser, 1994; Svarovsky, 2008; Huang *et al*., 2011; O'Brien and Lummis, 2011; Manjila *et al*., 2013). Typically, the operation involves a micro-particle accelerator, which can deliver gene-loaded micro-particles into a target (e.g. biological cells) to achieve the desired mass transfer effect (e.g. gene transfection). The PowderJect delivery system is a case in point, which has been applied to exploit the micro-particle gene transfer treatment (Dempster, 2000; Kendall, 2002). In most cases, these delivery systems are based on the principle that biocompatible micro-particles loaded with genes can be accelerated to a sufficient velocity so as to penetrate the barrier function of the target tissue and thereby achieve gene delivery (Bellhouse, 1999; Burkoth, 1999). However, cell and tissue damages are particular problems for these micro-particle delivery systems which are discussed further later.

It is obvious from previous research on micro-particle based gene delivery that knowledge of the velocity of the micro-particles and its effects on particle penetration is one of the major research points in development of these systems. A number of researchers have studied the particle velocity for various designs of gene guns. For example, Quinlan *et al.* (2001) have used a conical nozzle employed at 60 bar to accelerate polymeric micro-particles of 4.7, 15.5 and 26.1 μm diameters to velocities of 350, 460 and 465 m/s, respectively. Kendall *et al.* (2004a) have used a converging-diverging nozzle, which has been shown to accelerate polystyrene particles of diameter 4.7 μm to a velocity of 800 m/s at the same pressure as used by Quinlan *et al.* (2001). Such developments of the delivery systems can improve the velocity of micro-particles to achieve a higher speed if compared with conical nozzles (Quinlan *et al.*, 2001). Mitchell *et al*. (2003) have also studied the velocities of polystyrene particles (average size: 99 μm) for a light gas gun (LGG) proposed originally by Crozier (1957) and gold particles (average size: 3.03 μm) for a contoured shock tube (CST). The particle velocity is shown to achieve 170, 250 and 330 m/s at pressure of 20, 40 and 60 bar for the LGG, respectively. The gold particles have been shown to achieve an average velocity of 550 m/s at 60 bar based on the CST. Liu *et al.* (2004c) have also used a CST to accelerate gold particles of diameter 2.7 μm to a velocity of 626 m/s at 60 bar pressure. Subsequently, Liu *et al.* (2006) used polystyrene particles of 39 ± 1 μm diameter to study the particle velocity for CST and found improvements relative to the LGG, which is shown to achieve a velocity of 570 ± 14.7 m/s at 60 bar pressure (Liu *et al.*, 2006). In recent years, Soliman *et al.* (2011) have shown that a supersonic core jet can accelerate 1.8 and 5 μm diameters gold particles to velocities of 550 and 294 m/s at 30 bar pressure. O'Brien and Lummis (2011) have also used gold particles of core diameters 40 nm and 1 μm to achieve maximum depths of 31 ± 6 and 50 ± 11 μm in mouse ear tissue by using a Helios gene gun.

Although very high velocities of the micro-particles or/and gas may seem useful in delivering the particles deep into the target tissue, they may actually damage the target from their impacts. As such, it is logical that one controls both the velocity and, the mass of the micro-particles and gas that impact the target. This is somewhat reflected in a study by Belyantseva (2009) who has used a pressurized Helios gene gun to accelerate DNA-coated gold particles (1 μm diameter) where the pressure is controlled at 14 bar. The author shows that this pressure is adequate for the penetration of the particles without excessive tissue damage. Xia *et al*. (2011) have suggested that the pressure should be limited to around 14 bar to minimize damage for biolistic transfer to soft tissue. Uchida *et al*. (2009) have fired

plasmid DNA into cultured mammalian cells (e.g. human embryonic kidney cell (HEK293) and human breast adenocarcinoma (MCF7) cell) using a Helios gene gun, which shows that gene transfection is achieved in these cells but the cell damage occurs if the operating pressure in the gene gun is more than 200 psi (13.78 bar). O'Brien and Lummis (2011) have cultured HEK293 cells and used them as targets for biolistic transfection using a gene gun. This work has shown that nanoparticles can be utilised as gene carriers similar to micro-particles for biolistic transfection and lessen cell damage. These researches show that cell damage can be reduced if particle size and operation pressure are reduced as they lower the particle impact force on the cells/tissue such as those observed by Uchida *et al*. (2011). In most studies, the viable epidermis layer of skin is considered as the target tissue for gene loaded micro-particle delivery as the penetration depth is limited by a number of factors (Quinlan *et al*., 2001; Trainer *et al*., 1997).

In the particles delivery process, the material of the particles is also of crucial importance. In order to deliver gene loaded particles into cells effectively, high density materials are generally preferred since they carry a larger momentum and are expected to penetrate more into the target tissue as compared to particles of low density materials. The most common material of the particles is gold due to its high density, low toxicity and lack of chemical inactivity. However, gold is an expensive material. In principle, other materials such as biomedical grade stainless steel and polystyrene may be a good replacement for gold while reducing the cost due to the lower price of these materials in comparison to gold. However, these materials have lower density compared to gold and, as such, the momentum for these micro-particles would be less for the same particles size and velocity. This implies that other factor is needed to break the resistance of the target tissue for the particles to enter easily while also enhancing the penetration depths. Microneedles, which can break the resistance of the target tissue almost painlessly (Nayak *et al*., 2013; Ashraf *et al*., 2011; Al-Qallaf and Das, 2009a; Prausnitz, 2004; Henry *et al*., 1998b), seem to be a promising option in this regards. However, there is little or no study at the moment that demonstrates that microneedle can be useful in the delivery of dry particulates particularly at lower pressures as compared to most current gene guns which should be operated at very high pressure (Quinlan *et al*., 2001; Mitchell *et al*., 2003; Liu *et al*., 2006). Previously, several studies have shown that the effectiveness of the MN based drug delivery is limited by a wide varieties of variables, e.g. MN height, spaces between the needles, patch size, insertion forces, tissue characteristics such as viscoelastic properties, materials of MNs, etc, and as such, it is necessary to choose

the MNs for specific application as well as the target tissue (Olatunji *et al*., 2013; Olatunji *et al*., 2012; Yan *et al*., 2010; Donnelly *et al*., 2010b; Al-Qallaf *et al*., 2009a; Teo *et al*., 2006).

In addressing these points, microneedles have been used to enhance the penetration depths of low density micro-particles using an experimental set up that mimic particle accelerator (e.g. gene guns) in its operation principle. As model particles, we use biomedical grade stainless steel micro-particles. Further, a ground slide is used to prevent the impact of high pressure gas on the micro-particle target as discussed in more detail in the next section. The use of the ground slide gives lower particle velocities compared with the CST under the same operating conditions. However, the purpose of the micro-particle gun is to accelerate the particles to a sufficient velocity which can penetrate into a desired depth inside the target. For a microneedle based injection system, this objective could be achieved by first applying solid microneedles as they help in overcoming the tissue barrier (Stahl *et al*., 2012; Chu *et al*., 2010; Coulman *et al*., 2006). In this study, solid microneedles are used to create well defined holes in the target which remain open immediately after removing the microneedle. Hence, a number of micro-particles should penetrate into the target via the holes. Therefore, the application of the microneedle based particle delivery is a good improvement for particle injectors.

In addition to the aims discussed above, this chapter aims to investigate the significance of various important factors, e.g., the ground slide on the particle velocity for the microneedle assisted micro-particle injection. The micro-particles are mixed with PVP, compressed and bound as a cylindrical pellet for the purpose of this work. The pellet is mounted on a ground slide, which is accelerated along a barrel. The high velocity pellet is separated by a mesh which presents a partial blockage to the flow. The work in this chapter aims to determine the passage percentage and separated particle size. The chapter also aims to study the effect of the microneedle on the micro-particle penetration depth when they are fired into a homogeneous agarose gel which is used a as a model target. Agarose gel has the advantages that it can be produced with a controllable mechanical property and its transparency provides a good quality to view the micro-particle penetration using optical digital microscope. In agarose gel, the micro-particles follow two routes of delivery. The first route is that a number of micro-particles directly penetrate into the agarose gel without going through the holes reated by MNs. The second route is that the micro-particles are delivered through the pierced holes created by the MNs to enhance the penetration depth inside the agarose gel. In reality, the

target skin for these micro-particles may be different structurally and heterogeneous, and therefore the routes of the micro-particle delivery may be affected by its individual layers. However, this is not a consideration in this study as we carry out the experiments in a controlled manner using homogeneous agarose gels. The detailed information on the MN assisted micro-particle delivery system is described in section 3.3.2.

3.3 Material and Methodology

3.3.1 Materials

Biocompatible stainless steel micro-particles of high sphericity equalling approximately to 0.92 were bought from LPW Technology Ltd (Daresbury, UK). Detailed characterizations of these micro-particles are presented in section 3.3.3.2. Polyvinylpyrrolidone (PVP) purchased from Sigma-Aldrich Company Ltd. (Gillingham, UK) was dissolved in ethanol (analytical grade, 99%, obtained from Fisher Scientific Ltd., Loughborough, UK) and used to bind the micro-particles to form a cohesive mixture which could be compressed into a pellet (see section 3.3.3.3). Agarose powder (Sigma-Aldrich Company Ltd., Gillingham, UK) was used to prepare an agarose gel which was used a target for the micro-particles penetration experiments.

Photoelectric sensors were purchased from SICK Group (Waldkirch, Germany) to detect velocity of the micro-particles pellets loaded onto a ground slide. Meshes of three different pore sizes were obtained from Streme Limited (Marlow, UK). A solid microneedle array (Adminpatch) (Yuzhakov, 2008) which has 31 needles of 1500 μm length was purchased from nanoBioSciences Limited Liability Company (LLC)(Sunnyvale, CA, USA).

3.3.2 Experimental design

In order to study the micro-particle delivery process, an experimental rig was constructed as shown in Figure 3.1. Detailed information of the relevant parts of the experimental rig is listed in Table 3.1. The micro-particle transfer process in such systems can be divided into three stages: acceleration, separation and deceleration stage. For the acceleration stage, the pellet of micro-particles attached to ground slide is accelerated to a desired speed by a pressurized gas which was air in this study. The ground slide blocks the direct flow of gas out of the barrel and high pressure gas is released through a venthole, avoiding impact and gas damage on the skin, agarose gel or any other target of the micro-particles. Thus, there is no gas flow in the separation and deceleration stages. In the separation stage, the pellet is

released from the ground slide after hitting a stopping wall. The pellet is released from the ground slide, hits a mesh placed at the end of the barrel which then breaks into a dispersion of micro-particles by high speed impaction on an open mesh. For the deceleration stage, the separated micro-particle spray forward, penetrate into the target via holes created by microneedles and stop inside the target.

The detailed operating principle of the experimental rig is described as follows: a regulator is used to control the maximum gas pressure released from the gas cylinder. A control valve is located between the gas cylinder and receiver to manipulate the gas flow from the cylinder and store it in the receiver for the experiment. Additionally, a pressure transducer (PT-1) is placed after the control valve to measure the pressure inside the receiver. A solenoid valve is used to operate the gas release from the receiver. It can open and close the gate according to a predetermined time and control the amount of gas released as required.

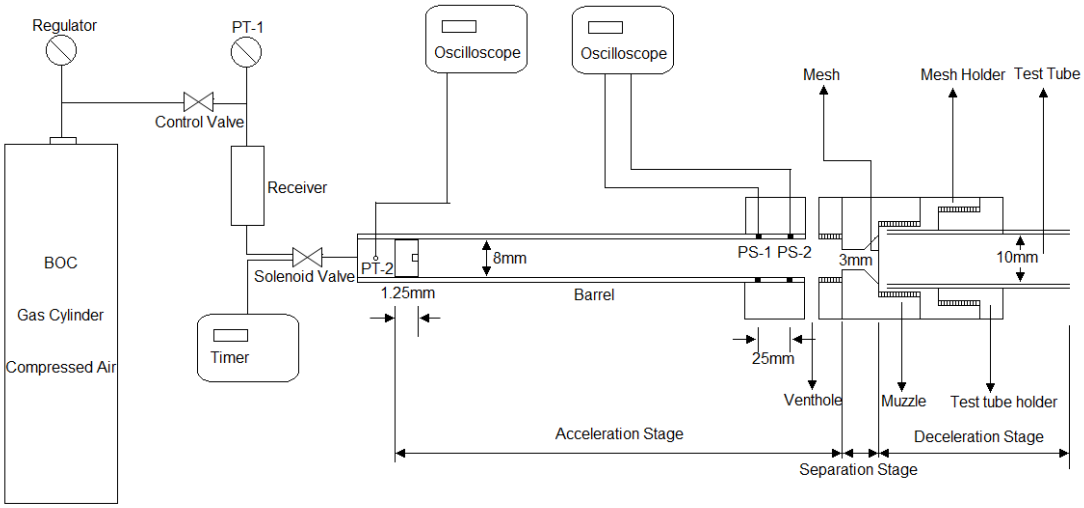

Figure 3.1: Schematic diagram of the experimental rig

For the experiments, the barrel is mounted horizontally. A second pressure transducer (PT-2) is located at the start of the barrel to detect the driving gas pressure for accelerating the ground slide. This is because a large pressure drop occurs between the receiver and the barrel due to the solenoid valve and the converging section of the receiver. It means that the pressure inside the receiver is not the same as the driving pressure for ground slide acceleration. The ground slide loaded with a pellet is placed at the start of the barrel. Two photoelectric sensors (PS) are located at the end of the barrel, which are separated by a distance of 25 mm. They are connected to an oscilloscope to record the relevant signals and measure the velocity of the

ground slide. The principle of the measurement of the ground slide speed is described in the section 3.3.3.1. In addition, two ventholes are made at the end of the barrel for release of the pressurized gas. Additionally, a mesh is placed into a muzzle at the end of the barrel and is held in place by a mesh holder. A test tube is also mounted in a holder placed at the end of the barrel to collect the separated particles and to determine the particle passage, stuck and rebound percentages (some particles remained trapped on the mesh and some rebound into the barrel). The detailed method is explained in section 3.3.3.1. In order to investigate the effect of microneedle indentation on the micro-particle penetration, the test tube is filled with agarose gel. The pellet is fired into this agarose gel to analyse the microneedle effects on particle delivery.

3.3.3 Methods

3.3.3.1 Experimental data acquisition

(a) The detection of the ground slide velocity

The velocity of the ground slide was detected by a pair of photoelectric sensors. The photoelectric sensors consist of a light source and receiver, and they are connected to an oscilloscope to record the relevant electrical signals. Two photoelectric sensors were located within the barrel, which are marked as PS-1 and PS-2 in Figure 3.1. The barrel was made of stainless steel, and the inside surface was polished smooth to reduce friction. The space between the two photoelectric sensors is set at 25 mm. The working principle in this case is that the oscilloscope starts to record the signal after the ground slide reaches the position of the first sensor and covers the laser light. After the ground slide passes the second sensor, the oscilloscope records the time for the ground slide to travel from the first sensor to the second one. As presented in Figure 3.2, the pink and green waves represent the signals receive from the first and second sensor, respectively. The breakage of the signal waves are caused by the ground slide/pressurized gas reaches the sensor to affect the operation of receiver to receive signal. As required, the second straight line of the green signal between two breakages of signals represents the travelling time in the space between two sensors. Thereby, an average velocity for the speed of the ground slide was obtained based on the known distance and recorded time.

Table 3.1: The used equipments and important parameter values for the experiment

Part name	**Important variable**	**Material/Chemical/other component**
Gas cylinder	Initial pressure: 200 bar Size: 146cm×23cm Mass: 82kg	Compressed air Supplier: BOC (UK)
Regulator	Pressure range: 0-300bar	Supplier: WIKA Instruments Limited (Redhill, UK)
Control valve	Pressure range: 0 – 100 bar	Supplier: Swagelok Company (Solon, USA)
Pressure transducer	Range : 0 -100 bar Type: XML-G100D71	Supplier: Druck Ltd. (Leicester, UK)
Receiver	Volume:1 L	Supplier: HOKE Inc.(Spartanburg, USA)
Solenoid valve	Pressure range: 0 – 100 bar	Supplier:Connexion developments Ltd(Yate, UK)
Timer	Range: 0.1 – 12 sec Type: H3DE-F	Supplier: OMRON Electronics Ltd (Milton Keynes, UK)
Ground slide	Diameter: 8 mm/15mm Length: 12.5 mm	PTFE
Pellet	Diameter: 2 mm Length: 2 mm	Stainless steel micro-particle
Barrel	Diameter: 8mm/15mm Length: 500 mm/250mm	Stainless Steel
Venthole	Diameter: 4 mm	n/a
Muzzle	Hole diameter: 3 mm	Stainless Steel
Mesh holder	n/a	Stainless Steel
Test tube holder	n/a	PTFE
Oscilloscope	Type: TDS 3034B	Supplier: Tektronix (Sweden, UK)
PS	Response time: 16μs Scanning range up to 20m Type: WLL180T	Supplier: SICK Group (Waldkirch, Germany)

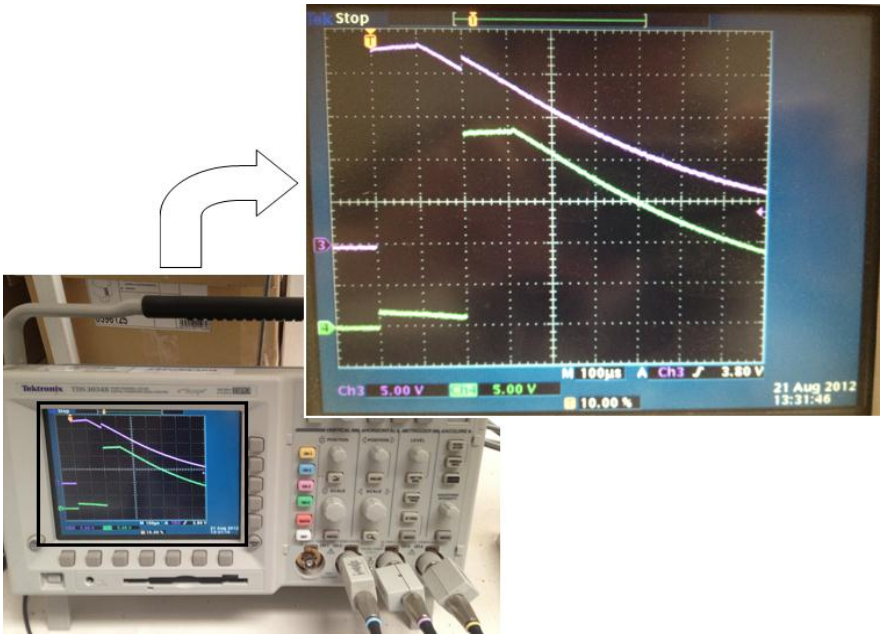

Figure 3.2: The detected signal waves of the round slide motion by a oscilloscope

(b) The analysis of the pellet separation

The micro-particles were compressed into the form of a cylindrical pellet for firing in the experimental rig. The preparation process of the pellet of micro-particles is explained in section 3.3.3.3 in detail. In the experiments, the pellet is separated by a mesh and fired into an empty test tube in the separation stage. However, some of the separated particles are unable to pass through the mesh due to the blockage of the mesh. The analysis of the pellet separation is mainly focused on studying the passage, stuck and rebound percentages and the size of the separated particle. Passage percentage represents the proportion of the pellet separate into smaller size of separated particles to passage through the mesh; stuck percentage indicates the rate of the pellet of micro-particles stick on the mesh; rebound percentage illustrates the proportion of the pellet separate into large agglomerates which rebound by the mesh. In this case, the mass of the pellet, mesh and test tube are measured before the experiment. The mass of the collected particles is obtained after measuring the mass of the test tube after firing. The mass of the stuck particles is obtained after measuring the mass of the mesh after firing. The passage, stuck and rebound percentages are calculated as:

$$\text{Passage percentage} = \frac{t_1 - t_2}{g} \times 100 \quad (3.1)$$

$$\text{Stuck percentage} = \frac{m_1 - m_2}{g} \times 100 \quad (3.2)$$

$$\text{Rebound percentage} = 100 - \text{Passage percentage} - \text{Stuck percentage} \quad (3.3)$$

where t_1 is the mass of the test tube after firing and t_2 is the mass of the test tube before firing, g is the initial mass of the pellet, m_1 is the mass of the mesh after firing and m_2 is the mass of the mesh before firing.

In addition, the separated particle sizes should be considered carefully to determine if any large agglomerates remained which could affect the performance of the system and penetration depth and damage to the target area. For this measurement, an adhesive-coated tape is placed at the end of the rig instead of the test tube (Figure 3.1). The pellet is directly fired into the tape through the mesh, where the particles get stuck. The particle laden adhesive-coated tape is then analysed in detail by scanning electron microscope (SEM).

3.3.3.2 Characterization of the micro-particle

(a) Particle size distribution

In order to confirm the size of the used stainless steel micro-particles, a particle size analyser (Coulter, LS130, BECKMAN COULTER, Inc.,) is used to analyse the size distribution of this micro-particles. As presented in Figure 3.3, the size distribution of stainless steel micro-particles is analysed in a logarithmic scale from 0 to 900 μm. Result shows that the diameter by volume only 10 % of micro-particles is over than 22.19 μm, 25 % of them are larger than 19.93 μm, 50 % of them are greater than 17.54 μm, 75 % of them are bigger than 15.12 μm and 90% of them are over than 12.72 μm. The mean diameter by mass (D [4, 3]) is around 18 μm.

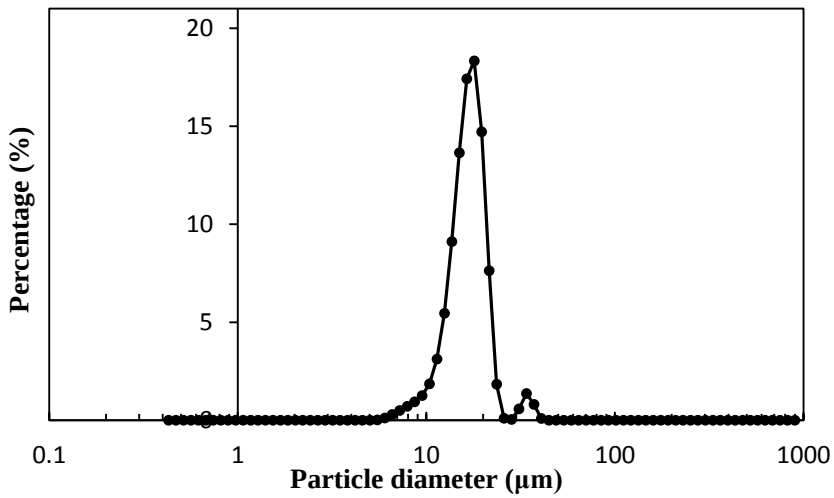

Figure 3.3: The particle size distribution of uniform stainless steel powder by a logarithmic scale from 0 to 900μm

(b) Methodology of the sphericity analysis

Figure 3.4 shows a SEM image of the stainless steel micro-particles before they are made into a pellet form in this study. As can be seen, the shape of micro-particles is very spherical and most of the particles range between diameters of 1 to 20 µm, although a few larger diameter particles were found to be present. Majority of the micro-particle was less than 15 µm in diameter. It matches well with the particle size distribution obtained from the Coulter (LS130, BECKMAN COULTER, Inc.,) previously. Based on the SEM image, the sphericity is analysed in this case.

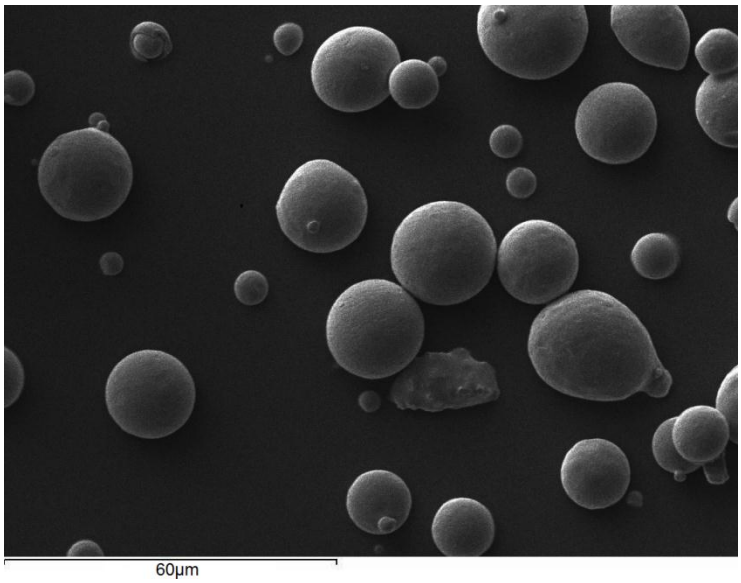

Figure 3.4: SEM image of the uniform stainless steel micro-particles

Previously, Riley (1941) has discovered a two sizeal analysis method for measuring the sphericity, namely, inscribed circle sphericity. As presented in Figure 3.5, the method is to define the circumscribed and inscribed circles to obtain the maximum circumscribed and inscribed cross-sectional areas. The sphericity is calculated as:

$$\emptyset = \sqrt{\frac{i}{D_c}} \qquad (3.4)$$

Where i is the inscribed diameter of the particle, Dc is the circumscribed of the particle and $\emptyset$ is the inscribed circle sphericity.

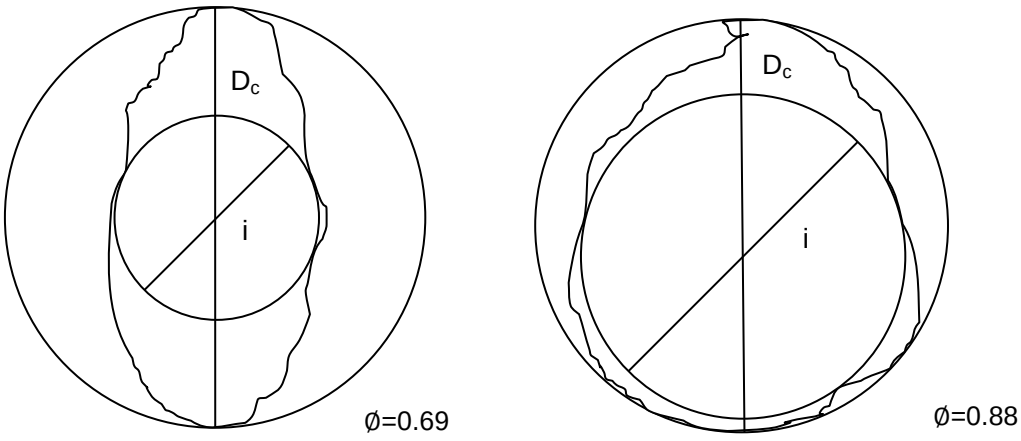

Figure 3.5: The circumscribed and inscribed circles for different shape particles

In this case, Image J is chosen to carry out the maximum circumscribed and inscribed cross-sectional area of micro-particles. From the SEM images, 30 randomly selected particles were analysed further to calculate the average sphericity of the micro-particle sample which is found to be 0.92 ± 0.05. The actual density of the micro-particles and the bulk density of the pellet without PVP are ~ 8 g/cm^3 and 4.98 ± 0.02 g/cm^3, respectively. The porosity of the pellet without PVP is 37.6 ± 0.3 %.

3.3.3.3 Characterization of the pellet

(a) The design of pellet press

For the MNs assisted micro-particles delivery, micro-particles are required to press into a pellet due to a small single micro-particle will loss more momentum during delivery process. In our case, a stainless steel pellet press is designed based on the macro-micro KBr pellet die (Sigma-Aldrich, Z506699, UK). As shown in Figure 3.6, it consists of a cover, shim, main body, base, rod and two seals. The size of the pellet is able to control by changing the length of the shim and the hole diameter of the pellet press. The operate procedure of this pellet press is as follows. The main body is placed on top of the base and one of the seals is inserted into the holes of the main body. Then the powdered stainless steel micro-particles containing PVP solution are added followed by the second seal. The rod is placed into the cover and inserted into the main body after placing the shim on the top of main body. Finally, the top cover is pressed until there is no space between the shim and the cover. Uniformly sized of pellet can be pushed out slowly using the rod directly into the ground slide to hold the pellet.

(b) The pellet making procedure

The pellet making procedure in our case was based on the method for making DNA-coated micro-particles (Thomas *et al*., 2001). PVP powder dissolved in ethanol was used to bind the stainless steel particles together (acting as a glue-like substance) as it has been used as a binder in many other pharmaceutical pellets (e.g., Svarovsky *et al*., 2008). The reason for choosing ethanol is that it helps to dry the pellet quickly due to its high volatility. The strength of the pellet is related to the PVP concentration and, as such the ethanol does not affect the binding strength of the pellet. In this study, five solutions of differing PVP concentrations were made, namely 40, 60, 75, 90 and 100 mg/ml PVP in ethanol. Based on the porosity of the micro-particle pellets (37.6%) and the size of the pellet, the desired amount of the PVP solution was added to 0.035 g of stainless steel powder by micro-pipette to fill the void space. We allow this mixture to dry for 1 – 2 minutes approximately at room temperature. When it is almost dry we transform the powdered stainless steel with PVP solution into a solid cylindrical pellet with 2 mm length and 2 mm diameter by a pellet press (Figure 3.6). The pellet is finally loaded into a ground slide and place into the ground slide holder (Figure 3.7), and record the position which convenient for differentiate the pellets due to its mass differences. In addition, a single use of PTFE ground slide is used to load the pellet due to it is low density and frictional properties, as show in Figure 3.7.

Figure 3.8(a) shows the fabricated pellets and the realistic pellet press. It demonstrates that the pellet press can produce a homogeneous size of pellet. The characterization of the pellet surface can refer to the SEM image in detail, as show in Figure 3.8(b). As expect, micro-particles are great stick together and form a uniformly pellet surface. However, PVP is distributed non-uniformly around the pellet, which may cause the pellet separate into a few agglomerates after the separation stage due to increased bind strength between some of micro-particles. This is because PVP solution may be settle in the stainless steel micro-particles during the drying process.

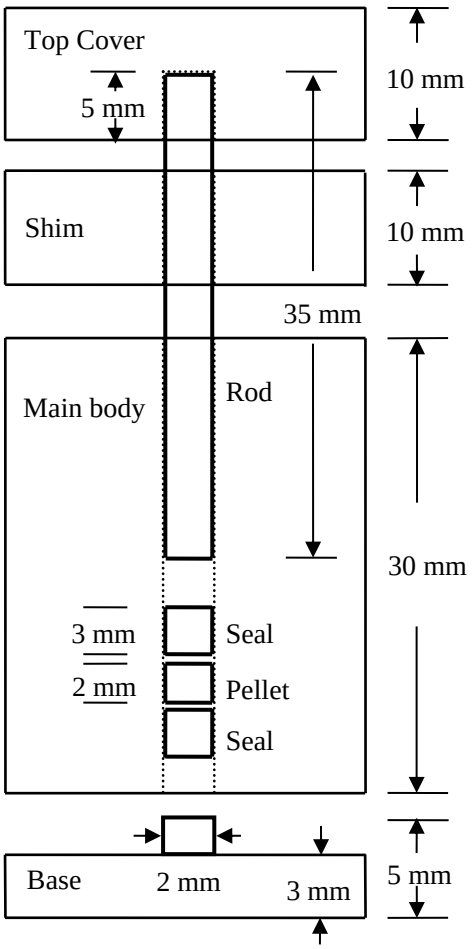

Figure 3.6: Schematic diagram of the pellet press

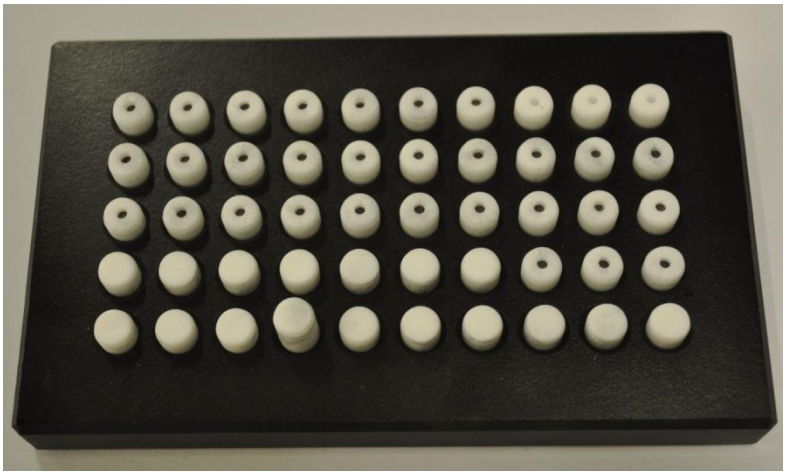

Figure 3.7: The ground slide holder

(a)

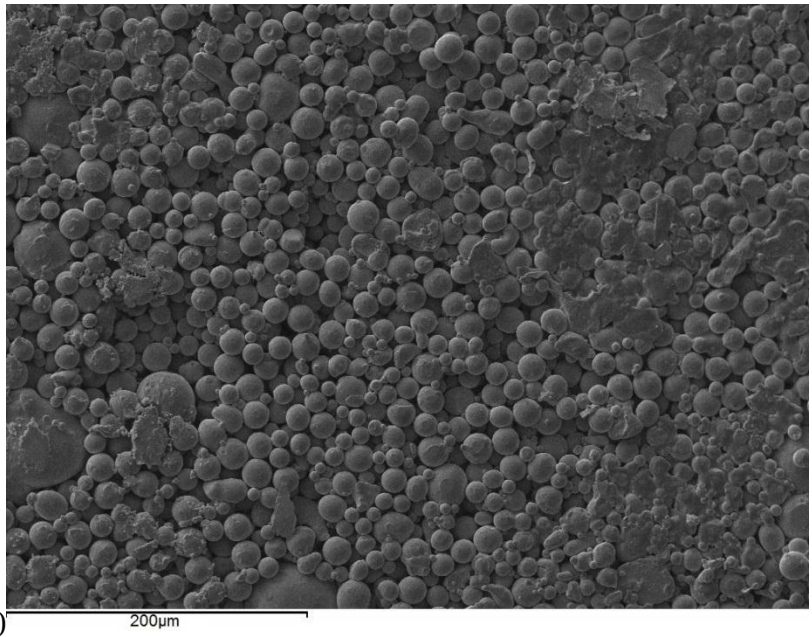

(b)

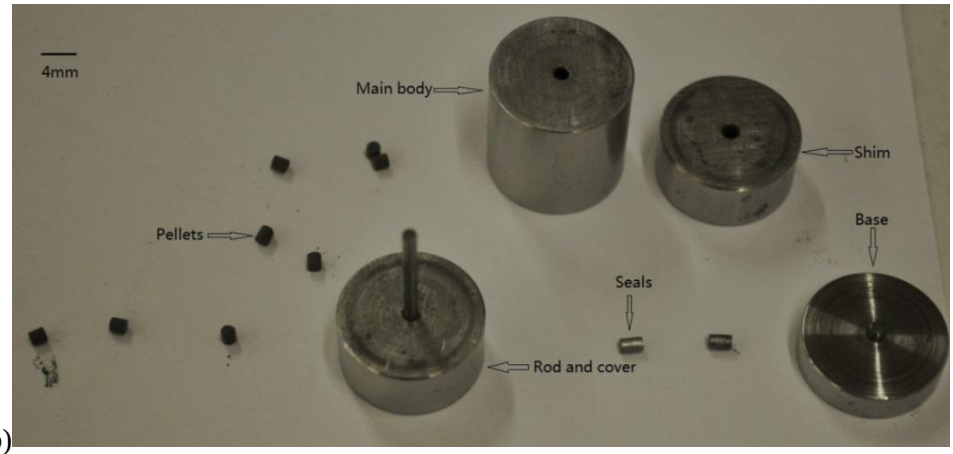

Figure 3.8: (a) The realistic pellet press and the fabricated pellets (b). SEM image of the top surface of the pellet

3.3.3.4 Characterization of the microneedle

A MN patch (Adminpatch 1500) which has 31 MNs on a 1 cm^2 circular patch was used. As show in Figure 3.9(a), the MNs are distributed as a diamond array on the patch. The space between two MNs on the side direction is 1546 µm. The spaces between two MNs on the two diagonal directions are 1970 and 3000 µm. In addition, a top view of a single microneedle and a side view of the microneedle array have taken by the SEM to analyse the width, thickness and length of the MN. As shown in Fig 3.9(b-c), the length, thickness and width of each MN are 1500, 78 and 480 µm, respectively. The characterization of the Adminpatch MN 1500 is listed in the Table 3.2.

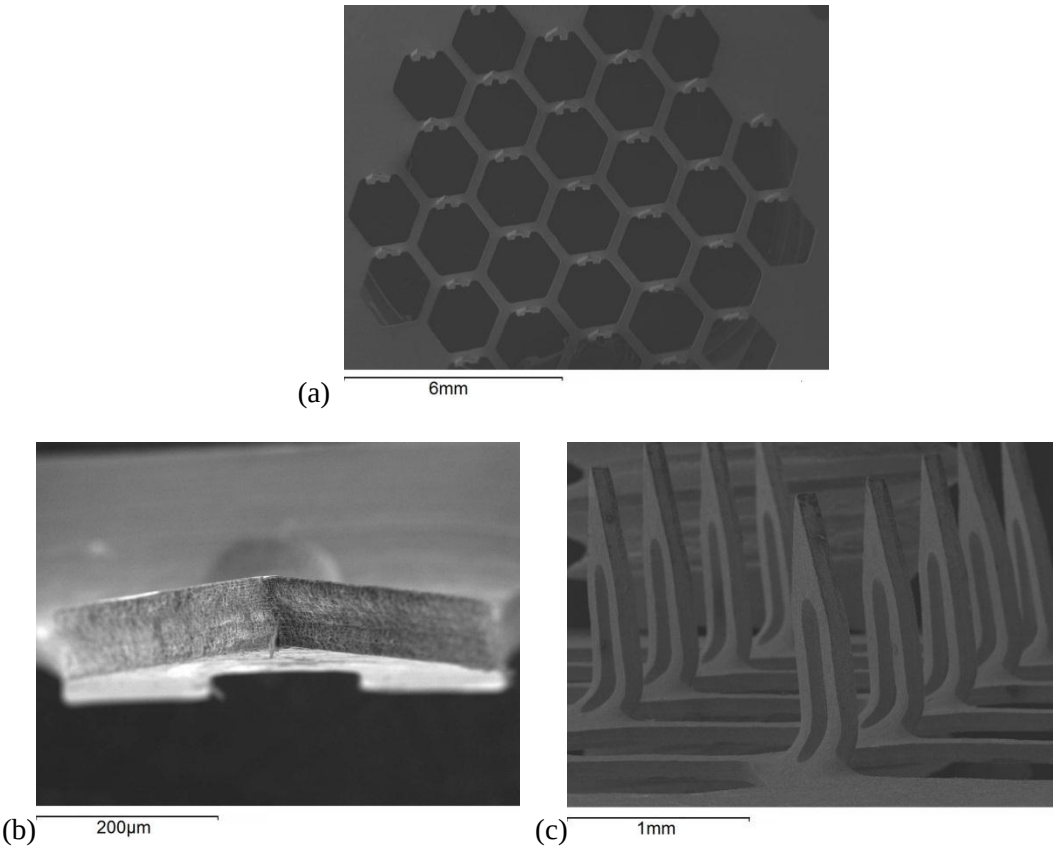

Figure 3.9: SEM images of the Adminpatch MN 1500: (a). The overall view (b). Top view of a single microneedle (c). Side view of a microneedle array

Table 3.2: The size of the Adminpatch 1500

Size	Length (µm)
Thickness	78
Length	1484
Width	480
Space on the Diagonal line direction 1	1970
Space on the Diagonal line direction 2	3000
Space on the side direction	1546

3.3.3.5 Characterization of the meshes

Stainless steel woven meshes were chosen in this case due to their strength, higher open area and their acceptance in pharmaceutical research. Three different mesh sizes were used in this study for pellet breakage, which are explained more in Table 3.3. As shown in the table, the mesh pore size decreases with an increase in mesh size. The wire diameter also has an effect

on the pore size and to some extent on the fractional open area. However, for the meshes used here the fractional open area remains approximately the same, which allows for easier comparison of the results for the different pore sizes.

Table 3.3: Important properties of the meshes

Mesh size	Pore size (µm)	Wire diameter (µm)	Open area (%)
50	310	0.20	37%
80	178	0.14	31%
120	122	0.09	33%

3.4 Results and Discussions

As stated earlier, the micro-particles delivery process can be divided into three stages, namely, acceleration, separation and deceleration. In the following sections the results corresponding to each of these stages are presented and discussed.

3.4.1 Particle acceleration stage

3.4.1.1 The velocity measurement of the ground slide

Some of the key variables of importance in this study are the operating pressure, the barrel diameter and length, and their effects on the velocity of the ground slide. The pellet velocity is also of importance which is equal to the ground slide velocity at the end of the barrel. The operating pressure of the receiver (Figure 3.1) is another major factor that affects the velocity of the ground slide. In the developed rig, a significant pressure drop occurs after the release of gas from the receiver due to a converging area of the receiver and losses in a solenoid valve attached to the receiver. Therefore, the pressure inside the receiver is not the actual pressure that accelerates the ground slide. The pressure at the start of the barrel is directly measured by a pressure transducer, as explained in the section 3.3.2. The pressure inside the gas receiver ranges from 10 to 40 bar while the actual pressure to accelerate the ground slide varies between 3 to 6 bar as measured by the pressure transducer, i.e. there is about 70 - 85 % pressure drop for the system as the gas is released from the receiver. In order to detect the effect of the barrel length on the velocity, two barrels of 250 and 500 mm lengths were used in the experiemnts. As shown in Figure 3.10, the velocity of the PTFE ground slide shows a positive correlation with the actual acceleration pressure. The particle velocity can achieve a maximum of 102, 123, 139 and 148 m/s at 3, 4.5, 5.5 and 6 bar pressures for the barrel with

500 μm length. Figure 3.10 shows a significant difference in velocity between the two different lengths of barrel; longer barrels allow a greater time for acceleration of the ground slide. For both barrels, the velocity increases at a low rate at higher pressure. The effect of pressure on the velocity of the ground slide decreases gradually, because of (i) increased friction and (ii) the length of barrel is fixed, so the time for acceleration is reduced, even though the acceleration rate itself increases.

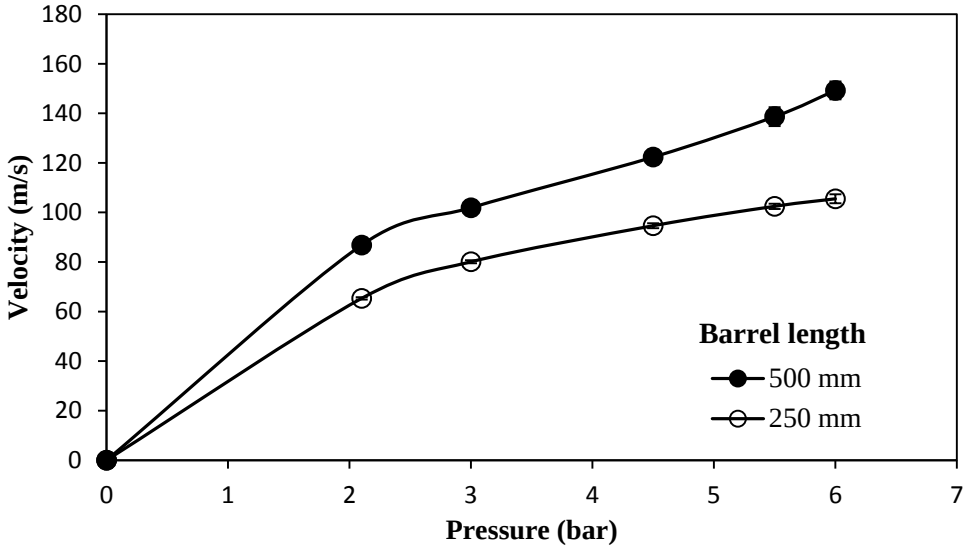

Figure 3.10: The velocity of solid PTFE ground slide against the operating pressure of gas receiver for different lengths of barrel

Table 3.4: The key variable effect on the mass of the ground slide

Material	Diameter(mm)	Length(mm)	Density(g/cm^3)	Mass(g)
PTFE	8	12.5	2.2	1.3
PTFE	15	12.5	2.2	4.85
Stainless steel	8	12.5	8.0	4.6
Stainless steel	15	12.5	8.0	17.7

In this study, PTFE and stainless steel ground slides have been prepared to investigate how the material density affects the ground slide acceleration. The mass of the ground slide for each material made is listed in Table 3.4 in detail. As shown in Figure 3.11, the velocity of the ground slide is very different for the PTFE and stainless steel materials at the same operating condition. The density of the material affects the mass of the ground slide, making it more difficult to accelerate; hence increased ground slide density has a negative effect on the acceleration. Similarly, Figure 3.11 shows that an increase of the barrel diameter causes a

decrease on ground slide velocity. The mass of the ground slide increases as the barrel diameter is increased.

Overall, it is obvious that the mass of the ground slide is important in the acceleration stage. As expected, the mass increases as the barrel diameter is increased. It also increases with an increase in the material density and ground slide length. On the other hand, the velocity of the ground slide decreases with the increase in its mass. These suggest that a narrow diameter should be used for such studies as it reduces not only the ground slide diameter but also its mass.

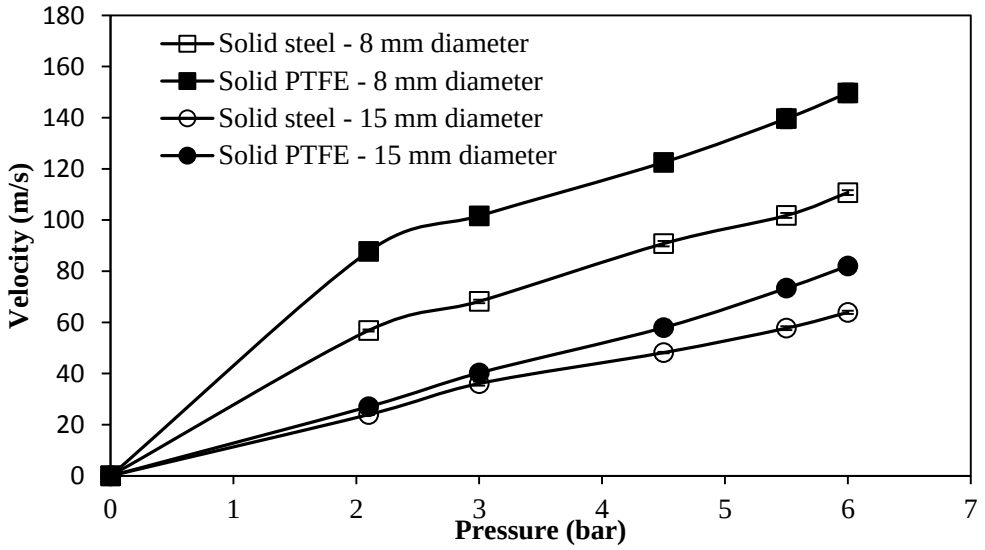

Figure 3.11: The comparison of the effect of material on ground slide acceleration in the wide and narrow barrel for two different diameters of barrel/ground slide

Based on the above results (Figure 3.10 and 3.11), a barrel with 8 mm diameter and 500 mm length and PTFE ground slide (12.5 mm long) were chosen for the following study on the particle separation stage. The velocity of solid PTFE ground slide is 148 m/s at 6 bar pressure. The micro-particles can achieve the speed over of 600 m/s at much higher pressure for a CST, e.g., at 60 bar (Liu *et al*., 2006; Mitchell *et al*., 2003). This is because the effect of the ground slide is to reduce the effect of the fired micro-particles. Mitchell *et al*. (2003) have used a LGG (Crozier, 1957) which loaded the micro-particles in a ground slide that the effect of the ground slide is investigated. It obtained that the; their particle velocity is slow downies were reduced to 170, 250, 330 m/s at 2, 4 and 6 MPa pressure. However, the pressure drop that occurs in our system means that all micro-particles are accelerated to the same extent for a

given barrel length. Therefore, an increased acceleration distance (barrel length) which makes up for the pressure drop effect for the current system has been chosen. Finally, the particle velocity for the current system is shown to be slightly different from that in the LGG (Crozier, 1957) operated at 20 bar pressure. As a result, the particle velocity is slower if compared with the velocity obtained for other types of gene gun, largely due to the pressure drop effect. A decreased velocity decreases the micro-particle penetration due to a reduction of particle momentum. However, the application of a solid microneedle patch has promised to remove this disadvantage since the pierced holes remain in the target tissue when the microneedle patch is removed and a number of micro-particles can then reach further depths via the pierced holes. This is explained more in the section 3.4.3.

3.4.2 Particle separation stage

The analysis of the pellet separation for microneedle assisted micro-particle delivery systemis described below. The passage percentage was analysed in relation to the known pellet separation variables of operating pressure, PVP concentration and mesh pore size. In addition, the micro-particles size resulting from the separation stage was studied using scanning electron microscope.

3.4.2.1 Effect of the operation pressure

Pellet was made using between 40 and 60 mg/ml PVP (pellet binder) concentration and results were obtained for operation between 2.4 to 4.5 bar pressures and for mesh with pore sizes of 310 and 178 μm. As shown in Figure 3.12a, with increasing pressure (and hence increasing velocity) the passage percentage increases rapidly at low pressures and then remains approximately constant. This is because the velocities of the pellets are larger under higher operating pressures, which cause the separated particles to gain more momentum before they are disrupted by passage through the mesh. The results show a significant increase in passage percentage from 2.4 to 3.5 bar followed by much slower increase from 3.5 to 4.5 bar. This means that at lower operating pressures there is a greater effect of pressure on the passage percentage. It is likely that the passage percentage reaches a maximum and then decreases due to some particles sticking to the mesh and some rebounding, hence not passing into the test tube (particle collector). At lower pressure conditions, the impact force on the mesh is smaller and hence the pellet is not broken up as effectively, sometime forming larger aggregates of particles, which block the mesh pores. Therefore, a larger amount of the separated particles were unable to pass through the mesh. Figure 3.12a also shows the passage

percentage increases with an increase of mesh pore size and a decrease of PVP concentration. The detailed effects of the PVP concentration and pore size on passage percentage are explained in the following sections.

Figure 3.12(b) shows that the rebound percentage is decreased from an increase of pressure. It presents a different performance with the passage percentage. All results present a significant decrease in passage percentage from 2.4 to 3.5 bar which is about 48%, but much lower from 3.5 to 4.5 bar at 5%. It is likely that the rebound percentage reaches a minimum due to the pellet is separated properly and the most of the particles are passed the mesh. In this condition, the stuck percentage on the mesh should be a constant due to the open area of the mesh is a constant which limit the amount of the particle stick on the mesh. As shown in Figure 3.12(c), the stuck percentage is kept to approximately 1% at each condition.

3.4.2.2 Effect of PVP concentration

In general, the binding strength of the pellet increases with an increase in the PVP concentration, which in turn causes the passage percentage to decrease. The effect is however quite weak, as shown in Figure 3.13 which suggests that the passage percentage only gradually decreases with an increase of PVP concentration. The fall in passage percentage with increasing PVP concentration is due to the greater adhesive forces and increased strength of pellet, which are present in the higher PVP concentrations. The larger particles or agglomerates, i.e. those which are greater in size than the mesh opening, are unable to break up as the PVP concentration increases which means that they cannot pass through the mesh. Instinctively, the effect of PVP concentration on passage percentage should be lower at higher operating pressure. This is because the impact force on the mesh is larger causing the pellet to separate more easily. However Figure 3.13 shows that the range of binder concentrations used here does not lead to a significant change in the percentage of the pellet which passes through the mesh.

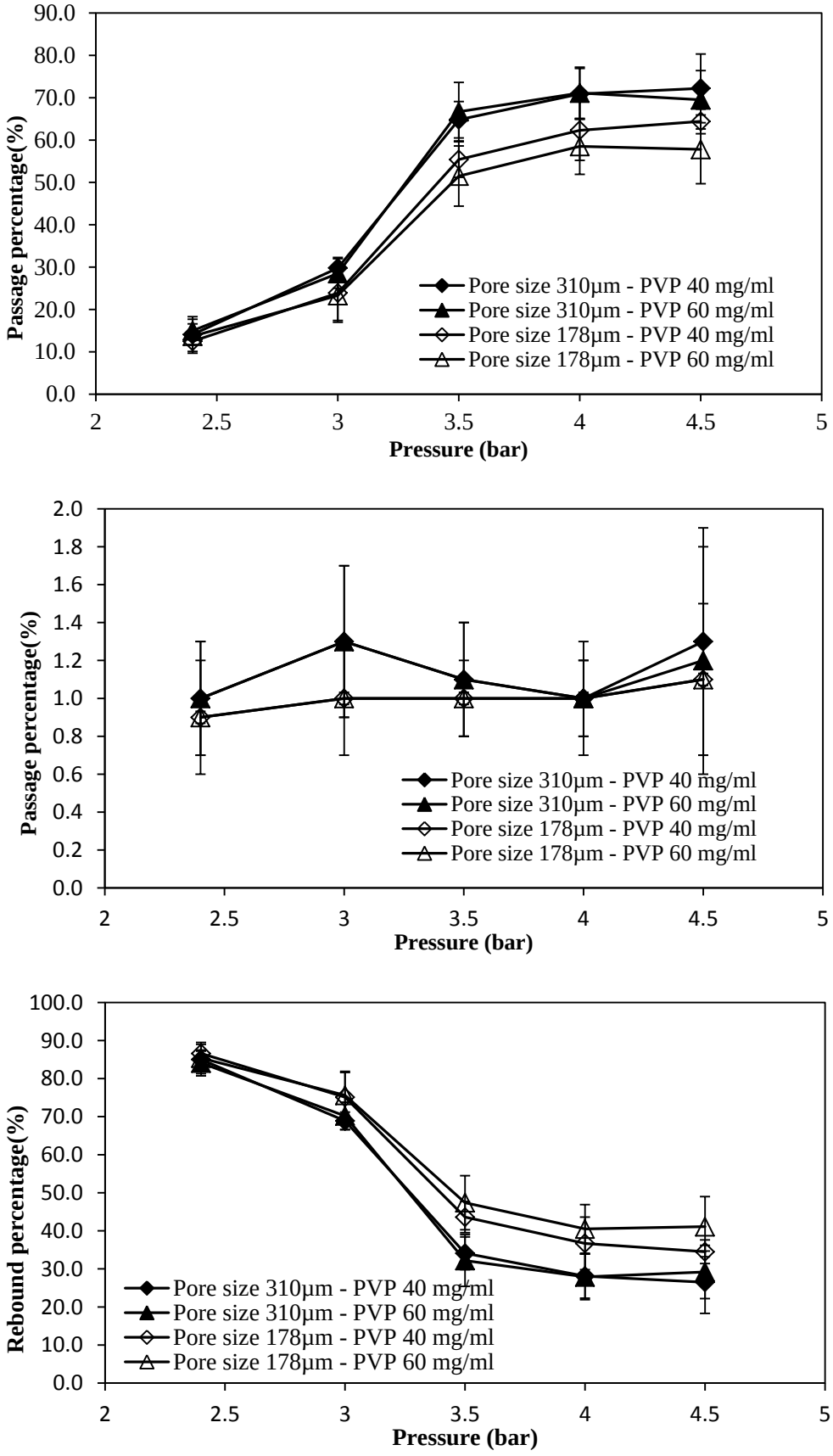

Figure 3.12: The effect of operating pressure on the pellet separation for two different PVP concentrations: (a). Passage percentage (b). Rebound percentage (c). Stuck percentage

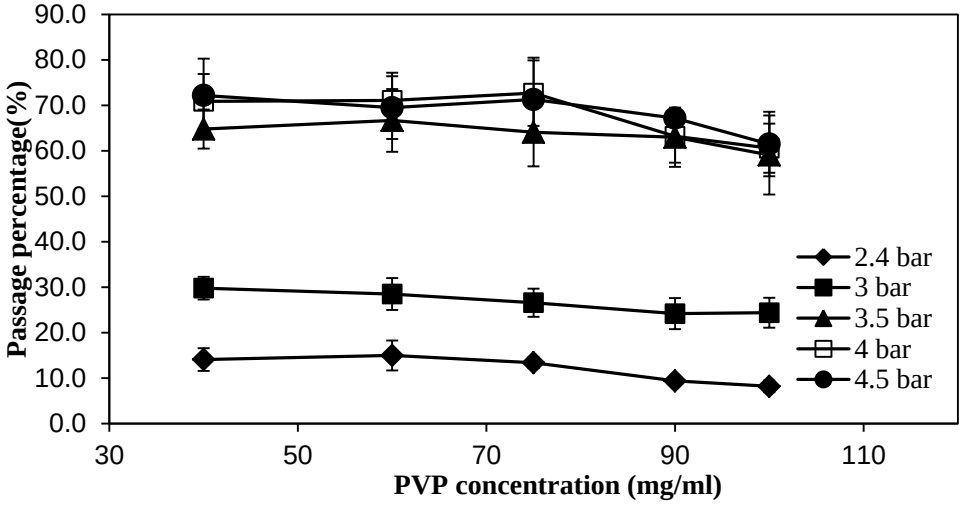

Figure 3.13: The PVP concentration effect on the particle passage percentage at various pressures

3.4.2.3 Effect of the mesh pore size

The effect of the mesh pore size on the pellet separation is one of the main variables that affect the particle separation. This is because the pore size is able to affect the size of the separated particles that pass through the mesh. This characteristic of the mesh could also affect the passage percentage, e.g. by blocking if the smallest mesh pores. To investigate the effect on the pellet separation, three different pore size meshes are studied at a constant pressure of 4.5 bar. The detailed information is explained in the Table 3.3, which shows that although the pore size changes, the fractional open area remains approximately constant for these meshes.

Figure 3.14 shows that the passage percentage exhibits significant differences for the various mesh pore sizes. As expected, the passage percentage has positive correlation with the pore size; larger pore sizes allow larger separated particles to pass through. In addition, the PVP concentration represented a negative effect on passage percentage especially for the smallest pore size mesh. The mesh with the largest pore size (about 310 μm) allowed the highest passage percentage of particles to pass through for each PVP concentration. In contrast, the mesh with the lowest pore size of 122 μm yielded the lowest passage percent. The next section discusses the effects of pore size and PVP concentration of the size distribution of the separated particles.

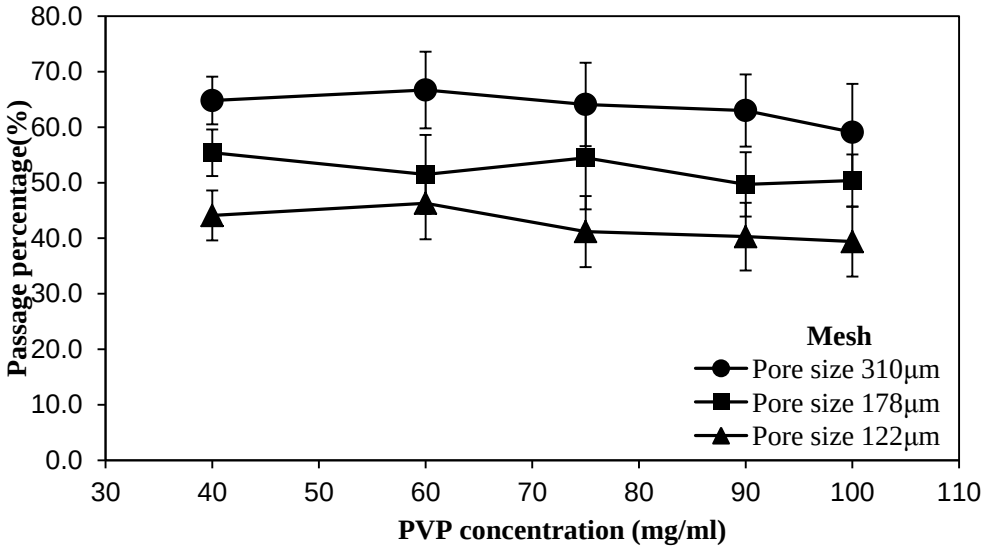

Figure 3.14: The particle passage percentage against PVP concentrations for various mesh sizes

3.4.2.4 The analysis of the separated particle size

To achieve the desired particle delivery, one of the factors that are crucial to control is the size distribution of the separated micro-particles. In general, the mesh pore size is able to manage the size distribution of the separated particle as it prevents passage of large particles. In this study, three different meshes were used at pressure of 4.5 bar in order to find out the effects of mesh pore size on the separated particles. The detailed information on the meshes is shown in Table 3.2. Figure 3.15a shows an SEM of the particles produced by the mesh with pore size 122 μm; the pellet has been efficiently broken into individual particles with only a few small agglomerated particles. The maximum size of the agglomerated particle is about 50 μm. As expected, this mesh resulted in a lower passage percentage compared to the results of the other two meshes. The passage percentage improved for the mesh with pore size 178 μm (as shown in Figure 3.14) and the resulting separated particles are shown in Figure 3.15b. This mesh also broke the pellet into individual particles and prevented passage of large sized agglomerates. The maximum size of the separated agglomerates is about 70 μm. The application of the mesh with pore size 310 μm gave the maximum passage percentage. However, as Figure 3.15c indicates some large agglomerated particles remain; the size of the largest agglomerate goes up to about 175 μm.

Overall, it can be concluded from this section that the size of the separated particles is controlled by the mesh pore size. The two smaller pore sizes resulted in effective pellet separation into individual particles, with relatively few large agglomerates.

(a)

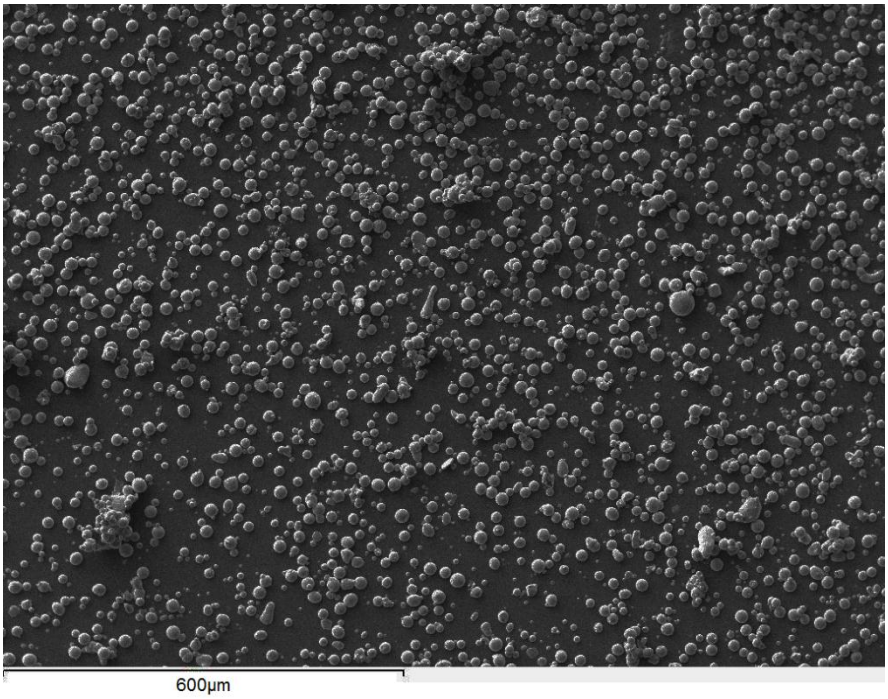

(b)

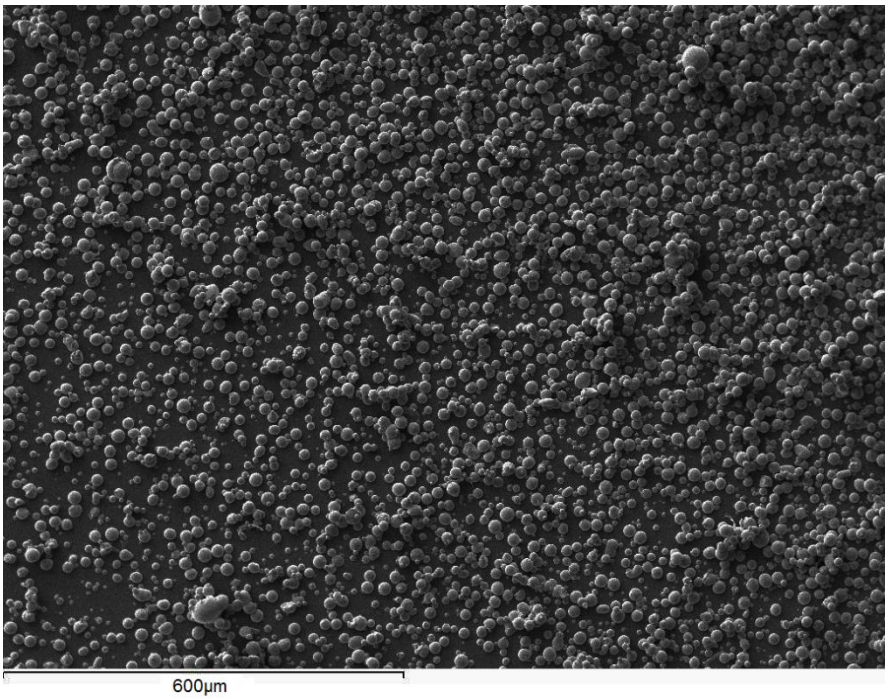

(c) 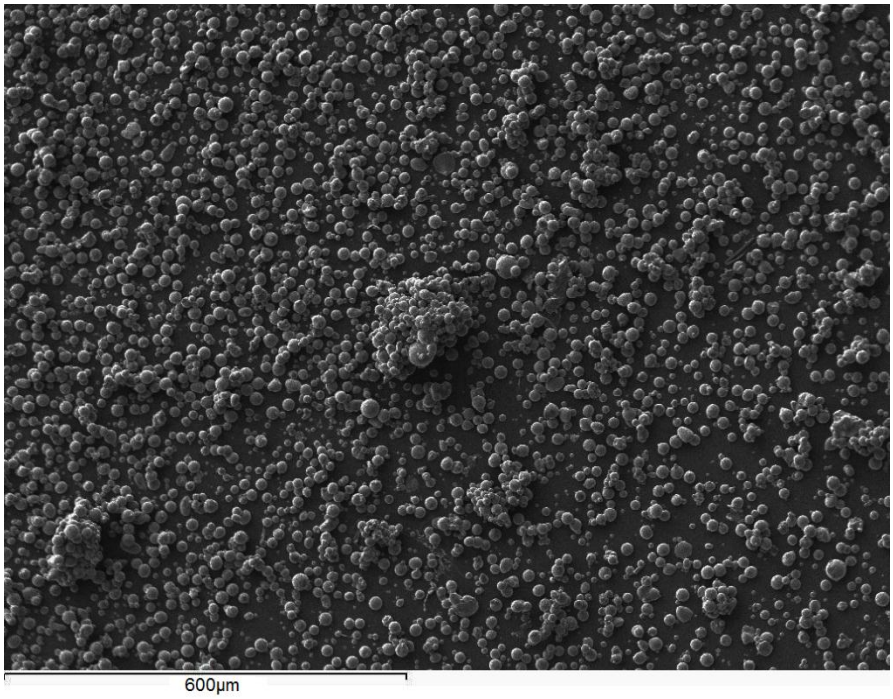

Figure 3.15: SEM image of the separated particle size which is made of 40 mg/ml PVP concentration and operated at 4.5 bar pressure: (a): 122 µm pore size (mesh 120), (b) 178 µm pore size (mesh 80), (c) 310 µm pore size (mesh 50)

The PVP concentration is also a major factor in determining the size distribution of the separated particles as it provides a binder which affects the strength of the pellet and binds the particles. Four different PVP concentrations were used to make the pellets which were fired at a pressure of 4.5 bar and mesh with pore size 178 µm. Figure 3.16a shows the separated particles for 40 mg/ml PVP concentration. As can be seen, the pellet was efficiently broken up into individual particles with only a few small agglomerated particles. The passage percentage decreased only slightly after increasing the PVP concentration to 60 mg/ml for the pellet and the resulting particles are shown in Figure 3.16b. A number of agglomerates were observed at this condition. As shown in Figure 3.14, the passage percentages are not significantly different for different PVP concentrations between 60 to 90 mg/ml. Figure 3.16b-d shows that some agglomerated particles were able to pass through pores of the 178 mm mesh. However, a 40 mg/ml PVP concentration made pellet provides a good control on the size distribution of the separated particle and a higher passage percentage, i.e. it has sufficient binder strength to form the pellet that can be manipulated and mounted on the ground slide, but not so much strength that it affects particle separation.

The results show that size distribution of the separated particle is tends to be narrow for the smaller mesh pore size. Meshes with pore size 122 and 178 μm displayed a good quality of the size distribution for 40 mg/ml PVP concentration made of pellet. In addition, a mesh with a pore size of 178 μm yields a higher passage percentage. Large separated particles can significantly damage the target tissue are detrimental and hence are not acceptable in this study. In addition, the strength of the pellet also does not allow the particles delivery due to a lack of particle separation. Most of the pellets should be separated into individual micro-particles, and the maximum agglomerated particle size should be kept below a target of 70 μm.

(a) 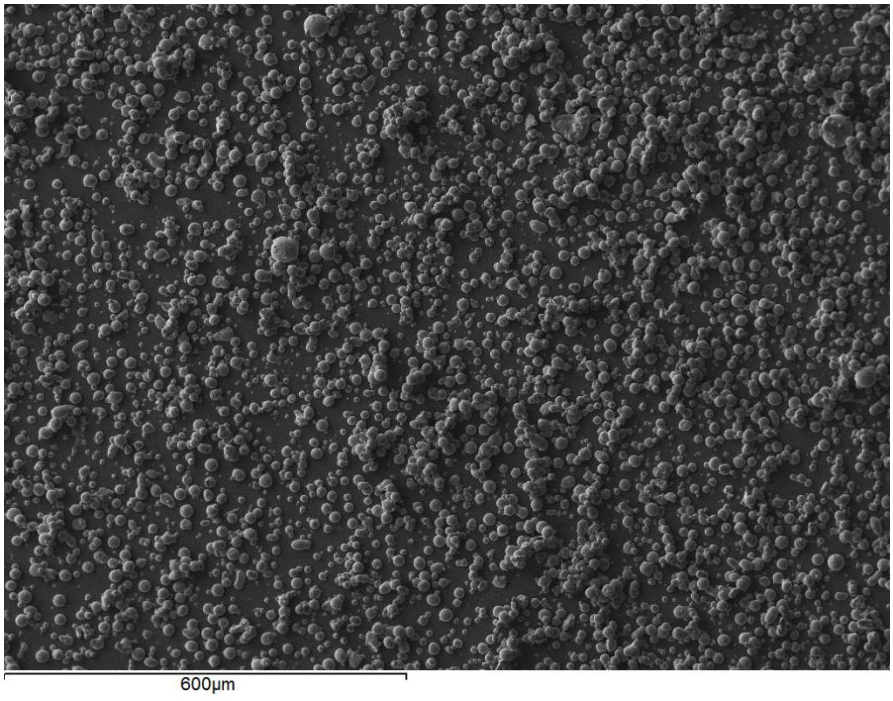

(b)

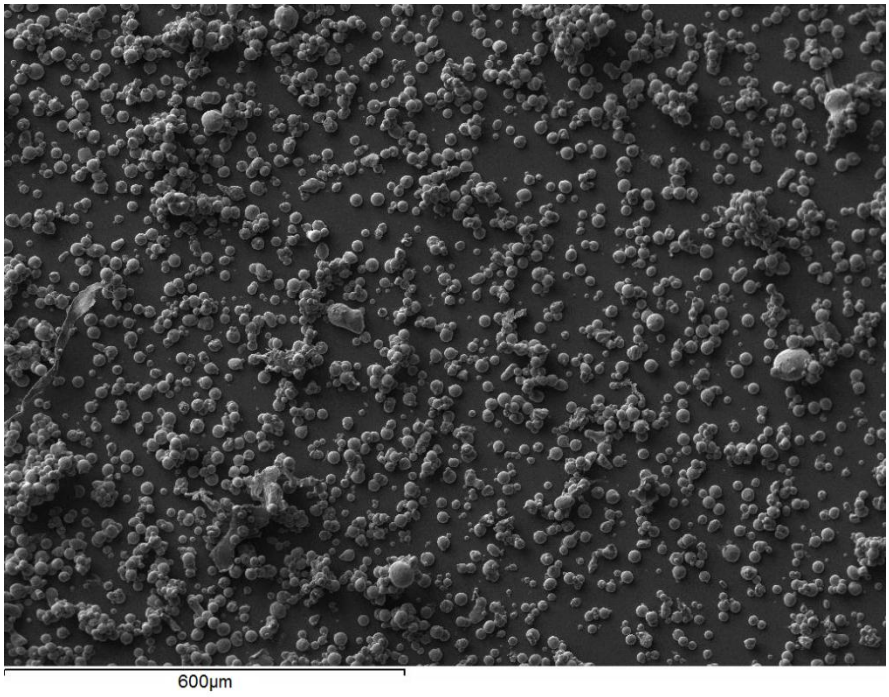

(c)

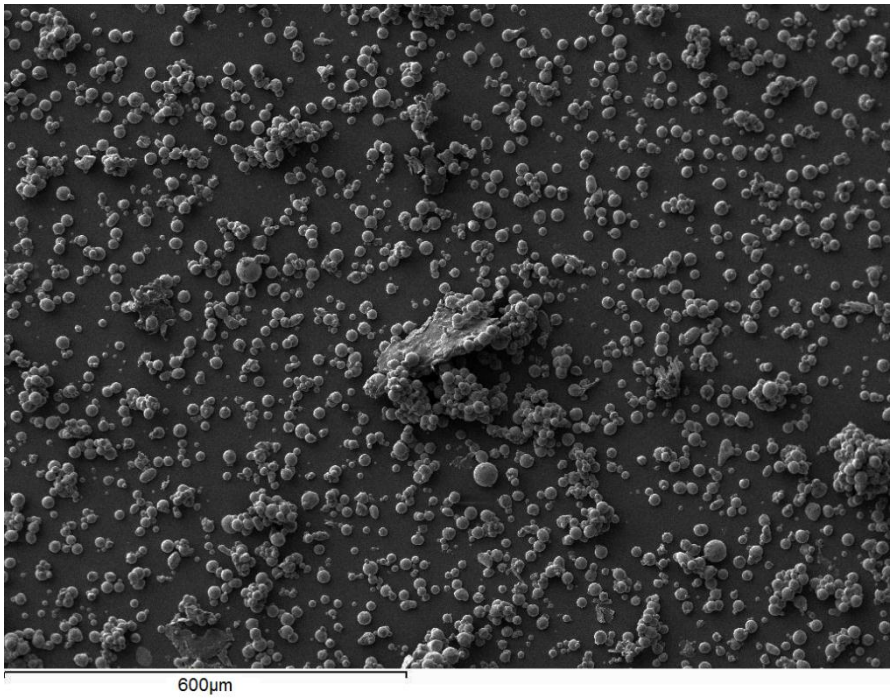

(d) 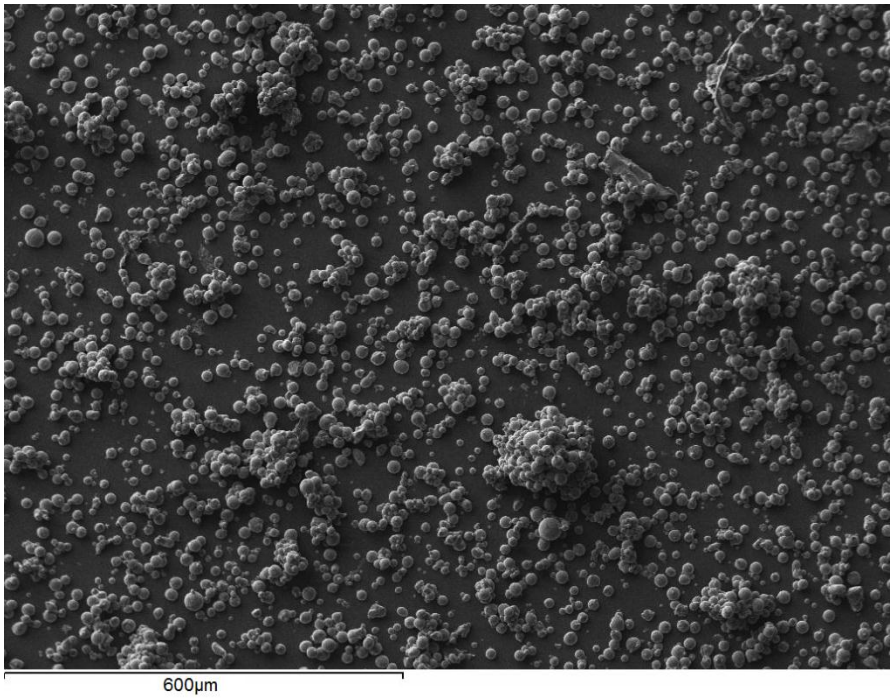

Figure 3.16: SEM image of the separated particle size which is operated at 4.5 bar pressure and mesh with pore size 178 µm: (a): 40 mg/ml PVP concentration made of pellet, (b): 60 mg/ml PVP concentration made of pellet, (c): 75 mg/ml PVP concentration made of pellet, (d): 90 mg/ml PVP concentration made of pellet

3.4.3 Deceleration stage

3.4.3.1 The micro-particle penetration in agarose gel

An aqueous gel made using 0.02 g/ml agarose was chosen as a target medium to study the effect of the solid microneedle application on the micro-particle penetration. In the experiment, agarose powder is dissolved into water and heated in a microwave heater which is then added into a sliced test tube. The test tube is covered solidly from one side with a removable film. Thus, a flat surface of agarose gel is obtained after the removal of the film when the gel is set in the test tube. The MN array is manually pressed by putting a flat plate on the back of the MN array which provides a uniform force to pierce the MN into the gel until the backing surface of the MN just contacts the gel surface. This flat surface is used as an object of reference for the determining the insertion of the MNs. Also it is used for the measurement of the particle penetration depth. Figure 3.17 shows a typical the distribution of the stainless steel micro-particles after impact on surface of the agarose gel. As can be seen, the micro-particles were non-uniformly distributed of the gel, with a maximum concentration at the centre coinciding with the impact position of the pellet on the mesh. In this experiment, the microneedle array (see Figure 3.9) had been pressed into the surface of the gel and then

removed. The holes created by the microneedle array are clearly visible and they remain on surface of the agarose gel. The size and shape of these holes change only very slowly with time after the microneedles are withdrawn. The agarose gel is a viscoelastic material like skin and the MN holes therein shrink with time. We have used 10 holes to obtain an average length of the pierced holes in the agarose gel which is found to be approximately 720 μm when Admipatch MN 1500 is inserted.

Figure 3.17: An image of the micro-particle sprayed on an agarose gel

Table 3.5: The penetration depth of the micro-particles

PVP concentration (mg/ml)	**Pressure (bar)**	**Maximum Penetration depth with hole (μm)**	**Penetration depth without hole (μm)**
40	4.5	515.7±124.3	221.4±44.8
	3	508.6±137.2	118.7±20.3

In order to determine the micro-particle penetration, agarose gel was cut into thin slices (approx. 1 mm thick) by razor sharp blades and analysed in more detail using a digital optical microscope (Eclipse 3100 and Digital Sight, Nikon). As shown in Figure 3.18, the holes were formed and remained in the gel after the application of the solid microneedle. Figure 3.18 also shows that the stainless steel micro-particles were visible in the gel surface and within the holes. As can be seen, the micro-particles seem to have a larger penetration depth compared to those that have not entered through the pierced holes on the left size of the figure. As expected, the micro-particles can penetrate into a deep area via the holes. The other micro-particles only have a little penetration without the hole. The maximum penetration depths are shown in Table 3.5 in detail.

As discussed before, Mitchell *et al*. (2003) used a LGG to accelerate 99 μm diameter polystyrene micro-particle and achieved a maximum penetration depth of 150 μm at 60 bar pressure. Kendal *et al*. (2004a) used a convergent-divergent device to accelerate gold particles of diameter 1.8 μm which achieved a maximum penetration depth of 78.6 μm at 60 bar. As can be seen from Table 3.5, the maximum penetration depth in this study seems to improve in comparison of the results of Mitchell *et al*. (2003) and Kendall *et al*. (2004a). However, an agarose gel of concentration 2% may not mimic the human skin properties exactly and as such, the implication of the mechanical properties of the target should be analysed in more detail. Nevertheless, the results in this section show that the application of a solid microneedle has a beneficial effect on the micro-particle penetration depth. In addition, the agarose gel provides a good condition for the measurement of the micro-particle penetration depth by a digital optical microscope. A skin mimicking agarose gel will be considered in another study to demonstrate further that microneedle based system has a positive effect for micro-particle delivery and the implications of the mechanical properties of the target tissue.

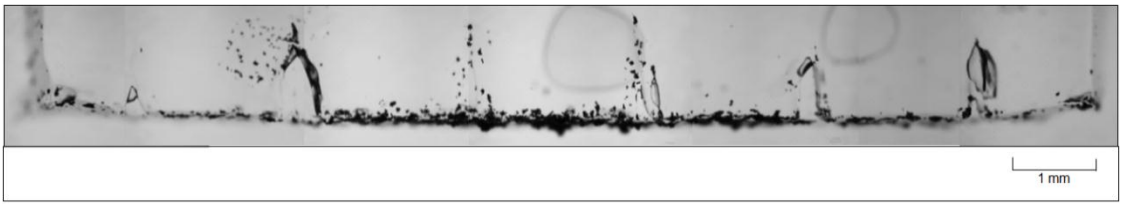

Figure 3.18: Optical microscope image of stainless steel micro-particle penetration into agarose gel (40 mg/ml PVP, 5 bar, Mesh with pore size 178 μm)

3.5 Chapter Summary

An experimental rig involving a micro-particle delivery and injection system has been built in this study to determine if solid MNs can enhance the penetration depths of the low density micro-particles which may be used to deliver genes and drugs. For the purpose of this design, the micro-particle delivery process has been separated into three stages. For the first stage, namely, the acceleration stage, the results show that an increase in the mass of the ground slide which carries the particles in the form of a pellet causes a negative effect on the ground slide acceleration and hence a reduced velocity of the micro-carrier pellet. The mass of the ground slide is related to its material density and size where the size is typically determined by the barrel diameter. Based on the present result, a narrow barrel was chosen for the study of the separation and deceleration stages as it has positive effect on the mass of the ground

slide and pressure drop. For the separation stage, the passage percentage was measured using an empty test tube to collect the separated stainless steel particles which had been broken by passage through a mesh. The results show that the passage percentage increases with pressure and mesh pore size but decreases with increasing pellet binder concentration. Increased binder concentration causes an increase of pellet strength, which seems to have a negative effect on the pellet separation. The mesh pore size affected the break up of the pellets into individual particles; larger mesh sizes allowed large agglomerated particles to pass through, which is not desirable. The mesh pore size has a significant effect on the size distribution of the separated particle and it can separate the pellet properly into individual particles. In addition, higher binder concentration pellets led to an increased number of large agglomerated particles. This is not desirable because the large particles can significantly damage the target tissue. Pellets bound with 40 mg/ml PVP yielded a higher passage percentage and a good control on the size distribution of separated particle based on the application of 178 μm pore size mesh. For the deceleration stage, 2% concentration of agarose gel was chosen as a transparent target material to study the effect of solid MN application on micro-particle delivery. The results show the pellet is well separated and sprayed onto the target; a number of stainless steel micro-particles can penetrate a deep area inside the gel due to the holes created by the solid MN application. The maximum penetration depth is comparable with previous study (e.g. Kendall *et al*., 2004a; Mitchell *et al*., 2003) and in some cases shows a significant improvement, but without the need for high pressure gas flows which can damage soft tissues. However this should be investigated further in a future study.

4. Microneedle assisted micro-particle delivery: Experiments using skin mimicking agarose gel

4.1 Chapter Overview

A set of laboratory experiments has been carried out to determine if microneedles (MNs) can enhance penetration depths of high speed micro-particles delivered by a type of gene gun. The micro-particles were fired into a model target material, agarose gel, which was prepared to mimic the viscoelastic properties of porcine skin. The agarose gel was chosen as a model target as it can be prepared as a homogeneous and transparent medium with controllable and reproducible properties allowing accurate determination of penetration depths. Insertions of various microneedles into gels have been analysed to show that the length of the holes increases with an increase in the agarose concentration. The penetration depths of micro-particle were analysed in relation to a number of variables, namely, the operating pressure, the particle size, the size of a mesh used for particle separation and the MN dimensions. The results suggest that the penetration depths increase with an increase of the mesh pore size, due to the passage of large agglomerates. As these particles seem to damage the target surface, then smaller mesh sizes are recommended; here a mesh with a pore size of 178 μm was used for the majority of the experiments. The operating pressure provides a positive effect on the penetration depth, i.e., it increases as pressure is increased. Further, as expected, an application of MNs maximizes the micro-particle penetration depth. The maximum penetration depth is found to increase as the lengths of the MNs increase. e.g., it is found to be 1272 ± 42 μm, 1009 ± 49 μm and 656 ± 85 μm at 4.5 bar pressure for spherical micro-particles of 18 ± 7 μm diameter when we used MNs of 1500 μm, 1200 μm and 750 μm length, respectively.

4.2 Introduction

Gene guns have been shown to be useful for delivery of DNA vaccines into tissues (Joseph *et al*., 2012; O'Brien and Lummis, 2011; Fuller *et al*., 2006; Trimble *et al*., 2003; Bellhouse *et al*., 1999). These delivery systems are primarily accelerators of micro-particles, which deliver DNA loaded micro-particles into target tissues to achieve the desired gene transfection (O'Brien and Lummis, 2011; O'Brien and Lummis, 2006; Zhang *et al*., 2001; Sanford *et al.*, 2000). The micro-particles are generally required to penetrate to epidermis layer within the target to carry out the desired effect of gene delivery and, as such, the penetration depth of the micro-particles is one of the major variables studied in gene delivery research. Ziegler (2008)

has indicated that an acceptable DNA delivery requires that the micro-particles penetrate into the target skin tissue by approximately 20 - 100 μm. However, the top layer of the skin, i.e., the stratum corneum (SC), limits the penetration depths for the particles (Kendall, 2006; Fuchs and Raghavan, 2002) due to its resistance to particle motion. Furthermore, whatever the particles achieve in terms of penetration depths in the target tissue, depends on a number of key variables such as the operating pressure, particle size, properties of the target tissue, etc. (Soliman and Abdallah, 2011; Arora *et al*., 2008; Zhang *et al*., 2007; Brown *et al*., 2006; Mitchell *et al*., 2003).

In general, the micro-particles follow two routes of penetration into the target tissue, which are the extracellular and intercellular routes (Mitchell *et al*., 2003). The extracellular route is followed during delivery of large particles, when the tissue is damaged between the cell boundaries. Soliman (2011) has suggested that particles which have larger diameters, e.g. 15 - 100 μm, are expected to penetrate by extracellular failures of the tissues. In this case, an increased size of lower density micro-particles can achieve sufficient momentum to breach the target layer and penetrate further to the desired depths inside the target tissue (Hardy *et al*., 2005; Chen *et al*., 2001). Due to their biocompatibility and low cost, biomedical grade stainless steel and polymeric micro-particles are considered to be good choices to replace high density gold particles. For example, polymeric micro-particles of 15.5 and 26.1 μm diameters have been delivered at 6 MPa in a conical nozzle by Quinlan *et al.* (2001). Kendall (2002) has also used converging-diverging nozzle to deliver polystyrene micro-particles of 26.1 and 39 μm average diameters at 4 MPa to velocities of 365 and 350 m/s, respectively. Truong *et al.* (2006) have used polystyrene particles of 15 and 48 μm diameter at 6 MPa in a contoured shock tube (CST). Liu *et al.* (2006) have operated with polystyrene particles of diameter 40 μm at 6 MPa to study the particle velocity for a CST. Mitchell *et al.* (2003) have used stainless steel micro-particles of 25 μm diameter and concluded that the particles can penetrate up to 150 μm into excised canine buccal mucosa at a velocity of 170 m/s. Polystyrene particles of 15.5, 25, 48 and 99 μm diameters have also been operated at 2, 4 and 6 MPa pressures in the light gas gun (LGG) by Mitchell *et al.* (2003).

Based on these previous studies, it can be concluded that the diameters of low density micro-particles (e,g., polystyrene and stainless steel) which have been used in gene delivery typically ranged between 15 to 100 μm. Furthermore the operating pressures for particle delivery fall in the range between 2 to 6 MPa, which may be considered to be high in many

devices. Xia *et al.* (2011) have indicated that 200 psi (1.4 MPa) should be the maximum pressure for biolistic transfer of micro-particles to tissue without any damage to the target material. Traditionally, heavy metal micro-particles including tungsten (Morgan *et al*., 2011; Williams *et al*., 1991; Zelenin *et al*., 1989; Klein *et al*., 1987) and gold (O'Brien and Lummis, 2011; Rinberg, 2005; Swain *et al*., 2000) coated with DNA have been used for targeting tissues. These elements have high densities and are well suited for particle bombardment. However, tungsten particles have several disadvantages such as non-biocompatibility, DNA degradation and toxicity to cells (Bastian *et al*., 2009; Yoshimisu *et al*., 2009; Russell *et al*., 1992). Gold particles carry the disadvantage of being very expensive. Cell damage is another problem for the biolistic micro-particle delivery. Sato *et al.* (2000) have used various types of gene guns to transfer genes into live rodent brain tissue, which confirmed mechanical damage on cells from micro-particles delivery. However, cell damage decreases from a decrease in particle size and operating pressure (O'Brien and Lummis, 2011; Xia *et al*., 2011; Uchida *et al*., 2009).

Addressing the points above, a method of delivering micro-particles is explored in this work using a model experimental rig, which mimics a typical gene gun for delivery of micro-particles. A model experimental rig is preferred over a gene gun as it allows control and monitoring of important operating variables. A polytetrafluoroethylene (PTFE) made ground slide is used in the current rig, which prevents impact of the pressurized gas onto the target skin and slows down the velocity of micro-particles while achieving the purpose of minimized cell damage. The rig also makes use of the application of the microneedle (MN) to overcome the effect of the barrier of micro-particle target, allowing a number of micro-particles to reach the deeper area of the target tissue via the holes created by MNs. Micro-particles of biocompatible stainless steel, which have a lower density compared to gold and tungsten and are cheaper than gold, are used in this work. The mechanisms of MN insertion in the skin and, in particular, its application in creating well-defined holes in the skin have been studied for some years. For example, McAllister *et al.* (2003) have observed that holes are created in skin indicating that there is an amount of residual strain that remains after the microneedles have been removed. They have used a cylindrical MN of 20 μm diameter to perform staining experiments which indicated that the holes remain after removal of the MNs. Davis *et al.* (2004) have used a conical hollow MN of 720 μm length and 30 - 80 μm tip radius to insert into the skin to study the holes created after removal the MN. In addition, Martanto *et al.* (2004) have used a MN array with a needle length of 1000 μm and width of

200 µm by 50 µm to create visible holes on a rat skin for drug delivery. Kalluri *et al.* (2011) have applied conical MNs of 559 ± 14 µm length, 213 µm base width and 4 µm tip radius on the skin and reported that they create micro-channels of 60 µm surface diameter and 160 ± 20 µm depth.

The above studies on gene gun show some situations where the gene guns could be coupled with MNs for improved delivery of micro-particle delivery from gene guns in the practice. This chapter is focused on developing a MN based system for micro-particle penetration. For the purpose of this chapter, agarose gel is chosen as a target, as it is a homogeneous and semi-clear material, providing the convenience to measure the micro-particle penetration depth by a digital optical microscope. Furthermore changing the agarose concentration allows alteration of the viscoelastic properties of the target from one experiment to another, which is difficult to achieve in the case of real tissue, e.g. porcine skin. In our experiments, agarose gel with viscoelastic properties which mimicked porcine skin is used to study micro-particle penetration. In addition, this chapter is aimed at studying the penetration depth in relation to important variables which affect the particle penetration, e.g., operating pressure, particle size and MN length, using the skin mimicked concentration of agarose and others.

4.3 Material and Methodlogy

4.3.1 Material

Irregular shaped and spherical micro-particles made of biocompatible stainless steel were purchased from Goodfellow Cambridge Ltd. (Huntingdon, UK) and LPW Technology Ltd. (Daresbury, UK), respectively. Detailed characterization of the micro-particles is introduced in section 4.3.3.2. Agarose powder was purchased from Sigma-Aldrich Company Ltd. (Gillingham, UK). Porcine ear skin samples were obtained from a local butcher.

Stainless steel meshes, used for micro-particle separation were bought from MeshUK, Streme Limited (Marlow, UK).Two different MN arrays (AdminPatch MN 1200 and 1500) which are 1200 and 1500 µm long were purchased from nanoBioSciences limited liability company (LLC) (Sunnyvale, CA, USA). In addition, an in-house stainless steel MN array which is made of 750 µm long was used in this study. The characterization of each MN array is explained in section 4.3.3.3.

4.3.2 Experimental design

A detailed description of a MN based micro-particle delivery system has been introduced in the previous chapter (see section 3.3.2). Generally, the system comprises an acceleration, a separation and a deceleration stage. In such a system a pellet of micro-particles is accelerated by a pressurized gas to a sufficient velocity in the acceleration stage. It is then separated into a number of small particles by impaction onto a mesh in the separation stage. Finally, the separated particles penetrate the target which is the final deceleration stage. In order to achieve the aims of this chapter and carry out an in-depth study of the penetration depth of the solid micro-particle, an improved version of the experimental rig (Figure 3.1) is used in this work. Figure 4.1a shows the sections corresponding to the acceleration, separation and deceleration stages. The improvement has been made in the deceleration stage which contains the target material for the particles to penetrate. For the purpose of this case, a sliced test tube (described below) has been placed in the deceleration stage to hold in place the agarose gel, which acts as a target for the micro-particles. Both ends of the glass tube are open, which make it convenient to remove the agarose gel without damage, following a penetration test.

In this work, an setup modified from Figure 3.1 is used. It is made by using a sliced test tube (see Figure 4.1b) which allows observation of particle penetration without the need to slice the gel. It is based on a polytetrafluoroethylene (PTFE) mold which is placed inside the sliced test tube, as shown in detail in Figure 4.1b. A test tube is sliced into approximately 1 cm thick sections where both sides are kept open. The mold is then inserted into a tube piece. The void space in the mold contains the agarose gel. The mold can separate into two parts, providing a convenient method for the removal of the gel. Based on the application of the mold, the agarose gel is prepared into uniform pieces of of 1 cm thickness with smooth surfaces on both sides to provide a good environment for a digital microscope to detect the micro-particle penetration.

4.3.3 Experimental methods

4.3.3.1 Data acquisition

(a) Preparation of skin mimicking agarose gel

In this work, agarose gel is used as a skin mimicking target, which allows visualization of the particles and measurement of the particle penetration depths as a function of number of variables as discussed later. The method of skin mimicking in this work is based on preparing an agarose gel, which has similar viscoelastic properties to porcine skin samples collected

from a local butcher. The skin samples used were the intact fresh skin collected from the ears of young piglets (5-6 months old).

The procedure to determine the skin mimicking agarose gel to be used as a target for micro-particles is as follows. First of all, a rotational viscometer with parallel plate geometry (AR 1000 – N, TA Instruments) was used to characterise the dynamic viscoelastic properties of the porcine skin samples. In order to increase the accuracy of the skin property measurement and avoid wall slippage, an upper plate of 2 cm diameter and containing teeth (1 mm deep) was chosen, whereas abrasive silicon carbide paper was fixed to the base plate. This ensures that internal viscoelastic properties of skin samples are measured, rather than characteristics of their wall slip. The porcine skin samples were cut into a number of small pieces which have the same size as the parallel plates for rheological analysis. The teeth plate was penetrated into the skin to avoid slippage and further to increase the accuracy to measure the rheology of skin tissue under the teeth. Oscillation test was chosen to analyse the skin and agarose gel samples in this work. In order to mimic the porcine skin properties using agarose gel, a wide range of angular frequencies has been used in the viscometer, to investigate the important time scales of the viscoelastic media. However, in the current experiment, results from only a narrow range of frequency are presented. All of the tests are performed in the linear regime, at constant strain and temperature of 1% and 20°C, respectively. The angular frequency was varied from 84 to 474 rad/sec to measure the dynamic viscoelastic properties.

(a)

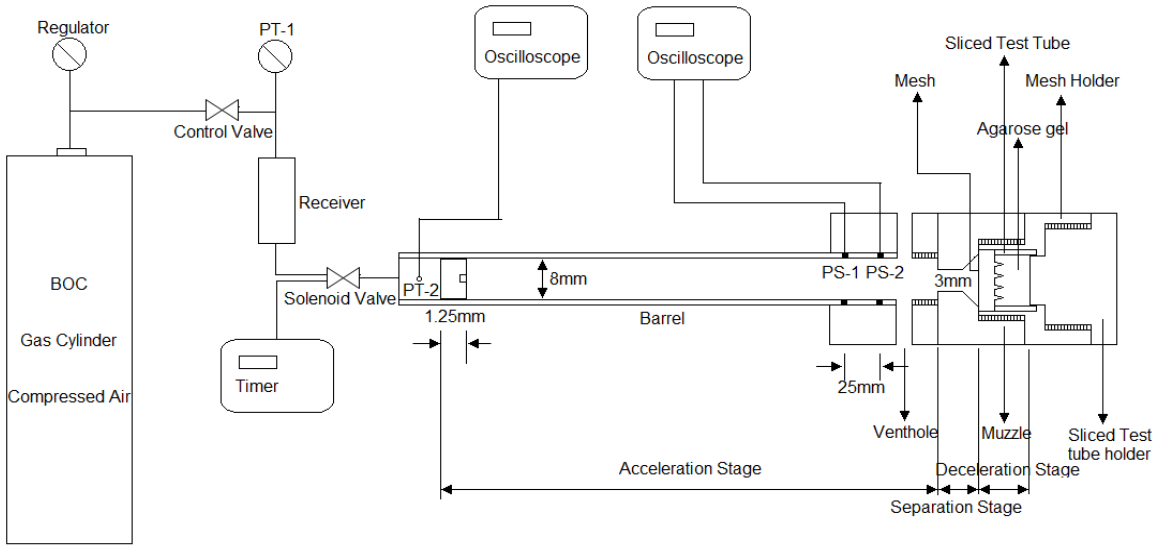

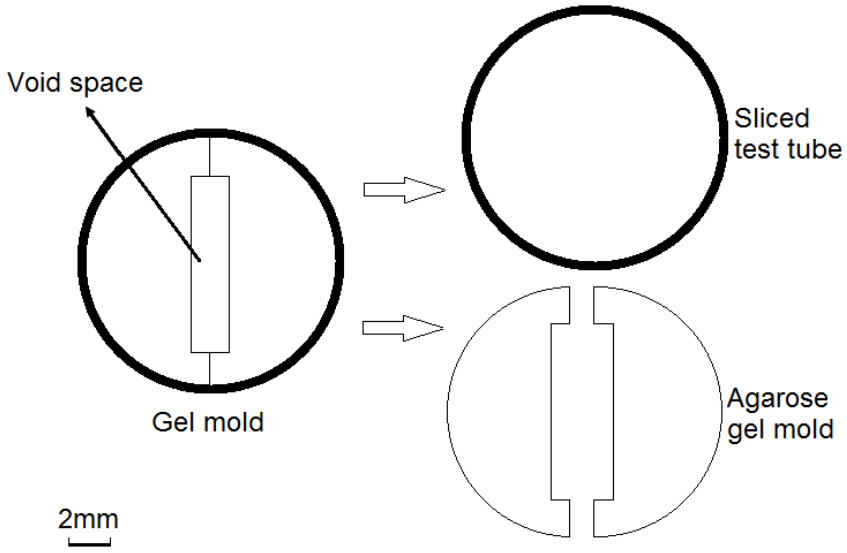

(b)

Figure 4.1: (a). A schematic diagram of the experimental rig which is an improved version of the Figure 3.1; (b). A schematic diagram of the agarose gel mold

After determining the dynamic viscoelastic properties of the porcine skin, agarose gels with different concentrations of agarose were analysed to identify the gel that best matches the dynamic viscoelastic property of the porcine skin. The gels were moulded into 2 cm diameter slices and a similar thickness as the porcine skin to provide comparability between results of the two materials.

The experimental data for both skin and agarose gels are used to determine the storage modulus (G') (see equation 4.1) and loss modulus (G'') (Meyers and Chawla, 1999) (equation 4.2). Those two moduli are related to the strain amplitude γ_0, stress amplitude σ_0 and a phase lag between the strain and stress δ of the material. G' of the samples shows the stored energy in the material and indicates the elastic properties. On the other hand, the G'' indicates the energy dissipated as heat and characterises the viscous properties. The data are used to calculate the friction coefficient between particle and skin tissue (μ') of the samples as functions of angular frequency ω (Meyers and Chawla, 1999).

$$G' = \frac{\sigma_0}{\gamma_0}\cos\delta \qquad (4.1)$$

$$G'' = \frac{\sigma_0}{\gamma_0}\sin\delta \qquad (4.2)$$

Where $$\sigma_0 = \sigma / \cos(\omega t) \qquad (4.3)$$

$$\gamma_0 = \gamma / \cos(\omega t - \delta) \quad (4.4)$$

$$\mu' = G'' / \omega \quad (4.5)$$

In the equations t, σ and γ represent the time, stress and strain, respectively.

(b) Determination of the micro-particle penetration depths and hole lengths

In section 3.4.3, we have shown that the particle penetration depths can be measured by a digital optical microscope (Eclipse 3100 and Digital Sight, Nikon). As described in §2.2, a mold is used to prepare the agarose gels to uniform size of 2 mm width, 8 mm length and 1 cm thickness (see Figure 4.1b) and avoided the need for later slicing. The gel was conveniently removable which avoids damage prior to further analysis. In the experiment, a uniform force to pierce the MN array into the gel was achieved by manually pressing it on a flat plate which is placed on the back of the MN array. The MN patch was pressed carefully until it reached the flat surface of the gel. The gel was taken out and analysed by microscope directly. Several digital images are taken, and the particle penetration depth was measured by an image processing software (Image J) using the digital images. Calibration of these images was conducted using a graticule. The time scale between MN removal and observation of holes was approximately 30 seconds. The experiment of MN insertion was repeated three times for the gel per concentration to increase the reliability of the results and verify the length of the pierced holes. For the measurement of the micro-particle penetration depth, the procedure was the same with the detection of the hole lengths. The only difference is that the micro-particles were fired into the gel. The time scale between firing micro-particles and observation of penetration depth was approximately 2 minutes.

4.3.3.2 Characterization of the irregular stainless steel micro-particles

Two supplies of biocompatible stainless steel made of both irregular and spherical micro-particles were chosen for the purpose of this case. Figure 4.2 shows a scanning electron microscopic (SEM) image of the applied irregular stainless steel micro-particles; most of the particles have rough surfaces and the average sphericity was determined as 0.66 ± 0.13 from image analysis. Based on the analysis of a particle size analyser (Coulter LS130, BECKMAN COULTER, Inc., USA), the particle size distribution was determined which is found to be in the range of 10 to 80 μm, while the the Sauter mean diameter of the particles is 30 ± 15μm. The bulk density and porosity of these micro-particles are 3.35 ± 0.05 g/cm^3 and 58.0 ± 0.6%, respectively. A second supply of micro-particles was discussed earlier in the section 3.3.3.2.

It was much more spherical with an average sphericity of 0.92 ± 0.05. Their size distribution range was between 1 and 20 μm and their Sauter mean diameter was 18 ± 7μm.

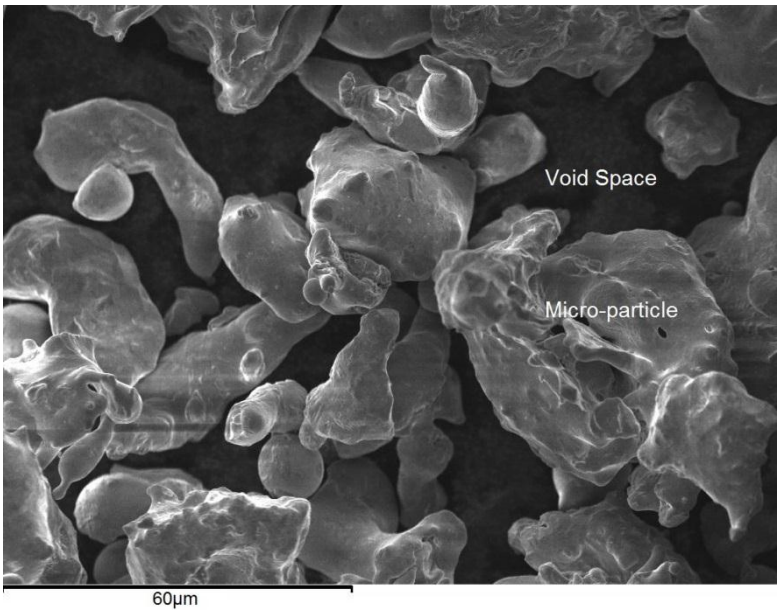

Figure 4.2: A SEM image of the irregular stainless steel (biocompatible) micro-particles

4.3.3.3 Characterization of the microneedles

In this work, three different MNs were used to determine the effects of geometry on the particle penetration process. Three different lengths of the MNs were chosen so as to confirm that the trend of results obtained from one particular MN length is observed for another length of MN.

First of all, a commercially available MN patch namely AdminPatch MN 1500 has been applied. This maintains continuity of our work as it is, the same MN that array was used in a previous work (see section 3.3.3.4). The array has a total of 31 MNs which are distributed as a diamond shape on a 1 cm^2 circular area. The spaces on the side line and diagonal lines are 1546, 1643 and 3000 μm (see Figure 3.9); the length, thickness and width of each of the MNs are 1500, 78 and 480 μm, respectively. In addition AdminPatch MN 1200 was used (see Figure 4.3a) which has 43 flat MNs and the MNs are distributed more closely on the same size patch as MN 1500. The spaces on the diagonal lines are 1252, 1970 and 2426 μm. The thickness and width of each MN are the same as AdminPatch MN 1500 array except the length is 1200 μm. Finally, an in-house fabricated MN array was also used in this work with a view to increase the range of variables which should provide a better understanding of the micro-particle delivery process. Figure 4.3b shows the in-house fabricated MN array which

consist of 3 cylindrical MNs on a circular patch. As can be seen, the tip of the needle, made of biocompatible stainless steel, is polished flat smooth using sand paper. The pitch, i.e., the centre-to-centre distance between two MNs is 500 μm, and the length and diameter of each MN are 750 and 250 μm, respectively. The main characteristics of the above three MN arrays are listed in Table 4.1.

Table 4.1: The characterizations of the MN array used in this study

Name	**Parameters**	**Value (μm)**
Adminpatch MN 1500	Length	1500
	Width	480
	Thickness	78
	Space between MNs	1546
Adminpatch MN 1200	Length	1200
	Width	480
	Thickness	78
	Space between MNs	1252
In-house fabricated MN	Length	750
	Diameter	250
	Space between MNs	500

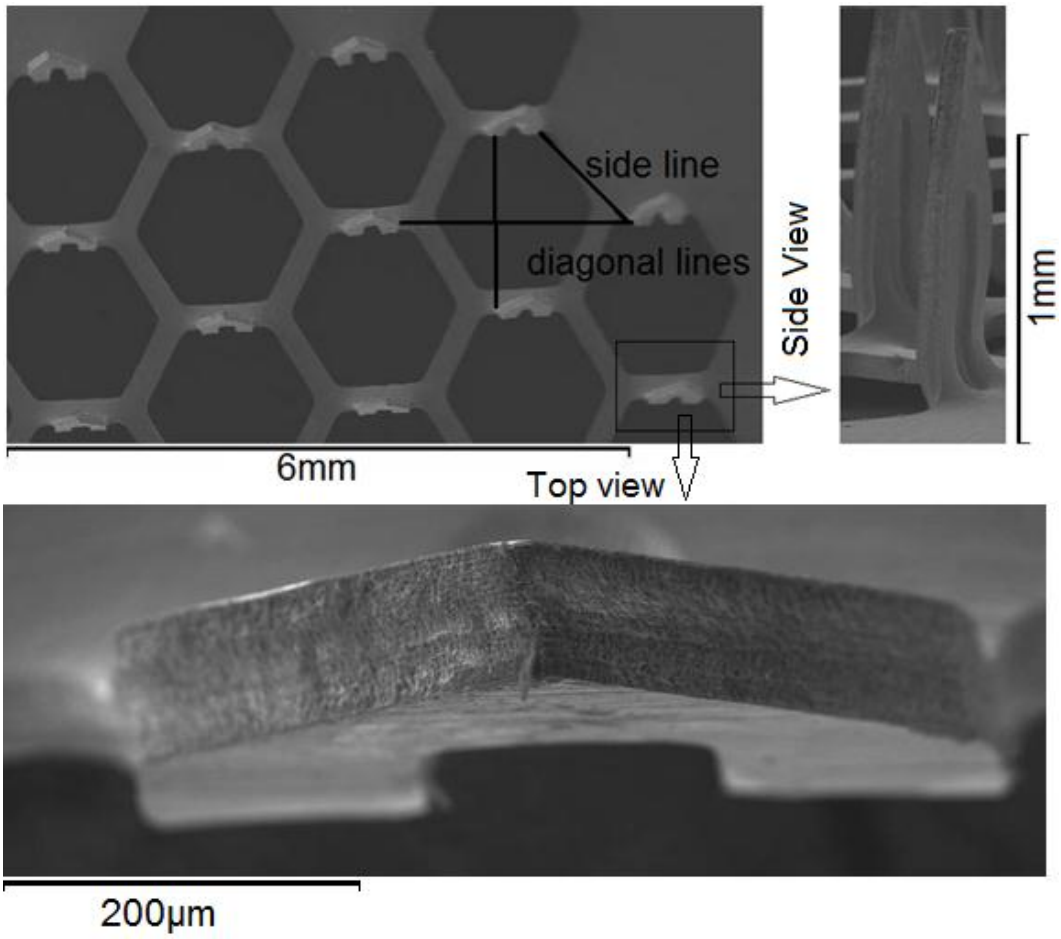

(a)

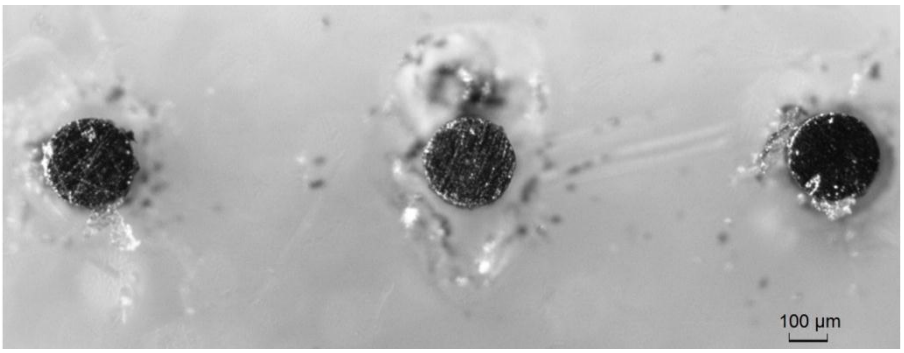

(b)

Figure 4.3: The image of MN arrays: (a) AdminPatch MN 1200 (b) In-house fabricated MN array

4.4 Results and Discussions

4.4.1 Preparation of skin mimicking agarose gel

Two 2000 µm thick porcine skin samples cut from ears were used to study the dynamic viscoelastic property properties, as described in section 4.3.3.1. The results are presented in section 4.4.1.1, whereas the dynamic viscoelastic properties of skin mimicking agarose gel are presented in section 4.4.1.2 in detail. Porcine skin has been used previously as a substitute

to human skin, as it has similar histological and physiological properties (Dominik et al., 2010; Edwards et al., 1995; Shergold et al., 2006) and is often used in transdermal drug delivery studies (Kong et al., 2011). Similarly, agarose gel has been used to mimick skin tissues in previous studies. For example, Koelmans *et al.* (2013) have used agarose gel as a skin simulant to mimic the dermis layer of the skin to study how MNs interact with soft tissue. Arora *et al.* (2007) have chosen agarose gel as a model tissue material to study the penetration of pulsed micro-jets. Some discussions on the rheology of these materials, which mostly relate to dynamic stress-strain relationship, can be found in the literature (Huang et al., 2013; Zeng et al., 2001; Sliver et al., 2001; Henry et al., 1997). We choose to determine the rheological properties in-house as it provides us the option to control the conditions under which they are measured.

4.4.1.1 Dynamic viscoelastic properties of porcine skin

In this set of experiments, the dynamic viscoelastic properties of porcine skin were tested at a constant strain value of 1% and wide range of angular frequency from 84 to 474 rad/s by a rotational viscometer with parallel plate geometry. Storage modulus (G') of the samples shows the stored energy and explains their elastic properties, whereas the loss modulus (G'') indicate the energy dissipated as heat and characterises the viscous properties. The temperature on the parallel plate during the experiment was controlled at 20℃ to reduce the thermal effects on the results. Figures 4.4a-c show the dynamic viscoelastic properties of two porcine skin samples as a function of angular frequency. As can be seen, both samples show that the G' and G'' increase due to an increase in angular frequency. Moreover, G' and G'' are found to match well for the two skin samples, showing consistency of the measurements. Although G'' shows a slight difference before 300 rad/s, the difference seems to be negligible for most practical purposes. Figure 4.4c shows that the friction coefficient between particle and skin tissue (ŋ') decreases with an increase of the angular frequency. The dynamic viscosities of the two skin samples match closely for angular frequencies above 240 rad/s. The above results, which suggest that reproducible skin properties can be obtained, provide some confidence to characterise the skin using this viscometer. Finally, it points out that the friction coefficient between particle and skin tissue over a wide range of strain rates remains approximately constant at about 20 Pa s.

4.4.1.2 Porcine skin mimicking agarose gel

In order to simulate the properties of skin by agarose gel, a gel that has the same size as the porcine skin sample was prepared using a mold and analysed by the viscometer at the same maximum strain and range of oscillation condition as was used for porcine skin. After testing a wide range concentration of agarose gel we find that the viscoelastic properties of the agarose gel where agarose concentration ranges from 0.026 to 0.027 g/ml is close to porcine ear skin. As presented in Figures 4.4a-c, the concentration of agarose gel is varied from 0.025 to 0.03 g/m. The results of gel which have agarose concentration lower than 0.025 g/ml are not presented as their viscoelastic behaviour are significantly different from those of the porcine skin. Figure 4.4a shows the storage modulus of the agarose gel increases with increasing angular frequency, in agreement with the results for the skin sample. In addition, the storage modulus of the 0.0265 g/ml agarose gel shows an excellent match with the porcine skin. For the loss modulus, the agarose gel shows a slight decreasing tendency with an increase of angular frequency. The results of porcine skin samples present a different performance with agarose gel. However, the gel concentrations which range from 0.0265 g/ml to 0.0280 g/ml represent good matches in terms of the loss modulus variations of porcine skin. Figure 4.4c shows the agarose gel has a friction coefficient between particle and gel that decreases with increasing angular frequency (shear-thinning) which shows a same performance with porcine skin. After the comparison, agarose gel of 0.0265 g/ml is considered to match with the porcine skin. The other concentration of agarose gel shows a significant difference with porcine skin at lower angular frequency. Overall, the results of 0.0265 g/ml concentration of agarose gel seem to fit better with the porcine skin samples, if compared with the results of other concentration of agarose gel. As expected, these results demonstrate that it is possible to mimic the porcine skin using an agarose gel, based on the matching of the dynamic viscoelastic properties of the skin. It is not possible to obtain an exact match over a whole range of deformation conditions, but nevertheless, the 0.0265 g/ml concentration of agarose gel provides a reasonable match and hence will be used to study micro-particle penetration for the remainder of the experiment.

(a)

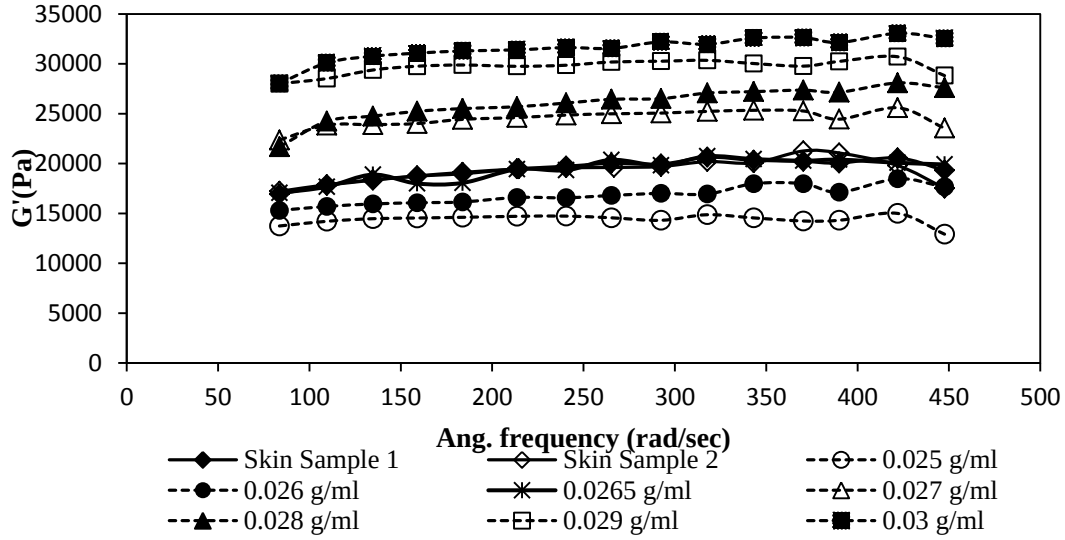
35000
30000
25000
20000
15000
10000
5000
0
G'(Pa)
0
50
100
150
200
250
300
350
400
450
500
Ang. frequency (rad/sec)
Skin Sample 1
Skin Sample 2
0.025 g/ml
0.026 g/ml
0.0265 g/ml
0.027 g/ml
0.028 g/ml
0.029 g/ml
0.03 g/ml

(b)

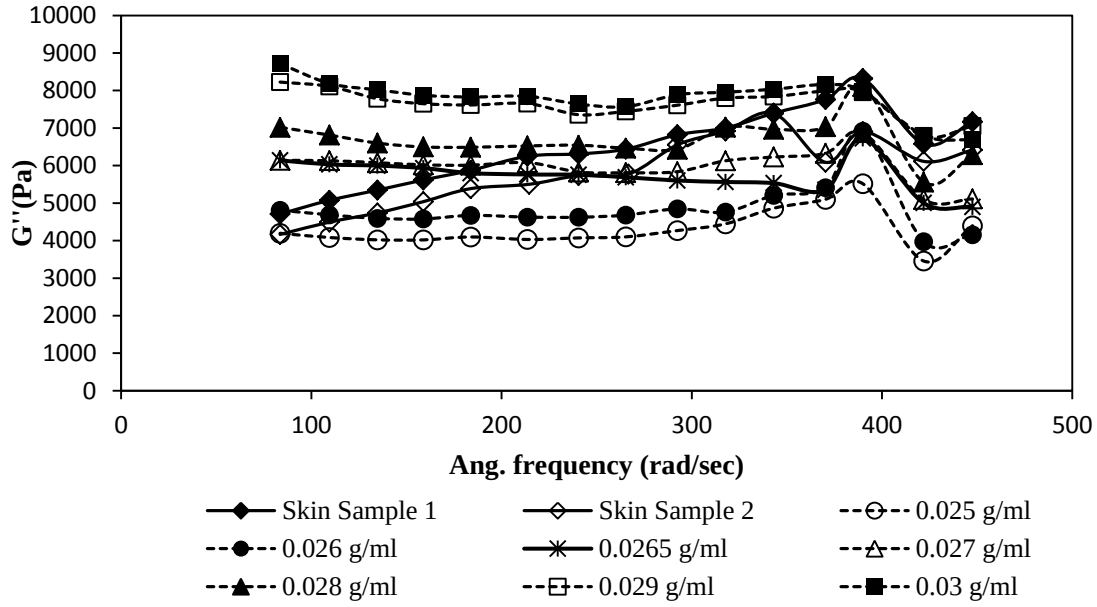
10000
9000
8000
7000
6000
5000
4000
3000
2000
1000
0
G''(Pa)
0
100
200
300
400
500
Ang. frequency (rad/sec)
Skin Sample 1
Skin Sample 2
0.025 g/ml
0.026 g/ml
0.0265 g/ml
0.027 g/ml
0.028 g/ml
0.029 g/ml
0.03 g/ml

(c)

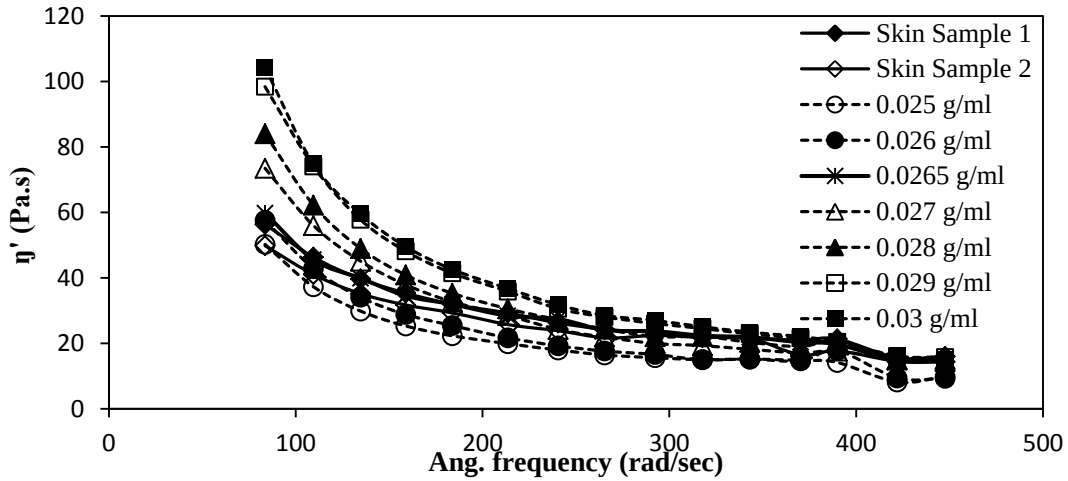

Figure 4.4: Skin mimicking based on the dynamic viscoelastic properties by using agarose gel: (a) storage modulus against angular frequency, (b) loss modulus against angular frequency, (c) friction coefficient between particle and porcine skin tissue/gel against angular frequency

4.4.2 Microneedle insertion

There has been a significant amount of MN insertion research which has focused on studying skin behaviour after a MN array has been applied. The skin reforms after the removal of the MN due to its inherent viscoelasticity (Olatunji *et al*., 2013; McAllister *et al*., 2003). Therefore, the length of the MNs is often longer than the desired depth in the skin (Bal *et al*., 2010; Donnelly *et al*., 2011; Kolli *et al*., 2008; Martanto *et al*., 2004). Furthermore, the holes created by the MN close up slowly after the MNs have been removed from the skin. In this case, the agarose gel is prepared into 1 cm thick section (see section 4.3.2). A skin mimicked agarose gel (0.0265 g/ml) is chosen to study the effect of the MN insertion on the lengths of hole created by them. In addition, different concentration of agarose were used to investigate the MN array effect on the hole lengths depending on different properties of the target material. The hole length is of significant importance in this study as it relates to the particle penetration depth, as discussed later. In the experiment, agarose gel is molded to give a flat surface which is used as an object of reference for the insertion of MN. Observations of MN insertion and removal into agarose gel, results in holes which are smaller than the dimensions of the MNs; these holes close rather quickly to an equilibrium size after the MN has been removed, indicating that the target material has relatively short relaxation times for its elastic response.

Figure 4.5 shows the length of the created holes by different MNs for various concentrations of agarose in the gels. As expected, the length of the hole is less than the MN length. This is because of the MNs do not penetrate into the gel fully. In addition, the results show that the hole length has a positive correlation with the concentration of agarose in the gel. This is because an increased concentration of gel causes an increase in both the loss and storage moduli and the friction coefficient between particle and gel, which help to retain the hole size for longer duration. Figure 4.5 also shows that the average hole lengths increased with increasing needle length. The holes created by AdminPatch MN 1500 and 1200 close up fully at 0.02 g/ml concentration of agarose. The thickness of the MNs (78 μm) on those AdminPatch designs are so small that the holes are unable to remain open when viscoelastic moduli and viscosities fall too low. However, the holes created by in-house fabricated needle remained intact at 0.02 g/ml concentration of agarose as the diameter of these needles is considerably larger at 250 μm.

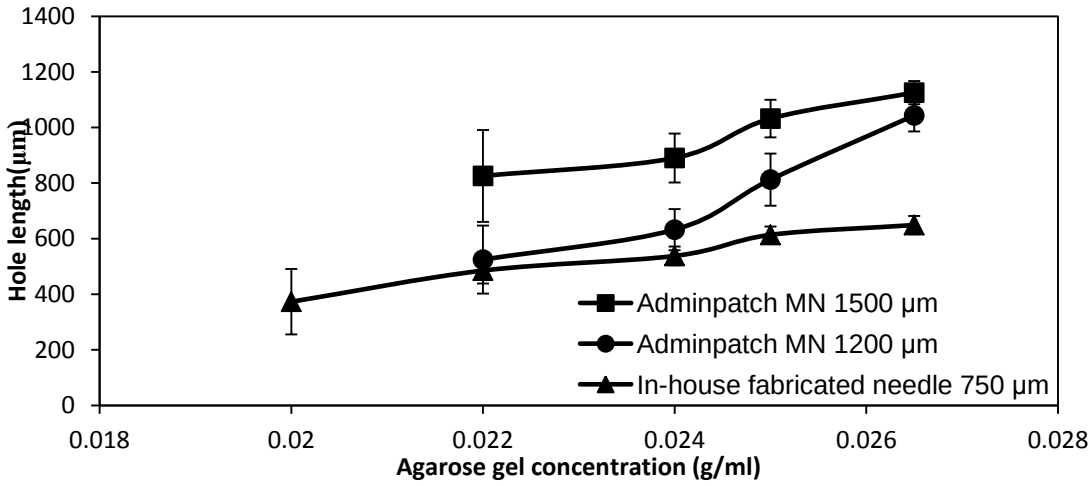

Figure 4.5: The MN insertion in the various concentration of agarose gel

In the experiment, 10 holes were measured to obtain the average lengths of the pierced hole. These experimental results suggest that the average hole lengths are 1149 ± 58, 1048 ± 69 and 656 ± 44 μm for skin mimicked agarose gel (0.0265 g/ml) for AdminPatch MN 1500 (length = 1500 μm), AdminPatch MN 1200 (length = 1200 μm) and in-house fabricated needle (length = 750 μm), respectively. The results indicate that the holes shrink to about 87% of the original lengths of the MN after approximately 1 minutes. In addition, the diameter of the holes created by the in-house fabricated needle shrink to about 156 ± 12 μm. For AdminPatch MN 1500 and 1200, the widths of the hole are 302 ± 26 and 292.8 ± 18 μm, respectively. The holes shrunk to about 62 % of the width of the MN. McAllister *et al.* (2003) reported a

residual hole radius of 6 μm following insertion of MNs with radius of 10 μm such that the holes shrunk to about 60 % of the radius of the MNs. It shows that the results of hole shrinkage between skin mimicked concentration of agarose and real skin are well correlated. The above results provide some confidence that the skin mimicked concentration of agarose is acceptable to replace the skin for further studies of the micro-particle penetration.

4.4.3 Measurements of the micro-particle penetration depth

In the previous chapter, wehas indicated that pellets which are bound together with 40 mg/ml PVP concentration provides a good pellet separation, if a mesh of 178 μm pore size is used. In continuation of the previous chapter, pellets of 40 mg/ml PVP concentration are applied in this work to find out the effect of the key variables on the micro-particle penetration depth. In this case, an agarose gel is prepared into 1 cm thick slice (see section 4.3.2) and used for the analyse of the penetration depth is analysed in relation to the mesh pore size, operating pressure, particle size, MN length and agarose gel concentration (this represents different viscoelastic properties). Each condition is studied three times to accurately determine the penetration depth of micro-particles and verify the accuracy of the results. It is worth mentioning that the maximum operating pressure is limited to 5 bar as the PTFE made ground slide might crash after the impaction at the end of the wall. The crashed ground slide may destroy the mesh and affect the experiment results.

4.4.3.1 Effect of the mesh pore size

In theory, the particle penetration depths should increase with an increase of the mesh pore size, which allows larger particles to pass through; consequently, they have more momentum to breach the target. In order to determine the significance of this effect for the particle delivery, two different meshes with pore size of 178 and 310 μm were applied and their effects on the micro-particle penetration were studied in this section. Figure 4.6a shows the side view of the micro-particles penetration in the skin mimicked agarose gel, without any MN application for a mesh of 178 μm pore size. As can be seen, the pellet has broken up into the micro-particles as it has passed through the mesh and the micro-particles are mainly distributed around the centre of the gel, i.e., the central impact point of the pellet on the mesh.

A large number of particles are visible close to the top surface, but the vast majority have penetrated only about 100 μm into the gel. There are such a large number of particles in this region close to the surface that individual penetrations are difficult to distinguish.

However, the top surface of the gel can be defined as shown in Figure 4.6a. Some micro-particles penetrate deep into the gel, which are clearly visible. There are about 30 micro-particles which have penetrated deeper into the gel and their positions are analysed by image processing software (ImageJ) to measure the average maximum penetration depth which is found to be 210 ± 23 μm at 5 bar operating pressure. It is worth mentioning that the penetration depths of micro-particles are obtained after zooming figure to measure the distance between micro-particle and top surface based on the scale. These are shown in the figure. In the magnified view of Figure 4.6a, it is clear that some particles penetrate deep into the gel, by creating a channel or hole, which remains open even after the particles have come to rest. The magnified view also shows that some of the particles with the largest penetration depths are agglomerates; increased agglomerate sizes would lead to higher particle momentum and hence greater penetration depths.

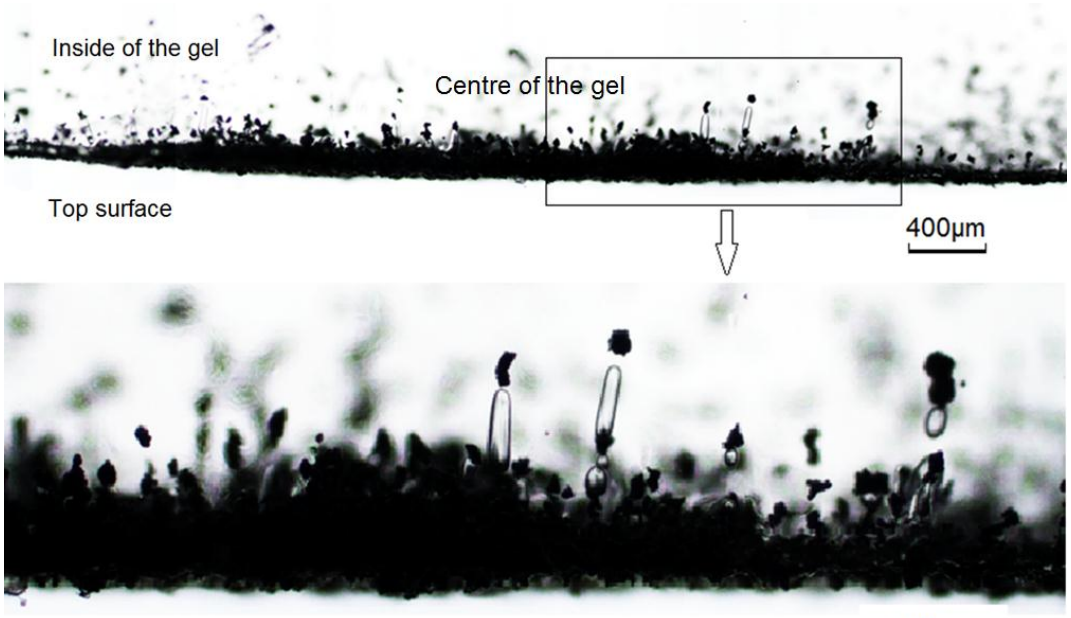

(a)

(b)

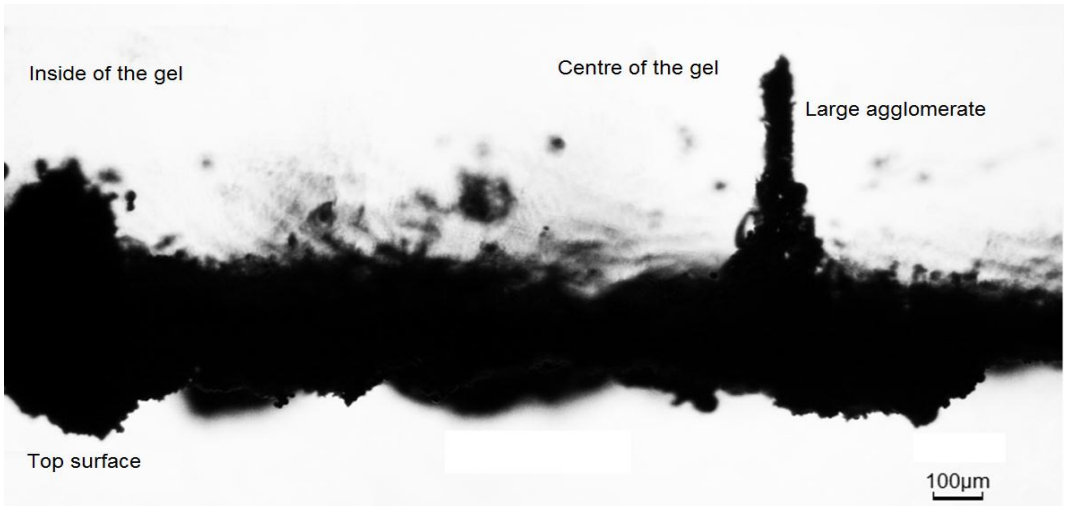

Figure 4.6: The effect of the mesh pore size on micro-particle penetration (a) particles passed through a mesh of 178 µm pore size (b) particles passed through a mesh of 310 µm pore size (operating pressure: 5 bar; agarose gel concentration: 0.0265 g/ml)

Figure 4.6b shows the micro-particle penetration without MN application following separation of the pellet by a mesh of 310 µm pore size at 5 bar driving pressure. As can be seen, a lot of micro-particles are distributed around the surface of the gel. Furthermore, larger penetration depths were often found due to the application of this mesh, because the large agglomerated particles have more momentum and hence are better at piercing the target. The maximum penetration depth in this case is more than for the results (Figure 4.6a) obtained from the mesh of 178 µm pore size. However, large agglomerated particles which pass the mesh may damage the target area, as is indicated by the uneven/broken surface of the gel. Therefore, these results suggest that the 310 µm mesh pore size may not be acceptable for the MN based system for the conditions chosen in these experiments. In addition, the application of mesh with 178 µm pore size is shown to have a higher passage percentage and a more effective pellet separation in a previous chapter (Chapter 3). Considering the passage percentage and pellet separation state, led to the conclusion that the 178 µm pore size of mesh should be used for the rest of the study for determining the effect of operating pressure, particle size, MN size and agarose gel concentration on the penetration depth.

4.4.3.2 Effect of the operating pressure and particle size

The operating pressure and the particle size are two major variables which affect the micro-particle penetration depths. The momentum of the particles is directly related to those two variables. Here the AdminPatch MN 1500 has been applied to investigate the MN effect

on the particle penetration depth and the combined effect of the operating pressure, particle size and MN array on the penetration depth is presented in Figure 4.7. In this case, spherical stainless steel micro-particle of 18 μm and irregular stainless steel micro-particle of 30 μm are used to study the particle size effect on the penetration depth. As expected, the application of a MN array has a very significant effect on the penetration depth. This is because the holes created by the MN array provide a selective path for the micro-particle penetration into the agarose gel. The holes created by the MN may close up after the particles enter the gel and, as such, they get fully embedded in the gel.

For the results without needle application, the penetration depths present a positive correlation with the operating pressure. The penetration depth increases gradually with an increase of the operating pressure due to the increased velocity and momentum of the particles entering the target material. In addition, the particle momentum increases due to increased particle size which also provides a positive effect on the penetration depth. The latter result agrees qualitatively with the effect of changing the mesh pore size on the penetration depth. In that case the larger particles sizes arose from agglomerates remain un-separated after passage through the mesh; these particles penetrated further.

For the result with MN applications, the operating pressure has a positive effect on the penetration depth for 30 μm diameter particle. However, it seems that the operating pressure and particle size are not necessarily the major variables that influence the particle penetration depths when MNs are applied. The length of the pierced holes is the primary factor which maximizes the particle penetration depth. As can be seen, the 18 μm diameter particles provide the maximum penetration depth for 3 to 5 bar operating pressures. The length of the pierced hole is 1149 ± 58 μm when AdminPacth MN 1500 is inserted (section 4.4.2). It helps the particles to enter into a deeper area at lower pressure. However, there is little difference between the penetration depths for those two particle sizes. This is because in practice it is not just the particle size, but an interplay of variables which determines the penetration depth. In this case, it seems that uniformity of the pore size forms fairly similar sized particle agglomerates. Therefore, the penetration depth is not directly influenced by the size of the individual particles.

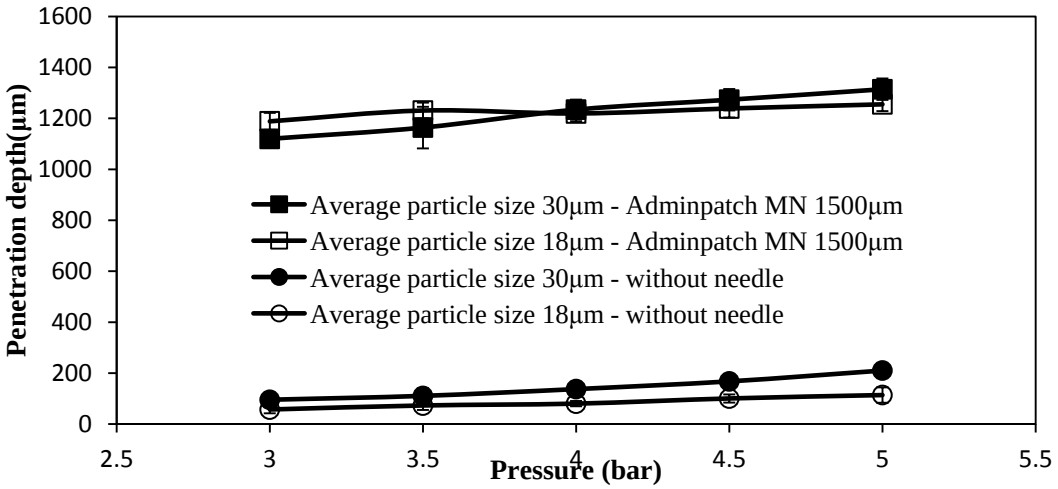

Figure 4.7: The effect of the particle size and operating pressure on the penetration depth (note: the 18 μm and 30 μm particles are the regular (spherical) and irregular stainless steel micro-particle, respectively (agarose gel concentration: 0.0265 g/ml)

Figure 4.8 shows the micro-particle penetration in the skin mimicked agarose gel after the application of AdminPatch MN 1500. As can be seen, there are a number of micro-particles in the gel which have entered through the pierced holes. Figure 4.8a shows the spherical micro-particles penetration in the agarose gel. As is evident, a large number of micro-particles have entered from the left size of the pierced hole. This is because the MN hole at the left side of the image is located around the central impact point of the pellet on the mesh. The number of micro-particles in the hole decreases as its position moves away from the central impact point. Figure 4.8b presents the irregular micro-particles penetration at the same operating condition as for Figure 4.8a. It shows that the amount of the irregular micro-particles penetrated in the pierced holes is less than that of the spherical micro-particle. This is can be explained as follows. The thickness of the MN is only 78 μm and the thickness of the pierced hole is further reduced due to the shrinkage of the gel. Furthermore, the average diameter of the irregular particles is about 30 μm and hence it may form larger agglomerates, which are comparable in size with the thickness of the holes. These factors may result in significant non-penetration of the irregular particles into the holes. On the other hand, the average diameter of the spherical particles is 18 μm which is significantly smaller than the thickness of the hole. Therefore, more spherical particles penetrate into the holes.

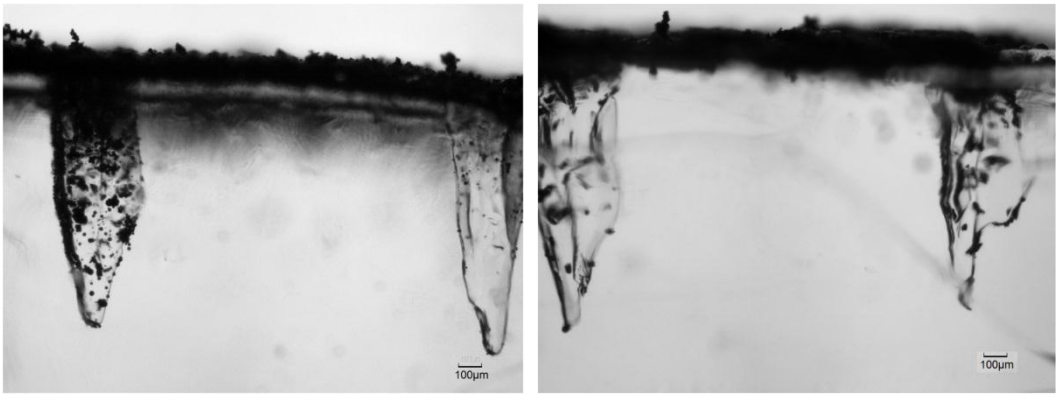

(a) (b)

Figure 4.8: The micro-particle penetration in the skin mimicked concentration of agarose gel based on the application of AdminPatch MN 1500 (a) Spherical micro-particle of 18 µm average diameter, and (b) irregular micro-particles of 30 µm average diameter (operating pressure: 4.5 bar, mesh pore size: 178 µm; agarose gel concentration: 0.0265 g/ml)

4.4.3.3 Effect of the microneedle length on particle penetration depth

In general, the maximum penetration depth is related to the size of the applied MN due to the effect of the holes created. However, as presented in Figure 4.9, the maximum micro-particle penetration depths differ significantly between each MN array at various operating pressure of 3 to 5 bar. In this case, spherical stainless steel micro-particle of 18 µm average diameter is used due to its uniform particle size distribution. Further, it seems that they can be easily identified inside the gel. As can be seen, the penetration depths increase with increasing MN length. An increased length of the MN makes longer holes which provide a positive effect on micro-particle delivery. Figure 4.9 also shows that the penetration depth gradual increases from an increase of operation pressure, which agrees with the result presented in the previous section. As expected, the three MN arrays used in this work provide a positive effect on the micro-particle penetration depth allowing operation a significantly lower driving pressure. From these results, the maximum penetration depth can reach 1273.2 ± 42.3, 1009 ± 49 and 659 ± 85 µm at 4.5 bar pressure for AdminPatch MN 1500 and 1200 and in-house fabricated needle, respectively. The results indicate that the maximum penetration depth could be controlled by the size of the MN and it is related to the desired depth of the target. MN assisted micro-particle delivery provides a controllable penetration depths of micro-particles inside the target using various MN sizes. In practice, it should allow micro-particles to penetrate into epidermis or further to dermis when the pierced holes cross the epidermis layer of skin. In addition, the maximum penetration depth increases gradually with the increase in

operating pressure. It can be safely stated that the effects of the holes on the micro-particle delivery (e.g., the penetration depth) can be fine-tuned by the operating pressure.

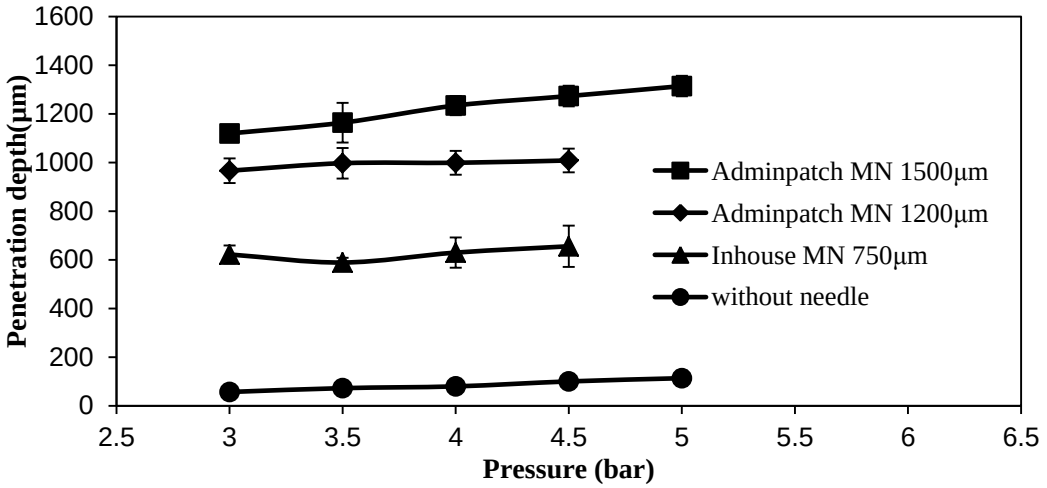

Figure 4.9: The effect of the MN length on the penetration depth (particle type: spherical stainless steel micro-particle; agarose gel concentration: 0.0265 g/ml)

4.4.3.4 Effect of the agarose gel concentration on the particle penetration depth

Generally, the resistance to the particle penetration into a target should be different if the rheological properties of the target change. However, it is not clear at this moment how significant the changes in the property of the target would be on determining the penetration depths. To address this issue, agarose gels of different concentrations were chosen to imitate the condition of different targets. In this case, spherical (regular) stainless steel micro-particles are used and the penetration of the micro-particles in gels of different agarose concentrations is studied in order to find out the effect of the target property on the micro-particle penetration depths.

Figure 4.10 shows the effect of the agarose gel concentrations on the particle penetration depth. As can be seen, the penetration depth decreases from an increase of the agarose gel concentration without MN. This is because the higher gel concentration has a greater friction coefficient which provides more resistance to the micro-particle delivery. However, this does not happen when a MN is used. As discussed in section 4.4.2, the lengths of the MN holes increase from an increase of the gel concentration, because the increased friction coefficient and elasticity are better able to hold the holes open. Therefore, the application of the MNs causes the penetration depths to increases as the agarose gel concentration increases. Figure 4.10 also shows that the experimental error is lower for higher concentration gel. This is

related to the lengths of the holes which remain intact for higher agarose concentrations. In addition, the figure shows that the length of the MN correlates well to the penetration depth, similar to the results in section 4.4.3.3.

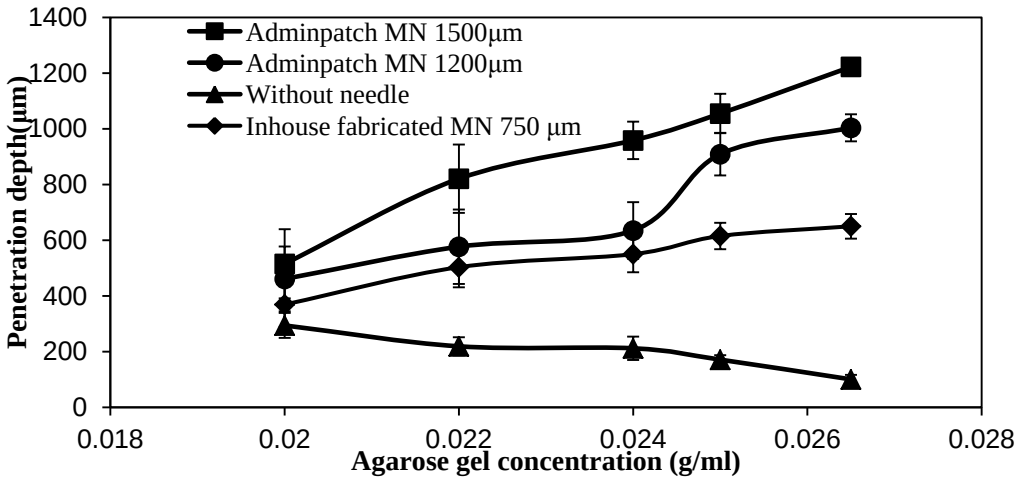

Figure 4.10: The effect of the agarose gel concentration on the penetration depth (operating pressure: 4.5 bar; mesh pore size: 178 μm; particle type: spherical stainless steel micro-particle)

4.4.3.5 Further discussion

The penetration route of micro-particles for the microneedle assisted micro-particle delivery is shown in Figure 4.11. The principle of this technique is that DNA is loaded on micro-particles which are accelerated to a sufficient velocity to pierce into the epidermis layer of the skin to achieve the DNA transfection. It presents a similar effect with the needle-free biolistic micro-particle delivery (see Figure 2.22d). However, a number of micro-particles penetrate through the pierced hole to reach the desired layer of skin. A controllable maximum penetration depth of micro-particles can be achieved by varying the hole length. It is more convenient and flexible, compared with needle-free micro-particle delivery. In addition, the micro-particles are able to deliver into the dermis layer of skin to allow deeper tissue to be transfected, depending on the length of hole created by the MN.

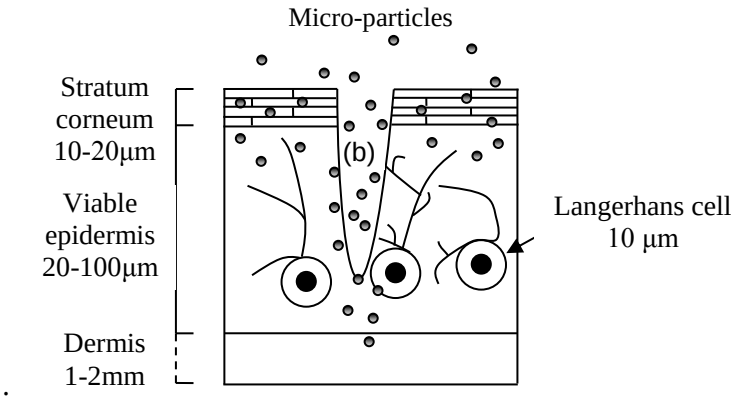

Figure 4.11: The penetration route of micro-particles for the microneedle assisted micro-particle delivery

The conditions considered in this case for micro-particle penetration study have been shown to be useful to gain an insight to the dependence of the penetration of the micro-particles on many key variables in relation to the MN assisted micro-particle delivery from gene guns. The penetration depths of the micro-particles were analysed with respect to variations in mesh pore size, operating pressure, particle size, MN length and agarose gel concentration.

For the effect of the mesh on penetration, larger pore sizes allow large agglomerated particles to pass through, providing a higher particle passage percentage of the micro-particles (Zhang *et al*., 2013). High-speed of large agglomerated particles carry higher momentum and penetrate further into the target, but they are also more likely to cause damage to external tissues. In the present case, a mesh with 310 μm of pore size allows the passage of larger agglomerates. Although itachieves a greater penetration depth in the skin mimicking agarose gel (see Figure 4.6a). It cannot be used for the micro-particle delivery due to the potential damage to skin. However, O'Brien and Lummis (2011) have shown that cell damage occurs after the impaction of high-speed micro-particles but it decreases with a decreased particle size. The use of a mesh with pore size of 178 μm yields well-separated particles which then can be discriminated as individual particles at a deeper level of the gel (see Figure 4.6b). It provides better operation due to the blockage of the largest agglomerated particle, despite the negative effect on the passage percentage.

Based on a consideration of particle momentum, the operating pressure and particle size are the key variables that affect the penetration depths. The impaction velocity of the particles is directly related to the operating pressures. An increased velocity implies that the micro-particles have more momentum to pierce into a deep level of the target. Therefore, the

penetration depth increases with an increase in the operating pressure. In addition, an increased particle size provides a positive effect on the penetration depth due to the increased momentum. In this case, the average penetration depth for the 30 μm diameter stainless steel micro-particles is 168 ± 24 μm at 5 bar pressure. For the stainless steel micro-particles of 18 μm diameter, it only has a penetration depth of 101 ± 16 μm. In section 3.4.1, the experiments have shown that the micro-particles reach a velocity of 122 m/s at 5 bar pressure using the MN based system. Earlier, Mitchell *et al.* (2003) have concluded that stainless steel micro-particles of 25 μm diameter can penetrate 150 μm into excised canine buccal mucosa at a velocity of 170 m/s. It matches well with the penetration of the stainless steel micro-particles in the skin mimicked concentration of agarose gel in this case. The penetration route for needle free biolistic micro-particle delivery is presented in section 2.5.2 (Figure 2.22d) in detail.

As expected, an application of a MN array provides a positive effect on the micro-particle penetration depth. The detailed penetration route of MN assisted micro-particle delivery is explained in Figure 4.11. The maximum penetration depth of the micro-particles is presented with a significant increment from the results without MN application. However, the length of the pierced holes became the primary factor which enhances the particle penetration depths. An increased needle length provides a positive effect on the length of the pierced holes, which maximize the penetration depth. However, the maximum penetration depth of the spherical micro-particles reaches 1272 ± 42, 1009 ± 49 and 656 ± 85 μm at 4.5 bar pressure for AdminPatch MN 1500 and 1200 and the in-house fabricated needle, respectively. Those penetration depths were never achieved previously. In our case, the applied operating pressure is lower than other relevant gene gun system. For example, Quinlan *et al.* (2001) have used a conical nozzle employed at 60 bar to accelerate polymeric micro-particles. Mitchell *et al.* (2003) have fired stainless steel micro-particle into canine buccal mucosa at 20 bar pressure using light gas gun. A lower operating pressure causes a decreased velocity of micro-particle which may avoid severe tissue damage. In addition, an increased penetration depth of micro-particle allows deeper tissue to be transfected to achieve an efficient DNA transfection in the tissue if DNA is coated on the micro-particle. Further, one of the main advantages of the current approach is that the use of the ground slide (see Figure 4.1a) slows down the velocities of micro-particles and prevents the pressurized gas to reduce the impact force on tissue to minimize the cell damage. Also it is worth mentioning that the viscoelastic properties of the target have two important effects on the penetration of the micro-particles; an increased

friction coefficient and elastic modulus provide (i) greater resistance to particle motion and (ii) affect the relaxation of the target material and hence determine the lengths of the pierced holes for a fixed geometry of MN. However, the desired depths can be achieved by changing the size of the MN and the operating pressure.

As mentioned earlier the aim of this chapter was to relate the penetration depth to various parameters. Indeed the extent of delivery, i.e., the mass of particles delivered with and without MNs, is a very important question that should be analysed in detail. This is related to a number of other issues (e.g., number of needles/holes per unit area (needle/hole density)). Furthermore, the effect of the operating pressure and/or particle size on the pore width at the target surface may be an important factor that controls the extent of delivery rate. These aspects were not studied in this paper but we plan to analyse these in the future.

4.5 Chapter Summary

In this chapter, a solid MN based system has been presented for an application on the study of micro-particle penetration. For the investigation of the particle penetration depth, agarose gel was chosen to mimic porcine skin due to its homogeneous and semi-clear properties which provides an ideal target material for measuring the micro-particle penetration depth as a function of other variables, e.g., pressure and particle size. For the purpose of this chapter, it was found that the dynamic viscoelastic properties of a gel with 0.0265 g/ml concentration of agarose were close to values for porcine skin; therefore this concentration of agarose gel was adopted for the bulk of the experiments in this work. Insertions of various lengths of MN in different concentrations of agarose gel have been examined to investigate the effect of the microneedle length of the pierced hole in the target. An increase in length of the MN or the gel concentration leads to an increased hole length. The penetration depth of the micro-particles in the skin mimicked concentration of agarose was analysed in relation to the pore size of mesh, operating pressure, particle size and MN size. It was shown that the penetration depth increases with an increase of the above four variables. In particular, the MN length is shown to be a primary variable which maximizes the penetration depth of the micro-particles. Finally, different concentrations of agarose gel were chosen to imitate the conditions of various targets. Based on a MN application, the maximum penetration depth was shown to provide a positive correlation with gel concentration. It indicates that the property of the target should be considered carefully before using the MN based system. Based on the target property, a specific length of MN array should be decided for the

micro-particle penetration to a desired depth. In conclusion, the MN based system is useful for micro-particle delivery where the damage of the target from the gas/particles is eliminated and the micro-particle system can be designed to reach the desired depth within the tissue.

5. Microneedle assisted micro-particle delivery: Mathematical model formulation and experimental verification

5.1 Chapter Overview

Gene gun is a micro-particle delivery system which accelerates DNA loaded micro-particles to a high speed so as to enable penetration into deeper tissues to achieve gene transfection. Previously, microneedle (MN) assisted micro-particle delivery has been shown to achieve the purpose of enhanced penetration depth of micro-particles based on a set of laboratory experiments. In order to further understand the penetration process of micro-particle, a mathematical model for MNs assisted micro-particles delivery is developed. The model mimics the acceleration, separation and deceleration stages of the operation of an experimental rig aimed at delivering micro-particles into tissues. The developed model is used to simulate the particle velocity and the trajectories of micro-particles while they penetrate into the target. The model mimics the deceleration stage to predict the linear trajectories of micro-particles which randomly select the initial positions in the deceleration stage and fired into the target. The penetration depths of micro-particles are analysed in relation to a number of parameters, e.g., operating pressure, particle size, and MNs length. Results are validated with experimental results obtained from the previous work. The results also show that the particle penetration depth is increased from an increase of operating pressure, particle size and MN length. The presence of the pierced holes causes a surge in penetration distance.

5.2 Introduction

Gene guns are aimed at delivering DNA loaded micro-particles into target tissues at high speed (O'Brien and Lummis, 2006; Yang *et al*., 2004; Lin, 2000). The penetration depth of the micro-particles are typically greater than the stratum corneum, i.e., the top layer of skin (Yager *et al*., 2013; Kendall *et al*., 2004a,b; Mitchell *et al*., 2003; Chen *et al*., 2002; Quinlan *et al*., 2001). To understand various features of the micro-particle delivery and evaluation of achievable performance from the gene guns, mathematical models are often developed which aim to simulate the micro-particle transfer process for specific gene delivery system. For example, Liu (2006) has focused on simulating the velocity distribution in the converging (conical) section of a venturi system developed for a gene gun, namely, the PowderJect system (maleo

et al., 1999, 2003, 2006). The particle velocity has been simulated based on a balance between the inertia of micro-particles and other forces acting on the particles. Zhang *et al*.

(2007) have used the programming platform MATrix LABoratory (MATLAB, the MathWorks Inc., Natick, USA; Shampine *et al*., 1997) to simulate three different stages of the particle delivery in a gene gun, namely, acceleration, separation and deceleration stages. In this work, the particle velocity is analysed on the basis of Newton's second law in the acceleration stage, energy conservation is applied to describe the separation of micro-carriers into micro-particles in the separation stage, and Stock's law is used to model the micro-particle penetration in the deceleration stage. Soliman and Abdallah (2011) have used a commercial turbo-machinery flow simulator, namely, FINE^{TM}/Turbo (NUMECA International, Brussels, Belgium) to simulate the behaviour of gas and particle flow in a supersonic core jet in a gene gun. This work used Newton's second law to mimic the particle trajectories and determine the penetration depths of micro-particles in the skin. As discussed below, a number of other studies have shown that the penetration depths of micro-particles depend on the momentums of the particles which again depend on the particle size, density and velocity.

As well known, human skin is a major component of the body that must be considered in the study of micro-particle penetration. The skin helps to prevent the entry of foreign substances into the body (Holbrook *et al*., 1974; Scheuplein *et al*., 1971). It also provides a great resistance to the moving micro-particles during a particle delivery process. The skin consists of three main layers, which are the stratum corneum (SC), viable epidermis (VE) and the dermis (Parker, 1991; Phipps *et al*., 1988). On average the stratum corneum is between 10 and 20 μm thick (Holbrook *et al*., 1974) which may vary in different regions of the body and amongst different groups of people. The thickness of the epidermis also varies in different regions of the body but it has been reported to have an average thickness of 20 to 100 μm (Matteucci *et al*., 2009; Schaefer *et al*., 1997). In addition, the thickness of the dermis varies between 1.5 and 3mm (Lambert *et al*., 2008) and especially on the back it can be up to 4 mm thick (Rushmer, 1966). The VE of the skin is the target layer for of DNA vaccination for previous needle free gene gun systems.

In the previous work, it has been shown that the penetration depth of micro-particles could be improved further to the dermis layer based on the use of MNs by creating holes on the target which allow a percentage of micro-particles penetrate through to achieve the purpose of improved penetration depth. In addition, pellets bound with 40 mg/ml concentration of Polyvinylpyrrolidone (PVP) concentration is found to yield approximately 70% of passage

percentage of pellet mass with good control on the size distribution of separated micro-particle using a mesh of 178 μm pore size. In the section 4.3.2, we have discussed an experimental rig for MN assisted micro-particle delivery, which consists of acceleration, separation and deceleration stages (see Figure 4.1). An improvement of the MN based system has been proposed by using an array of solid MNs to overcome the effect of the skin on the particle penetration. The solid microneedle is aimed to create pores/holes in the target tissue which remain for sufficiently long time after removing the MN. Within that time, micro-particles can be fired in the same tissue. It has been shown that a number of micro-particles can penetrate into the tissue via the holes while other micro-particles may be stopped from penetrating into the target by the non-porous (i.e., without MNs created holes) area of the tissue. The micro-particle transfer process of this system is divided into three stages, which are the acceleration, separation and deceleration stages. For the acceleration stage, a ground slide carries a pellet of micro-particles which are accelerated together to a desired speed by high pressure compressed air. In the separation stage, the pellet will be released from the ground slide after it reaches a stopping wall in a barrel; thereby it separates into micro-particles by a stopping screen with high speed. For the deceleration stage, the separated micro-particle spray forward, penetrate into the target via the holes made by solid microneedle and stop inside the target.

In a previous chapter (section 4.4.3), we have shown that the penetration depth of stainless steel micro-particles is enhanced in a skin mimicking agarose gel by using MNs. The work uses an agarose powder to prepare an agrose gel of a specific concentration (2.65 g/ml) to mimic the porcine skin based on its viscoelastic properties. This skin mimicking agarose gel is considered as a target instead of human skin to analyse the penetration depth of stainless steel micro-particles in relation to the operating pressure, particle size and MN length due to their homogeneity and transparency provide a good environment to observe the penetration by a digital optical microscope. The penetration depth of micro-particles in the gel is analysed by an image processing software, namely, ImageJ (National Institutes of Health, Maryland, USA) (ImageJ, 2013). The experimental results have shownthat the penetration depth increases with an increase of operating pressure, particle size and MN length in a previous chapter (Chapter 4). Especially, the high-speed micro-particles penetrate further into the target via the pierced holes which are created by MNs. However, the maximum penetration depth depends on the MN length which makes different lengths of holes on the target.

In order to further understand the characteristics of MNs assisted micro-particles delivery, the present study aims to build a mathematical model to mimic the operation process of the experimental rig (Figure 4.1) for delivering micro-particles into a target. The micro-particles are compressed into a cylinder pellet, loaded into a ground slide, and accelerated by a pressurized air. Thus, the velocity of the pellet is equal to the velocity of the ground slide at the end of the barrel for this set up. The pellet is broken up into separated micro-particles which pass through a mesh. As expected, the velocity of the separated micro-particle decreases due to energy loss from the impaction and passage though the mesh.

In this chapter, a mathematical formulation is presented where the initial velocity of the separated micro-particle is one of the variables that determine the penetration depth of the micro-particle in the deceleration stage. The detailed mathematical principle of the model is presented in section 5.3.1. The presented model is formulated to mimic the acceleration, separation and deceleration stages of MNs assisted micro-particles delivery using MATLAB (Version R2012b). It quantifies the effect of operating pressure on the velocity of the ground slide and compares the results with previous experimental data obtained from section 3.4.1.1 to verify the acceleration stage of the model. In addition, the trajectories of the micro-particles in the deceleration stage are simulated to determine the routes of the micro-particles and distribution of the micro-particles in the three layers of skin. The developed model is used to study the penetration depth of micro-particles in relation to operating pressure, particle size and MN length and these are compared with a selection of experimental results obtained in previous chapter (Chapter 4).

5.3 Material and Methodology

5.3.1 Governing equations for micro-particle delivery in various stage

As discussed earlier, the MNs assisted micro-particles delivery process consists of acceleration, separation and deceleration stages. Brief operation principles of each stage and the corresponding governing equations that have been used to quantify the process are presented in the following sections.

5.3.1.1 Acceletration stage

Acceleration stage uses a compressed gas as a driving force to accelerate the ground slide to a certain velocity which is controlled by the operating pressure in the receiver (see Figure 4.1). A compressed gas (air in this case) is released from a gas cylinder and stored in the receiver.

The pressure inside the receiver is detected by a sensitive pressure transducer. Before the solenoid valve of the system is opened, the initial volume and pressure inside the receiver are V_1 and P_1. After the valve is opened, the gas expands and accelerates the ground slide. The volume of air increases to V_2 and the pressure decreases to P_2. Assuming that the gas expands adiabatically, we can apply the Boyle's law (Webster, 1995) to obtain:

$$P_1 V_1^{\nu} = P_2 (V_1 + V_2)^{\nu} \tag{5.1}$$

Where ν is the heat capacity ratio. This process defines gas as a fluid where ν = 1.4 for diatomic gas and ν = 1.6 for a monatomic gas.

In the acceleration stage, only air does work on the ground slide. The work done by the gas is:

$$\int_0^L P_2 \pi R^2 dl = E \tag{5.2}$$

Where L is the length of the acceleration stage and R is the radius of the ground slide.

We define the final velocity of ground slide before reaching the stopping wall as u, and the mass of ground slide with the pellet as M. The kinetic energy of the ground slide is therefore given as:

$$\frac{1}{2} M u^2 = E \tag{5.3}$$

The sliding friction of the ground slide travelling in the channel is neglected in this formulation. Based on the law of conservation of energy, the velocity of the ground slide is given as:

$$\sqrt{\frac{2P_1 V_1^{\gamma}[(V_1 + \pi R^2 L)^{1-\gamma} - (V_1)^{1-\gamma}]}{M(1-\gamma)}} = u \tag{5.4}$$

5.3.1.2 Separation stage

In the separation stage, the compressed air is released from the vent hole (see Figure 4.1) and the ground slide blocks the gas from flowing into the deceleration stage. Further, the pellet is broken up and separated into individual micro-particles by a mesh which then move across the mesh into the deceleration stage. In this process, the initial velocity of the pellet is equal to u which is the velocity of the ground slide. The pellet may lose some energy due to its impact on the mesh which separates it into individual micro-particles. Assuming that the energy loss is x in this process, the process is described based on the law of conservation of energy and given as:

$$\frac{1}{2}nmu_1^2 = (1-x)\times\frac{1}{2}m_p u^2 \quad (5.5)$$

Where n is the number of micro-particles in the pellet; m is the mass of a single micro-particle; u_1 is the velocity of micro-particle after passing through the stopping screen and m_p is the mass of the pellet which can described as $m_p = nm$

The rearranged equation (5.5) gives:

$$\sqrt{1-x}\times u = u_1 \quad (5.6)$$

5.3.1.3 Deceletration stage

The deceleration stage can be separated into two parts. In the first part, the particle travels between the mesh and the target. There is a gap between the mesh and target which allows spraying of the micro-particles on a large-area of the target tissue. Thus, the air drag force acting on the separated micro-particles should be considered in this process. The second step involves modelling the process of the particle penetration in the skin, which requires consideration of the resistance force from the skin on the micro-particle delivery. The micro-particles need to breach the SC and pierce the subsequent layers, e.g., the epidermis layer. The detailed mathematical principles of these two steps are explained in sections (a) and (b).

The trajectories of the micro-particles in the deceleration stage are simulated in two dimensions (2D). The initial positions and moving directions of high-speed micro-particles are randomly chosen from the beginning in the first step of the deceleration stage. The motion is considered to be linear but varying in velocity of the particles due to the effects of drag force on the particles. The particles are allowed to impact on the boundary of the gap between the mesh and skin. We define that these impacts are elastic collisions and the particles rebound on the boundary in the model. The detailed physical-mathematical principle of the micro-particle trajectories are discussed in section (c).

(a) Micro-particles travel in the gap between mesh and skin

The separated particles decelerate in air before hitting the target. This process is described by the following energy balance equation:

$$\frac{1}{2}mu_1^2 = E_2 + E_{sfe} + E_d \tag{5.7}$$

Where E_2 is the final kinetic energy of the separated micro-particle. E_{sfe} is the surface free energy of the pellet and E_d is the energy lost due to the frictional drag force from the micro-particle in the air.

The frictional drag force on a micro-particle in the air is given as:

$$\frac{1}{2}\rho u_2^2 C_d A_p = F_d \tag{5.8}$$

Where F_d is the force of drag, ρ is the density of air, A_p is the projected cross-sectional area of the separated micro-particle, C_d is the air drag coefficient and u_2 is the velocity of the separated particle in the space between mesh and target.

The energy loss due to the drag force is given as:

$$\int_0^{L_1} F_d dl = E_d \tag{5.9}$$

After differentiating the energy loss E_d with the distance *l* we obtain:

$$\frac{dE_d}{dl} = F_d \tag{5.10}$$

Where l is the gap between the mesh and target.

The final kinetic energy of the separated particles before they hit the target is given as:

$$\frac{1}{2}mu_2^2 = E_2 \tag{5.11}$$

Based on equations (5.8) and (5.10), the relationship between the particle velocity and travel distance is given as

$$-mu_2\frac{du_2}{dl} = \frac{1}{2}\rho u_2^2 C_d A_p = F_d \tag{5.12}$$

The drag coefficient C_d in equation (5.12) is an important parameter in the modelling of gas and particle interactions. This coefficient is a function of the particle Reynolds number (Re) (see Appendix A), which depends on the gas viscosity (μ) and density (ρ), particle diameter (d), and relative velocity (u_3). For the purpose of this case, the Reynolds number is defined as:

$$\frac{\rho u_2 d}{\mu} = Re \tag{5.13}$$

(b) Micro-particles penetration in the target tissue

The particle deceleration in the target skin has the same principle with the particle travel in the air. In the deceleration stage, the separated micro-particles are resisted by the tissue and their velocities are slowed down. Based on the law of conservation of energy, the drag force can be expressed as:

$$f_d = -m\frac{du_d}{dt} \tag{5.14}$$

Where f_d is the drag force for the micro-particles, u_d is the velocity of separated micro-particle in the tissue.

For the penetration in the target, various studies have adopted that the resistant force on the micro-particle is separated into three components, namely, yield force (F_y), frictional resistive force (F_f) and resistive inertial force of target material (F_i) (Soliman *et al*., 2011; Liu, 2007; Mitchell *et al*., 2003; Kendall *et al*., 2001; Dehn, 1987). In consistent with these previous studies, we adopt the following the force balance equation:

$$m\frac{du_d}{dt} = -(F_i + F_f + F_y) \tag{5.15}$$

The equation for each component of the resistant force is as shown below:

$$F_i = 6\pi\mu_t r_p u_d \tag{5.16}$$

$$F_f = \frac{1}{2}\rho_t A_p u_d^2 \tag{5.17}$$

$$F_y = 3A_p\sigma_y \tag{5.18}$$

Where μ_t is the friction coefficient between particle and target, r_p is the radius of the micro-particle, ρ_t is the density of the target and σ_y is the yield stress of the target.

(c) The mathematical-physical principle and determination of micro-particle trajectory in deceleration stage

To determine the trajectory of the micro-particles, the mathematical statement is formulated in two dimensions. Depending on the velocity, size of particle, etc., other important features of this is the possibility of different angles and positions of particle entrance which have direct implication on the velocity of the micro-particles. The air in the deceleration stage

might move forward when the high pressure gas pushes the ground slide forward. Although the ground slide can stop the gas from entering the deceleration stage, the air flow still happens in the front of the ground slide and causes pressure drop in the deceleration stage. Hence, the axial gas pressure drop is greater than that in the radial direction, i.e.

$$\frac{dP_z}{dz} >> \frac{dP_r}{dr}$$

As $\frac{dP_z}{dz} >> \frac{dP_r}{dr}$, the axial (z) velocity component is greater than the radial (r) component.

Further, the initial velocity of micro-particle in the deceleration stage is u_3.

Therefore

$$u_2^2 = u_z^2 + u_r^2 \tag{5.19}$$

We define that the radial velocity component as k percentage of the axial component.

Therefore

$$u_r = ku_z \tag{5.20}$$

In our case, k is defined to be 0.2.

(d) The micro-particle travel between mesh and target

In the first part of the deceleration stage, the air drag force is presented in equation (5.8). According to Newton's second law:

$$F_d = ma = m\frac{du_2}{dt} \tag{5.21}$$

Substitution of equation (5.8) into equation (5.21) provides:

$$m\frac{du_2}{dt} = \frac{1}{2}\rho u_d^2 C_d A_p \tag{5.22}$$

For axial component, we have

$$m\frac{du_r}{dt} = \frac{1}{2}C_d \rho u_d u_x A_p \tag{5.23}$$

For radial component

$$m\frac{du_z}{dt} = \frac{1}{2}C_d \rho u_d u_y A_p \tag{5.24}$$

At the same time, the radial displacement component is:

$$\frac{dl_r}{dt} = u_r \tag{5.25}$$

The axial displacement component is:

$$\frac{dl_z}{dt} = u_z \tag{5.26}$$

The program uses an *if* statement to define the axial displacement component of the micro-particle is smaller than the space between the mesh and target or the radial displacement component is smaller than l_y, the particle will impact on the walls before entering the skin.

(e) Micro-particle penetration in skin

Once the micro-particles reach the surface of the target tissue, an increased resistance from the target prevents those micro-particles to move forward. The initial velocities of the micro-particles in axial and radial components equal the velocity at the end of the first step of deceleration stage. The following velocity change of the micro-particles is calculated based on the Newton second law and it is shown in equation (5.27) which is obtained from equation (5.15):

$$m\frac{du_d}{dt} = \frac{1}{2}\rho_t u_d^2 A_p + 3A_p\sigma_y + 6\pi\mu_t r_p u_d \tag{5.27}$$

For the axial component of equation (5.27), we have

$$m\frac{du_r}{dt} = \frac{1}{2}\rho_t u_d u_r A_p + 3A_p\sigma_y \frac{u_r}{u_d} + 6\pi\mu_t r_p u_r \tag{5.28}$$

On the other hand, the radial component of equation (5.27) is

$$m\frac{du_z}{dt} = \frac{1}{2}C_d\rho_t u_d u_y A_p + 3A_p\sigma_y \frac{u_z}{u_d} + 6\pi\mu_t r_p u_z \tag{5.29}$$

In the program, we use an *if* statement to define the location of micro-particle. If the axial displacement component of a micro-particle is larger than the space between the mesh and target, and the radial displacement component is located at a space between two holes, the particle will pierce into the target skin. If the axial displacement component of the micro-particle is larger than the space between the mesh and target and the radial displacement component is located at a hole area created by the MN, the particle is defined to be delivered in a hole. Thus, a micro-particle is defined to travel forward in the hole, penetrate

into the skin, and achieve a further penetration depth inside skin. The model behaviour is explained in the section 5.3.3 in detail.

(f) Quantitative description of the events involving micro-particle rebound between mesh and target

In the first step of deceleration stage, the micro-particles may impact on the boundary of the gap between the mesh and target skin. We define that the particles impact on the boundary of the gap between the mesh and skin is an elastic collision, see Figure 5.1.

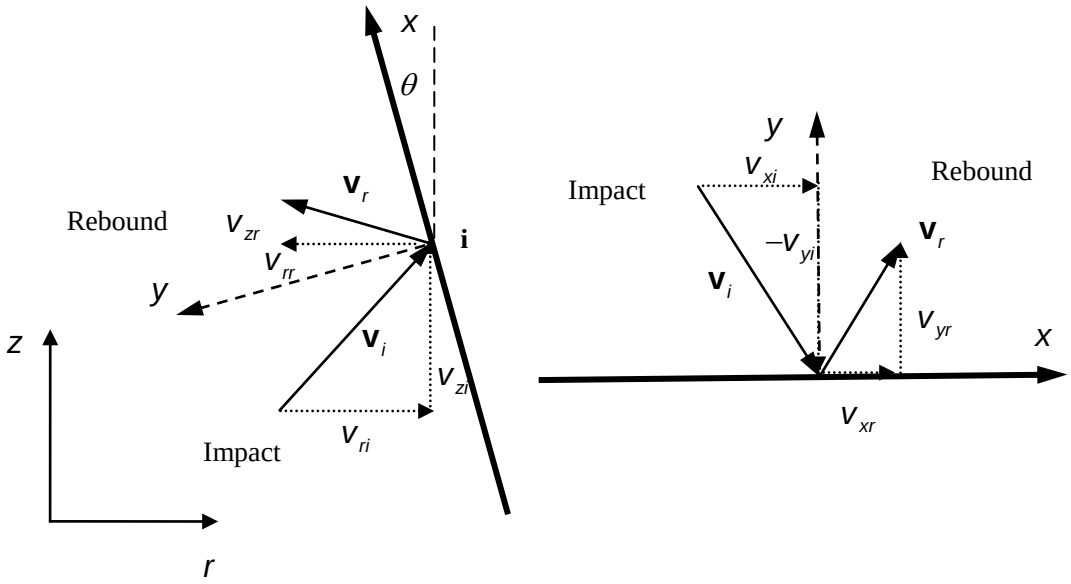

Figure 5.1: The trajectory of particle impact on a planar wall

Table 5.1: The meaning of each variable in Figure 5.1

Variables	Description
V_i	The velocity on impact
V_{ri}	The radial velocity component on impact
V_{zi}	The axial velocity component on impact
V_r	The velocity on rebound
V_{rr}	The radial velocity component on rebound
V_{zr}	The axial velocity component on rebound
Θ	The angle of boundary of the gap between mesh and skin
I	The impact point

V_{xi}	The tangential velocity component on impact
V_{yi}	The normal velocity component on impact
V_{xr}	The tangential velocity on rebound
V_{yr}	The normal velocity on rebound

The coordinates of radial and axial velocity components at a point on (x,y) axes are defined as ($V_{x,}$ V_y). From Figure 5.1, it can be seen that in order to change from (x,y) axes to (r,z) axes, a rotation through $\left(\frac{\pi}{2}+\theta\right)$ is required. The new coordinates of the tangential and normal velocity components of that point are (V_r, V_z) on (r, z) axes. Using the standard matrix rules (Eberly, 2002) to perform the axes- rotation of the velocity vectors gives

$$\begin{pmatrix} V_r \\ V_z \end{pmatrix} = \begin{pmatrix} \cos\left(\frac{\pi}{2}+\theta\right) & -\sin\left(\frac{\pi}{2}+\theta\right) \\ \sin\left(\frac{\pi}{2}+\theta\right) & \cos\left(\frac{\pi}{2}+\theta\right) \end{pmatrix} \begin{pmatrix} V_x \\ V_y \end{pmatrix} = \begin{pmatrix} -\sin\theta & -\cos\theta \\ \cos\theta & -\sin\theta \end{pmatrix} \begin{pmatrix} V_x \\ V_y \end{pmatrix} \quad (5.30)$$

When inverted, equation (5.30) gives

$$\begin{pmatrix} V_x \\ V_y \end{pmatrix} = \begin{pmatrix} -\sin\theta & \cos\theta \\ -\cos\theta & -\sin\theta \end{pmatrix} \begin{pmatrix} V_r \\ V_z \end{pmatrix} \quad (5.31)$$

Equation (5.31) therefore suggests that for the velocity on impact, the tangential and normal velocity components on the impact plane are

$$\begin{aligned} V_{xi} &= -V_{ri}\sin\theta + V_{zi}\cos\theta \\ V_{yi} &= -V_{ri}\cos\theta - V_{zi}\sin\theta \end{aligned} \quad (5.32)$$

For the velocity on rebound, the tangential and normal velocity components may be written in terms of the following coefficients of restitution

$$\begin{aligned} V_{xr} &= e_t V_{xi} \\ V_{yr} &= -e_n V_{yi} \end{aligned} \quad (5.33)$$

Hence rotating back through $\left(\frac{\pi}{2}+\theta\right)$, using equation (5.30), to get the radial and axial velocity components on rebound provide:

$$\begin{aligned} V_{rr} &= -e_t\sin\theta(-V_{ri}\sin\theta + V_{zi}\cos\theta) + e_n\cos\theta(-V_{ri}\cos\theta - V_{zi}\sin\theta) \\ V_{zr} &= e_t\cos\theta(-V_{ri}\sin\theta + V_{zi}\cos\theta) + e_n\sin\theta(-V_{ri}\cos\theta - V_{zi}\sin\theta) \end{aligned} \quad (5.34)$$

We define the collision between micro-particle and the boundary of the gap between mesh and skin is elastic collision, and then the coefficient of restitution is equal to 1. It means that there is no energy lost due to the rebound; only the direction of motion has been changed.

5.3.2 Selection of modelling parameters

The impact velocity, particle size and density, target properties are defined as the major variables affecting the penetration depth. The layers of the skin are considered to mimic the human skin in the model (see Figure 5.2a). The skin is divided into two distinct macroscopic layers known as the dermis and the epidermis (Parker, 1991; Phipps, 1988). Stratum corneum is considered as a part of the epidermis layer. Therefore, the skin is considered to have three layers in the model, which are shown in Figure 5.2b which is a magnified profile of a section of the model geometery shown in Figure 5.2a. The thicknesses of the different skin layers differ which are listed in Table 5.2. The friction coefficient between particle and each skin layer is treated as the same in the model. Previously (section 4.4.1), we have analysed the friction coefficient between particle and porcine skin tissue using a rotational viscometer, which will be used as a replacement for human skin in the model and shown in Table 5.2. For example, the density of the stratum corneum and viable epidermis are defined as 1.5 and 1.15 g/cm^3, respectively, in consistent with the results of Duck (1990). Wildnauer *et al*. (1971) have shown that the yield stress of stratum corneum range from 3.2 to 22,5 MPa, which have been obtained from the measurements of stress-strain characteristics of the human stratum corneum samples.

Table 5.2: Skin properties used in the model

Parameter	**Value**	**Reference**
Thickness of VE, T_{ve} (m)	0.0001	Holbrook *et al*. (1974);
Thickness of SC, T_{sc}(m)	0.00002	Matteucci *et al*. (2008);
		Schaefer *et al*. (1997)
Yield stress of SC , Y_{sc} (MPa)	3.2 - 22.5	Wildnauer *et al*. (1971)
Density of SC, ρ_{sc} (g/cm^3)	1.5	Duck (1990)
Density of VE, ρ_{ve} (g/cm^3)	1.15	Duck (1990)
Yield stress of VE, Y_{ve} (MPa)	2.2	Kishino *et al*. (1988)
Friction coefficient between particle and porcine skin tissue, μ' (Pas)	19.6	This work (Chapter 4)

In order to investigate the microneedle effect on the penetration depth, an in-house fabricated MN, Adminpatch MN 1500 and 1200 are (nanoBioSciences limited liability company, Sunnyvale, CA, USA) chosen for both model and experiments. The detailed characterizations of each MN are explained in the previous work (see Table 4.1). Previously, Adminpatch MN 1500 has been chosen to analyse the MNs assisted micro-particles delivery and show that the lengths of pierced holes vary after the removal of the MNs. But, the length of the pierced holes are considered uniform in the model and presented in Table 5.3. It is worth mentioning that the lengths of the pierced holes are from a study of the insertion of MN in a skin mimicking agarose gel (0.0265 g/ml of agarose), which was obtained in the section 4.4.1.2.. McAllister *et al*. (2003) have assumed that after the removal of the MNs the surface area of the hole shrink to 60 percent of that the MNs which originally create the holes. In consistent with McAllister *et al*. (2003), the hole width is considered to be 60% of the width/radius of the MN (Table 5.3) at the time the micro-particles are delivered. The details can be shown in Figure 5.2a, which presents the pierced holes as uniform cones.

Table 5.3: Relevant constants used in the developed model

Parameter	**Value**
Mass of ground slide with the pellet, M (g)	1.25
Length of barrel, L(m)	0.5
Radius of barrel/ground slide, R(m)	0.00375
Volume of receiver, V_1 (L)	1
Space between mesh and skin, L_1 (m)	0.05
Density of stainless steel (g/cm^3)	8
Average Diameter of spherical stainless steel particle (μm)	18
Average Diameter of Irregular stainless steel particle (μm)	30
Viscosity of air, μ (Pas)	1.78
Length of pierced holes L_p(μm) Adminpatch 1500	1149
Adminpatch 1200	1048
In-house fabricated MN	656
Width of pierced holes L_w (μm) Adminpatch 1500	302
Adminpatch 1200	302
In-house fabricated MN	156

The relevant simulation parameters of the the proposed gene gun system are obtained from an experimental rig, which include the mass of the ground slide with pellet, volume of receiver, barrel length and radius and space between mesh and target (skin). Spherical and irregular stainless steel particles of 18 and 30 μm average diameters are chosen to study the effects of particle size on the penetration depth for both the model and experiment. The details of the relevant parameters used in the model are listed in Table 5.3.

5.3.3 Model behaviour of microneedle assisted micro-particle delivery

The governing equations for modelling the MNs assisted micro-particles delivery is solved using MATLAB (Version R2012b). MATLAB is a powerful programming software for computing and data processing and visualisation. For our case, we use MATLAB's in-built programming language to simulate the particle delivery process in each stage. The detailed code for the model of the MN assisted micro-particle delivery is shown in the Appendix B. The presented model consists of a main program to explain the overall process of the micro-particle delivery, several function programs to input the integration of the required mathematical equations, event programs to define the event locators of the rebound and impact points. All constant variables (e.g. skin properties, particle properties) are included as declared global variables at the start of the program with comments in the main program for the following simulation (see Tables 5.2 - 3). The acceleration stage is analysed in one-dimensional using equation (5.4) in the main program to predict the velocity from the beginning to the end of the barrel at various pressures. The separation stage is implemented using equation (5.6) in the main programme to define the energy loss of micro-particles during separation stage and then to calculate the velocity of micro-particle after the passage through the mesh.

The presented model is focused on determining the trajectories of micro-particles in the deceleration stage. Firstly, the initial velocity of separated micro-particles in the deceleration stage (u_3) is defined to be equal to u_2 which is the final velocity of the separated micro-particle after passing though the mesh. The velocity of the separated micro-particles is then analysed in relation to time. After that a two dimensional figure corresponded to the structure of the deceleration stage is prepared based on the size of experimental set up as shown in Figure 5.2. The initial position and moving direction of high-speed micro-particles are randomly chosen from the beginning in the first step of the deceleration stage to mimic

the condition of micro-particles passage through the mesh. The motion is considered to be linear but varying in velocity of the particles due to the effect of drag force. However, the mathematical equations used to determine the particle velocity are implemented in a separate function. An *if* statement is used to determine the selection of equations to calculate the particle velocity at different positions. This program is implemented to the main program by considering the condition of the function program (stiff/non-stiff) to choose a suitable *ode* solver to determine the velocity changing of micro-particles and plot the trajectories in the pre-plotted figure (Figure 5.2). The penetration depth of micro-particles in the skin is obtained from the figure. In addition, equations (5.12, 5.15) are solved using a separately function program and implemented into the main program to predict the penetration depth of micro-particle with/without using MNs in one-dimensional simulation. A *for* statement is used to repeat the same procedure to simulate a number of micro-particle trajectories in the program. However, the number of micro-particles is defined as a constant and inputted at the start of the main program.

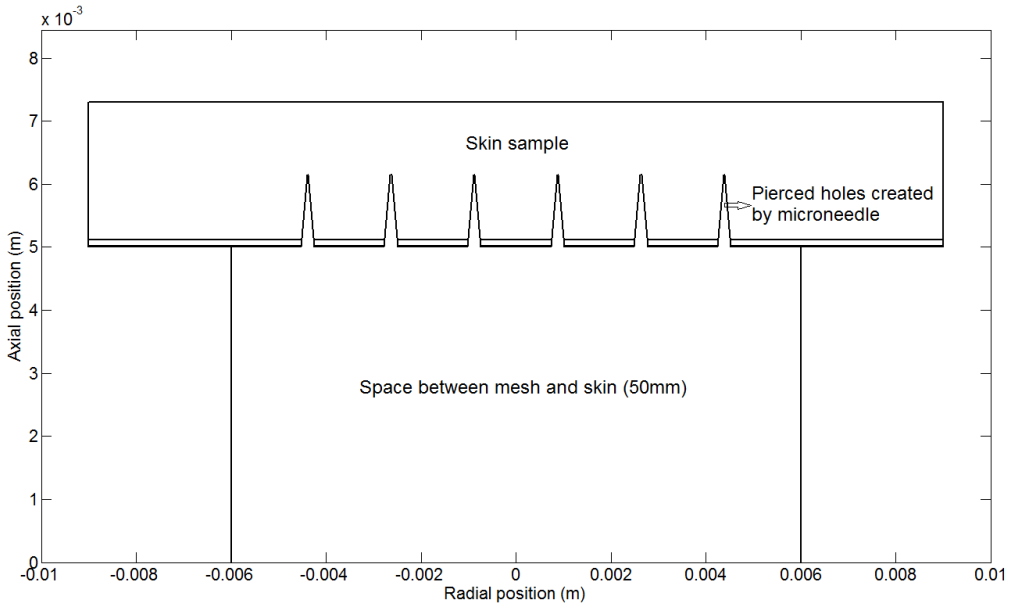

(a)

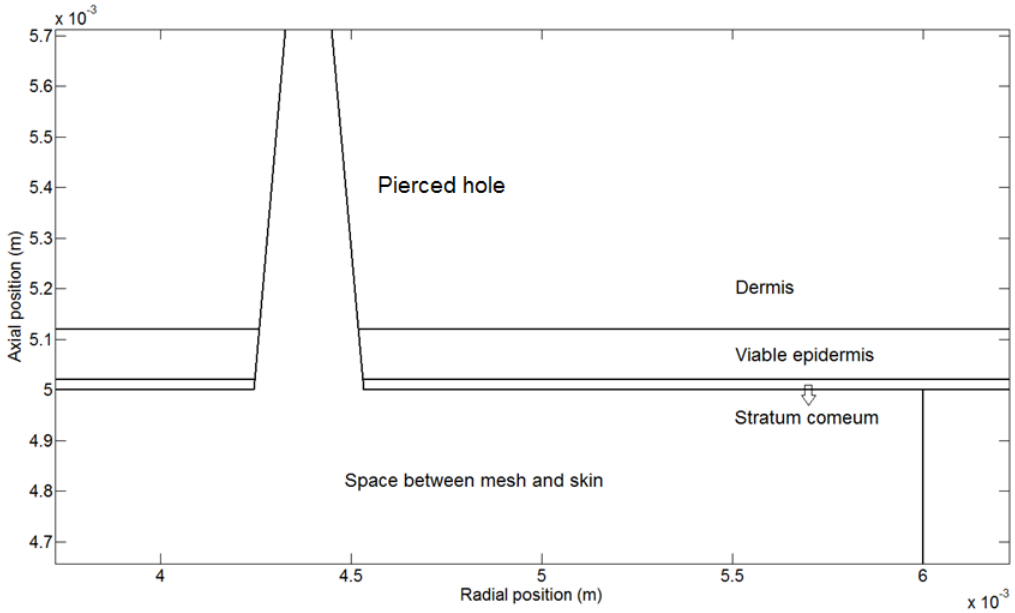

(b)

Figure 5.2: Structure of the deceleration stage (Adminpatch 1500) (a). The overall view of the deceleration stage (b). The zooming view to show the skin layers

Event program is used to define the impact points on the skin and the boundary of the gap between mesh and skin, and further to point out the end position of micro-particles inside the skin. Setting the events cause the solver to stop the integration when the micro-particle impact on the skin and the boundary of the gap between mesh and skin, and then restarts the integration corresponding to the continuous moving of a micro-particle. In addition, an event causes the solver to stop the integration when the velocity of micro-particles is less than 10^{-10} m/s. This event program is implemented in the main program to predict the events of micro-particles (e.g. impact on the boundary, penetrate into the skin) and show on the particle trajectories.

5.4 Results and Discussions

5.4.1 Acceletration stage

The micro-particle velocity is a key variable in the microneedle assisted micro-particle delivery process which is discussed in this section. As mentioned earlier, the developed mathematical model is built to simulate the acceleration stage of this process where a number of variables are considered such as the mass of the ground slide (including the pellet), volume of the gas receiver and, barrel length and diameter. The above relevant constants are listed in Table 5.3.

The operating pressure is another key variable of importance in the model which affects the velocity of the ground slide. The principle of modelling the acceleration stage is explained in section 5.3.1.1. The model results show that the operating pressure has a significant effect on the ground slide velocity (Figure 5.3). As can be seen, an increase in the operating pressure causes an increased ground slide velocity. The velocities of ground slide reach 85.5, 102.2, 125.1, 138.3 and 144.5 m/s at 2.1, 3, 4.5, 5.5 and 6 bar pressures, respectively.

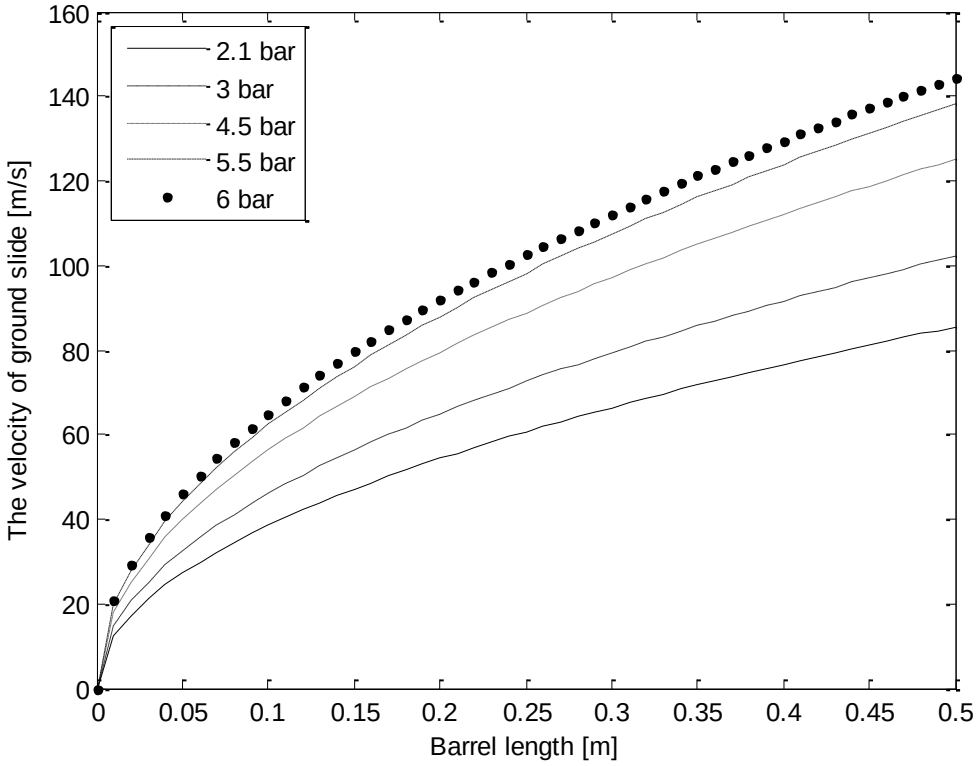

Figure 5.3: Effect of the operating pressure on the ground slide velocity (modelling results)

A pair of photoelectric sensors has been used to test the velocity of the ground slide in a set of experiments. A comparison is made between the results from the developed model and experiments (obtained from section 3.4.1.1)which are shown in Figure 5.4. As can be seen, both sets of results compare well at each pressure. The velocity increases from an increase of operating pressure due to an increased kinetic energy of the ground slide. This set of results provides the confidence that the developed model is suitable for modelling the acceleration stage of the microneedle assisted micro-particle delivery.

It is seen that the predicted velocity is comparable with the velocity of the ground slide based gene gun system, e.g. light gas gun (Crozier, 1957; Mitchell *at al*., 2003) which can accelerate the micro-particles to a velocities of 170, 250, 330 m/s at 20, 40 and 60 bar pressure. In this

work the ground slide is operated at 6 bar which shows that the velocity is slightly different with the LGG operated at 20 bar pressure. However, the velocity is much slower if it is compared with that of other gene gun systems, e,g. contoured shock tube (Truong *et al*., 2006; Mitchell *et al*., 2003), converging-diverging nozzle (Kendall *et al*., 2004a) and conical nozzle (Quinlan *et al*., 2001). The micro-particles normally can achieve a supersonic speed based on a needle free powder injection system, such as golden particle injector which may reach a velocity over than 600m/s at 60 bar pressure using contoured shock tube (Liu *et al*., 2006; Mitchell *et al*., 2003). This is because the effects of the ground slide which slows down the particle velocity.

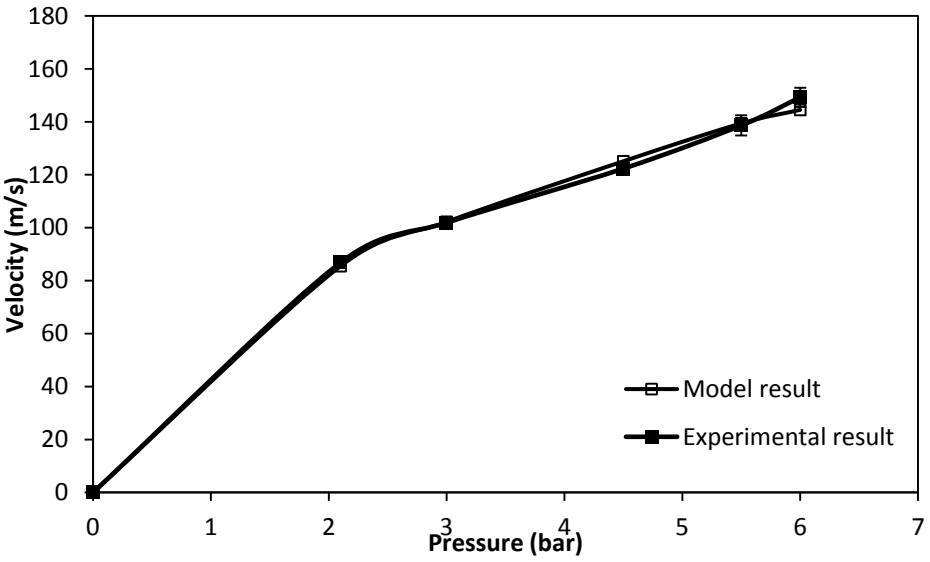

Figure 5.4: Comparison of modelling (this work) and experimental results (obtained from section 3.4.1.1) of the ground slide velocity against the operating pressure. The experimental results in the figure are generated from three repeats of experiments.

An insufficient velocity may mean that the micro-particle cannot reach the desired depth inside the target due to the insufficient momentum. It can make up for an increase of operating pressure as 6 bar is a low pressure to operate most gene gun system. However, the operating pressure is limited in the experimental set up in our case. As such, the velocity of the ground slide is simulated to reach a velocity of 457 m/s at 6 MPa using the model, which is much higher than the result obtained from LGG. In section 3.4.1.1, the experimental results have shown that the velocity increases with a decrease in barrel diameter and ground slide mass. Therefore, the velocity can improve by changing those two objects in the experimental set up if higher velocity is necessary. Furthermore, we suggest that the penetration depth is

maximized by using MNs in this case. MN also makes up for the insufficient velocity of the micro-particle since the pierced holes created by MN provides a positive effect on the penetration depth. This is explained more in section 5.4.2.

5.4.2 Deceleration stage

5.4.2.1 The trajectory of the micro-particles

In the section 3.4.2.4, we have shown that a pellet can be separated into individual particles with a few agglomerates using a mesh which then can penetrate into the target. In this case, the presented mathematical model is used to simulate the trajectories of stainless steel micro-particles of 30 μm average diameter in the deceleration stage. As presented in Figure 5.5a, the velocity of the micro-particle is represented by the coloured trajectory. It is found that the velocity variation is negligible before they reach the target as the effect of air drag force on the micro-particles is low. It is also found that the velocity reaches approximately 131 m/s at 5 bar operating pressure according to the results in the figure. In addition, the micro-particle rebound on the boundary of the gap between mesh and skin is clearly shown in Figure 5.5a. However, the penetrations of micro-particles in the target are not visible in this figure.

In theory, the particle velocity must decease very fast after penetrating into the skin due to an increased resistance to its motion. The variation of the velocity is shown in more detail in Figure 5.5b, which is obtained from zooming in a part of Figure 5.5a. As can be seen, the micro-particles only penetrate slightly in the skin layer of stratum corneum. The detailed penetration depth refers to the result of dashed line in Figure 5.6 (see the zoomed view of the axis), which shows that the stainless steel micro-particles of 30 μm diameter only penetrate around 1.9 μm inside the stratum corneum.

Figure 5.5a also shows that a number of the micro-particles achieve a further penetration depth via the pierced holes. Some of them reaches the hole tip area as shown in Figure 5.5c. The velocity is changed only slightly in the pieced holes and decrease fast after penetrating the dermis layer of the skin. The penetration depth of the micro-particle via the pierced holes is shown in Figure 5.6 (see the zoom in view of the axis). As can be seen, the penetration depth of the micro-particles reaches 1151.1 μm when Adminpatch MN 1500 is used. However, some particles cannot reach the hole tip and penetrate through the skin surface of

the pierced holes to achieve a further depth inside the epidermis/dermis layer of the skin as shown in Figure 5.5d.

Finally, an arbitrarily selected number of micro-particles, namely one hundred micro-particles, have been simulated to determine the particle's final location in each layer of skin. As presented in Figure 5.7, it shows that about 75% of micro-particles is stopped inside the stratum corneum, 2% is located within the epidermis layer, and 23% penetrates further into the dermis layer. In addition, the micro-particles stopped inside the epidermis or dermis layer are considered to penetrate through the pierced holes which illustrate the use of the Adminpatch MN 1500 allowing approximately 25% of the micro-particles penetration in the skin via the pierced holes. The detailed effects of the MN length, particle size and operating pressure on the penetration depth are explained in the following sections.

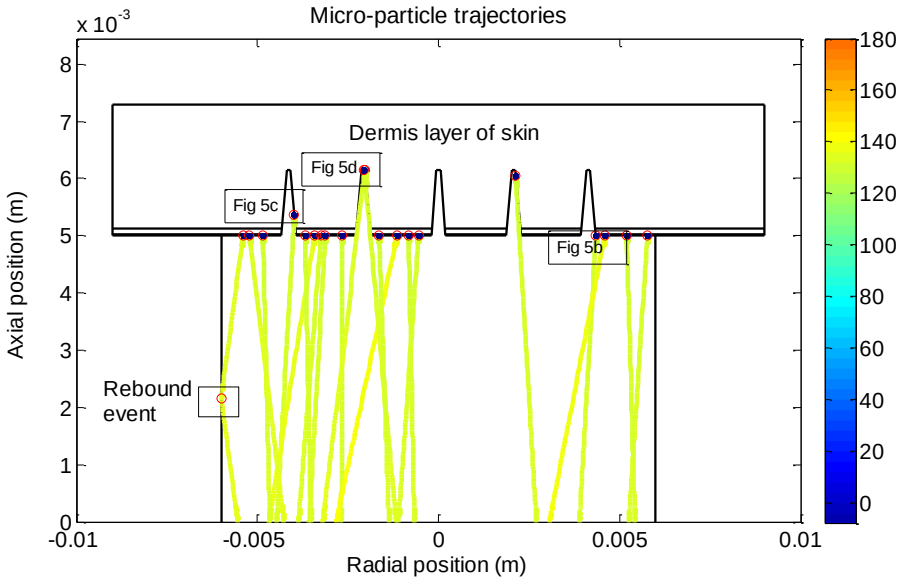

(a)

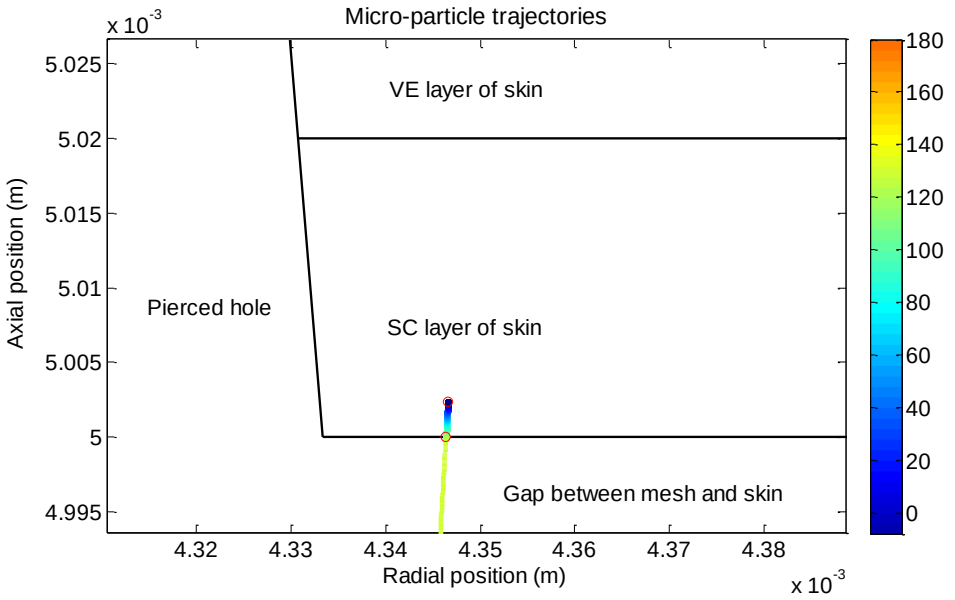
Micro-particle trajectories
x 10^-3
5.025
5.02
5.015
5.01
5.005
5
4.995
Axial position (m)
VE layer of skin
Pierced hole
SC layer of skin
Gap between mesh and skin
4.32
4.33
4.34
4.35
4.36
4.37
4.38
Radial position (m)
x 10^-3
180
160
140
120
100
80
60
40
20
0

(b)

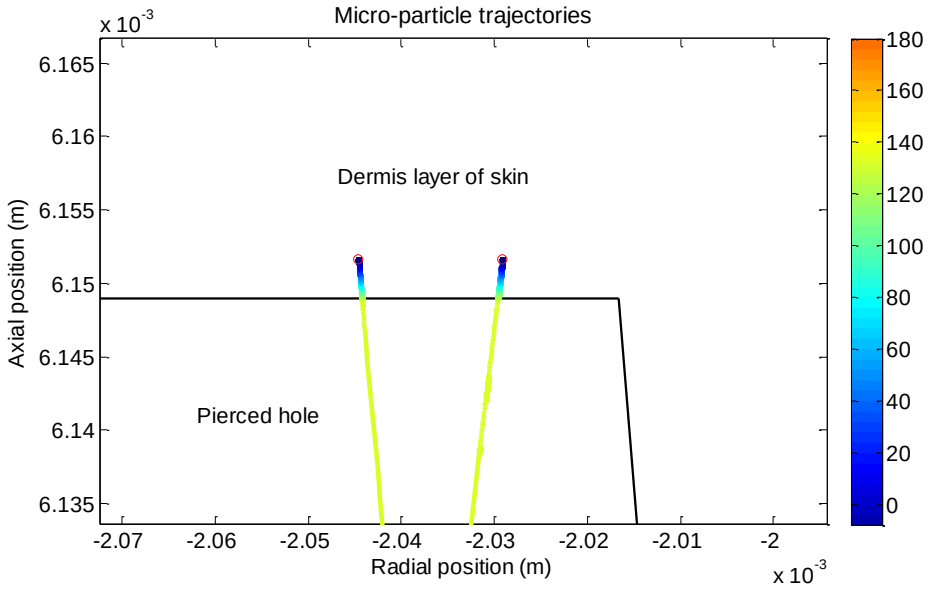
Micro-particle trajectories
x 10^-3
6.165
6.16
6.155
6.15
6.145
6.14
6.135
Axial position (m)
Dermis layer of skin
Pierced hole
-2.07
-2.06
-2.05
-2.04
-2.03
-2.02
-2.01
-2
Radial position (m)
x 10^-3
180
160
140
120
100
80
60
40
20
0

(c)

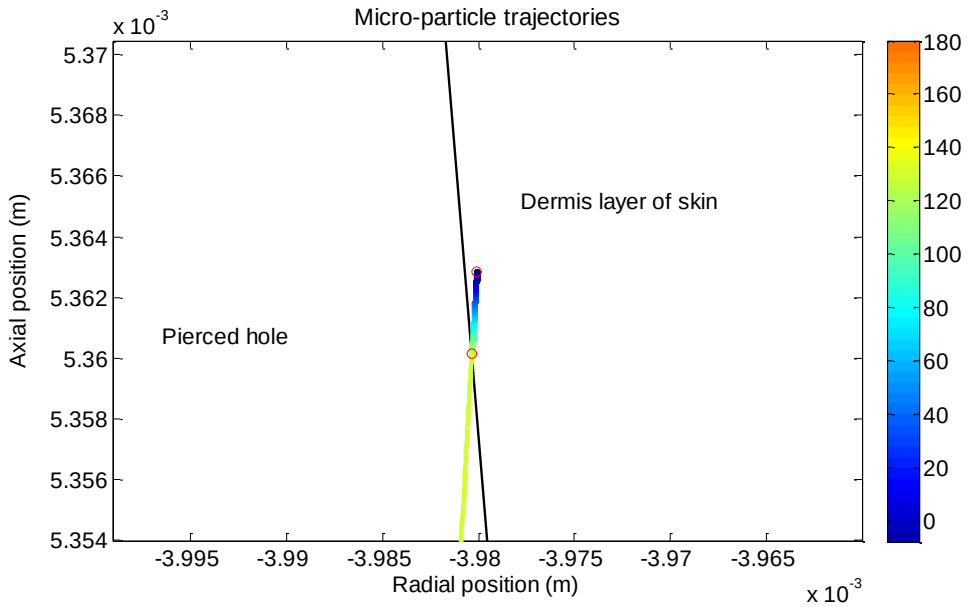

(d)

Figure 5.5: The trajectories of the micro-particles in the deceleration stage for the MN assisted micro-particle delivery: (a).The overall view of the micro-particle trajectories (b).The particle penetration at the area without needle hole (c). The particle penetration at the hole tip area inside skin (d). particle penetrates into the side surface of the needle hole inside skin (stainless steel micro-particle of 30 diameter; pressure: 5 bar)

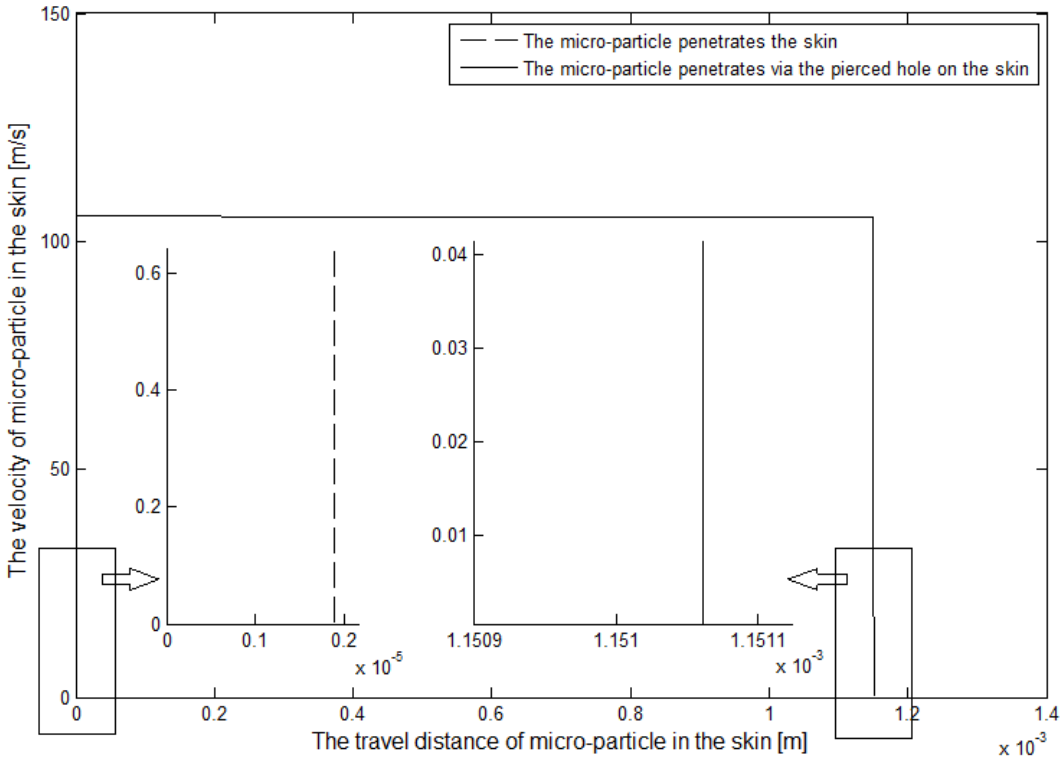

Figure 5.6: The travel distance of micro-particle in the skin against the velocity.

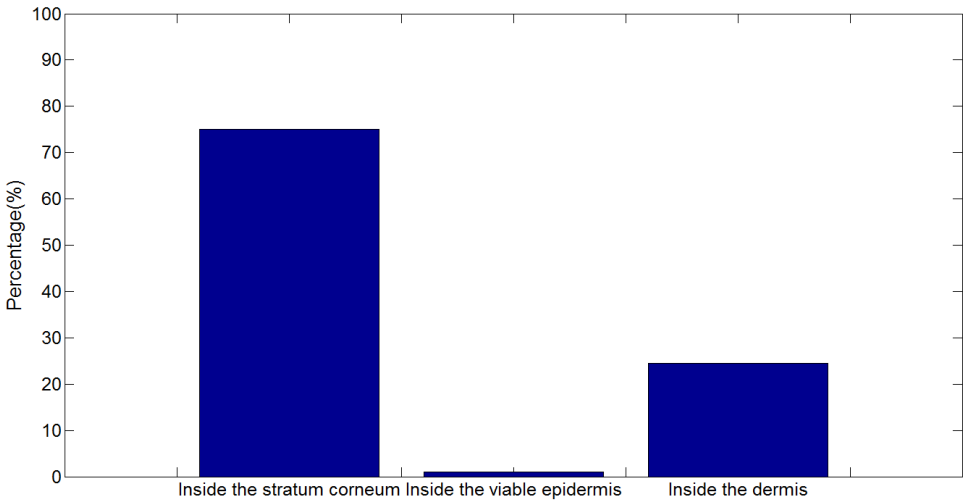

Figure 5.7: The distribution of the micro-particles in different layers of skin

5.4.2.2 Comparsion with experimental resutls

In section 4.4.1, agarose gel has been used to mimic the skin on the basis of rheological properties using a rotational viscometer. The work shows that the rheology of 0.0265 g/ml concentration of agarose gel matches well with that the porcine skin, and this skin mimicking agarose gel is used as a target instead of human skin to analyse the penetration depth in relation to the operating pressure, particle size and needle length. The operating pressure is varied from 3 to 5 bar to accelerate biomedical grade stainless steel micro-particles of 18 and 30 μm average diameters to analyse the effect of the particle size and operating pressures on the penetration depths of the particle. Three different lengths of microneedle arrays, which are in-house fabricated MN (750 μm) and Adminpatch MN 1500 (1500 μm) and 1200 (750 μm) are chosen to investigate the effect of MN length on the penetration depth. Results show that the penetration depth of micro-particles increases from an increase of particle size, operating pressure and MN length.

In the following sections of this chapter, the experimental results obtained from the previous work are compared with model results to verify the applicability of the model and further understand the MNs assisted micro-particles delivery.

(a) The effect of the operating pressure and particle size on the penetration depth

In general, operating pressure is one of the major variables which affect the momentum of the micro-particles and is expected to affect the penetration depths of the micro-particles inside a target. To confirm the significance of this effect, delivery of stainless steel micro-particles of 18 and 30 μm average diameters are simulated at operating pressure varies from 3 to 60 bar. The results of these simulations are presented in Figure 5.8. In the figure, the solid lines represent the micro-particle delivery without the MN pierced holes and they correspond to the primary y axis (y1). The penetration depth of the micro-particle via the pierced hole is considered through the secondary y axis (y2). As can be seen, the results show that an increase of the operating pressure causes a slight increase in the penetration depth. It shows that stainless steel micro-particle of 18 μm diameter can penetrate only from 0.58 to 2.59 μm in the skin (inside the stratum corneum) in the pressure ranging from 3 to 60 bar. However, a number of micro-particles delivered through the pierced holes penetrate into the dermis layer. The penetration depth inside the dermis layer is slightly more than the stratum corneum due to a decreased yield stress. As expected, the pierced hole has a greater effect on the penetration depth. The penetration depth rises from 1149.58 to 1151.66 μm when Adminpatch MN 1500 is used for the pressure ranging from 3 to 60 bar. In addition, Figure 5.8 shows the penetration depth of 18 μm diameter of stainless steel micro-particle is less than 30 μm diameter. The effect of the micro-particle size on the penetration depth is discussed in the following section.

The penetration depth of the micro-particles is also related to the size of the micro-particle which is one of the major variables that affects the particle momentum. As presented in Figure 5.9, the diameter of the micro-particle shows a positive correlation with the penetration depth. In this figure, the results plotted in solid line are for the penetration of the micro-particles without pierced holes and are referred by the primary y axis. The secondary y axis explains the result plotted in the dashed line and show the maximum penetration depth of the micro-particle which goes through the pierced hole. The penetration depth is found to be from 0.71 to 37.12 μm in the top two layers of the skin (stratum corneum and viable epidermis layers) at operating pressure of 5 bar while the particle diameter ranges from 18 to 140 μm. It indicates that the small micro-particle cannot penetrate further in the skin so much as they are rebounded by the skin due to the insufficient momentum. However, this condition may be fixed by the use of a MN array. As shown in Figure 5.9, the penetration depth increases from 1149.75 to 1189.73 μm, which is enhanced by delivering a number of micro-particles through the pierced holes created by the Adminpatch MN 1500. The

penetration depth in dermis layer varies from 0.75 to 40.73 μm which is more than the penetration in top layer.

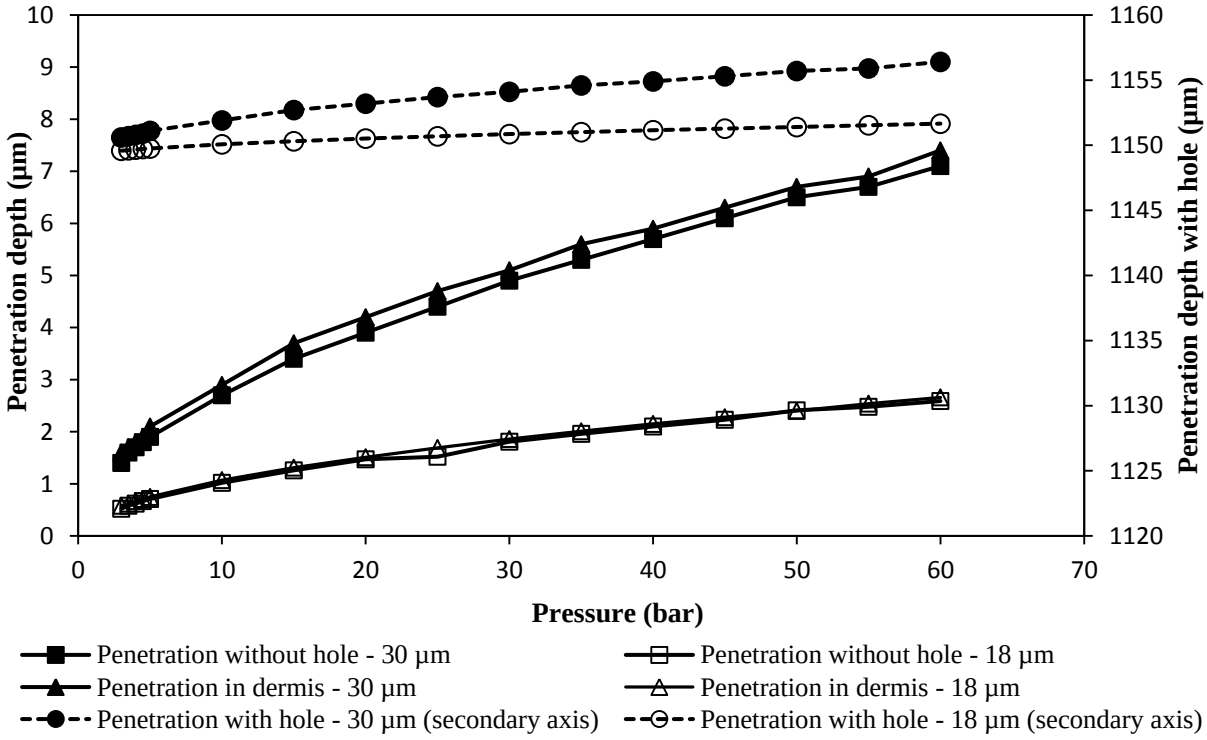

Figure 5.8: The effect of the operating pressure on the penetration depth of the micro-particle in the skin (stainless steel micro-particles: 18 and 30μm average diameters; MN: Adminpatch MN 1500; solid line: primary y axis; dashed line: secondary y axis)

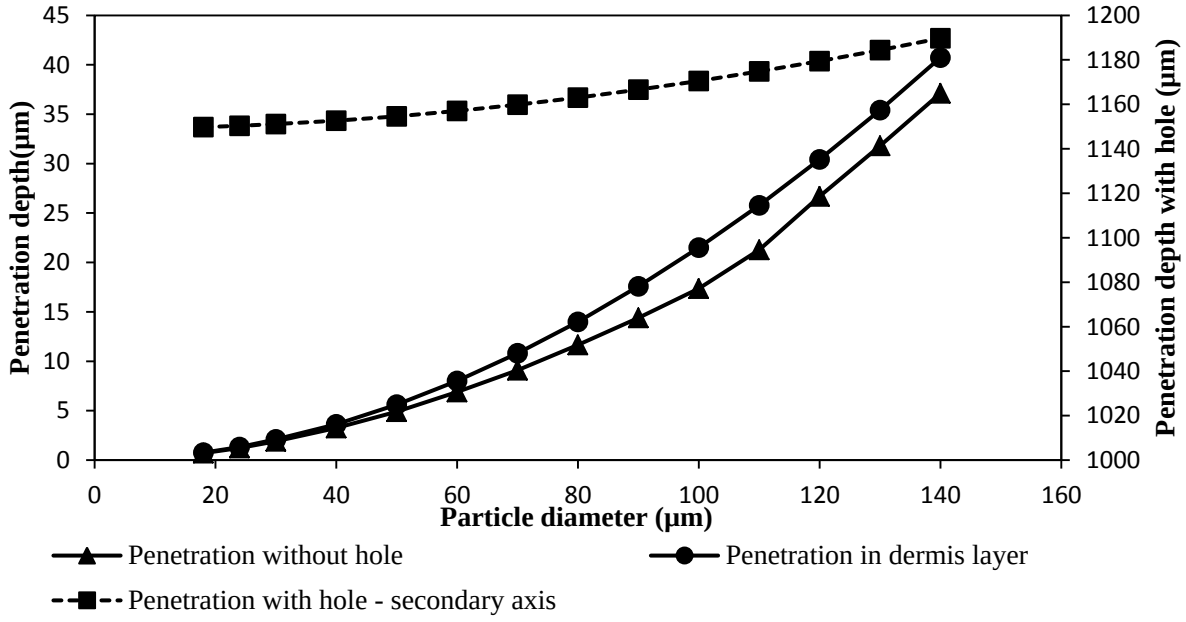

Figure 5.9: The penetration depth of stainless steel micro-particle in side skin against the particle diameter (operating pressure: 5 bar; MN: Adminpacth MN 1500; solid line: primary y axis; dashed line: secondary y axis)

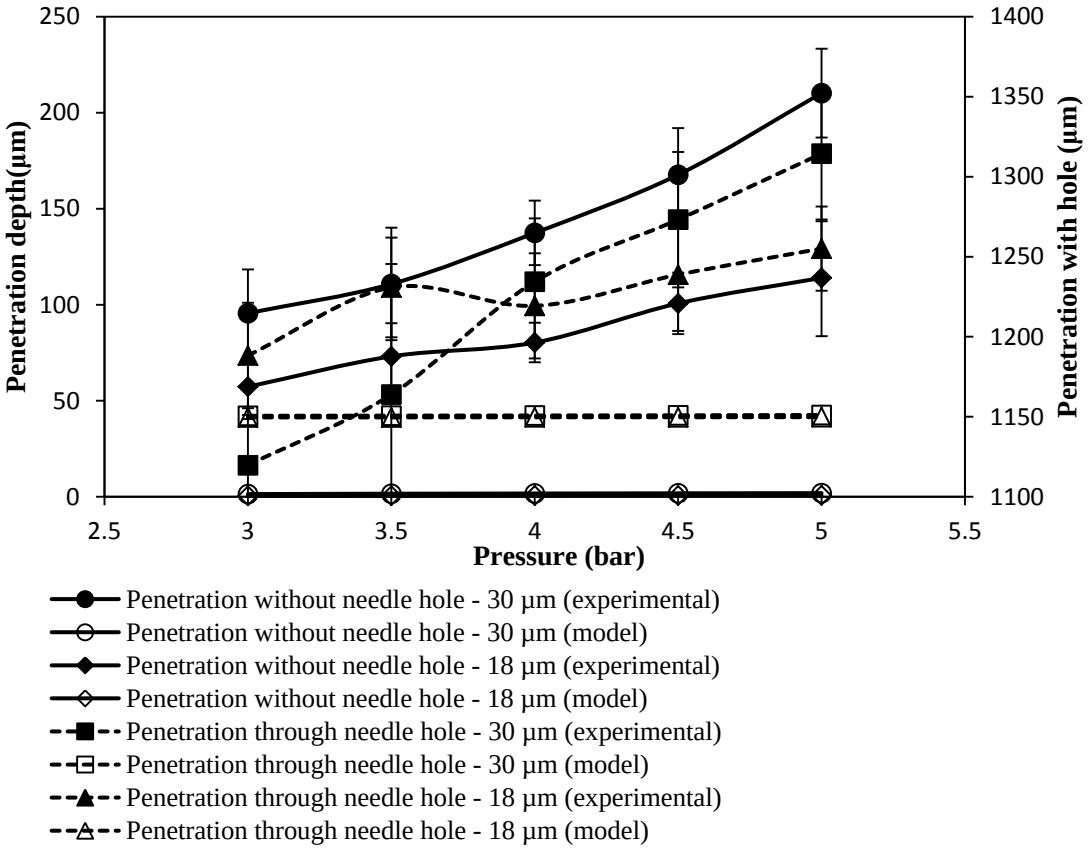

Figure 5.10: A comparison between model and experimental results at various operating pressures (stainless steel micro-particles: 18 and 30 diameters; MN: Adminpatch MN 1500; solid line: primary y axis; dashed line: secondary y axis). The experimental results in the figure are generated from three repeats of experiments.

A comparison between model and experimental results is shown in Figure 5.10. Micro-particle penetration without (solid lines) and with (dashed lines) pierced holes refer to the primary and secondary axes, respectively. As can be seen, the operating pressure and particle size have a greater effect on the penetration depth for the experimental results. The penetration depth rises fast while the operating pressure is increased. It also shows a significant different between stainless steel micro-particles of 18 and 30 μm diameter, which demonstrates that an increased particle size has a positive correlation on the penetration depth. However, those two variables only have slight effect on the penetration depth according to the model result. This is because the pellet is considered to be separated into individual particles perfectly in the mathematical model which does not happen in practice. In the previous work (Chapter 3), different pore sizes of meshes are used to break up the pellet separation and control the size distribution of the separated particles, which show that the pellet has been

broken into individual particles effectively with only a few small agglomerated particles. These agglomerated particles may cause an increased penetration depth and further improve the effect of the operating pressure on the penetration.

Figure 5.10 also shows that the micro-particles penetration through the pierced holes varies between model and experimental results. For the model result, the length of the pierced holes is considered to be a constant. Thus, the penetration difference between stainless steel micro-particles of 18 and 30 μm diameters is only slight since the momentum of those two particles are insufficient to penetrate further in the skin. These differ with experimental results which show that the penetration depth varies at the operating pressure ranges from 3 to 5 bar. This is because the length of the pierced holes is varied after the removal of the MNs in the experiment. It directly affects the micro-particle penetration depth, such as small particles may penetrate further than larger particles. As present in Figure 5.10, the penetration depth of stainless steel micro-particles of 18 μm diameter is more than 30 μm diameter at 3 and 3.5 bar pressure. However, the experimental results show that the stainless steel micro-particles of 30 and 18 μm diameters reach the penetration depth from 1119.7 to 1314.4 μm and from 1188.3 to 1255.1 μm while the pressure varies from 3 to 5 bar, respectively. The operating pressure only presents a slight effect at this condition. As expected, the length of the pierced holes becomes the primary factor which maximizes the penetration depth. It directly relates to the length of MN. The effect of the microneedle length on the penetration depth is discussed in the following section.

(b) The effect of microneedle length

In principle, the length of the pierced hole depends on the length of the microneedle. An increased length of MNs causes an increase in the pierced holes and thereby increases the penetration depth of micro-particles. As presented in Figure 5.11, the penetration depths of the micro-particle differ significantly between each application of MNs. Both model and experimental results present that the penetration depth increases from an increase of MN length. For the model result, the operating pressure does not show a great effect on the penetration depth. For the experimental result, the penetration depth is varied at the operating pressure ranges from 3 to 5 bar. This is because of the effect of the agglomerates and the unmaintainable length of pierced holes, which are presented in previous section. The operating pressure presents a positive effect on the penetration depth, which agrees with the model result.

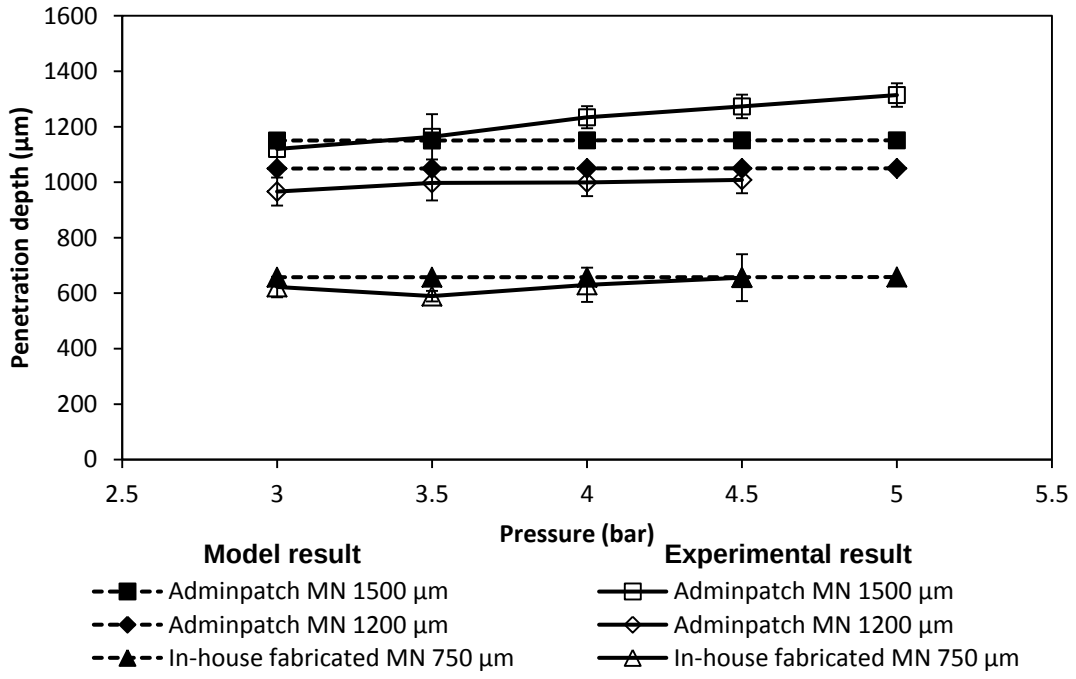

Figure 5.11: The effect of the microneedle length on the penetration depth of the stainless steel micro-particle (30 µm). The experimental results in the figure are generated from three repeats of experiments.

In conclusion, the experimental results match well with the model results in Figure 5.11. It confirms that this mathematical model is suitable for modelling MNs assisted micro-particles delivery. It also indicates that the micro-particles can be deposited at a desired depth in a target based on a use of specific lengths of MNs. In addition, the penetration depth gradually increases with the increase in operating pressure. It can be considered that based on the assistance of the holes on the micro-particle delivery, the penetration depth can be fine tuned by the operating pressure.

(c) Further discussion

In the above sections, the penetration depths of micro-particles are analysed with respect to variations in operating pressure, particle size, MN size using modelling and experimental results. It is evident that the particle penetration depth increases from an increase of the operating pressure and particle size as the particle momentum is related to those two key variables. In the experiment, the agglomerates present a greater effect on the particle penetration depth. It shows that the model result cannot match well with the experimental result. However, the agglomerates can be prevented by using a smaller pore size of mesh to

allow individual micro-particles to pass through and obtain a uniform penetration depth which is comparable with the model results.

As expected, an application of MN array provides a positive effect on the micro-particle penetration. The maximum penetration depth of the micro-particles is presented a significant increment from the result without MN application. For the MN assisted micro-particle delivery, the penetration depth reaches the dermis layer inside skin, which was never achieved in the previous gene gun systems (e.g., injection jet, light gas gun, contoured shock tube, etc). Mitchell *et al*. (2003) have used a light gas to accelerate the stainless steel micro-particles of 25 μm diameter to a velocity of 170 m/s (20 bar) and penetrate 150 μm into excised canine buccal mucosa. Kendal (2001) has suggested that the 1 ± 0.2 μm diameter gold particles can reach a velocity of 580 ± 50 m/s at 40 bar pressure using a contoured shock tube and penetrate 66 μm in the skin. The epidermis has been generally normally considered as the target tissue for gene loaded particle delivery as the devices may be limited by the penetration depth they achieve (Trainer *et al*., 1997). But now the target tissue may be the dermis layer as the use of MNs promise to increase the penetration depth further. In other words, the MN may be useful for the injection of micro-particle especially the targets which require a deep injection of the particles.

5.5 Chapter Summary

A mathematical model is built for solid MNs assisted micro-particles delivery. MNs assisted micro-particles delivery is studied in this chapter. For the acceleration stage, the particle velocity is analysed in relation to the operating pressure and these result compare well with the experimental result obtained from the previous work (section 3.4.1.1). For the deceleration stage, an individual micro-particle trajectory has been simulated in the model. Additionally, the distribution of the micro-particles in three different layers has been determined using modelling results. These results show that about 75% of particles penetrate into the stratum corneum without going through the holes, and 23 and 2% of particles penetrate into epidermis and dermis layers via the pierced holes, respectively. The presented model for MN assisted micro-particle delivery takes into consideration possible change in operating pressure, particle size, MN length due to the micro-particle delivery is directly related to those key variables. Model results obtained indicate that increasing the operating pressure and particle size would increase the penetration depth of the micro-particles inside skin due to the increased momentum. In addition, the hole length is shown to be a major

variable which maximizes the particle penetration depth. The model results match well with the experimental results for the penetration depth of micro-particles. In conclusion, the presented model is shown to be useful for simulating micro-particle trajectories and penetration depth for MN assisted micro-particle delivery.

6. Microneedle assisted micro-particle delivery: Experiment and modelling on the effects of particle characteristics

6.1 Chapter Overview

The assistance of microneedles (MN) has been proven to overcome the resistance of target materials and further enhance the penetration depths of micro-particles, which are moving at high speeds such as those in gene gun. This chapter aims to investigate the penetration of model materials, namely, tungsten (< 1 μm diameter) and stainless steel (18 and 30 μm diameters) micro-particles into a skin mimicking agarose gel to determine the effect of particle characteristics. A number of experiments have been processed to analyse the passage percentage and the penetration depth of these micro-particles in relation to the operating pressures and MN lengths. A comparison between stainless steel (18 and 30 μm diameters) and tungsten micro-particles has been discussed, e.g. passage percentage, penetration depth. The passage percentage of tungsten micro-particles is found to be less than the stainless steel. It is worth mentioning that the tungsten micro-particles present unfavourable results which show that they cannot penetrate into the skin mimicking agarose gel without the help of MN due to insufficient momentum due to the smaller particle size. This condition does not occur for stainless steel micro-particles. In order to further understand the penetration of tungsten micro-particles, a mathematical model has been built based on the experimental set up. The penetration depth of the micro-particles is analysed in relation to the size, operating pressure and MN length for conditions which cannot be obtained in the experiment.In addition, the penetration depth difference between stainless steel and tungsten micro-particles is studied using the developed model to further understand the effect of an increased particle density and size on the penetration depth.

6.2 Introduction

Gene gun systems have been designed primarily as needle free techniques which can accelerate DNA loaded micro-particles to provide them with sufficient momentums so as to breach the outer layer of the skin and achieve the purposes of gene transfection (Kis *et al*., 2012; Soliman, 2011; Walters and Roberts, 2007; Kendall *et al*., 2004). Generally, the epidermis layer of the skin is considered as the main target of the micro-particles (Soliman *et al*., 2011; Liu, 2006; Quinlan *et al*., 2001; Bennett *et al*., 1999; Trainer *et al*., 1997). However, cell and tissue damages are particular problems for the use of gene guns (O'Brien and Lummis, 2011; Uchida *et al*., 2009; Thomas *et al*., 2001; Sato *et al*., 2000; Yoshida *et al*.,

1997). In principle, reduction of the operation pressure (Xia *et al*., 2011; Uchida *et al*., 2009; Yoshida *et al*., 1997) and particle size (O'Brien and Lummis, 2011) can minimize the cell damage but these tend to decrease the particle momentum and, hence, the penetration depth of the micro-particles in the tissue. In addressing these issues, a series of experiments which combines solid microneedles (MNs) with an in-house micro-particle delivery system has been discussed earlier in the chapter 4 and 5.

MNs are minimally invasive microstructures that pierce the outer layer of skin, namely the *stratum corneum*, almost painlessly which has been shown to enhance drug delivery rate (e.g., Olatunji and Das, 2011; Nayak et al., 2013; Olatunji et al., 2013; Donnelly et al., 2012). They are generally classified into 'solid' and 'hollow' microneedles (e.g., Al-Qallaf et al., 2009; Olatunji and Das, 2010; Olatunji et al., 2012; Nayak and Das, 2013; Han and Das, 2013; Zhang et al., 2013a,b,c). The solid MNs are able to penetrate the human skin to make holes (Kalluri *et al*., 2011; Davis *et al*., 2004; McAllister *et al*., 2003) as well as deliver drugs/genes which are coated (Cormier *et al*., 2004) or encapsulated (Miyano *et al*., 2005).The MN holes can also be used by the biolistic system for the delivery of the micro-particles. As envisaged, micro-particles can penetrate with less resistance into the skin through the holes and further achieve an enhanced penetration depth to allow gene transfection in deeper tissue. In our previous work (see Chapter 4), the experimental setup of MN assisted micro-particle delivery system has been used to fire stainless steel micro-particles having average diameters of 18 μm into a skin mimicking agarose gel. The results have shown that a number of micro-particles are penetrated through the holes and achieve a considerable increase in the maximum penetration depth of 1272 ± 42 μm inside the gel using 1500 μm length of MNs (AdminPatch MN 1500) as compared to the cases where no microneedles are applied.

As discussed earlier, the overall process of MN assisted transdermal micro-particle delivery from gene guns consists of three stages, which are the acceleration, separation and deceleration stages. These stages are identified in Figure 4.1a. The system stores the pressurized gas in a gas receiver to a desired pressure which is detected by a digital pressure transducer. The release of the pressurized gas is operated by a solenoid valve. In addition, it is worth mentioning that the system uses a ground slide which can prevent the impact of pressurized gas on the target tissue and release the gas from the ventholes. The acceleration stage is a major part of the particle delivery process as it is within this stage the micro-particles are accelerated to sufficient velocities using a pressurized gas as a driving

source. To achieve these, the micro-particles are compressed and bound loosely into a pellet form and loaded into a ground slide in the system. As the ground slide is accelerated by the pressurised gas, the pellet containing the micro-particles is also accelerated. The separation stage is then followed which is aimed at separating the pellet into individual particles by a mesh although it is possible that this stage produces a few agglomerates.

The deceleration stage involves two steps as follows: (i) the transport of the micro-particles in a space between mesh and target and (ii) the penetration of micro-particles into the chosen target. Previously, an experimental rig (Figure 4.1a) has used to deliver stainless steel micro-particles into a skin mimicking agarose gel so as to demonstrate the feasibility of MN assisted micro-particle delivery. The results have shown that an enhanced penetration depth of micro-particles inside the agarose gel can be achieved using MN assisted micro-particle delivery at a much lower injection pressure compared to typical gene guns.

Generally, the route of the micro-particle penetration in the target tissue is divided into two types which are the extracellular and intercellular routes (Soliman and Abdallah, 2011; Mitchell *et al*., 2003). The extracellular route may occur with large particles due to failures between the cell boundaries (Soliman, 2011). For example, Mitchell *et al*. (2003) have fired stainless steel micro-particles of 25 μm average diameter into canine buccal mucosa using light gas gun (Crozier *et al*., 1957), which is governed by the micro-particle transport through extracellular route. However, the disadvantage of this is that large particle sizes may cause a lot of damage or destroy the skin surface.

The intercellular route is considered to be important in the case of delivering small particles, which pass through individual cell membranes and can be used for particle mediated DNA immunization (Soliman and Abdallah, 2011; Hardy *et al*., 2005). Dense materials (e.g. gold and tungsten) are often made into small particles of a diameter ranging from 0.6 to 6 μm (Soliman, 2011; Hardy *et al*., 2005) which are smaller than the cell diameter. The particles can be accelerated to higher speeds to obtain enough momentum to breach the skin and penetrate through the individual cell membranes. Although gold is recommended for the particle delivery due to its high density, low toxicity and lack of chemical reactivity (Macklin, 2000), it is an expensive method. Several studies for the golden micro-particle delivery have been made, which show that the gold micro-particles can breach the human skin and penetrate to a depth ranging from 35 - 135 μm at 30 bar operating pressure (Arora *et al*., 2008; Giudice

et al., 2006). Kendal *et al*. (2004) have used a convergent-divergent device to accelerate gold particles of 1.8 μm diameter which achieves a maximum penetration depth of 78.6 μm at 60 bar pressure. Mitchell *et al*. (2003) have found that gold particle of 1 - 3 μm diameter can reach a depth of around 60 μm in canine tissue at an injection particle velocity of 550 ± 50 m/s. Recently, O'Brien and Lummis (2011) have reported that the penetration depth of golden micro-particles of 1 μm diameter in mouse ear tissue is 50±11 μm when the Helios gene gun is used at an operating pressure of 5.1 bar (75 psi).

In general, the intercellular route is the preferred penetration route due to less cell and tissue damages for the small micro-particles. In order to validate the effect of the MN assisted micro-particle delivery on the small micro-particles, tungsten micro-particles may be chosen to analyse the penetration in the skin mimicking agarose gel. Tungsten micro-particles are considered to be a good substitute for golden micro-particles for research of biolistic micro-particle delivery because of their cost effectiveness compared to gold particles, despite the fact they can be toxic to cells (Bastian *et al*., 2009; Yoshimisu *et al*., 2009; Russell *et al*., 1992). For example, Klein *et al*. (1987) first used a particle gun to accelerate spherical tungsten particles of 4 μm diameter into epidermal cells of onions. Williams *et al*. (1991) have used a helium-driven apparatus to study 3.9 μm average diameter tungsten and of golden particles, with a diameter ranged from 2 to 5 μm, on mouse liver.

Motivated by the above work, this chapter aims to investigate the effects of particle characteristics on MN assisted micro-particle delivery by using micro-particles (e.g. tungsten micro-particles, biomedical grade stainless steel) of different densities and particle sizes. The study gives an indirect comparison between the extracellular and intercellular routes using MN assisted micro-particle delivery. In Chapter 3, we have determined the passage percentage of stainless steel micro-particles at various conditions, e.g., mesh pore size, Polyvinylpyrrolidone (PVP - binder) concentration and operating pressure. The required mesh pore size and PVP concentration of pellets for MN assisted micro-particle delivery for given particle size is pointed out. This chapter aims to revisit the same questions to determine the dependence of particle characteristics using tungsten and stainless steel micro-particles with the help of the experimental rig (Figure 4.1). A skin mimicking agarose gel is used as a target to determine the difference in penetration depth between tungsten and stainless steel micro-particles. In order to further understand the particle size and density effect on the penetration depth, a mathematical model of MN assisted micro-particle delivery is built based

on the experimental rig using MATLAB (Version R2012b). The model is used to analyse the theoretical penetration depth of those two materials of micro-particles and further to verify the experimental result. In addition, the model also aims to investigate the effect of the target properties (e.g. density, friction coefficient) on the maximum penetration depth of micro-particles. In particular, the developed model is used to determine the characteristics of the micro-particle delivery where experimental data are not readily available.

6.3 Material and experimental methods

6.3.1 Characterization of tungsten micro-particles

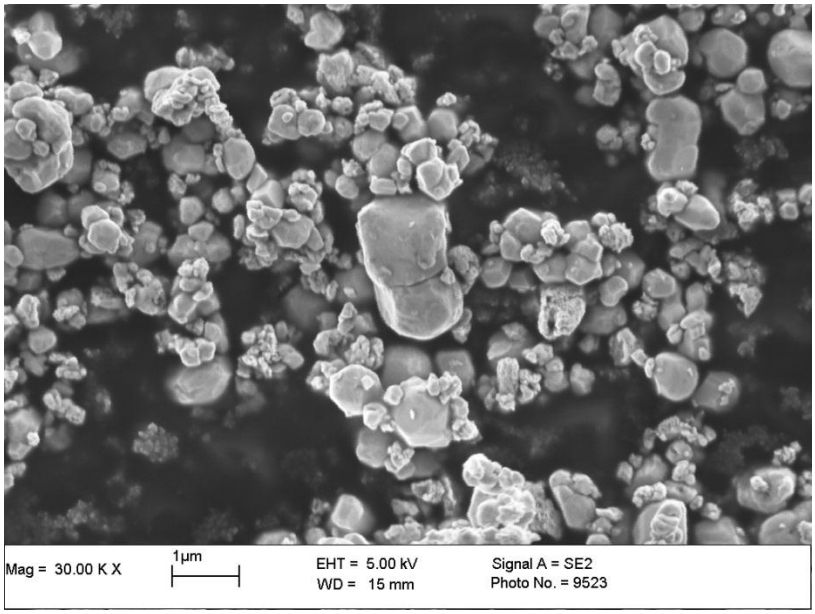

Figure 6.1: A SEM image of irregular tungsten powder (Sauter mean diameter: 0.49 µm)

Irregular shaped tungsten micro-particles were purchased form Sigma-Aldrich Company Ltd (Gillingham, UK). It is considered as a good replacement for gold particles because its density is similar to gold and has a low cost (Menezes *et al*., 2012). The particle size distribution of tungsten powder is analysed by a particle size analyser (Mastersizer 2000, Malvern Instruments, Ltd, Malvern, Worcestershire, UK). It is found to range from 0.198 to 1.439 µm with a mean diameter of 0.58 µm and Sauter mean diameter of 0.49 µm. The particles can be viewed in the SEM image in Figure 6.1. The tungsten particles are highly agglomerated and have rough surfaces. From the SEM image, 50 random micro-particles are chosen to measure the average sphericity of the tungsten micro-particles which is found to be 0.66 ± 0.13 µm. The average bulk density and porosity of tungsten powder are 7.43 ± 0.08 g/cm^3 and 59.6 ± 0.4%. Ultimately, by combining the SEM image results with the size

distribution, gained from particle size analyser it is possible to confirm that the tungsten particles are a nano-size powder.

6.3.2 A further invertigation of the characterization of the pellet

For the MN assisted micro-particle delivery, the micro-particles are required to be in the form a compressed cylindrical pellet which is prepared by a pellet press as described in section 3.3.3.3. Furthermore, the packing density should be homogeneous within the pellet as far as possible so as to increase the possibility that when the pellet is broken into particles, one obtains uniformly separated particles. Heterogeneity in the packing of the pellet is likely to create more uncertainty in the distribution of the separated particles. To prepare the cylindrical pellet, we have mixed 40 mg of PVP in 1 ml of ethanol in which an amount of 0.035 g stainless steel micro-particles has been added and bind the particles together. The mixture is transferred to a pellet press and compressed into a solid cylindrical pellet. Ethanol is evaporated due to their high volatility and therefore, it is not present in the dry pellet which is used in experiments. A similar method was followed to produce the pellets in this work. Further, the homogeneity of the micro-particle packing was checked using a micro computed tomography (micro-CT) (Ritman, 2004). Micro-CT is an advanced non-destructive 3D imaging technique which can be used to clearly understand the internal microstructure of the samples (Ritman, 2004). Micro-CT is used to detect the internal damages or heterogeneity in the structure of pellet in this case. As an example, a three dimensional view of the stainless steel pellet is shown in Figure 6.2a. As can be seen, the stainless steel micro-particles are compressed into a homogenous cylindrical pellet with approximately 2 mm in diameter and length. Although the top and button surfaces of the pellet are slightly rough because the pellet gets stuck on the pellet press, it is not a big concern. The internal top view of the pellet at the position of 1.08 mm on the z axis is shown in Figure 6.2b and the size view of the internal structure of the pellet at the position of 1.08 mm on the y-axis is shown in Figure 6.2c. It shows that PVP (white spots) is non-uniformly distributed in the pellet. PVP is fills the void space between micro-particles causing them to bind strongly together as indicated by the white circles (PVP) in the Figures 6.2b-c. The above figures cannot clearly show the PVP combination of the pellet. A view can be obtained by referring to the SEM image of the top surface of the pellet (see Figure 6.3).

Figure 6.3 clearly shows the characterization of the pellet top surface. As can be seen, the micro-particles are bound to form a uniform pellet surface. As expected, the PVP is

distributed non-uniformly around the pellet, which agrees with results detected by the micro-CT (Figure 6.2). Thus, it may cause the pellet to separate into a few agglomerates after the separation stage due to increased bind strength between some of micro-particles. Previously (see Chapter 3), we have analysed the passage percentage of the pellet and size distribution of the separated particles using various operating pressure and different binder (PVP) concentration. 40 mg/ml PVP in a pellet is shown to ideal as it almost separates the pellet into individual micro-particles with some small agglomerates using 178 μm pore size of mesh. As discussed earlier in the Figures 3.15b and 3.16a (see section 3.4.2.4), the application of mesh pore size presents a good control of the size distribution of the separated micro-particles and uses to the following experiments for the investigation of the penetration depth of tungsten micro-particles in the skin mimicking agarose gel.

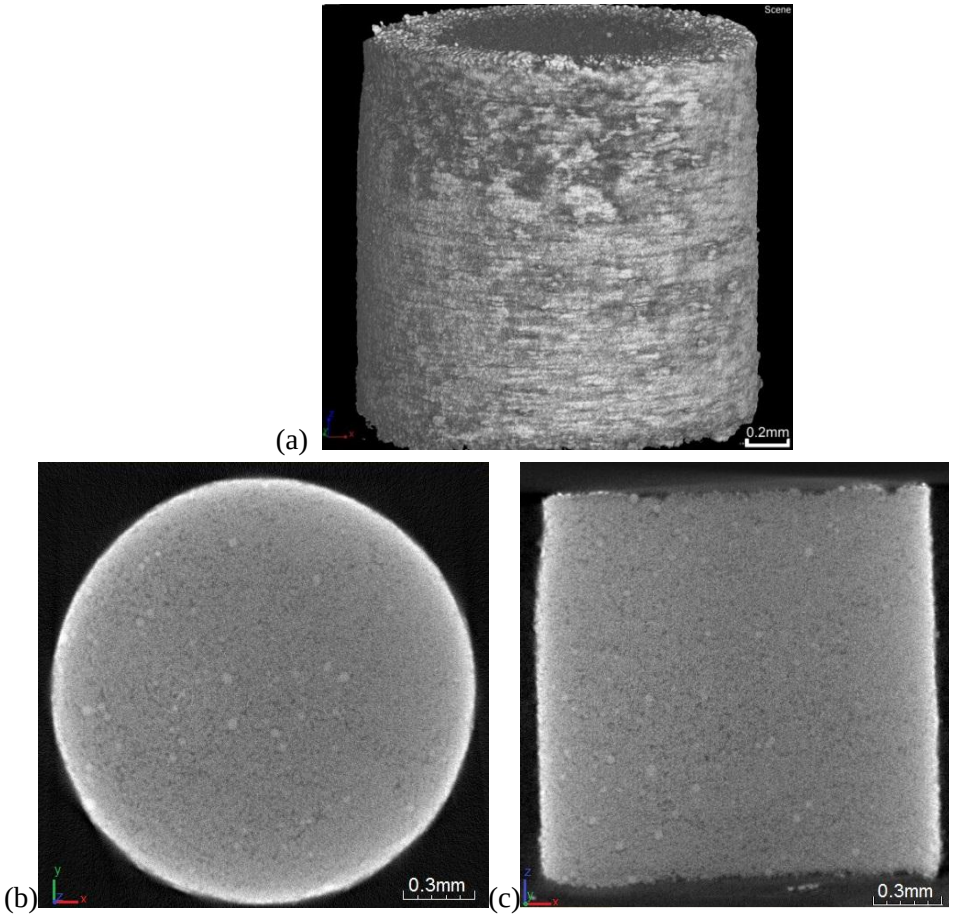

Figure 6.2: Micro-CT images of a stainless steel micro-particle pellet made of 40 mg/ml PVP concentration (a) reconstructed three dimension view of the pellet (b) top internal view across the pellet at the position of 1.08 mm on the z axis (c) side internal view across the pellet at the position of 1.08 mm on the y axis. The images show homogeneity of the packing of the micro-particles

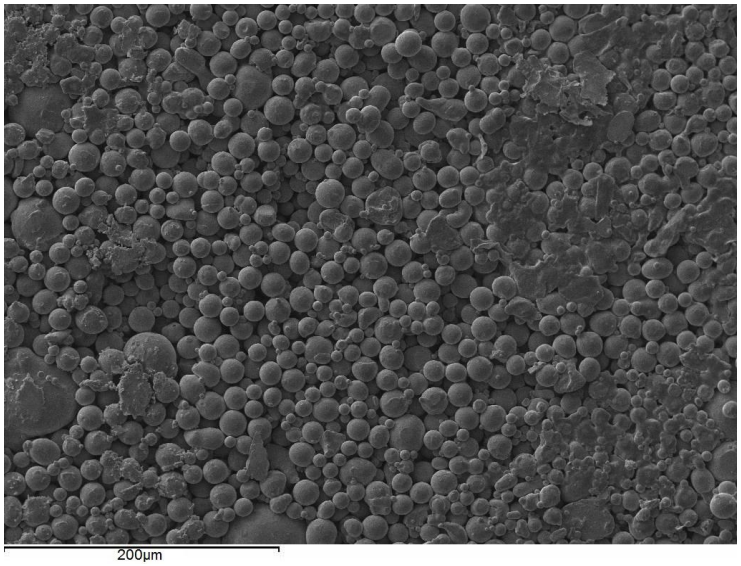

Figure 6.3: SEM image of the top surface of the pellet

6.3.3 Modelling strategy and parameters

In previous chapter, the detailed mathematical principle of the microneedle assisted micro-particle delivery is discussed. MATrix LABoratory (Matlab) is used to build and solve the theoretical model for MN assisted micro-particle delivery. The detailed model behaviour is described previously in the section 5.3.3. Generally, it consists of three main parts including a main program, an event program and two function programs (acceleration and deceleration stage). The main program simulates the whole process of the MN assisted micro-particle delivery. The event program defines the impact points of the micro-particles on the skin, rebound points on the boundary of the gap between mesh and skin and the end points inside the skin. The function programs input the equations, which are used to determine the theoretical results. The function programs are implemented to the main program by choosing a suitable *ode* solver which requires considering the condition of the function program (stiff/non-stiff). In addition, an *if* statement has been used to define the position of the micro-particles and further to confirm the selection of the equations to calculate the theoretical velocity of micro-particles at different position. A *for* statement has been used to repeat the simulation of a number of micro-particles in the deceleration stage.

In the model, human skin is considered as a target for micro-particles in the model. The three main layers of human skin, stratum cornum (SC), viable epidermis (VE) and dermis layers are considered in the model. The detailed skin properties are listed in the Table 5.2. It is worth to mention that the yield stress and density of the dermis layer is considered the same with the

viable epidermis layer. In the Chapter 4, we have used porcine skin instead of human skin to analyse the friction coefficient between particle and skin tissue by using a rotational viscometer with parallel plate geometry. The result will be used in this study, which is shown in Table 5.2. The friction coefficient between particle and each skin layer is treated as the same in the model.

In this case, this model is chosen to analyse the delivery of tungsten micro-particles. In a previous work (section 3.4.2.4), the pellet is shown to be separated into individual particles with a few agglomerates using a mesh and then penetrates into the target. It illustrates that a number of the tungsten particles agglomerated after the separation stage in the experiment. In order to correlate the model with the realistic experiments, a number of tungsten micro-particles are considered to the diameter of tungsten particle are considered to agglomerate together to be 3 μm diameter after the separation stage in the model. The other relevant constants used in the developed model are listed in the Table 5.3, e.g. the size of the experimental rig, particle size and hole size.

6.4 Results and Discussions

The purpose of this section is compare tungsten micro-particle with stainless steel micro-particles for the microneedle assisted micro-particle delivery based on the analysis of the passage percentage and the penetration depth inside target. The maximum penetration depth of micro-particles is analysed in relation to the operating pressure (see section 6.4.2.1) and microneedle length (see section 6.4.2.2). In addition, a theoretical model is used to analyse the penetration depth in relation to above two parameters to compare tungsten particle with stainless steel micro-particle and then to further understand the particle density effect on micro-particle penetration.

6.4.1 Analysis of passage percentage

In a previous study, stainless steel micro-particles is shown to yield a higher passage percentage and a good quality size distribution of separated micro-particles if 40 mg/ml PVP (binder) concentration and a mesh with pore size of 178 μm are used. Here, the pellets of tungsten micro-particles are operated at the same conditions as the previous study of the stainless steel micro-particles and to make a comparison of the passage percentage between those two micro-particles. The passage percentage is analysed in relation to the operating pressure which is varied from 2.4 to 4.5 bar. As shown in Figure 6.4, the passage percentage is increased due to an increase in the operating pressures for each micro-particle. This is

because the pellets gain more momentum at higher operating pressures, which in turn also causes the separated particles to gain more momentum while passing through the mesh. In the Chapter 3, we have indicated that the passage percentage of stainless steel micro-particles reaches a maximum due to some particles sticking to the mesh and some rebounding, hence not passing into the test tube (particle collector). As expected, the tungsten micro-particles show a similar performance to stainless steel. Figure 6.4 shows the passage percentage of tungsten micro-particles is less significant than stainless steel micro-particles. It might be the size of the tungsten particles is too small, which causes the velocity of the separated particles to decrease faster after passage through the mesh and travel in air and stick on the mesh or the gap between mesh and target except the agglomerates.

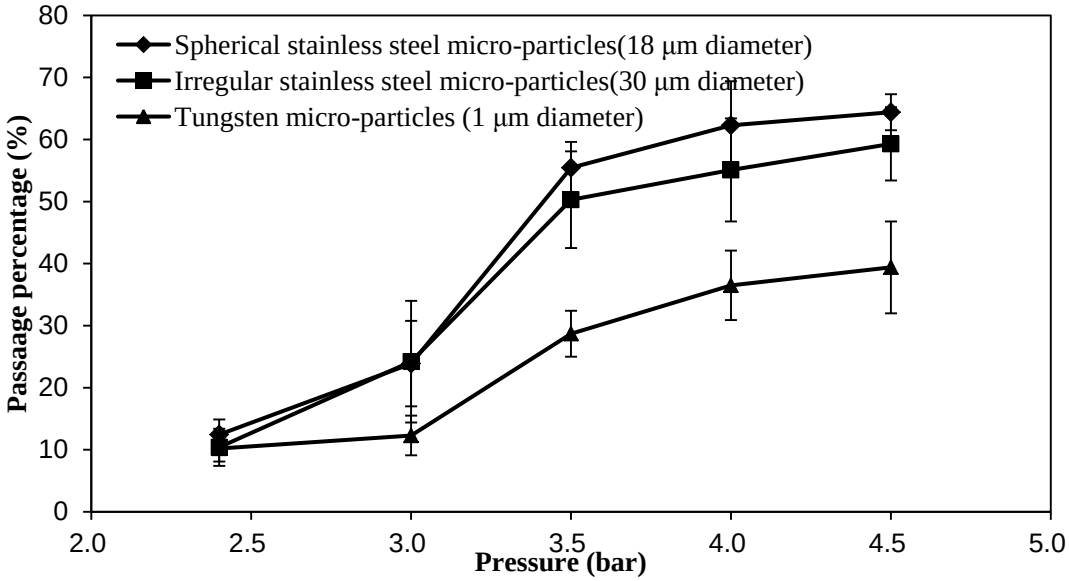

Figure 6.4: The effect of operating pressure on the passage percentage of the pellet separation. Each curve in the figure is generated from three repeats of experiments. (Mesh pore size: 178μm, PVP concentration: 40 mg/ml)

6.4.2 Experimental analysis of the penetration depth of micro-particles

6.4.2.1 Effect of the operating pressure

The operating pressure is shown to be a key variable on the penetration depth of stainless steel micro-particles of 18 and 30 μm average diameters by us in Chapter 4. In this case, we aim to investigate the difference of the penetration depth between the larger stainless steel micro-particle and smaller tungsten micro-particles at various pressures. The tungsten micro-particles cannot penetrate into the skin mimicking concentration of agarose gel. This is because the momentum of the particles is insufficient to breach the surface of the gel. In the experiment, the operating pressures are only kept between 3 to 5 bar which are low for the

small particles to achieve velocity to breach the target. It requires a higher pressure for the small particles to achieve sufficient momentum to penetrate further into the target. In addition, a comparison between tungsten and stainless steel micro-particles is shown in Figure 6.5. As can be seen, irregular and spherical stainless steel particles of 30 and 18 μm average diameters achieve good penetration depths inside the skin mimicking agarose gel. Although the density of the stainless steel is lower than tungsten, larger diameters of stainless steel micro-particles increase their masses which lead to increased momentum of the micro-particles so as to penetrate further in the target (skin mimicking agarose gel). The two micro-particles show that the penetration depths increase due to an increase in the particle size.

To further understand the effect of the particle density and size on the penetration depth in the target, the theoretical model is used to analyse the penetration of above two materials of micro-particles in a same target, which is discussed in the section 6.4.3.2.

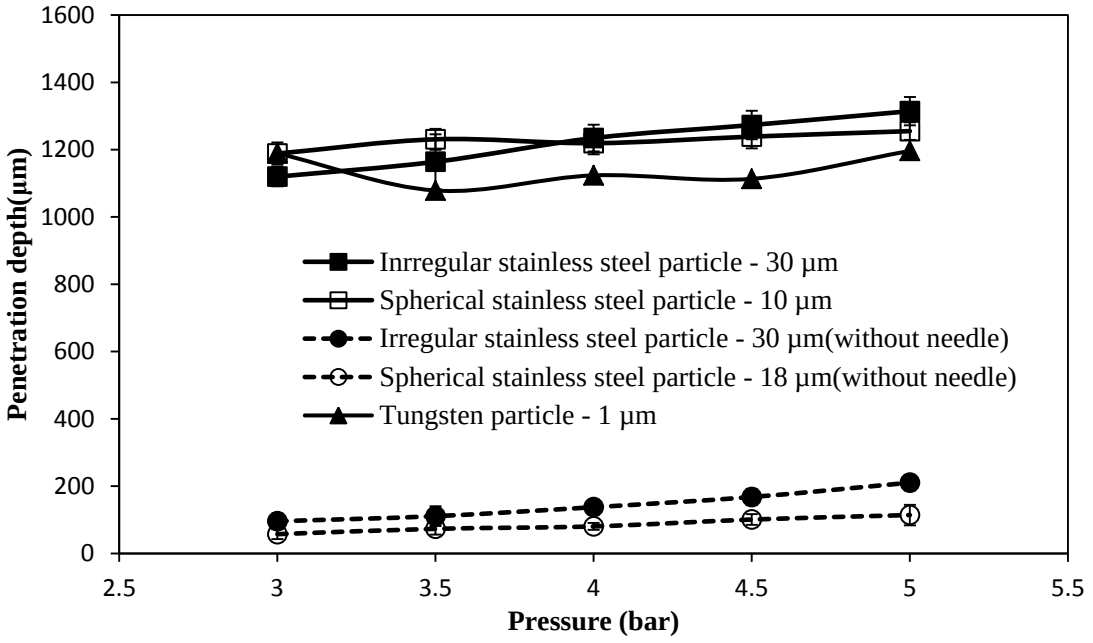

Figure 6.5: The effect of the operating pressure on the penetration depth of different type of particles (Mesh: 178 μm of pore size: Dash line: Particle penetration without using MN; Solid line: Particle Penetration with MN) Each curve in the figure is generated from three repeats of experiments.

When the MNs are inserted into the skin, it is creates holes which remain there after their removal. The micro-particles can be delivered through these holes, thus compensating for the insufficient momentum. As presented in Figure 6.5 the penetration depth of the tungsten particles is greater inside the agarose gel when Adminpatch MN 1500 is used. This is because a number of particles can penetrate through the pierced holes. However, the maximum penetration depth of the micro-particles is varied while the pressure increases from 3 to 5 bar. In a previous work (section 4.4.2), the result of the MN insertion in an agarose gel has shown that the length of the pierced holes is unable to maintain constantly, which varies the maximum penetration depth of the micro-particles inside the target. Thus, the variation in the length of the pierced holes directly affects the penetration depth of the micro-particles. It means that the holes length is a major factor to maximize the penetration depth in the MN assisted micro-particle delivery. The MN length effect on the micro-particle penetration depth is discussed in the section 6.4.2.2 in detail. Figure 6.5 also shows that the penetration depths of those two stainless steel micro-particles are more than the tungsten micro-particles. It indicates that an increased momentum due to increase in particle size/operating pressure of micro-particles affect the penetration depth in the MN assisted micro-particle delivery.

6.4.2.2 Effect of the microneedle length

In previous work (Chapter 4), three different lengths of MNs have used to study the maximum penetration depth differences of stainless steel micro-particles of 18 and 30 μm diameters in a skin mimicking agarose gel. The characterizations of those three MNs are presented in Table 4.1. To further determine the effect of MN length on the penetration depth of small and dense micro-particles, those three MNs are used in this case. Figures 6.6a-b show the penetration of the tungsten micro-particles in the skin mimicking agarose gel based on the assistance of Adminptach MN 1500 and the in-house fabricated MN 750, respectively. As can be seen, the maximum penetration depth of micro-particles after using Adminptach MN 1500 is more than in-house fabricated MN 750, but the number of micro-particles entering the pierced holes is less obvious. This is because a long needle increases the length of pierced holes in the agarose gel, which maximizes the penetration depth of micro-particles. In addition, the diameter of the in-house fabricated MN is greater than the thickness of the Adminptach MN 1500 microneedle (see Table 4.1), which creates wider holes to provide the convenience for particle penetration. It indicates that a desired penetration depth and amount of micro-particles can be controlled by changing the MN length and width for further research.

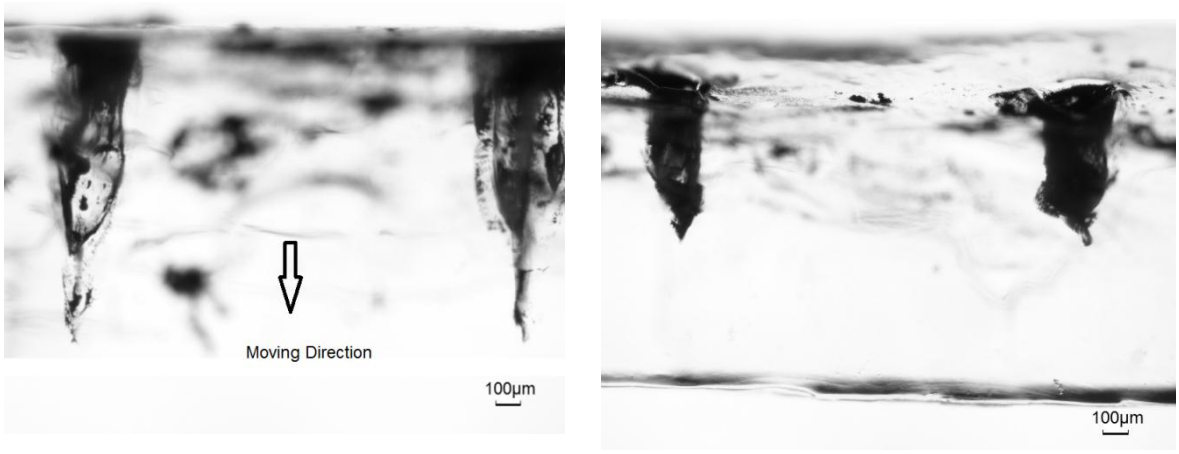

(a) (b)

Figure 6.6: The penetration of tungsten micro-particles in the skin mimicking agarose gel based on the assistance of MNs (a) Adminpatch MN 1500 (b) In-house fabricated MN 750

Previouly, we have fired spherical and irregular stainless steel micro-particles in the skin mimicking agarose gel. The results show that a number of micro-particles penetrated further through the pierced holes (see Figure 4.9). It presents the same effect with the tungsten micro-particles. From Figure 4.9, we have also indicated that the amount of micro-particle in the pierced holes decreases from an increase in particle size. This is because of the hole is reformed after the removal of the MN, reduced the opening area of the hole on the top gel surface and further to affect the micro-particle penetration. In addition, the thickness of the hole is only 78 μm after the removal of Adminpatch MN 1500. It limits the amount of the micro-particles to penetrate into the holes, especially to the large size of irregular stainless steel micro-particles. Thus, the amount of the stainless steel micro-particles that penetrates into the pierced holes is less than tungsten micro-particles if compared with the result in Figure 6.6. However, the maximum penetration depth of each micro-particle is close but related to length of the pierced holes.

The maximum penetration depths of tungsten micro-particles show significant differences between each MN array as shown in Figure 6.7. It increases from an increase in MN length. As expected, a longer MN increases the length of the pieced holes and thereby increases the maximum penetration depth of micro-particles. However, the maximum penetration depth is varied at different operating pressure. This is because the length of the pierced holes is varied after the removal of the MN array. The above results show the advantage of MN assisted

micro-particle delivery which provides a positive effect on the particle penetration even if the momentum of the particle is insufficient to breach the target.

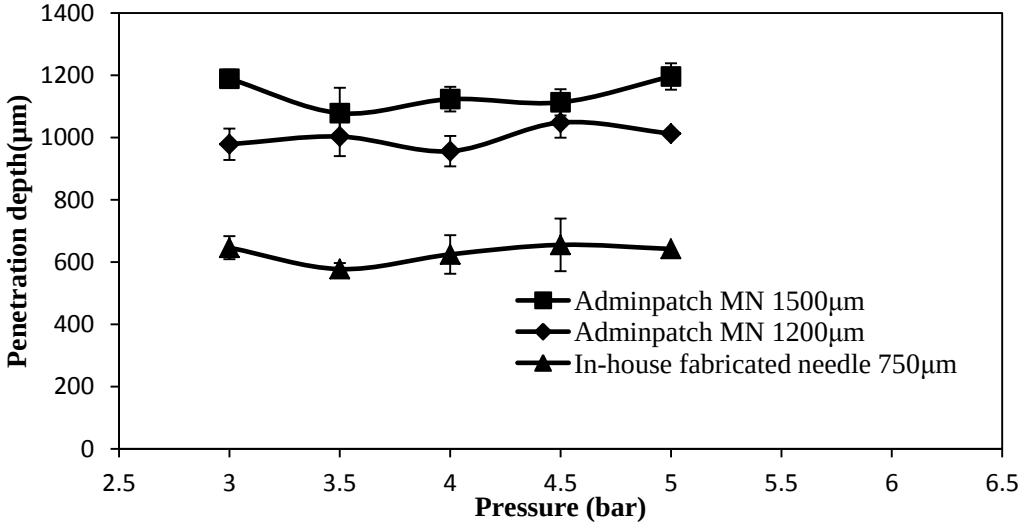

Figure 6.7: The maximum penetration depth of tungsten micro-particles in the skin mimicking based on the assistance of MNs. (mesh pore size: 178 μm) Each curve in the figure is generated from three repeats of experiments.

6.4.3 Modelling the penetration of micro-particles in skin

Firstly, this section aims to understand the microneedle assisted micro-particle delivery based on the modelling of the trajectory of tungsten micro-particles in the deceleration stage. It is worth to mention that the tungsten micro-particle and stainless steel micro-particle may vary in shape and size which may affect results in reality. However, the both the stainless steel and tungsten micro-particles are assumed to be spherical with uniform size (average diameter) in the model. The maximum penetration depth is analysed in relation to the operating pressure, microneedle length, particle size and density to further understand the difference between tungsten and stainless steel micro-particles for the microneedle assisted micro-particle delivery. Finally, a further analysis of the effect of each resistive force on the maximum penetration depth of micro-particles is discussed to verify the main factor which minimizes the penetration depth.

6.4.3.1 Modelling for the delivery of tungsten micro-particles

Figure 6.8a shows the trajectories of increased diameter of tungsten micro-particles in the deceleration stage. The initial positions of the micro-particles are randomly selected at the beginning to mimic the separation of the pellet of tungsten micro-particles. In this case, we

assumed that a number of tungsten micro-particles are stuck together where the micro-particles are spherical in shape and each micro-particle has diameter of 3 μm after the separation stage (mesh). The trajectory is considered to be linear. The velocity decrease is represented by the colour change of the trajectory which corresponds to the colour bar in the figure. The velocity decreases slowly from approximately 135 to 110 m/s from the mesh to the target. Figure 6.8a shows that a number of the micro-particles achieve further penetration depths via the pierced holes. The figure presents the similar performance of the developed model with experimental results. The detailed penetration process of tungsten micro-particles in the skin are shown in Figures 6.8b-c. Figure 6.9b shows the penetration of tungsten micro-particles in the top skin layer of stratum corneum at 5 bar operating pressure. As can be seen, the particle velocity deceases very fast in the stratum corneum due to an increased resistance; the penetration depth is approximately 0.7 μm which could be ignored. Some particles are delivered through the pierced holes and then penetrate into the epidermis/dermis layer of the skin (side surface of the pierced holes), as shown in Figure 6.8c. It shows that the variation of the velocity is changed slightly in the pieced holes and decreased fast after penetrating the skin. It shows a similar performance as the penetration in the stratum corneum due to an increased resistance. Based on the above figures the penetration depth of tungsten micro-particles is negligible in the skin, which matches well with the experimental results.

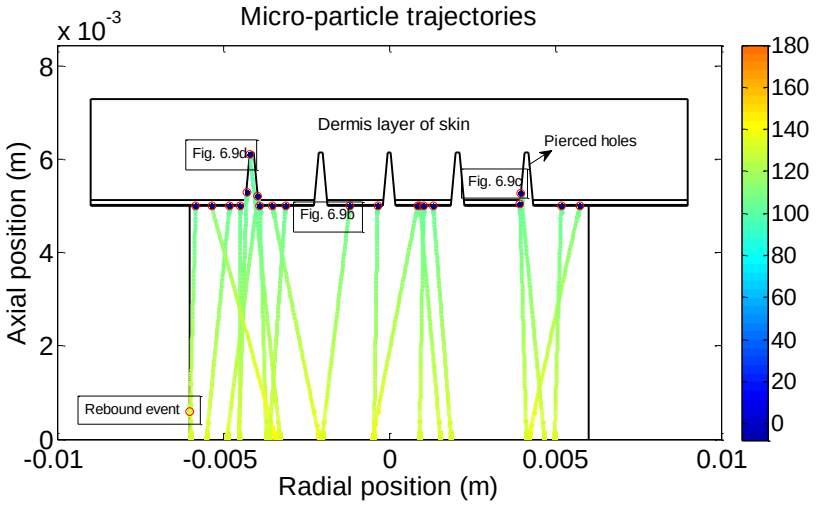

(a)

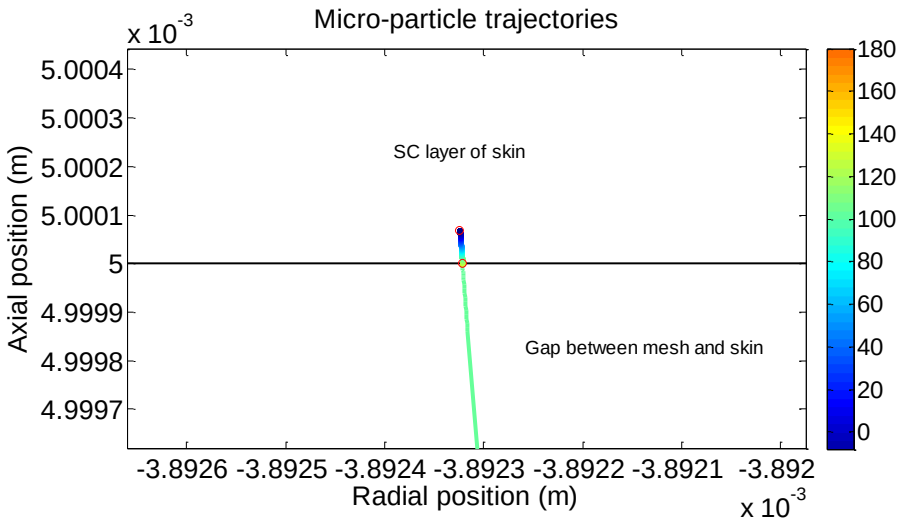

(b)

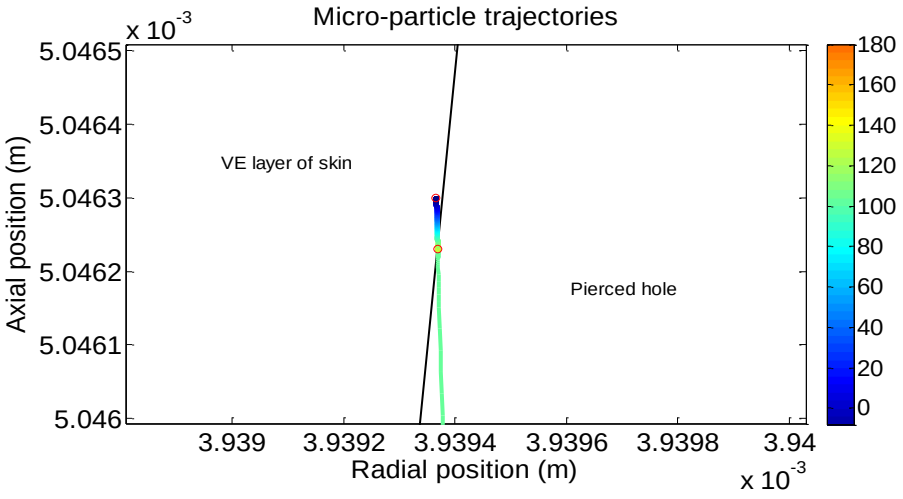

(c)

Figure 6.8: The trajectories of the tungsten micro-particles in the deceleration stage: (a). The overall view of the micro-particle trajectories (b).The particle penetration at the area without needle hole (c).The view of the micro-particle penetrate through the needle hole (pressure: 5 bar)

6.4.3.2 The effect of the operating pressure and particle size on the penetration depth

In the experimental results, the operating pressure only presents a slight effect on the penetration depth of the tungsten micro-particle without using MN. The pressures are varied from 3 to 5 bar, which are too low for small micro-particles when compared with previous gene gun research (Arora *et al*., 2008; Giudice *et al*., 2006; Kendal *et al*., 2004; Mitchell *et al*., 2003). In order to further understand the effect of the operating pressures on the penetration depth of this tungsten micro-particle, the penetration depth is analysed at various operating pressures which range from 3 to 60 bar in the model. As presented in Figure 6.9 the penetration depth of the tungsten particle is increased from 0.04 to 0.28 μm without using

MNs while the pressure varies from 3 to 60 bar. The penetration depth is negligible. It illustrates that the tungsten particle of 3 μm diameter are too small for penetration even if the operating pressure increases to a great value. Figure 6.9 also shows the tungsten particle achieves a great penetration depth after using MNs. However, the penetration depth is increased slightly from an increase in operating pressure.

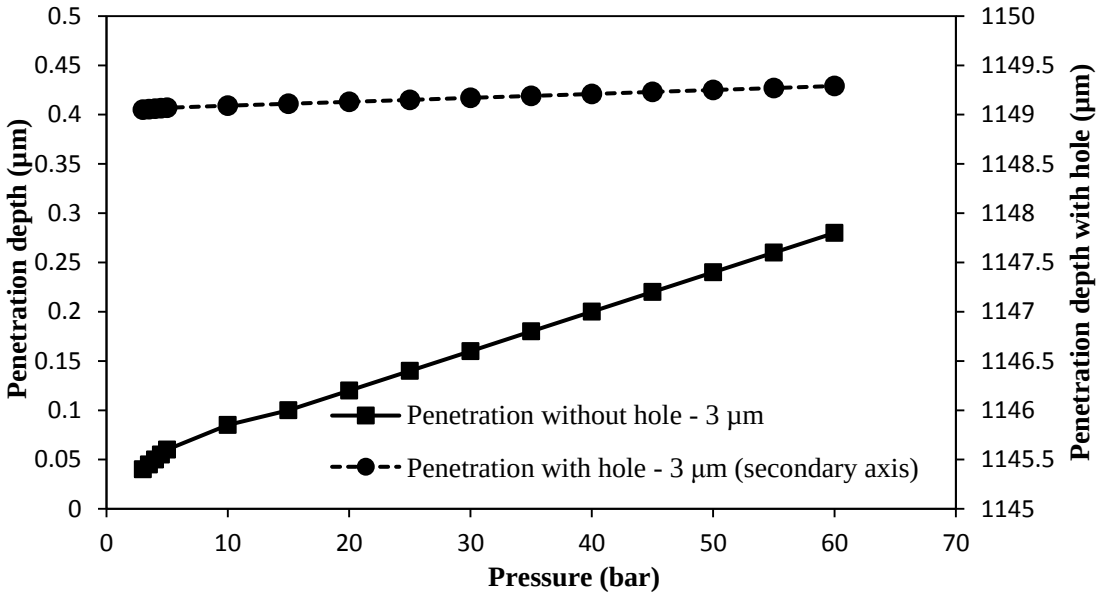

Figure 6.9: The effect of the operating pressure on the penetration of tungsten particle

To further understand the effect of particle size and density on the penetration depth, the particle is assumed to be spherical in shape with uniform size and the particle diameter is varied from 3 to 100 μm for both stainless steel and tungsten micro-particles using the presented model. As presented in Figure 6.10 the penetration depth of tungsten micro-particles increases from 0.07 to 65.61 μm in the skin without using MNs and from 1149.07 to 1214.61μm using Adminpatch MN 1500 at 5 bar pressure. It shows more penetration depth than stainless steel which only penetrates 0.02 to 17.36 μm in the skin and 1149.02 to 1170.5 μm using a same MN as tungsten while the particle diameter ranges from 3 to 100 μm. This comparison directly shows the advantage of dense particles on the penetration in the target for gene gun systems.

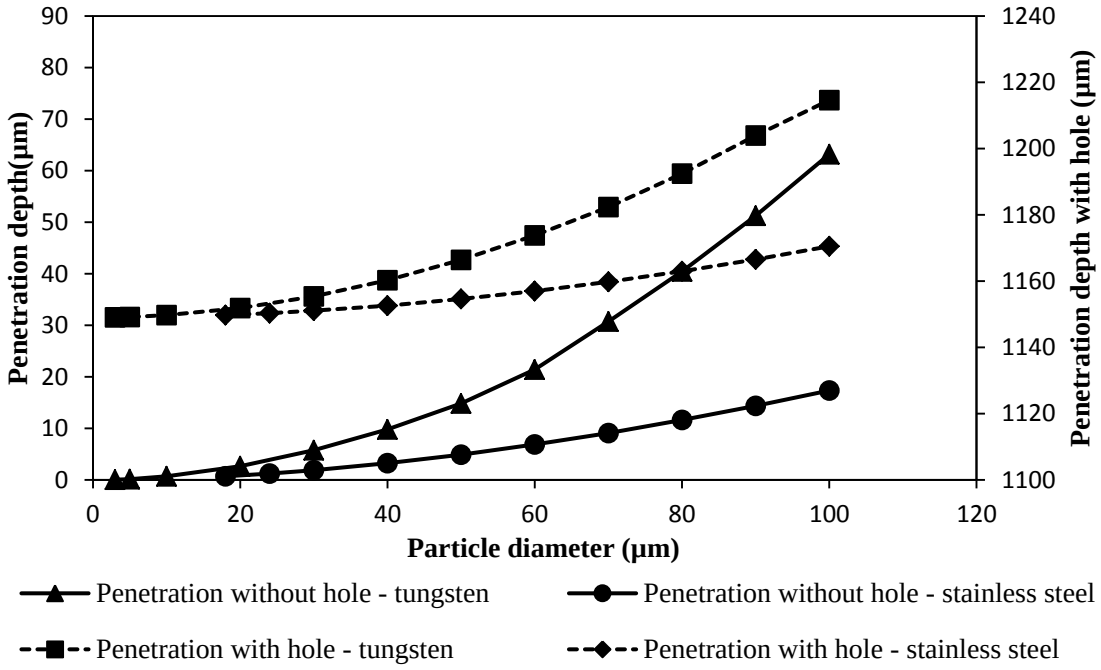

Figure 6.10: The effect of the tungsten particle size on the penetration depth (operating pressure: 5 bar)

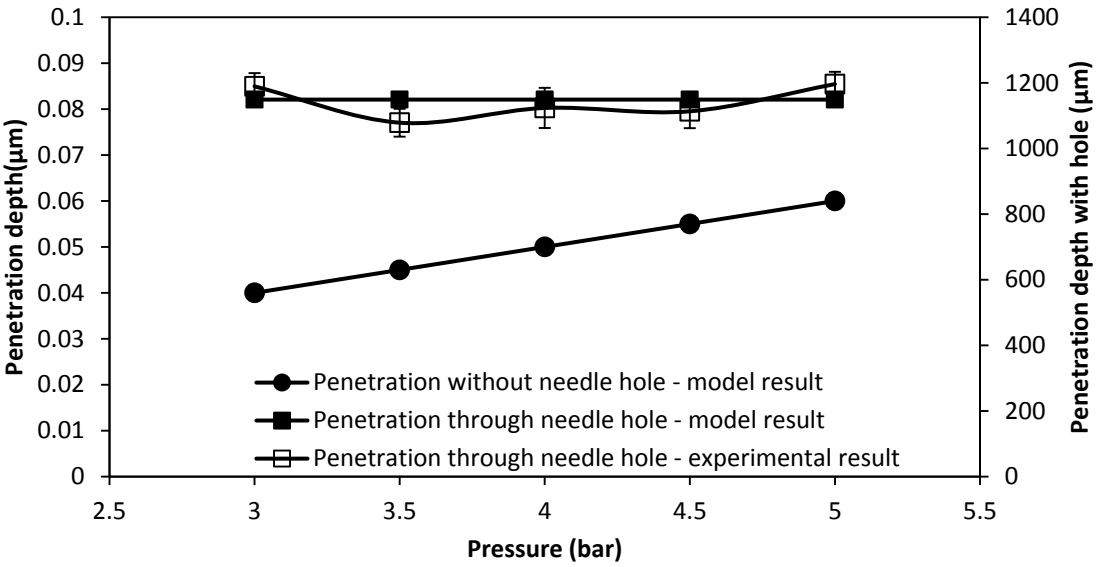

Figure 6.11: A comparison of penetration depth between model and experimental results (particle type: tungsten micro-particle of 3 μm diameter). The experimental results in the figure are generated from three repeats of experiments.

A comparison of the penetration depth of the tungsten micro-particles (3 μm) between model and experimental results is shown in Figure 6.11. It is worth to mention that the difference between experiment and modelling may be due to the assumption that the particle shape of

the tungsten particle is regular after the separation stage in the model. As can be seen, the tungsten particle penetrates less than 0.1 μm without using MN for the model result. It matches well with the experimental results which show the tungsten micro-particles cannot penetrate into the skin mimicking agarose gel. However, this condition can be made up by using MNs. As presented in Figure 6.11 the tungsten micro-particles reaches a further depth using Adminpatch MN 1500, but the maximum penetration depths are varied at pressure ranges from 3 to 5 bar. This is because it is not possible to ensure that the length of the pierced holes is constant each time using the same MN. As expected, the model results match well with the experimental results. In conclusion, the maximum penetration depth of tungsten micro-particles is directly related to the length of the pierced holes, and the operating pressure only presents a slight effect on the penetration depth in this case. To further understand the effect of pierced holes on the penetration depth of tungsten micro-particles, three different lengths of MNs (see Table 4.1) have used and discussed in the following section.

6.4.3.3 The effect of the microneedle length

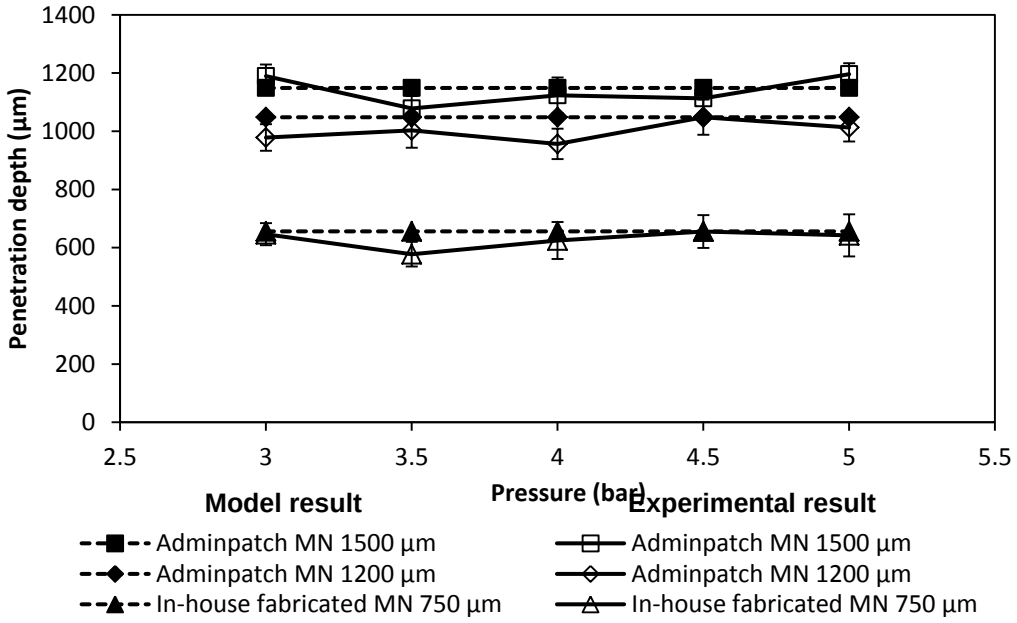

Figure 6.12: The effect of the microneedle length on the maximum penetration depth of the tungsten particle (operating pressure: 5 bar; particle type: tungsten micro-particle of 3 μm diameter). The experimental results in the figure are generated from three repeats of experiments.

In the real experiments, some tungsten micro-particles may be agglomerate after the separation stage. However, any effects of the particle agglomeration on the model results are not accounted for directly at this moment. This may be the reason why there are some differences between the experimental and modelling results; however, all comparison have produced reasonable match between the experimental and modelling results. In section 4.4.3.3, the experimental results have shown that the length of pierced holes has a greater effect on the maximum penetration of stainless steel particles, which is related to the MN length. As expected, it agrees with the results of tungsten micro-particles show in the Figure 6.12. As can be seen, the maximum penetration depth of tungsten micro-particles seems to be increased with an increase in the MN length. In principle, the length of pierced holes is directly related to the MN length which maximizes its length. An increased length of the pieced holes allows a number of micro-particles which deliver into the holes to penetrate further inside the target and maximizes the penetration depth. As expected, the experiment results are varied for each application of MNs due to difficulties maintaining a constant hole length. However, the model results match well with the experimental results, which illustrate the applicability of the model for MN assisted micro-particle delivery.

6.4.3.4 Dependence of particle penetration depth to particle size and density in relation to the resistive forces in the dermis layer of the human skin

The skin properties vary with one person to another, e.g., the gender, age, race and the various anatomical areas of the body of the same person (Xu *et al.*, 2007; Vexler *et al.*, 1999). As discussed earlier, the penetration depth of micro-particles is related to the yield force (F_y), a frictional resistive force (F_f) and a resistive inertial force of target material (F_i) which decelerate the high-speed micro-particles inside the target (see equation 5.15). However, the yield force depends on the yield stress of the target (see equation 5.18). Further, the resistive inertial force is related to the friction coefficient between particle and target (equation 5.16) and the frictional resistive force depends on the density of the target material (equation 5.17). In view of these inter-dependencies which in turn affect the micro-particle delivery, this section aims to analyse the effects of each force on the penetration depth of micro-particle to further investigate the major factor which presents a greater effect on the penetration depth.

For the MN assisted micro-particle delivery, the main point is the maximum penetration depth of the micro-particle in the skin. As discussed already, a number of the micro-particles penetrate through the holes made by the MNs to the dermis layer of the skin. In order to

investigate the effect of each force on the maximum penetration depth of micro-particle, we assume that the micro-particles penetrate into the dermis layer at the tip area of the hole to obtain the maximum penetration depth of micro-particles. In addition, we kept one of those three resistive forces as constant and ignored the other two forces to analyse the variation of the penetration depth in the model. As shown in Figure 6.13, stainless steel micro-particle penetrated further than the tungsten particle due to the difference in particle size. Figure 6.13 also shows that the frictional resistive force provided a minimum effect on the micro-particle penetration. The effect of the yield force on the penetration depth is greater than the frictional resistive force. However, the major factor is the resistive inertial force which causes the penetration depth of micro-particles is almost negligible if the hole length (1149 μm) is subtracted.

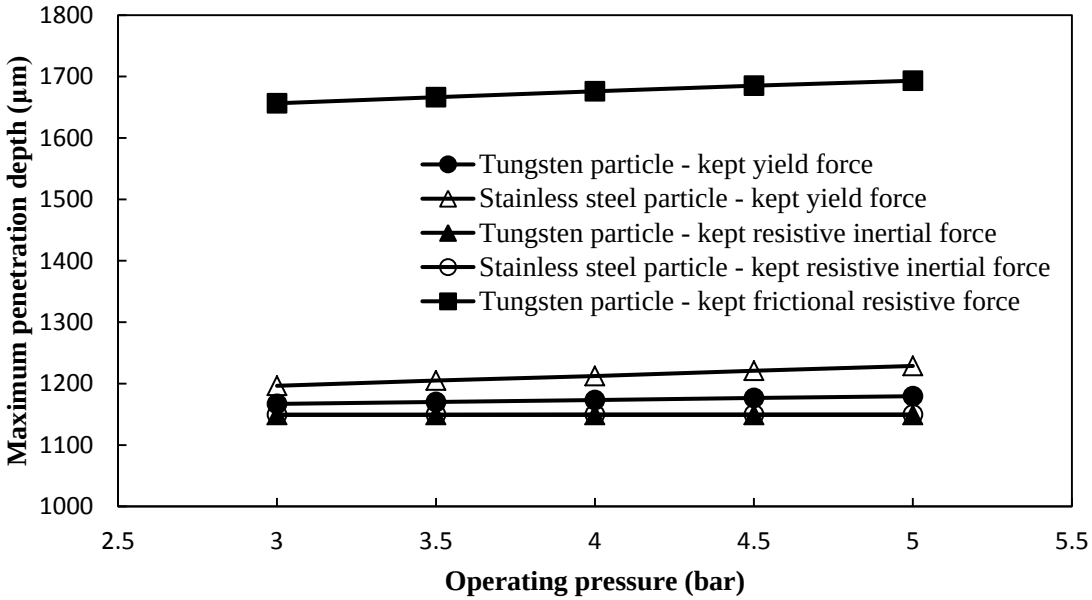

Figure 6.13: The effect of each resistive force on the maximum penetration depth of micro-particles (stainless steel particle: 18 μm diameter; tungsten particle: 3 μm diameter; Hole length: 1149 μm)

As discussed earlier, the resistive inertial force is a major component that determines the penetration depth of micro-particles for the gene gun based micro-particle delivery. Friction coefficient between particle and target directly affects the resistive inertial force. In order to further understand the effect of the resistive inertial force on the particle maximum penetration depth, the theoretical model is used to simulate the effect of varying the friction coefficient between particle and dermis layer from 5 to 19.6 MPa where we kept the yield

stress and density (see Table 5.2) and the hole length constant and operated the system at 5 bar operating pressure. As presented in Figure 6.14, the maximum penetration depth decreased from an increase in friction coefficient between particle and dermis layer. This is because an increased resistive inertial force slows down the particle velocity rapidly. Figure 6.14 also shows that the effect of a decreased friction coefficient between particle and dermis layer on the maximum penetration depth is increased from an increase in particle size and density due to an increased momentum. The maximum penetration depth of small micro-particle (tungsten particle of 3 μm diameter) is kept to approximately a constant when the friction coefficient between particle and dermis layers is changed.

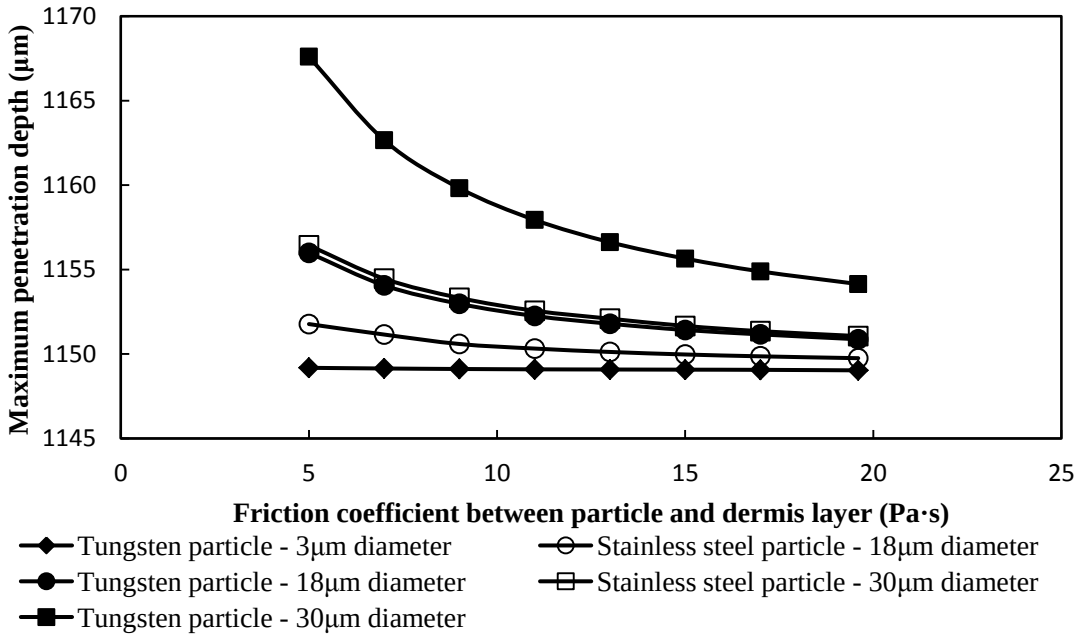

Figure 6.14: The effect of the friction coefficient between particle and dermis layer on the maximum penetration depth of micro-particles (operating pressure: 5 bar; hole length: 1149 μm)

6.4.3.5 Further Discussions

A comparison between stainless steel and tungsten micro-particles on the penetration depth in the skin mimicking agarose gel has been made in this study. Tungsten micro-particles are unable to penetrate the skin mimicking agarose gel / skin without using MN in the experimental result, which is different from the results of stainless steel micro-particles. The reason is that the diameter of tungsten micro-particles is less than 1 μm which is too small when compared with the stainless steel micro-particles of 18 and 30 μm diameters. As a result the momentum of the tungsten micro-particles is too low to allow the particles to breach the

gel surface. In section 3.4.1.1, the velocity of ground slide is measured which only reaches around 122 m/s at 5 bar pressure, using a photoelectric sensor, which means that the particle velocity is less due to the energy loss. This velocity is less than some previous studies for gold particles, e.g. Kendal (2001) has investigated that 1 ± 0.2 μm diameter of gold particles can reach a velocity of 580 ± 50 m/s at 40 bar pressure using a contoured shock tube (CST). The ground slide presents a significant negative effect on the particle velocity, but it has safety advantage which prevents the pressurized gas from impacting the human body. Thus, the operating pressure is mimicked from 3 to 60 bar to study the penetration differences of tungsten micro-particles after increases the momentum in the theoretical model. However, these tungsten micro-particles still cannot achieve the expected penetration depth. It indicates that a ground slide based gene gun system is not useful for the intercellular route because micro-particles cannot reach velocities high enough to breach the skin. Increasing the particle size will increase the moment but cause damage to the surface of the skin. As a result the extracellular route is the expected solution for normally ground slide based gene gun system.

However, the use of MN meets the purpose of an intercellular route to deliver micro-particle to a greater penetration depth in the skin using a ground slide based gene gun system. Previously, The experimental results have shown that the penetration depth of stainless steel micro-particles is increased while using a MN (see section 4.4.3). In this case, the tungsten micro-particles are investigate using modelling and experiments with MN assisted micro-particle delivery. As expected, both model and experimental results show that the use of MN maximizes the penetration depth of tungsten micro-particles. However, the maximum penetration depth of micro-particles depends on the length of pierced holes which is created by MNs. The maximum penetration of tungsten micro-particles reaches around 1149 μm using Adminpatch 1500 MM, which never reach for other relevant gene gun system. For example, Kendal (2001) has indicated that gold particles of 1 ± 0.2 μm diameters can penetrate 66 μm in the skin at velocity of 580 ± 50 m/s using a contoured shock tube (CST). Kendal *et al*. (2004) have also used a convergent-divergent device to accelerate 1.8 μm diameter gold particles which achieves a maximum penetration depth of 78.6 μm at 60 bar. Mitchell *et al*. (2003) has shown that gold particles of 1-3 μm diameters can reach a maximum depth of around 60 μm in canine tissue at a velocity of 550±50 m/s. It is concluded that the diameters of gold particles ranges from 1 to 3 only can penetrates to a depth from 60 to 78.6 μm (epidermis layer) which is less than the maximum penetration depth of the tungsten particles after using MNs. It shows that the improvement of the penetration depth

using MN assisted micro-particle delivery, which achieves depths never reached before. In conclusion, the results show that the intercellular route is feasible for the MN assisted micro-particle delivery. In theory, it is the preferred route for MN assisted micro-particle delivery due to the cell damage is minimized from a decrease in particle size (O'Brien, 2011), although extracellular route presents more penetration depth. It could be proved by firing the above stainless steel/tungsten micro-particles into cell cultured skin mimicking agarose gel to analyse the cell damage in the further work.

6.5 Chapter Summary

This study shows an effective method for relating the use of MNs to create holes on the target for micro-particle delivery to improve the penetration depth of micro-particles. The experimental rig considers possible changes in the operating pressure to analyse the penetration depth and passage percentage of tungsten and stainless steel micro-particles. Results show that the passage percentage increases due to an increase in operating pressure until a maximum value. Tungsten micro-particles used in this study present a lower passage percentage than stainless steel due to an insufficient momentum to reach the target (particle collector). In addition, tungsten micro-particles are stopped by the skin mimicking agarose gel even if the operating pressure is increased. But an increased operating pressure improves the penetration of stainless steel particle without using MNs. This is because the diameter of tungsten micro-particles is small (< 1 μm). To further understand the particle size and density effect on the penetration depth, a theoretical model is used to mimic the operating pressure ranges from 3 to 60 bar to accelerate tungsten and stainless steel micro-particles while the diameter ranges from 3 to 100 μm. The results show a great improvement in the penetration depth of tungsten micro-particles which is more than stainless steel micro-particles. However, both model and experimental results show that a use of MNs provides an improvement on the penetration although the momentum is insufficient to breach the skin. The maximum penetration depth of micro-particles up to dermis layer has not been reached before. It is related to length of MNs which determine the length of pierced holes. As expected, model results matches well with the experimental results, which illustrates the applicability of the model for the MN assisted micro-particle delivery. MN assisted micro-particle delivery improves safety because an intercellular route can be chosen to reduce the damage from particle impact and the pressurized gas is prevented by the ground slide. In addition, it also enhances the penetration depth of micro-particles properly if compared with any other gene gun systems. An increased penetration depth allows deeper tissue to be transfected, which

provides more effective gene transfection in the target. Future work could be to attach the genes on the micro-particles, fired into the cells using MN assisted micro-particle delivery and then analyse the DNA profile of the cells to verify the advantage of MN assisted micro-particle delivery.

7. Conclusions and Further works

7.1 Conclusions

Gene gun systems are advanced and flexible devices for the researches of genetic engineering, molecular biology and gene therapy, which can be operated in various operating pressures and particle properties (e.g. size, density). They could be used to vary the particle velocity and penetration depth to achieve the purpose of DNA transfection in the desired area of target (e.g. skin, plants). This offers the advantage of delivering genes to the target cells through varying the operating pressure or particle properties. However, cell death is inevitable because of the impaction of the pressurized gas and micro-particles on the tissue. In this study, a new concept which combines microneedle (MN) with gene gun system for micro-particle delivery, namely, MN assisted micro-particle delivery, is pointed out. It is expected to reduce the cell damage and enhance the penetration depth in the target. The developed conceptual system uses a ground slide to prevent the pressurized gas and slow down the velocity of micro-particles to reduce the impact force on the target to achieve the purpose of cell damage reduction. An improvement is proposed by using an array of MNs to overcome the target barrier to allow a number of micro-particles penetrating further through needle holes to let deeper tissue to be transfected.

To confirm the proposition of MN assisted micro-particle delivery, an experimental rig is designed, which consists of three stages, namely, particle acceleration, separation and deceleration stages. Well-defined experiments are conducted to determine the practicability of the concept for each stage. For the first stage, the velocity of the ground slide is analysed in relation to the material, barrel diameter and operating pressure. The results show that micro-particle velocity is increased from a decrease in material density and barrel diameter and an increase in operating pressure. It indicates that the velocities of the particles are definitely slower than other gene gun systems (e.g. contoured shock tube (CST), PowderJect). In addition, the pressurized gas is almost prevented by the ground slide in the experiments. These results suggest that cell damage is possibly reduced using this system. Certainly, it would require one to use the method of MN assisted micro-particle delivery to deliver genes coated micro-particles into cells to confirm the conditions of the gene expression and cell damage in the further work.

For the separation stage, the work shows that it is possible to compress the micro-particles into a cylindrical pellet using an in house pellet press for the purpose of facilitated loading it

in the ground slide. Various concentrations of binder (PVP) can be used to form different strengths of pellets and fire them at various pressures to obtain different passage percentage. The work also confirms that it is possible tp optimize binder concentration for MN assisted micro-particle delivery.

In the work various pore sizes of meshes are used to separate the pellets in the experiment. Results show that the passage percentage is increased from an increase in operating pressure and mesh pore size and a decrease in binder concentration. However, large agglomerates are not desirable because of it may cause significant damage to the target tissue.

The results in this work show that the size of separated particles is controllable using various pore sizes of meshes. Larger pore size of mesh allows large agglomerates to pass through with higher pellet passage percentage. A decrease in mesh pore size blocks the agglomerates but decrease the passage percentage. In addition, higher binder concentration enhances a number of agglomerates. Based on the consideration of the passage percentage and the size distribution of separated particles, pellets bound with 40 mg/ml PVP yielded a higher passage percentage and a good control on the size distribution of separated particle based on the application of 178 μm pore size mesh. Therefore, 40 mg/ml binder concentration and mesh of 178 μm pore size are considered to our following works.

For the deceleration stage, a skin mimicking agarose gel (0.0265 g/ml) is used as a target instead of the human skin in the experiment. Three different lengths of solid MNs are used to study the MN assisted micro-particle delivery. In the early stage, stainless steel of 18 and 30 μm average diameters are analysed to confirm the feasibility of MN assisted micro-particle delivery. The penetration depths of micro-particles in the skin mimicking agarose gel are analysed in relation to the operating pressure, mesh pore size, particle size and MN length. Results show that the penetration depths of micro-particles increase from an increase of the above four variables. In particular, the MN length is shown to be a dominant variable which maximizes the penetration depth of the micro-particles. However, large pore size of mesh is not accepted because of a significant damage presents on the target because of the agglomerates, but the pellet is almost separated into individual particles and penetrated into the gel without showing damages when a small pore size of mesh is used. The pierced holes created by MNs have been found to allow a number of micro-particles penetrating further in the target. It indicates that the MN assisted micro-particle delivery is useful where the damage

of the target from the gas/particles is reduced and a number of micro-particles reach the desired depth more easily.

To further understand the MN assisted micro-particle delivery, a mathematical model is built on the basis of the experimental rig. The equations are implemented into MATLAB using ode function, which mimic the operation processes of acceleration, separation and deceleration stages of the rig. As expected, model results of the ground slide veolcity match perfectly with the experimental results. In addition, the trajectories of micro-particles in the deceleration stage are simulated from a random selection of the initial position and moving direction after the separation stage, and the velocity variation of micro-particles is defined by using colormap function in the model. An event program is implemented into the model to define the impact points and final positions of micro-particles in the deceleration stage. The model mimics the deceleration stage to predict the linear trajectories of micro-particles to determine the distribution of the micro-particles in the three layers of skin. As expected, model results show increasing the operating pressure, particle size and hole length would increase the penetration depth of the micro-particle inside skin, which matched well with the experimental results for the penetration depth of micro-particles.

Finally, tungsten micro-particle of 0.5 μm average diameter is analysed to compare with stainless steel micro-particles. Results show that the passage percentage increases from an increase in operating pressure until reaches a maximum value, but tungsten micro-particles present a lower passage percentage than stainless steel due to its momentum is insufficient to reach the target (particle collector). In addition, tungsten micro-particles are fired into skin mimicking agarose gel at various pressures. Results show that tungsten micro-particles are unable to penetrate into the skin mimicking agarose gel without using MNs, but great amounts of micro-particles are penetrated through the pierced holes to reach an enhanced penetration depth inside the gel. Additionally, the mathematical model simulates the penetration of the tungsten micro-particles in the skin, which also results those micro-particles cannot penetrate into the skin but reach a further depth inside skin via the holes. As expected, model results matches well with the experimental results, which illustrates the applicability of the model for the MN assisted micro-particle delivery.

In conclusion, MN assisted micro-particle delivery is a safe method which promises much to deliver gene loaded micro-particles into cells with less tissue damage because of the

pressurized gas is prevented and the velocity of micro-particles is deceased. Especially, tungsten particles of 0.5 μm diameter can deliver to a further penetration depth in the skin mimicking agarose gel based on this method, which can predict the practicability of this new concept for micro-particle delivery. In addition, the maximum penetration depth of micro-particles is enhanced properly if compare with any other gene gun systems (e.g. CST, Helios gene gun), which allows deeper tissue to be transfected to provide more effectively gene expression in the target. In the furfure work, genes will be attached on the micro-particles which are fired into the cultured cells to analyse the DNA profile to verify the reduction of cell damage. The detailed work proposal is discussed in the following section of further works.

7.2 Further works

This research points out a new concept of microneedle (MN) assisted micro-particle delivery for gene gun systems. A set of well-defined experiments has been processed to show that the use of ground slide prevents the pressureized gas to impact on target and slows down the velocity of micro-particles, which aims to reduce the cell damage. The use of MNs can enhance the penetration depth of micro-particles, which allows deeper tissue to be transfected if DNA is attached to the micro-particles. Thus, further studies could fire DNA (e.g. plasmid) coated micro-particles into the cultured cells to explore the DNA transfection and cell damages to verify the advantage of MN assisted micro-particle delivery. Therefore, an effective method for cell culture and DNA coating on the micro-particles are necessary to consider.

Several studies have shown the preparation of DNA coated golden micro-particles for Helios gene guns (O'Brien and Lummis, 2011; Svarovsky *et al*., 2008; O'Brien and Lummis, 2006; Thomas *et al*., 2001). Two chemical, namely, spermidine and calcium chloride, are required to coat DNA on micro-particles. Spermidine can wrap the DNA to form a protective layer (Mertens *et al*., 2011). Calcium chloride ($CaCl_2$) would play the function like a binder to stick DNA onto the micro-particles (Hall, 1990). Thomas *et al*. (2001) have introduced the detailed procedure to prepare DNA coated micro-particles as: micro-particles require washing by 100% ethanol about three times to remove the impurities, and then DNA, spermindine and calcium chloride are added and vortexed vigorously to make sure that DNA are even distributed in the suspension. After that, the ethanol is requires to remove to get totally dried DNA coated micro-particles. A future work can use a similar method to coat DNA onto the micro-particles.

In our research, micro-particles should be compressed into a cylinder pellet. Thus, we can add PVP solution on the dried DNA coated micro-particles and then compress into a pellet. The detailed pellet making pressure is described in the section 3.3.3.3.

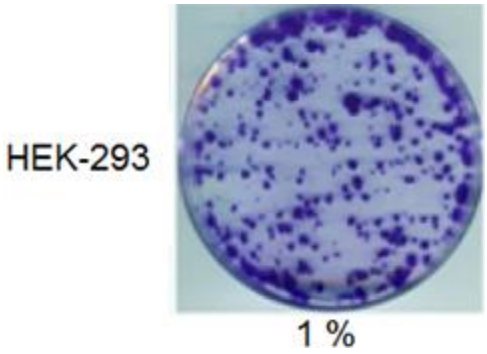

Figure 7.1: HEK-293 cells culture in agarose-medium gel (Yang *et al*., 2009)

Cell culture is a technology to grow cells outside the natural environment at controlled conditions. Culture medium is firstly required to consider for the growth of cells, which can be separated into two types are liquid and solid culture media. For liquid culture media, cells are required to maintain at specific conditions in a cell culture media, e.g. Dulbecoo's Modified Eagle's Medium (DMEM) which often used for cell maintenance (O'Brien and Lummis, 2011; Yang *et al*., 2009; Napolitano *et al*., 2007). For example, Yang *et al*. (2009) have maintained cells in the DMEM media at 37 ℃ in a humidified incubator supplied with 5% CO_2. O'Brien and Lummis (2011) have maintained HEK293 cells in DMEM/F12 at 7% CO_2. Solid culture media forms by adds a certain volume of coagulant in the liquid culture media. Agarose gel is the most common coagulant used for the solid culture media (Yang *et al*., 2009; Napolitano *et al*., 2007). Figure 7.1 shows HEK-293 cells culture in 1 % of agarose-medium gel. Previously, a skin mimicking agarose gel is found in our research, thus, we can mix liquid culture media with skin mimicking concentration of agarose solution and pour into petri dish to solidify to provide an agarose-medium gel to culture cells. A further task of delivering DNA coated micro-particle into the skin mimicking agarose-medium gel to analyse the DNA transfection and cell damage for MN assisted micro-particle delivery is necessary, the results will be compared with other relevant biolistic transfection in skin/cultured cells (e.g. CST, Helios gene gun) to prove the advantage of MN assisted micro-particle.

However, the cell viability requires the supplements of the nutrition and moisture to cells. In addition, Yang *et al*. (2009) have indicated that the cell viability is different at various

concentration of agarose gel. The work found 1 % agarose gel is the optimal concentration to cover cells at room temperature for 1 to 3 days. Thus, a project of using MN assisted micro-particle delivery method to deliver DNA coated micro-particles into different concentrations of agarose-medium gel to obtain the optimal concentration for DNA transfection will be considered in the further works.

As discussed in the thesis, MNs present a great effect on the maximum penetration depth of micro-particles. The quantity of micro-particles in the pierced holes is related to the particle size and the opening area of the pierced hole. Previously (section 4.4.3.2), The experimental results have shown that the amount of micro-particles goes into the holes is decreased from an increase in particle size when Adminpatch MNs (1500/1200) is used. However, the amount is increased from an increase of the opening area of the holes which is related to the geometry of the MNs. Generally, an increased amount improves the effect of DNA transfection on the target area. In addition, an increase in MN number may increases the particle number goes into the holes in theory. Thus, a task of changing the geometry (e.g. cross-section area, MN number) of MNs is necessary to analyse the effect on the amount of micro-particles penetration through the pierced holes if the length of MNs is fixed.

In addition, the effect of DNA transfection and cell damage requires to consider when the amount of micro-particles goes into the target is increased. In theory, an increased particle amount is increased the number of cells to be transfected in the target area if micro-particles are coated with DNA (e.g. plasmid). However, a great amount of micro-particles impacts on the target and goes into the pierced holes may cause damages on the target area due to the some particles are penetrated closely as a large particle on the target during the penetration process. Thus, a task of analysing the cell damage and DNA transfection varies with the amount of DNA coated micro-particles in different locations of target area is required in the further work.

It is worth to mention that the current system size of MN assisted micro-particle delivery is too large and difficult to handle, which is differed with other hand-hold gene gun systems (e.g. InjectionJet). Thus, minimize the MN assisted micro-particle delivery system is necessary for the mass production and further to the practical application to daily life in the future. The work can be achieved based on the theoretical model which varies the dimension of the system to analyse the particle velocity and penetration depth whether achieve the desired

effect to verify the suitable size for the MN assisted micro-particle delivery system. However, good-looking appearance and simple operation of the system design is an indispensable part for the production in the future.

8. References

Ahlen G., Sallberg M., Frelin L., (2013). Methods for monitoring gene gun-induced HBV- and HCV-specific immune responses in mouse models, *Methods Mol. Biol.*, **940**:239-267

Alexander H., Cook T., (2006). Variations with age in the mechanical properties of human skin *in vivo*, *J. Tissue Viability*, **16**(3): 6-11

Al-Qallaf B., Das D.B., Mori D., Cui Z.F., (2007). Modelling transdermal delivery of high molecular weight drugs from microneedle systems, *Philosophical Transactions of The Royal Society A*,, **365**: 2951-2967, DOI: 10.1098/rsta.2007.0003.

Al-Qallaf B. and Das D.B., (2008). Optimization of square microneedle arrays for increasing drug permeability in skin, *Chemical Engineering Science*, **63**: 2523-2535, DOI: 10.1016/j.ces.2008.02.007.

Al-Qallaf B. and Das D.B., (2009a). Optimizing microneedle arrays for transdermal drug delivery: Extension to non-square distribution of microneedles, *Journal of Drug Targetting*, **17**(2), pp.108-122, DOI: 10.1080/10611860802472370.

Al-Qallaf B. and Das D.B., (2009b). Optimizing Microneedle Arrays to increase Skin Permeability for Transdermal Drug Delivery, *Annals of the New York Academy of Sciences*, **1161**: 83-94, DOI: 10.1111/j.1749-6632.2009.04083.x.

Al-Qallaf B., Das D.B., Davidson A., (2009a). Transdermal Drug Delivery by Coated Microneedles: Geometry Effects on Drug Concentration in Blood, *Asia-Pacific Journal of Chemical Engineering*, **4**(6): 845-857, DOI: 10.1002/apj.353.

Al-Qallaf B., Mori D., Olatunji O., Das D.B., Cui Z.F., (2009b). Transdermal Drug Delivery by Microneedles: Does Skin Metabolism Matter?, *International Journal of Chemical Reactor Engineering*, **7**: A69.1-A69.23.

Aravindaram K., Yang N.S., (2009). Gene gun delivery systems for cancer vaccine approaches, *Methods Mol. Biol.*, **542**: 167-178

Armaleo D., Ye G.N., Klein T.M., Shark K.B., Sanford J.C., Johnston S.A., (1990). Biolistic nuclear transformation of Saccharomyces cerevisiae and other fungi, *Curr. Genet.*, **17**: 97-103

Arora A., Hakim I., Baxter J., Rathnasingham R., Srinivasan R., Fletcher D.A., Mitragotri S., (2007). Needle-free delivery of macromolecules across the skin by nanoliter-volume pulsed microjets, *Proceedings of the National Academy of Sciences of the U.S.A. (PNAS)*, **104**(11): 4255-4260

Arora A., Prausnitz M.R., Mitragotri S., (2008). Micro-scale devices for transdermal drug delivery, *Int. J. Pharm.* **364**:227-236

Ashraf, M.W., Tayyaba, S., Afzulpurkar, N., (2011). Micro electromechanical systems (MEMS) based microfluidic devices for biomedical applications. *Int. J. Mol Sci.*, **12**: 3648-3704.

Badran, M. M., Kuntsche, J., Fahr, A., (2009). Skin Penetration Enhancement by a Microneedle Device (Dermaroller®) in vitro: Dependency on Needle Size and Applied Formulation, *Pharm Sci.*, **36**: 511- 523.

Bal S.M., Caussin J., Pavel S., Bouwstra J.A. (2008). *In vivo* assessment of safety of microneedle arrays in human skin, *European Journal of Pharmaceutical Sciences*, **35**(3): 193-202.

Bal, S.M., Kruithof, A.C., Lieb, H., Tomerius, M., Bouwstra, J., Lademann, J., Meinke, M. (2010). *In vivo* visualization of MN conduits in human skin using laser scanning microscopy, *Laser Physics Letters*, **7**(3): 242-246.

Bastian S., Busch W., Kuhnel D., Springer A., Holke R., Scholz S., Pompe W., Gelinsky M., Potthoff A., Richter V., Ikonomidou C., Schirmer K., (2009). Toxicity of tungsten carbide and cobalt-doped tungsten carbide nanoparticles in mammalian cells in vitro, *Environ. Health Perspect.*, **117**(4): 530-536

Bellhouse B.J., Sarphie D.F., Greenford J.C., (1999). Needleless syringe using supersonic gas flow for particle delivery, Patents No: (US5899880 A), *United States Patent*

Bellhouse B.J., Bell J., Millward H.R., Phillips M.J., Nabulsi S.M., (2003). Particle delivery, US Patent: US 6592545 B1, *United States Patent*

Bellhouse B.J., Greenford J.C., Sarphie D.F., (2006). Particle delivery, Patent: EP 1637173 A2

Belyantseva I.A., (2009). Helios Gene Gun–Mediated Transfection of the Inner Ear Sensory Epithelium, *Auditory and Vestibular Research: Methods and Protocols, Chapter 7, Editor Sokolowski B.*, **493**:103-123

Bennett A.M., Phillpotts R.J., Perkins S.D., Jacobs S.C., Williamson E.D., (1999). "Gene gun mediated vaccination is superior to manual delivery for immunisation with DNA vaccines expressing protective antigens from Yersinia pestis or Venezuelan Equine Encephalitis virus", *Vaccine*, **18**(7–8): 588–596.

Bio-Rad Laboratories, (2013). USA. (also see, http://www.bio-rad.com/)

Binyamin G., Shafi B.M., Mery C.M. (2006). Biomaterials: A primer for surgeons, *Seminars in Pediatric Surgery*, **15**(4): 276-283.

Biopex, (2013). SJ-500 Portable gene gun (also see, http://www.biopex.com/SJ-500-Portable-gene-gun-28-10.html)

Brown M.B., Martin G.P., Jones S.A., Akomeah F.K., (2006). Dermal and transdermal drug delivery systems: current and future prospects, *Drug Delivery*, **13**(3): 175-187

Bryan M., Guyach S., Norris K.A., (2013). Biolistic DNA vaccination against trypanosome infection, *Methods Mol. Biol.*, **940**: 305-315

Buchowicz J. and Krysiak C., (2003). Genotoxic effects of tungsten microparticles under conditions of biolistic transformation in Genetic transformation of plants, Jacson J.F., Linskens H.F. (Ed.), *Springer*, New York: 175–188

Burkoth T.J., Bellhouse B.J., Hewson .G, Longridg eD.J., Muddle A.G., Sarphie D.F., (1999). Transdermal and transmucosal powdered drug delivery, *Crit. Rev. Drug Carrier System*, **16**(4): 331-84

Cao Y., Zhao B., Han Y.H., Zhang J., Li X.Z., Qiu C.H., Wu X.J., Hong Y., Ai D.Z., Lin J.J., Fu Z.Q., (2013). Gene gun bombardment with DNA-coated golden particles enhanced the protective effect of a DNA vaccine based on thioredoxin glutathione reductase of Schitosoma japonicum, *Biomed. Res. Int.*, **2013**: Article No. 952416, doi: 10.1155/2013/952416

Chabrai F., Bouris K., Jones T., Barrow D., Allender C., Hann A., Brain K., Birchall J., (2004). "Microfabricated silicon microneedles for nonviral cutaneous gene delivery". *British Journal of Dermatology*, **150**(5): 869-877

Chen B., Wei J., Tay F.E.H., Wong Y.T., Iliescu C., (2008). Silicon microneedle array with biodegradable tips for transdermal drug delivery, *Microsystem Technologies*, **14**: 1015-1019

.

Chen D., Erickson C.A., Endres R.L., Periwal S.B., Chu Q., Shu C., Maa Y.F., Payne L.G., (2001). Adjuvantation of epidermal powder immunization, *Vaccine*, **19**(20-22): 2908-2917

Chen D., Maa Y., Haynes J.R., (2002). Needle-free epidermal powder immunization. *Expert Rev. Vaccines*, **1**(3): 89-100

Chen P.C., Hsieh S.J., Chen C.C., Zou J., (2013). A three-diemsional enormous surface area aluminium microneedle array with nanoporous structure, *Journal of Nanomaterials*, **2013**, 6 page, doi: 10.1155/2013/164953

Christou P., Mccabe D.E., Swain W.F., (1990). Soybean genetic-engineering commercial production of transgenic plants, *Trends in biotechnology*, **8**: 145 -151

Chu L.Y., Choi S.O., Prausnitz M.R., (2010). Fabrication of dissolving polymer MNs for controlled drug encapsulation and delivery: Bubble and pedestal MN designs, *J Pharm. Sci.* **99**(10): 4228-4238

Cormier M., Johnson B., Ameri M., Nyam K., Libiran L., Zhang D. D., and Daddona P.. (2004). Transdermal delivery of desmopressin using a coated microneedle array patch system. *J. Control. Release*, **97**: 503-511

Coulman S., Allender C., Birchall J., (2006). Microneedles and other physical methods for overcoming the stratum corneum barrier for cutaneous gene therapy, *Ther. Drug Carrier Syst.*, **23**(3): 205-258

Crozier W.D., Hume W., (1957). High velocity light gas gun, *Journal of Applied Physics*, **28**(8): 892-895

Da'dara A.A., Skelly P.J., Fatakdawala M., Visovatti S., Eriksson E., Harn D.A., (2002). Comparative efficacy of the schistosoma mansoni nucleic acid vaccine, sm23, following microseeding or gene gun delivery, *Parasite Immunology*, **24**: 179-187

Davidson A,, Al Qallaf B,, Das D.B., (2008). Transdermal Drug Delivery by Coated Microneedles: Geometry Effects on Effective Skin Thickness and Drug Permeability, *Chemical Engineering Research and Design*, **86**: 1196-1206, DOI: 10.1016/j.cherd.2008.06.002.

Davis S.P., Landis B.J., Adams Z.H., Allen, M.G., Prausnitz, M.R., (2004). Insertion of microneedles into tissue: measurement and prediction of insertion force and needle fracture force, *Journal of Biomechanics*, **37**: 1155-1163

Dehn J., (1987). A Unified theory if penetration, *International journal of impact engineering*, **5**: 239-248

Dempster A.C. Topham S.J., Johnson M.J., Hickey P.L., Longridge D.J., (2000). Comparison of epidermal thickness to skin response in various species following systemic drug delivery using a dermal PowderJet particle delivery system, *J Pharm Pharmcol*, **52**: 49

Diridollou S., Black D., Lagarde J.M., Gall Y., Berson M., Vabre V., Patat F., Vaillant L., (2000). Sex- and site-dependent variations in the thickness and mechanical properties of human skin *in vivo*, *Int. J. Cosmet. Sci.*, **22**(6): 421-435

Disegi J.A., Eschbach L., (2000). Stainless steel in bone surgery, *Injury*, **31**(4): 2-6

Dominik L., Erwin G., Paul W.D., Hagen V.B., Paul M., (2010). Neuro-Muscular Differentiation of Adult Porcine Skin Derived Stem Cell-Like Cells, *PLoSONE*, **5**(1): 8968-8976

Donnelly R.F., Raj S.T.R., Woolfson A.D., (2010a). Micronneedle-based drug delivery systems: microfabrication, drug delivery, and safety, *Drug Deliv.*, **17**(4): 187-207

Donnelly R.F., Garland M.J., Morrow D.I.J., Migalska K., Singh T.R.R., Majithiya R., Woolfson D.A., (2010b). Optical coherence tomography is a valuable tool in the study of the effects of microneedle geometry on skin penetration characteristics and in-skin dissolution, *J. Cont. Rel.*, **147**: 333-341.

Donnelly R.F., Majithiya R., Singh T.R.R., Morrow D.I.J., Garland M.J., Demir Y.K., Migalsks K., Ryan E., Gillen D., Scott C.J., Woolfsoon D.A. (2011). Design, optimization and characterisation of polymeric MN arrays prepared by a novel laser-based micro moulding technique. *Pharm. Res.*, **28**: 41-57.

Donnelly R.F., Garland M.J., Singh T.R.R., Migalska K., Majithiya R., McCrudden C.M., Kole P.L., Mahmood T.M.T., McCarthy H.O., Willfson A.D., (2012). Hydrogel-Forming microneedle array for enhanced transdermal drug delivery, *Adv. Funct. Mater.*, **22**: 4879-4890

Duck F.A., (1990). Physical Properties of Tissue: A Comprehensive Reference Book, London: Academic Press, Harcourt Brace Jovanovich

Eberly D., (2002). Rotation representations and performance issue, Geometric Tools, LLC (http://www.geometrictools.com/Documentation/RotationIssues.pdf) [Accessed on 3/6/2013]

Edwards C., Marks R., (1995). Evaluation of biomechanical properties of human skin, *ClinDermatol*, **13**: 375-380

Ettinger M., Peckl S.D., Gruber C., Laimer M., Thalhamer J., Hintner H., Gratz I.K., Bauer J.W., (2012). Transcutaneous gene gun delivery of hNC16A induces BPAG2-Specific tolerance, *Journal of Investigative Dermatology*, **132**(6): 1665-1671

Fuchs E.E., Raghavan S., (2002). Getting under the skin of epidermal morphogenesis, *Nature reviews. Genetics*, **3**: 199-209

Fuller D.H., Loudon P., Schmaljohn C., (2006). Preclinical and clinical progress of particle-mediated DNA vaccines for infectious diseases, *Methods*, **40**(1): 86-97

Gardeniers H.J.G.E., Luttge R., Berenschot E.J.W. de Boer M.J., Yeshurun S.Y., Hefetz M., van't Oever R., van den Berg A., (2003). "Silicon Micromachined Hollow Microneedles for Transdermal Liquid Transport". *Journal of Microelectromechanical Systems*, **12**(6): 855-862

Giudice E.L., Campbell J.D., (2006). Needle-free vaccine delivery, *Adv.Drug Deliv. Rev.* **58:** 68-89

Glenn G.M., Kenney R.T., Ellingsworth L.R., Frech S.A., Hammond S.A., Zoeteweweij J.P., (2003). Transcutaneous immunization and immunosticmulant strategies: capitalizing on the immunocompetence of the skin, Expert Rev., *Vaccines*, **2**(2): 253-267

Gill, H.S., Denson, D.D., Burris, B.A., Prausnitz, M.R., (2008). Effect of Microneedle design on pain in Human subjects, *Clin. J. Pain*., **24**:585-594.

Gu B., Kale S.D., Wang Q.H., Wang D.H., Pan Q.N., Cao H., Meng Y.L., Kang Z.S., Tyler B.M., Shan W.X., (2011). Rust secreted protein Ps87 is conserved in diverse fungal pathogens and contains a RXLR-like motif sufficient for translocation into plant cells, *PLoS One.*, **6**(11): e27217

Gupta J., Park S.S., Bondy B., Felner E.I,, Prausnitz M.R., (2011a). Infusion pressure and pain during microneedle injection into skin of human subjects, *Biomaterials*, **32**: 6823-6831

Gupta J., Gill H.S., Andrews S.N., Prausnitz M.R., (2011b). Kinetics of skin resealing after insertion of microneedles in human subjects, *Journal of Controlled Release*, **154**: 148-155

Hall, R.D., (1990). Plant cell culture protocols, Methods in molecular biology, Methods in Molecular Biology, *Humana Press Inc.*, Totowa, USA, **111**: 79

Han R., Peng X., Reed C.A., Cladel N.M., Budgeon L.R., Pickel M.D., Christensen N.D., (2002). Gene gun-mediated intracutaneous vaccination with papillomavirus E7 gene delays cancer development of papillomavirus-induced skin papillomas on rabbits, *Cancer Detect Prev.*, **26**(6): 458-467

Han M., Hyun D.H., Park H.H., Lee S.S.L., Kim C.H., Kim C.G., (2007). A novel fabrication process for out-of-plane microneedle sheets of biocompatible polymer, J. Micromech. Microeng., **17**: 1184-1191.

Han T., Das D.B., (2013). Permeability enhancement for transdermal delivery of large molecule using low-frequency sonophoresis combined with microneedles, *Journal of Pharmaceutical Science*, **102**(10): 3614-3622

Han X., Wang D.K., Wang Y., (2008). "Development of Transdermal Delivery System of Microneedles", *Chinese Journal of Pharmaceutics*, **6**(5): 296-300

Haq M.I., Smith E., John D.N., Kalavala M., Edwards C., Anstey A., Morrissey A., Birchall J.C., (2009). Clinical administration of microneedles: skin puncture, pain and sensation, *Biomed. Microdevices*, **11**: 35-47

Hardy H.P., Quinlan N.J., Kendall M.A.F., Bellhouse B.J. (2001). Numerical study of a prototype needle-free powdered vaccine and drug delivery system. *In: ISSW 23, Austin, TX, USA*, 23-37

Hardy M.P., Kendall M.A.F., (2005). Mucosal deformation from an impinging transonic gas jet and the ballistic impact of microparticles, *Phys. Med. Biol.*, **50**(19): 4567-4580

Heiser W.C., (1994). Gene transfer into mammalian cells by particle bombardment, Analytical Biochemistry, **217**(2): 185-196

Henry F., Pierard F.C., Cauwenbergh G., Pierard G.E., (1997). Age-related changes in facial skin contours and rheology. Journal of the American Geriatrics Society, **45**(2): 220-222

Henry, S., McAllister, D.V., Allen, M.G., Prausnitz, M.R. (1998a). Microfabricated microneedles: a novel approach to transdermal drug delivery, *J. Pharm. Sci.*, **87**: 922-925.

Henry S., McAllister D.V., Allen M.G., Prausnitz M.R., (1998b). "Micromachined needles for the transdermal delivery of drugs", *Proc. IEEE Micro Electro Mechanical Systems*, MEMS'98, Heidelberg Germany, **25**(29): 494–498

Holbrook, K.A. (1994). Ultrastructure of the Epidermis: Chapter 1 of the Keratinocyte Handbook, edited by Leigh, I.M. and Lane, E.B., Watt, F.M., Cambridge, Great Britain, *Cambridge University Press*. Page: 3–39.

Holbrook, K. A., Odland, G.F. (1974). Regional Differences in the thickness (cell layers) of the human stratum corneum: an ultrasound analysis, *J Invest Dermatol*., **62**: 415-422.

Hou L.Y., Wang P.Y., Kong F.T., Park H., Kobiro K. and Ohama T., (2013). Mesoporous TiO2 nanoparticles: A new material for biolistic bombardment, *Phycological Research*, **61**: 58-60

Huang H.Y.S., Huang S., Gettys T., Prim P.M., Harrysson O.L., (2013). A biomechanical study of directional mechanical properties of porcine skin tissue, Proceedings of the ASME 2013 International Mechanical Engineering Congress & Exposition (IMECE2013), San Diego, California, USA, November 13-21

Huang P.H., Chen P.Y., (2011). Design of a two-stage electromagnetic impulse force circuit for gene gun, *Journal of Marine Science and Technology*, **19**(6): 686-692

Ikemoto K., Sakata I., Sakai T., (2012). Collision of millimetre droplets induces DNA and protein transfection into cells, *Scientific Reports*, **2**: Article No. 289, doi: 10.1038/srep00289

ImageJ, (2013). ImageJ (http://rsbweb.nih.gov/ij/disclaimer.html) [Accessed on 3/6/2013]

Joseph S.K., Sambanthamoorthy S., Dakshinamoorthy G., Munirathinam G., Ramaswamy K., (2012). Protective immune responses to biolistic DNA vaccination of Brugiamalayi abundant larval transcript-2, *Vaccine*, **30**(45): 6477-6482.

Kalluri H., Banga A.K. (2011). Formation and closure of microchannels in skin following microporation, *Pharm. Res.*, **28**: 82-94

Kaushik S., Hord A.H., Denson D.D., McAllister D.V., Smitra S., Allen M.G., Prausnitz M.R., (2001). Lack of pain associated with microfabricated microneedles, *Anesth. Analg.*, **92**(2): 502-504

Kendall M.A.F., Carter F.V., Mitchell T.J., and Bellhouse B.J., (2001). Comparison of the transdermal ballistic delivery of micro-particle into human and porcine skin, *Proceedings of the 23rd Annual International Conference of the IEEE*: October 25-28, Istanbul, Turkey, Vol 3, 2991–4, doi: 10.1109/IEMBS.2001.1017423, ISBM: 0-7803-7211-5

Kendall M.A.F., (2002). The delivery of particulate vaccines and drugs to human skin with a practical, hand –held shock tube-based system, *Shock Waves*, **12**: 23-30

Kendall M.A.F., Quinlan N.J., Thorpe S.J., Bellhous B.J., Ainsworth R.W. (2004a). Measurements of the gas and particle flow within a converging-diverging nozzle for high speed powdered vaccine and drug delivery, *Exp. Fluids*, **37**: 128-36

Kendall M.A.F., Rishworth S., Carter F., Mitchell T., (2004b). Effects of relative humidity and ambient temperature on the ballistic delivery of micro-particles to excised porcine skin, *J. Invest. Dermatol*., **122**: 739-746

Kendal M.A.F., (2006). Engineering of needle-free physical methods to target epidermal cells for DNA vaccination, *Vaccine*, **24**: 4651-4656

Kim Y.C., Quan F.S., Compans R.W., Kang S.M., Prausnitz M.R., (2010). Formulation of microneedles coated with influenza virus-like particle vaccine, *AAPS PharmSciTech*,, **11**(3): 1193-1201

Kim Y.C., Park J.H., Prausnitz M.R, (2012). Microneedles for drug and vaccine delivery, *Advanced Drug Delivery Reviews*, **64**: 1547-1568

Kis E.E., Gerhard W., Myschik J., (2012). Devices for intradermal vaccination, *Vaccine*, **30**: 523-538

Kishino A., Yanagida T., (1988). Force measurements by micromanipulation of a single actin filament by glass needles, *Nature*, **334**: 74-76

Klein T.M., Wolf E.D., Wu R., Sanford J.C., (1987). High-velocity microprojectiles for delivery of nucleic acids into living cells, *Nature(London)*, **327**: 70-73

Klein T.M., Arentzen R., Lewis P.A., McElligott F.S., (1992). Transformation of microbes, plants by particle bombardment, *Biotechnology*, **10**: 286-291

Koelmans W.W., Krishnamoorthy G., Heskamp A., Wissink J., Misra S., Tas N., (2013). Microneedle Characterization using a double-layer skin simulant, *Mechanical Engineering Research*, **3**(2): 51-63

Kolli, C.S., Banga, A.K. (2008).Characterization of solid maltose MNs and their use for transdermal delivery, *Pharmaceutical Research*, **25**:104-113.

Kong R., Bhargava R., (2011). Characterization of porcine skin as model for human skin studies using infrared spectroscopic image. *PubMed*, **136**(11): 2359-2366

Kuriyama S., Mitoro A., Tsujinoue H., Nakatani T., Yoshiji H., Tsujimoto T., Yamazaki M., Fukui H., (2000). "Particle-mediated gene transfer into murine livers using a newly developed gene gun", *Gene Ther.*, **7**: 1132-1136.

Kuriakose B., Du T.E.S., Jordaan A., (2012). Transient gene expression assays in rose tissues using a Bio-Rad Helios ® hand-held gene gun, *South African Journal of Botany*, **78**: 307-311

Lambert P.H., Laurent P.E., (2008). Intradermal vaccine delivery: Will new delivery systems transform vaccine administration?. *Vaccine*, **26**: 3197–3208.

Lin M., (2000). The gene gun: current applications in cutaneous gene therapy, *Int. J. Dermatol.*, **39**: 161-170

Liu Y., Kendall M.A.F., (2004a). "Numerical study of a transient gas and particle flow in a high-speed needle-free ballistic particulate vaccine delivery system", *Journal of Mechanics in Medicine and Biology*, **4**(4): 559-578

Liu Y., Kendall M.A.F., (2004b). Numerical simulation of heat transfer from a transonic jet impinging on skin for needle-free powdered drug and vaccine delivery, Proceedings of the institution of mechanical engineers, part C: *J. Mech, Eng, Sci*,, **218**(11): 1373-1383

Liu Y., Truong N.K., Kendall M.A.F., (2004c). Numerical studies of contoured shock tube for murine powdered vaccine delivery system, *15th Australasian Fluid Mechanics conference*.

Liu Y., Kendall M.A.F., (2006). Numerical analysis of gas and micro-particle interactions in a hand-held shock tube device, *Biomed Microdevices*, **8**: 341-351

Liu Y., (2006). Physical-mathematical modelling of fluid and particle transportation for DNA vaccination, *International Journal of Engineering Science*, **44**(15-16): 1037-1049

Liu Y., Truong N.K., Kendall M.A.F., Bellhouse B.J., (2007). Characteristics of a micro-biolistic system for murine immunological studies, *Biomed. Microdevices* 9:465-474

Liu Y., Costigan G., Bellhouse B.J., (2008). Swirling effects on the performance of the micro-particle acceleration and penetration: parametric studies, *Powder Technol.* **183**: 189-195

Liu Y., (2008). Simulation of transient shock motion within a biological contoured shock tube system, *Physica D: Nonlinear Phenomena*, **237**(2): 233-242

Macklin, M.D., Drape, R.J., Swain, W.F., (2000). Preparation for particle-mediated gene transfer using the Accell gene gun, *Methods in molecular medicine*, **29**: 297-303

MacNeil S., (2007). Progress and opportunities for tissue-engineered skin, *Nature*, **445**: 874-880

Manjila S.B., Baby J.N., Bijin E.N., Constantine I., Pramod K., Valsalakumari J., (2013). Novel gene delivery system, *International Journal of Pharmaceutical Investigation*, **3**(1):1-7

Marks J.G., Miller J.J., Lookingbill D.P., (2006). Principles of Dermatology, 4 eidition, *Saunders Elsevier*: 1-7, ISBN: 1416031855

Marrion M.C., Gostigan G., Bellhouse B.J., Flow separation control in over-expanded supersonic nozzle, *35th AIAA fluid dynamics conference and exhibit*. Toronto, ON, Canada, 6-9 June, 2005, Chapter DOI: 10.2514/6.2005-5266

Martanto W., Davis S.P., Holiday N.R., Wang J., Gill H.S., Prausnitz M.R. (2004). Transdermal delivery of Insulin using microneedles *in vivo*, *Pharmaceutical Research*, **21**: 947-952.

Matteucci M., Fanetti M., Casella M., Gramatica F., Gavioli L., Tormen M., Grenci G., De Angelis F., Di Fabrizio E. (2009). Poly vinyl alcohol re-usable masters for microneedle replication. *Microelectronic Engineering*, **86**(4-6): 752-756, doi:10.1016/j.mee.2009.01.068

Mcallister D.V., Allen M.G., (2000). Prausnitz MR. Microfabricated microneedles for gene and drug delivery, *Annual Review Biomedical Engineering*, **2**: 289 –313.

McAllister D.V., Wang P.M., Davis S.P., Park J.H., Canatella P.J., Allen M.G., Prausnitz, M.R. (2003). Microfabricated needles for transdermal delivery of macromolecules and nanoparticles: fabrication methods and transport studies. *PNAS*, **100**: 13755–13760.

Meacham J.M., Durvasula K., Degertekin F.L., Fedorov A.G., (2013). Physical methods for intracellular delivery: Particle aspects from laboratory use to industrial-scale processing, *Journal of Laboratory Automation*, DOI: 10.1177/2211068213494388

Memon S., Pathan D.N., Ziyaurrrahman A.R., Bagwan A., Sayed B., (2011). Microneedle as a novel drug delivery system: A review, *Internation Research Journal of Pharmacy*, **2**(2): 72-77

Menezes V., Mathew Y., Takayama K., Kanno A., Hosseini H., (2012). Laser plasma jet driven microparticles for DNA/drug delivery, *PLoS ONE*, **7**(11): e50823

Mertens J., Tamayo J., Kosaka P., and Calleja M., (2011). Observation of spermidine-induced attractive forces in self-assembled monolayers of single stranded DNA using a microcantilever sensor, *Applied Physics Letters*, **98**(15): 3704 - 3707

Meyers M.A., Chawla K.K., (1999). Mechanical behaviour of materials, 1st Edition, *Prentice Hall*, 98-103, ISBN: 9780132628174

Mikolajewska P., Donnelly R.F., Garland M.J., Morrow D.I.J., Singh T.R.R., Lani V., Moan J., Juzeniene A., (2010). Microneedle pre-treatment of human skin improves 5-aminolevulininc acid (ALA) and 5-aminolevulinic acid methyl ester (MAL) induced PpIX production for topical photodynamic therapy without increase in pain or erythema, *Pharm. Res.*, **27**: 2213-2220

Mikszta J.A., Alarcon J.B., Brittingham J.M., Sutter D.E., Pettis R.J., Harvey N.G., (2002). Improved genetic immunization via micromechanical disruption of skin-barrier function and targeted epidermal delivery, *Nat. Med.*, **8**: 415–419.

Mitchell T.J., Kendall M.A.F., Bellhouse B.J., (2003). A ballistic study of micro-particle penetration to the oral mucosa, *International Journal of Impact Engineering*, **28**: 581-599

Miyano T., Tobinaga Y., Kanno T., Matsuzaki Y., Takeda H., Wakui M., and Hanada K., (2005). Sugar micro needles as transdermic drug delivery system. *Biomed. Microdevices*, **7**: 185-188

Mohammed D., Matts P.J., Hadgraft J., Lane M.E., (2012). Variation of stratum corneum biophysical and molecular properties with anatomic site, *The American Association of Pharmaceutical Scientists*, **14**(4): 806-812

Morgan J.L., Kerschensteiner D., (2011). Shooting DNA, Dyes, or Indicators into Tissue Slices using the gene gun, *Cold Spring Harb. Protoc.*, **12**: 1512-1514

Morsi S.A., Alexander A.J., (1972). An investigation of particle trajectories in two-phase flow systems, *Journal of Fluid Mechanics*, **55**(2): 193-208

Nagata T., Koide Y., (2010). Induction of specific $CD8^+$ T cells against intracellular bacteria by CD 8^+ T-cell-oriented immunization approaches, *Journal of Biomedicine and Biotechnology*, **2010**: Article No. 764542, DOI: 10.1155/2010/764542.

Napolitano A.P., Dean D.M., Man A.J., Youssef J., Ho D.N., Rago A.P., Lech M.P., Morgan J.R., (2007). Scaffold-free three-dimensional cell culture utilizing micromolded nonadhesive hydrogels, *BioTechniques*, **43**: 494-500

Nayak A. and Das D.B., (2013). Potential of biodegradable microneedles as a transdermal delivery vehicle for lidocaine, *Biotechnology Letters*, **35**(9): 1351-1363, DOI; 10.1007/s10529-013-1217-3

Nayak A., Das D.B., Vladisavljević, GT (2013). Microneedle-Assisted Permeation of Lidocaine Carboxymethylcellulose with Gelatine Co-polymer Hydrogel. Pharmaceutical Research, DOI: 10.1007/s11095-013-1240-z (in press)

Nguyen-Hoai T., Hohn O., Vu M.D., Baldenhofer G., Sayed A.M.S., Dorken B., Norley S., Lipp M., Pezzutto A., Westermann J., (2012). CCL19 as an adjuvant for intradermal gene gun immunization in a Her2/neu mouse tumor model: improved vaccine efficacy and a role for B cells as APC, *Cancer Gene Ther*., **19**(12): 880-887

Nordquist L., Roxhed N., Griss P., Stemme G., (2007). Novel microneedle patches for active insulin delivery are efficient in maintaining glycaemic control: an initial comparison with subcutaneous administration, *Pharmaceutical Research*, **24**(7): 1381–1388

O'Brien J.A., Lummis S.C.R., (2011). Nano-biolistics: a method of biolistic transfection of cells and tissues using a gene gun with novel nanometer-sized projectiles, *BMC Biotechnology*, **11**: 66

O'Brien J.A., Lummis S.C.R., (2007). Diolistics: incorporating fluorescent dyes into biological samples using a gen gun, *Trends in Biotechnology*, **25**(11): 530-534

O'Brien J.A., Lummis S.C.R., (2006). Biolistic transfection of neuronal cultures using a hand-held gene gun, *Nat. Protoc.* **1**(2): 977-981

Oh j., Park H., Do K., Han M., Hyun D., Kim C., Kim C., Lee S., Hwang S., Shin S., Cho C., (2008). Influence of the delivery systems using a microneedle array on the permeation of a hydrophilic molecule, calcein. *European Journal of Pharmaceutics and Biopharmaceutica*. **69**: 1040-1045.

Olatunji O., Das D.B., (2010). Painless Drug delivery using microneedles. Current technologies to increase the transdermal delivery of drugs (Editor: Joan Escober Chavez). Sharjah: *Bentham Science Publishers*, 96-110, ISBN:978-1-60805-191-5 (available online at http://www.benthamdirect.org/pages/b_getarticlebybook.php).

Olatunji O., Das D.B., (2011). Drug delivery using Microneedles. Comprehensive Biotechnology (Editor: Zhanfeng Cui). 2nd Edition, MS number 501. MRW, Elsevier, The Boulevard, Langford Lane, Oxford, United Kingdom. 625-642, ISBN: 13: 978-0-444-53352-4

Olatunji O., Das D.B., Nassehi V. (2012). Modelling transdermal drug delivery using microneedles: Effect of geometry on drug transport behaviour. *Journal of Pharmaceutical Sciences*, **101**(1): 164–175, January, DOI: 10.1002/jps.22736.

Olatunji O., Das D.B., Garland M.J., Belaid L., Donnelly R.F., (2013). Influence of array interspacing on the force required for successful microneedle skin penetration: theoretical and practical approaches, *Journal of Pharmaceutical Sciences*, **102**(4): 1209–1221, April, DOI: 10.1002/jps.23439

Palastanga N., Field D., Soames R.W., (2006). Anatomy and human Movement: Structure and function, 5th edition, London: *Elsevier Health Science*, ISBN-13: 9780750688147

Park J.H., Allen M.G., Prausnitz M.R., (2005). Biodegradable polymer microneedles: fabrication, mechanics and transdermal drug delivery, *Journal of Controlled Release*, **104**(1): 51-66.

Park J.H., Allen M.G., Prausnitz M.R., (2006). Polymer microneedles for controlled-release drug delivery, *Pharm. Res.*, **23**: 1008-1019.

Parker E.R., Rao M.P., Turner K.L., Meinhart C.D., MacDonald N.C. (2007). Bulk micromachined titanium microneedles, *Journal of Microelectromechanical System*, **16**: 289-295.

Parker, F. (1991). Structure and Function of the Skin: Chapter 1 in Dermatology edited by Orkin, M. and Maibach, H. I. and Dahl, M. V., *1st edition* (Norwalk, Connecticut: Appleton and Lange).

Phipps, J. B. Padmanabhan, R. V. Lattin, G. A. (1988). Transport of Ionic Species Through Skin. *Solid State Ionics*, **28**: 1778–1783.

Pierard G.E., Lapiere C.M., (1977). Physiopathological variations in the mechanical properties of skin, *Archives of Dermatological Research*, **260**(3):231-239

Prausnitz M.R., (2004). microneedles for transdermal drug delivery. *Advanced drug delivery reviews*. **56**: 581–587.

Prausnitz M.R., Langer R., (2008). Transdermal drug delivery, *Nat. Biotech.*, **26**(11): 1261-1268

Qi P., Chen G.G., Wei P., (2007). "Research and Development of Microneedles for Transdermal Drug Delivery", *Journal of Nanjing University of Technology (Natural Science Edition)*, **29**(4): 57-63

Quan F.S., Kim Y.C., Compans R.W., Prausnitz M.R., Kang S.M., (2010). Does sparing enabled by skin immunization with influenza virus-like particle vaccine using microneedles, *J. Control Release*, **147**(3): 326-332

Quinlan N.J., Kendall M.A.F., Bellhouse B.J., Ainsworth R.W., (2001). Investigations of gas and particle dynamics in first generation needle-free drug delivery device, *Shock Waves*, **10**: 395-404

Raju P.A., Truong N.K., Kendall M.A.F., (2006). Assessment of epidermal cell viability by near infra-red two-photon microscopy following ballistic delivery of gold micro-particles, *Vaccine*, **24**: 4644-4647

Rao W., (2010). A proteomic analysis of lipid raft and GPI anchored protein in Caenorhabditis elegans, University of Leeds (UK), *Thesis for the degree of Doctor of Philosophy*

Rasel M.A.I., Taher M.A., Kim H.D., (2013). A study on the gas-solid particle flows in a needle-free drug delivery device, *Journal of Thermal Science*, **22**(4): 340-344

Rinberg D., (2005). Pneumatic capillary gun for ballistic delivery of micro-particles, *Applied Physics Letters*, **87**: 014103

Ritman E.L., (2004). Micro-computed tomography – Current status and developments, *Annual review of Biomedical Engineering*, **6**: 185-208

Rosi N.L., Giljohann D.A., Thaxton C.S., Lytton-Jean A.K., Han M.S., Mirkin C.A., (2006). Oligonucleotide-modified gold nanoparticles for intracellular gene regulation, *Science*, **312**: 1027-1030

Rushmer R. F., Buettner K. J. K., Short J. M., and Odland G. F., (1966). The Skin, *Science*, **154**: 343–348.

Russell J.A., Roy M.K., Sanford J.C., (1992). Physical trauma and tungsten toxicity reduce the efficiency of biolistic transformation, *Plant Physiol.*, **98**: 1050-1056

Sachdeva V., Banga A.K., (2011). Microneedles and their applications, *Recent Pat. Drug Delivery Formulation*, **5**: 95-132

Sakai T., Hisaeda H., Nakano Y,, Ishikawa H., Maekawa Y., Ishii K., Nitta Y., Miyazaki J., Himeno K., (2000). Gene gun-mediated delivery of an interleukin-12 expression plasmid protects against infections with the intracellular protozoan parasites leishmania major and Trypanosoma cruzi in mice, *Immunology*, **99**: 615-624

Sanford J.C., Klein T.M., Wolf E.D., Allen N., (1987). Delivery of substances into cells and tissues using a particle bombardment process, *Particulate Science and Technology*, **5**(1): 27-37

Sanford J.C., Smith F.D., Russell J.A., (1993). Optimizing the biolistic process for different biological applications, *Methods Enzymol.*, **217**: 483-509

Sanford J.C., (2000). Turning point article –The development of the biolistic process, *In Vitro Cell. Dev. Biol.*, **36**: 303-308

Satish D., (2009). In vitro manipulation of pollen for transformation in cotton and tomato, University of Agricultural Sciences (India), *Thesis for the degree of Doctor of Philosophy*

Sato H., Hattori S., Kawamoto S., Kudoh I., Hayashi A., Yamamoto I., Yoshinari M., Minami M., Kanno H., (2000). *In vivo* gene gun-mediated DNA delivery into rodent brain tissue, *Biochem. Biophys. Res. Commun*. **270**(1): 163-170.

Schaefer, H., Redelmeier, T.E. (1997). Skin barrier: Principles of percutaneous absorption, *Arch Dermatol.,* **133**(7): Article No. 924, doi:10.1001/archderm.1997.03890430146031.

Scheuplein R.J., Blank I.H. (1971). Permeability of the skin, *Physiol. Rev.*, **51**: 702-747.

Shah U.U., Roberts M., Gul M.O., Teleu C., Beresford M.W., (2011). Needle-free and microneedle drug delivery in children: a case for disease-modifying antirheumatic drugs (DMARDs), *International Journal of Pharmaceutics*, **416**: 1-11

Shampine L.F., Reichelt M.W., (1997). The matlab ode suite, SIAM Journal on Scientific Computing, **18**(1): 1-22, DOI: 10.1137/S1064827594276424

Shergold O.A., Fleck N.A., Radford D., (2006). The uniaxial stress versus strain response of pig skin and silicone rubber at low and high strain rates, *Int. J. Impact Eng.*, **32**: 1384-1402

Silpi C., Manish B., Kumar T.R., (2011). Microneedles in transdermal drug delivery: An unique painless option, *International Research Journal of Pharmacy*, **2**(4): 72-78

Silver F.H., Freeman J.F., Devore D., (2001). Viscoelastic properties of human skin and processed dermis. Skin Research and Technology, **7**(1): 18-23

Smith F.D., Harpending P.R., Sanford J.C., (1992). Biolistic transformation of prokaryotes: factors that affect biolistic transformation of very small cells. *J. Gen. Microbiol.*, **138**: 239-248

Singh R., Dahotre N.B., (2007). Corrosion degradation and prevention by surface modification of biometallic materials, *J. Mater. Sci. Mater. Med.*, **18**(5): 725-751

Soliman S.M. (2011). Micro-particle and Gas Dynamics in an Axi-symmetric Supersonic Nozzle, University of Cincinnati (Cincinnati, USA), *Thesis for the degree of Doctor of Philosophy in Aerospace Engineering*.

Soliman S.M., Abdallah S., (2011). CFD investigation of powdered vaccine and gas dynamics in biolistic gun, *Powder Technology*, **214**: 135-142

Soliman S.M., Abdallah S., Gutmark E., Turner M.G., (2011). Numerical simulation of microparticles penetration and gas dynamics in an axi-symmetric supersonic nozzle for genetic vaccination, *Powder Technology*, **208**: 676-683

Stahl J., Wohlert M., Kietzmann M., (2012). MN pretreatment enhances the percutaneous permeation of hydrophilic compounds with high melting points, *BMC Pharmacology and Toxicology*, **13**: 1-7

Stoeber B., Liepmann D., (2000). Fluid injection through out-of-plane microneedles, *Proceedings of the 1st Annual International IEEE-EMBS Special Topic Conference on Microtechnologies in Medicine and Biology, Lyon, France*, **14**: 224-228.

Sung H.W., Chen M.C., Lee P.W., Tu H.S., (2011). Nanoparticles for protein/peptide delivery and delivery means thereof, Patent No. US7901711 B1 (Granted), *United States Patent*, USA

Svarovsky S., Borovkov A., Sykes K., (2008). Cationic gold microparticles for biolistic delivery of nucleic acids, *Biotechniques*, **45**(5): 535-540

Swain W.E., Heydenburg F.D., Wu M.S., Barr L.J., Fuller J.T., Culp J., Burkholder J., Dixon R.M., Widera G., Vessey R., Roy M.J. (2000). Tolerability and immune responses in humans to a PowderJect DNA vaccine for hepatitis B., *Dev. Biol (Basel)*. **104**: 115-119.

Tekeuchi Y., Doston M., Keen N.T., (1992). Plant transformation: a simple particle bombardment device based on flowing helium, *Plant Mol. Biol.*, **18**: 835-839

Teo A.L., Shearwood C., Ng K.C., Lu J., Moochhala S., (2006). Transdermal microneedles for drug delivery applications, *Materials Science and Engineering*, **132**: 151-154.

Thomas J.L., Bardou J., Mauchamp B. et al., Chavancy Gerard (2001). A helium burst biolistic device adapted to penetrate fragile insect tissues, *Journal of Insect Science*, **1**(9): 1-10

Tortora G.J., Derrickson B.H., (2011). Principles of Anatomy and Physiology, 13 edition, *Wiley*, ISBN-13: 978-0470565100

Trainer A.T., Alexander M.Y., (1997). Gene delivery to the epidermis, Human Molecular *Genetics*, **6**(10): 1761 - 1767

Trimble C., Lin C., Hung C., Pai S., Juang J., He L., Gillison M., Pardoll D., Wu L., Wu T., (2003). Comparison of the CD8+ T cell responses and antitumor effects generated by DNA vaccine administered through gene gun, biojector, and syringe, *Vaccine*, **21**: 4036–4042.

Truong N.K., Liu Y., Kendall M.A.F., (2006). Gas and particle dynamics of a contoured shock tube for pre-clinical micro-particle drug delivery, *Shock Waves*, 1**5**: 149-164

Tuan-Mahmood T.M., McCrudden M.T.C., Torrisi B.M., McAlister E., Garland M.J., Singh T.R.R., Donnelly R.F., (2013). Microneedles for intradermal and transdermal drug delivery, *European Journal of Pharmaceutical Sciences*, doi: 10.1016/j.ejps.2013.05.005. (in press)

Uchida M., Li X.W., Mertens P., Alpar H.O., (2009). Transfection by particle bombardment: Delivery of plasmid DNA into mammalian cells using gene gun, *Biochim. Biophys. Acta.*, **1790**(8): 754-764

Valenstein J.C., (2012). Developing nanotechnology for biofuel and plant science applications, Iowa State Univeristy (USA), *Thesis for the degree of Doctor of Philosophy*

Verbaan, F.J., Bal, S.M., van den Berg, D.J., Dijksman, J.A., van Hecke, M., Verpoorten, H., van den Berg, A., Luttge, R., Bouwstra, J.A. (2008). Improved piercing of microneedle arrays in dermatomed human skin by an impact insertion method, *Journ. Contrl. Rel.*, **128**: 80–88.

Vexler A., Polyansky I., Gorodetsky R., (1999). Evaluation of skin viscoelasticity and anisotropy by measurement of speed of shear wave propagation with viscoelasticity skin analyser, *Journal of Investigative Dermatology*, **113**: 732-739

Walters K.A., Roberts M.S., (2007). Dermatologic, Cosmeceutic, and Cosmetic Development, *Therapeutic and Novel Approaches, CRC press*, **Chapter 36**: 591-611

Webster C., (1995). The Discovery of Boyle's law, and the concept of the Elasticity of Air in the Seventeenth Century, *Arch. Hist. Exact Sci.*, **2**: 441-502

Wildnauer R.H., Bothwell J.W., Douglas A.B., (1971). Stratum corneum properties I. Influence of relative humidity on normal and extracted stratum corneum, *J. Invest. Dermatol.*, **56**: 72-78

Williams R.S., Johnston S.A., Riedy M., DeVit M.J., McElligott S.G., Sanford J.C., (1991). Introduction of foreign genes into tissues of living mice by DNA-coated microprojectiles, *Proc. Natl. Acad. Sci. U.S.A.*, **88**: 2726-2730

Xia J.X., Martinez A., Daniell H., Ebert S.N., (2011). Evaluation of biolistic gene transfer methods *in vivo* using non-invasive bioluminescent imaging techniques, *BMC Biotechnology*, **11**: 62-72

Xu F., Wen T., Seffen K.A., LuT.J., (2007). Characterization of Thermomechanical behaviour of skin tissue – Viscoelastic behaviour, *Proceedings of the World Congress on Engineering*, **2**, WCE 2007

Yager E.J., Stagnar C., Gopalakrishnan R., Fuller J.T., Fuller D.H., (2013). Optimizing particle-mediated epidermal delivery of an influenza DNA vaccine in ferrets, *Methods Mol. Biol.*, **940**: 223-237

Yan G., Warner K. S., Zhang J., Sharma S., Gale B. K., (2010), Evaluation needle length and density of microneedle arrays in the pretreatment of skin for transdermal drug delivery, *International journal of Pharmaceutics*. **391**: 7-12.

Yang C.H., Shen S.C., Lee J.C., Wu P.C., Hsueh S.F., Lu C.Y., Meng C.T., Hong H.S., Yang L.C., (2004). Seeing the gene therapy: application of gene gun technique to transfect and decolour pigmented rat skin with human agouti signalling protein cDNA, *Gene Ther.*, **11**(13):1033-1039

Yang L.Z., Li C.F., Chen L., Li Z.Y., (2009). An agarose gel based method for transporting cell lines, *Current Chemical Genomics*, **3**: 50-53

Yang N.S., Burkholder J., Roberts B., Martinell B., McCabe D., (1990). *In vivo* and in vitro gene transfer to mammalian somatic cells by particle bombardment, *Proc. Natl. Acad. Sci. U.S.A.*, **87**: 9568-9572

Yen M.C., Lai M.D., (2013). Biolistic DNA delivery to mice with the low pressure gene gun, *Methods Mol. Biol.*, **940**:169-174

Yoshida Y., Kobayashi E., Endo H., Hamamoto T., Yamanaka T., Fujimura A., Kagawa Y., (1997). Introduction of DNA into rat liver with a hand-held gene gun: Distribution of the expressed enzyme, [32P] DNA, and Ca2+ flux, *Biochem. Biophys. Res. Commun.* **234**(3): 695 -700.

Yoshimitsu Y., Tanaka K., Tagawa T., Nakamura Y., Matsuo T., Okamoto S., (2009), Improvement of DNA/Metal Particle Adsorption in Tungsten-Based Biolistic Bombardment; Alkaline pH is Necessary for DNA Adsorption and Suppression of DNA Degradation, *Journal of Plant Biology*, **52**: 524-532.

Yuzhakov V.V., (2008). Tissue conforming microneedle array and patch for transdermal drug delivery or biological fluid collection, World Intellectual Property Organization, Patent: WO 2008/067290 A2;

Zelenin A.V.,Titomirov A.V., Kolesnikov V.A., (1989). Genetic transformation of mouse cultured cells with the help of high velocity mechanical DNA injection, *FEBS Lett.*, **244**(1): 65-67

Zeng Y.J., Huang K., Xu C.Q., Zhang J. and Sun G.C., (2001). Biorheological characteristics of skin after expansion. Biorheology, **38**(5-6): 367-378

Zhang, D, Das, DB, Rielly, CD (2013). An experimental study of microneedle assisted micro-particle delivery. *Journal of Pharmaceutical Sciences*, **102**(10): 3632-3644

Zhang G., Selzer M.E., (2001). *In vivo* transfection of lamprey brain neurons by gene gun delivery of DNA, *Exp. Neurol*, **167**(2): 304-311.

Zhang M.J., Tao W.M., Pianetta P.A., (2007). Dynamics modelling of biolistic gene guns, *Phys. Med. Biol.*, **52**:1485-1493

Zhao H.Y., Avenarius M.R, Gillespie P.G., (2012). Improved biolistic transfection of hair cells, *PLoS ONE*, **7**(10): e46765

Zhao Y., J., Zhang J.,Y., Yang X.,L., (2006). Design and Manufacture of Microneedles Array for Transdermal Drug Delivery, *Chinese Journal of Medical Instrumentation*, **30**(1): 33-38

Zhou F., (2000). High-pressure Gas Gene Gun, Chinese Patent No. CN 1262323A (Granted), *State Intellectual Property Office of the P.R. China*, China

Zhou F., (2007). Liquid Gene Gun, Chinese Patent No.CN 189217A (Granted), *State Intellectual Property Office of the P.R. China*, China

Zhou W.Z., (1995). Gene Gun, Chinese Patent No. CN 2196119Y (Granted), *State Intellectual Property Office of the P.R. China*, China

Zhu, M., Chen, Y., Wang, Z. Lu, Y., Ge, H., Tang, Y. (2012). Fabrication Method for Hollow Microneedles for Drug Delivery. Nanjing University, Patent US 8137736 B2 (Granted), *United States Patent*, USA

Ziegler A.S., (2008). Needle-free delivery of powdered protein vaccine: a new and rapidly developing technique, *J. Pharm. Innov.*, **3**: 204-213

Zilony N., Tzur-Balter A., Segal E., Shefi O., (2013). Bombarding Cancer: Biolistic delivery of therapeutics using porous Si carriers, *Scientific Reports*, **3**: article number 2499

Zuraida A.R., Rahiniza K., Hafiza M.R.N., Roowi S., Zamri Z., Subramaniam S., (2010). Factors affecting delivery and transient expression of gusa gene in Malaysian indica rice MR 219 callus via biolistic gun system, *African Journal of Biotechnology*, **9**(51):8819-8818

Appendix A: The drag coefficient equations (Morsi *et al*, 1972)

$C_d = 24.0/\mathrm{Re}$ for Re<0.1,

$C_d = 22.73/\mathrm{Re} + 0.0903/\mathrm{Re}^2 + 3.69$ for 0.1<Re<1.0,

$C_d = 29.1667/\mathrm{Re} - 3.8889/\mathrm{Re}^2 + 1.222$ for 1.0<Re<10.0

$C_d = 46.5/\mathrm{Re} - 116.67/\mathrm{Re}^2 + 0.6167$ for 10.0<Re<100.0

$C_d = 98.33/\mathrm{Re} - 2778/\mathrm{Re}^2 + 0.3644$ for 100.0<Re<1000.0

$C_d = 148.62/\mathrm{Re} - 4.75\times10^4/\mathrm{Re}^2 + 0.357$ for 1000.0<Re<5000.0

Appendix B: The mathematical model of the microneedle assisted micro-particle delivery

(1). Main code for the microneedle assisted micro-particle delivery

```
clear all
global theta1 R1 theta2 Rb sigma1
global rhof muf mp rp Rc mc
global Ln Rt d Lm R2 n tol
global mum rhosc rhove sigma2 Tsc


rhos = 19920;                    % the density of micro-particle (kg/m3)

%rhos = 8000;                     % the denisty of steel
rhof = 1.29;                     % the density of fluid (kg/m3)
rhosc = 1500;                     % the density of sc(kg/m3)
rhove = 1150;                    % the density of ve(kg/m3)
rp = 1.5e-6;                      % the radius of the micro-particle (m)
sigma1 = 10000000;                % the yield stress of SC(Pa)
sigma2 = 2200000;                 % the yield stress of epidermis(Pa)
Rc = 0.001;                      % the radius of cluster (m)
mc = 0.001;                      % the mass of cluster (kg)
mp = 4*pi*rp^3*rhos/3;             % mass of the micro-particle (kg)
muf = 1.85e-5;                    % the viscosity of fluid (Pa s)
Rb = 0.006;                      % Nozzle entry radius (m)
Rt = 0.006;                      % Nozzle exit radius (m)
Ln = 0.005;                      % the length of nozzle(m)
Lm = 0.001149;                    % the length of microneedle hole(m)
Tsc = 2e-5;                      % the thickness of sc(m)
Tve = 1e-4;                      % the thickness of epidermis(m)
muw = 8.9e-4;                     % the viscosity of water (Pa s)
mum = 19.6;                        % the friction coefficient between
                                     particle and skin
theta2 = atan((Rt-Rb)/Ln);         % wall angle (rad)
en = 1.0;                        % normal coeff of restitution (-)
et = 1.0;                        % tangential coeff of restitution (-)
Np = 1;                          % number of particle trajectories
n = 5;                           % number of microneedle
m = n+1;                         % number of space
R1 = 0.00020;                     % needle entry radius (m)
R2 = 0.00005;                     % needle exit radius (m)
d = (2*Rt-n*2*R1)/m;                % the space between each microneedle
ncol = 200;                      % number of color
theta1 = atan((R1-R2)/Lm);         % microneedle angle (rad)
```

```
tol = 1e-7;
La = 0.003;                    % the length of agarose
Ra = 0.009;                    % the radius of agarose
fr = 0.5;                      % the fraction of microneedle length
inserted in the skin
Ar = 2;                        % the ratio between muscle thickness and
microneedle length
sum = 0;                       % the number of micro-particle pass through
the needle at the begining
sum1 = 0;                      % the number of micro-particle stopped at
sum2 = 0;                      % the number of micro-particle stopped at

%The acceleration stage
%Constant
Rw=0.00375;                      % the radius of the barrel(m)
V1 = 0.001;
y=1.4;                         % the heat capacity ratio
M1 = 0.00125;

La=[0:0.001:0.5];                % the lenght of acceleration stage(m)

P1 =300000;
u1=sqrt(2*(P1*V1^y*(((V1+pi*Rw^2*La)).^(1-y)-(V1^(1-y))))/(M1*(1-y)))
;

figure(1)
plot(La,u1,'b-')
xlabel('The acceleration stage distance [m]')
ylabel('The velocity of ground slide [m/s]')

grid


%The deceleration stage

options = optimset('TolFun',1E-6,'Display','off');

%intial states and simulation length for the cluster decelerated in the
air
l2=linspace(0,0.01,10);

%simulation
[D1,u2]=ode45('rhs_fun_ac',l2,u1(end), options);
```

```
figure(2)
plot(D1,u2,'b-')
xlabel('The travel distance of cluster in the air [m]')
ylabel('The velocity of cluster in the air [m/s]')

grid

%The energy lost during the separation stage
u3 = u2(end)*0.8;


%intial states and simulation length for the micro-particle decelerated
in the nozzle
figure(3)
clf
set(gca,'xlim',[-0.01 0.01],'ylim',[0 Ln+(Ar+1)*Lm]);
box on
hold on;
xlabel('Radial position (m)','fontsize',20);
ylabel('Axial position (m)','fontsize',20);
set(gca,'FontName','arial','FontSize',20);

% Plot the location and structure of nozzle and agarose gel in the figure
3
plot([-Rt -Rt], [0 Ln], '-k','LineWidth',2);
plot([Rt Rt], [0 Ln], '-k','LineWidth',2);
plot([Ra Ra],[Ln Ln+(Ar)*Lm],'-k','LineWidth',2);
plot([-Ra -Ra],[Ln Ln+(Ar)*Lm],'-k','LineWidth',2);
plot([Rt Ra],[Ln Ln],'-k','LineWidth',2);
plot([-Rt -Ra],[Ln Ln],'-k','LineWidth',2);
plot([-Ra Ra],[Ln+(Ar)*Lm Ln+(Ar)*Lm],'-k','LineWidth',2);
plot([Rt-d-(Tsc*tan(theta1)) Ra],[Ln+Tsc Ln+Tsc],'-k','LineWidth',2);
plot([-Rt+d+(Tsc*tan(theta1)) -Ra],[Ln+Tsc
Ln+Tsc],'-k','LineWidth',2);
plot([Rt-d-((Tsc+Tve)*tan(theta1)) Ra],[Ln+Tsc+Tve
Ln+Tsc+Tve],'-k','LineWidth',2);
plot([-Rt+d+((Tsc+Tve)*tan(theta1)) -Ra],[Ln+Tsc+Tve
Ln+Tsc+Tve],'-k','LineWidth',2);


for i= -Rt+d:2*R1+d:Rt-d-2*R1

plot([i i+R1-R2], [Ln Lm+Ln], '-k','LineWidth',2);
```

```
end

for i= -Rt+2*R1+d : 2*R1+d : Rt-d

plot([i i-R1+R2], [Ln Lm+Ln], '-k','LineWidth',2);

end

for i= -Rt : 2*R1+d : Rt

plot([i i+d], [Ln Ln], '-k','LineWidth',2);
end

for i= -Rt+d+R1-R2 : 2*R1+d : Rt-d-R1+R2

plot([i i+2*R2], [Ln+Lm Ln+Lm], '-k','LineWidth',2);
end

for i= -Rt+2*R1+d-((Tsc+Tve)*tan(theta1)) : 2*R1+d:
Rt-d-2*R1+((Tsc+Tve)*tan(theta1))

plot([i i+d+2*((Tsc+Tve)*tan(theta1))], [Ln+Tsc+Tve Ln+Tsc+Tve],
'-k','LineWidth',2);
end

for i= -Rt+2*R1+d-((Tsc)*tan(theta1)) : 2*R1+d:
Rt-d-2*R1+((Tsc)*tan(theta1))

plot([i i+d+2*(Tsc*tan(theta1))], [Ln+Tsc Ln+Tsc], '-k','LineWidth',2);
end
%vrexit = [];
%vzexit = [];



% Simulation of micro-particles travelling along a nozzle and agarose gel

for i=1:Np

    tstart = 0;

    vz0 = u3;                          % particle initial axial velocity (m/s)
    a = 20;                              % radial velocity (% of axial
velocity)
```

```
    r0 = Rb*rand*sign(rand-0.5);
    z0 = 0;

    % choose radial component to be normally distributed with a mean of
0
    % and a standard deviation of a% of vz0

    vr0 = a/100*vz0*randn;

    y0 = [r0; 0; vr0; vz0];          % [ r (signed), z, vr (signed), vz]

    tfinal = 2*Ln/y0(4);              % estimate the max residence time
    refine = 6;
    options = odeset('RelTol',1e-7,...
                  'Events',@event_locator2,'Refine',refine);  %
    tout = tstart;
    yout = y0.';
    teout = [];
    yeout = [];
    ieout = [];

       while tstart < tfinal

          [t,y,te,ye,ie] = ode15s(@rhs_fun2,[tstart
tfinal],y0,options);

          cmap = jet(ncol);
          npts = length(y(:,1));
          maxspeed = 180;
          minspeed = 0;
          for j = 2 : npts
              speed = sqrt((y(j,3)^2+y(j,4)^2));
              col = max(ceil(((speed - minspeed)/(maxspeed -
minspeed))*ncol),1);

               plot([y(j-1,1) y(j,1)],[y(j-1,2)
y(j,2)],'color',cmap(col,:),'LineWidth',3);

          end

       % Accumulate output

          nt = length(t);
          tout = [tout; t(2:nt)];
```

```
            yout = [yout; y(2:nt,:)];
            teout = [teout; te];    % Events at tstart are never reported.
            yeout = [yeout; ye];
            ieout = [ieout; ie];

        % Set the rebound conditions

            y0(1) = y(nt,1);
            y0(2) = y(nt,2);
            vri = y(nt,3);
            vzi = y(nt,4);


        % Check if particle has collided with wall of nozzle
            if abs(Ln - y0(2))/Ln > tol
              if y0(2) <Ln
                if y0(1) < 0
                  theta_1 = theta2;
                else
                  theta_1 = -theta2;
                end

                  y0(3) =
-sin(theta_1)*et*(cos(theta_1)*vzi-vri*sin(theta_1))+ ...

cos(theta_1)*(-vri*cos(theta_1)-sin(theta_1)*vzi)*en;
                  y0(4) =
cos(theta_1)*et*(cos(theta_1)*vzi-vri*sin(theta_1))+ ...

sin(theta_1)*(-vri*cos(theta_1)-sin(theta_1)*vzi)*en;

              end

            end


              if speed < 1e-5
                break
              end

         % Check if particle has stoped in the agarose gel


            tstart = t(nt);
```

```
        end
     % Interpolate to obtain exit velocities and store in vectors

    if  y0(2) >= Ln & y0(2) < Ln+Tsc
        sum = sum +1;
    else
        sum = sum;
    end

    if  y0(2) >= Ln+Tsc & y0(2) < Ln+Tsc+Tve
        sum1 = sum1 +1;
    else
        sum1 = sum1;
    end

    if  y0(2) >= Ln+Tsc+Tve
        sum2 = sum2 +1;
    else
        sum2 = sum2;
    end

    title('Micro-particle trajectories','fontsize',20);
    figure(3)
    if ~isempty(yeout)
        plot(yeout(:,1),yeout(:,2),'or');
    end

end

% plot a colorbar in the figure 3 to show a scale of velocity range

colorbar1 = colorbar('ylim',[3 50], ...
       'YTickLabel',...

{'0','20','40','60','80','100','120','140','160','180'},'fontsize',18
);

figure(4)

clf
set(gca,'xlim',[0 4],'ylim',[0 100]);
box on
```

```
hold on

N1 = (sum/Np)*100;% Measure the percentage of micro-particle can pass
through the needle
N2 = (sum1/Np)*100;
N3 = (sum2/Np)*100;
N = [N1  N2  N3];

bar(N);

set(gca,'XTickLabel',{'','','Inside the stratum corneum','','Inside the
viable epidermis','','Inside the dermis'});

ylabel('Percentage(%)','fontsize',20);
set(gca,'FontName','arial','FontSize',19);

%The deceleration stage in the agarose gel

l=linspace(0,0.0025,1);
options = optimset('TolFun',1E-4,'Display','off')

[D3,u4] = ode15s('rhs_fun1',l,u3, options);
[D4,u5] = ode23('rhs_fun3',l,u3, options);

figure(5)
clf
set(gca,'xlim',[0 0.0025],'ylim',[2 150])
box on
hold on;
plot(D3,u4,'k--',D4,u5, 'k-' )
xlabel('The travel distance of micro-particle in the skin
[m]','fontsize',12)
ylabel('The velocity of micro-particle in the skin [m/s]','fontsize',12)
legend('The micro-particle penetrates the skin','The micro-particle
penetrates via the pierced hole on the skin')
```

(2). Function code to calculate the velocity of micro-particles before impact on the mesh

```
%this code is for calculation of velocity
function du=fun_ac(l,u)

global rhof muf Rc mc
```

```
%differential equation

Re=rhof*u*2*Rc/muf;     %Cluster Reynolds number in the channel

if Re<=0.1
   Cd=24.0/Re;
elseif Re<=1
   Cd=22.73/Re+0.0903/Re^2+3.69;
elseif   Re<=10
   Cd=29.1667/Re-3.8889/Re^2+1.222;
elseif   Re<=100
   Cd=46.5/Re-116.67/Re^2+0.6167;
elseif   Re<=1000
   Cd=98.33/Re-2778/Re^2+0.3644;
else
   Cd=148.62/Re-47500/Re^2+0.357;
end

du=-Cd*rhof*u*pi*Rc^2/(2*mc);
end
```

(3). Function code for two dimension analysis of micro-particles decelerating in the deceleration stage

```
function dydt = rhs_fun(t,x)

global rhof muf mp rp Ln Lm d R1 n Re R2 sigma1 rhosc mum rhove sigma2
Tsc

vr = x(3);
vz = x(4);

v = sqrt(vr^2+vz^2);              % absolute velocity of micro-particle

Re = rhof*v*2*rp/muf;              % micro-particle Reynolds number

if Re <= 0.1
   Cd = 24.0/Re;
elseif Re<=1
   Cd = 22.73/Re+0.0903/Re^2+3.69;
elseif   Re <= 10
   Cd = 29.1667/Re-3.8889/Re^2+1.222;
elseif   Re <= 100
   Cd = 46.5/Re-116.67/Re^2+0.6167;
elseif   Re <= 1000
```

```
   Cd = 98.33/Re-2778/Re^2+0.3644;
else
   Cd = 148.62/Re-47500/Re^2+0.357;
end

rho=0;
sigma_y=0;

if x(2) > Ln & x(2) < Ln+Tsc
    rho = rhosc;
    sigma_y = sigma1;
elseif x(2) > Ln+Tsc
    rho = rhove;
    sigma_y = sigma2;
end

 if   x(2) < Ln | x(2) < Ln+Lm & rem(n,2) == 0 & abs(rem(x(1),d+2*R1)) >
0.5*d & abs(rem(x(1),d+2*R1)) <  0.5*d+2*R1 &  x(2) <
(Lm/(R1-R2))*abs(rem(x(1),d+2*R1))+Ln-0.5*d*(Lm/(R1-R2)) & x(2) <
(Lm/(R2-R1))*abs(rem(x(1),d+2*R1))+Ln-(0.5*d+2*R1)*(Lm/(R2-R1))...
       | x(2) < Ln+Lm & rem(n,2) == 1 & abs(rem(x(1), d+2*R1)) >  R1+d
& abs(rem(x(1), d+2*R1)) < d+2*R1  & x(2) <
(Lm/(R1-R2))*abs(rem(x(1),d+2*R1))+Ln-(R1+d)*(Lm/(R1-R2))| x(2) <
Ln+Lm & rem(n,2) == 1 &  abs(rem(x(1), d+2*R1)) < R1 & x(2) <
(Lm/(R1-R2))*abs(rem(x(1),d+2*R1))+Ln+R1*(Lm/(R1-R2)) & x(2) <
(Lm/(R2-R1))*abs(rem(x(1),d+2*R1))+Ln-R1*(Lm/(R2-R1))

   dydt(1) = vr;                          % radial velocity
   dydt(2) = vz;                          % axial velocity
   dydt(3)=-Cd*rhof*vr*v*pi*rp^2/(2*mp);   % radial drag
   dydt(4)=-Cd*rhof*vz*v*pi*rp^2/(2*mp);   % axial drag
   dydt = dydt';


 else
   dydt(1) = vr;                          % radial velocity
   dydt(2) = vz;                          % axial velocity
   dydt(3)=
-(3*sigma_y*pi*vr*rp^2/(mp*v))-(0.5*rho*vr*v*pi*rp^2/(2*mp))-(6*pi*rp
*mum*vr/mp); % radial drag
   dydt(4)=
-(3*sigma_y*pi*vz*rp^2/(mp*v))-(0.5*rho*vz*v*pi*rp^2/(2*mp))-(6*pi*rp
*mum*vz/mp); % axial drag
   dydt = dydt';
```

```
 end
```

(4). Function code to measure the penetration depth of micro-particles without using microneedle

```
function du = rhs_fun1(l,v)

global  mp rp sigma1 rhosc mum rhove sigma2 Tsc

rho=0;

sigma_y=0;

if l < Tsc
    rho = rhosc;
    sigma_y = sigma1;
else
    rho = rhove;
    sigma_y = sigma2;
end

du = -(3*sigma_y*pi*rp^2/(mp*v))-(0.5*rho*v*pi*rp^2/(2*mp))
-6*pi*rp*mum/mp;   % axial drag
```

(5). Function code to measure the penetration depth of micro-particles through the pierced holes

```
function du = rhs_fun3(l,v)

global  mp rp mum sigma2 muf rhof Lm rhove
 Re = rhof*v*2*rp/muf;              % micro-particle Reynolds number

if Re <= 0.1
   Cd = 24.0/Re;
elseif Re<=1
   Cd = 22.73/Re+0.0903/Re^2+3.69;
elseif   Re <= 10
   Cd = 29.1667/Re-3.8889/Re^2+1.222;
elseif   Re <= 100
   Cd = 46.5/Re-116.67/Re^2+0.6167;
elseif   Re <= 1000
   Cd = 98.33/Re-2778/Re^2+0.3644;
else
   Cd = 148.62/Re-47500/Re^2+0.357;
end
```

```
if l < Lm
du = -Cd*rhof*v*pi*rp^2/(2*mp);  %micro-particle travel in the needle
hole
else
du = -(3*sigma2*pi*rp^2/(mp*v))-(0.5*rhove*v*pi*rp^2/(2*mp))
-6*pi*rp*mum/mp;   % micro-particle penetrate into the skin
end
```

(6). Event code to define the event locators of the rebound and impact points

```
unction [value,isterminal,direction] = event_locator2(t,y)
% Locate the time when height passes through zero in a
% decreasing direction and stop integration.

global theta1 R1 theta2 Rb Ln d n

   if y(2) < Ln

      value1 = Rb+y(2)*tan(theta2)-abs(y(1));    % Detect impact

   elseif   rem(n,2) == 1 & abs(rem(y(1),d+2*R1)) <= d+R1 &
abs(rem(y(1),d+2*R1))  >= R1   % the location of the space between each
microneedle

            % when the number of microneedle is a odd number

          value1 = Ln-abs(y(2));    % Detect impact


   elseif rem(n,2) == 0 & abs(rem(y(1),d+2*R1)) <= 0.5*d &
abs(rem(y(1),d+2*R1)) >= 0 ...
          | rem(n,2) == 0 & abs(rem(y(1),d+2*R1)) >= 0.5*d+2*R1 &
abs(rem(y(1),d+2*R1))  <= d+2*R1

          value1 = Ln-abs(y(2));


   else
      if rem(n,2) ==1

        if   abs(rem(y(1), d+2*R1))> d+R1 & abs(rem(y(1), d+2*R1))<
d+2*R1...
```

```
            value1 = R1-(y(2)-Ln)*tan(theta1)-abs(abs(rem(y(1),
d+2*R1))-d-2*R1);
        elseif    abs(rem(y(1), d+2*R1)) < R1
             value1 = R1-(y(2)-Ln)*tan(theta1)-abs(rem(y(1), d+2*R1));
        end
      else
         if  abs(rem(y(1), d+2*R1)) > 0.5*d & abs(rem(y(1), d+2*R1)) <
0.5*d+2*R1
             value1 = R1-(y(2)-Ln)*tan(theta1)-abs(abs(rem(y(1),
d+2*R1))-0.5*d-R1);
         end
      end
   end

value2 = sqrt(y(3)^2+y(4)^2)-1e-10;  % velocities < 1e-10 m/s have
effectively stopped

value=[value1; value2];
isterminal = [1; 1];      % Stop the integration
direction = [-1; -1];     % decreasing function only
```